Studies on irradiated pixel detectors for the ATLAS IBL and HL-LHC upgrade

vorgelegt von
Dipl.-Ing.
Christian Gallrapp
aus Erlangen

Von der Fakultät IV - Elektrotechnik und Informatik
der Technischen Universität Berlin
zur Erlangung des akademischen Grades

Doktor der Ingenieurwissenschaften
Dr.-Ing.

genehmigte Dissertation

Promotionsausschuss:	
Vorsitzender:	Prof. Dr.-Ing. Roland Thewes
Gutachter:	Prof. Dr.-Ing. Christian Boit
Gutachter:	Prof. Dr. Claus Gößling
Gutachter:	Dr. Dipl.-Ing. Heinz Pernegger
Tag der wissenschaftlichen Aussprache:	04.12.2014

Berlin — 2015

Zusammenfassung

Der steigende Bedarf der Hochenergiephysik nach höherer Luminosität ist die Ursache für die ständigen Bemühungen die eingesetzten Beschleuniger sowie die Experimente an die damit zunehmenden Anforderungen anzupassen. Das Upgrade-Programm der Experimente und der Beschleuniger am CERN umfasst bereits mehrere Ausbaustufen des Large Hadron Colliders (LHCs), die die Luminosität sowie den Energiebereich des Beschleunigers erhöhen werden. Die Experimente am LHC arbeiten gleichzeitig daran, die einzelnen Sub-Detektoren auf die steigenden Anforderungen in den kommenden Jahren vorzubereiten. Speziell Tracking Detektoren müssen in Zukunft für in Hochenergie Physik Experimenten bislang ungesehenen Fluenzen zurechtkommen. Mit dem Anstieg der Fluenz nehmen ebenfalls Strahlenschäden zu, die die Lebensdauer der Detektoren durch abnehmende Leistungsfähigkeit begrenzt. Um diesen Effekt zu kompensieren, werden für die kommenden Upgrade-Schritte neue und strahlenhärtere Detektorkonzepte mit längeren Lebensdauern notwendig.

Diese Arbeit konzentriert sich darauf, die Einflüsse von Strahlenschäden auf verschiedene Pixel Sensor Technologien zu untersuchen. Die untersuchten Technologien sind mögliche Kandidaten für den Einsatz im kommenden Updgrade des ATLAS Pixel Detektors sowie für Anwendungen im ATLAS Experiment unter HL-LHC Bedingungen. Die betrachteten Sensoren umfassen verschiedene Designs basierend auf Silizium und Diamant als Sensormaterial. Die untersuchten Silizium Designs beinhalten ein planar Pixel Design, das breits im ATLAS Experiment eingesetzt wird sowie ein 3D Pixel Design, bei dem der Sensor über die gesamte Dicke von Elektroden durchzogen ist. Das Diamant Design nutzt auf dem Sensor angebrachte Elektroden ähnlich den planar Designs, wobei Diamant Sensoren aus single- und polykristallinem Material zur Verfügung stehen.

Um die Eigenschaften der Sensoren zu untersuchen, werden diese vor und nach Bestrahlung durch Protonen oder Neutronen getestet und charakterisiert. Ein Teil dieser Messungen untersucht das Zusammenspiel der Ausleseelektronik und der Sensoren, um sicherzustellen, dass die Signale auch nach Bestrahlung zuverlässig ausgelesen werden können. Weitere Tests konzentrieren sich auf die Eigenschaften der Sensoren selbst, was zum einen das Strom-Spannungs-Verhalten sowie die Eigenschaften bezüglich der Ladungssammlung umfasst. Hierzu stehen Messungen mit radioaktiven Quellen sowie Teilchenstrahlen aus Pionen und Elektronen zur Verfügung.

Abschließend werden die durchgeführten Entwicklungsschritte des für 2013/2014 geplante IBL Upgrades des ATLAS Pixel Detektors zusammengefasst. Dies beinhaltet unter anderem den Ablauf des Qualitätssicherungsverfahrens sowie die Herstellung eines Prototypen der Strukturelemente für die neue Pixeldetektorlage. Mit diesem Prototypen eines sogenanten Staves wurde daraufhin der komplette Stave Produktionsablauf getestet.

Abstract

The constant demand for higher luminosity in high energy physics is the reason for the continuous effort to adapt the accelerators and the experiments. The upgrade program for the experiments and the accelerators at CERN already includes several expansion stages of the Large Hadron Collider (LHC) which will increase the luminosity and the energy of the accelerator. Simultaneously the LHC experiments prepare the individual sub-detectors for the increasing demands in the coming years. Especially the tracking detectors have to cope with fluence levels unprecedented for high energy physics experiments. Correspondingly to the fluence increases the impact of the radiation damage which reduces the life time of the detectors by decreasing the detector performance and efficiency. To cope with this effect new and more radiation hard detector concepts become necessary to extend the life time.
This work concentrates on the impact of radiation damage on the pixel sensor technologies to be used in the next upgrade of the ATLAS Pixel Detector as well as for applications in the ATLAS Experiment at HL-LHC conditions. The sensors considered in this work include various designs based on silicon and diamond as sensor material. The investigated designs include a planar silicon pixel design currently used in the ATLAS Experiment as well as a 3D pixel design which uses electrodes penetrating the entire sensor material. The diamond designs implement electrodes similar to the design used by the planar technology with diamond sensors made out of single- and poly-crystalline material.
To investigate the sensor properties characterization tests are performed before and after irradiation with protons or neutrons. The measurements are used to determine the interaction between the read-out electronics and the sensors to ensure the signal transfer after irradiation. Further tests focus on the sensor performance itself which includes the analysis of the leakage current behavior and the charge collection properties. The sensor responds to the passing of a charged particle are measured with radioactive sources and particle beams of electrons and pions.
To conclude the sensor research the accomplished development stages of the IBL upgrade of the ATLAS pixel detector foreseen for 2013/2014 are summarized. This includes among other things, the progress of the quality assurance process as well as the production of a first stave prototype used to test the stave production process.

Contents

Introduction

Since the first fabrication of a pn-junction the application of semi-conductor material became indispensable in our daily live. Further developments related to semi-conductor devices advanced products and technologies in different ways. One of the research fields affected by these new developments focuses on the application of electronic components in environments with ionizing radiation. Space or high altitude flights, nuclear reactors and particle accelerators for high energy experiments or medical applications as X-ray detectors, tomography and particle therapy for cancer treatment are only few of the domains which need to cope with the effects of ionizing radiation.
Particle accelerators in high energy physic experiments or particle therapy centers need to accelerate charged particles creating high energetic radiation. The different atomic interactions taking place in a nuclear reactor create all kind of radiation creating an overall hostile environment for electronic equipment. Long time space missions such as the ISS, missions to distant planets but also satellites are exposed to cosmic radiation. Electronic components start to deteriorate in these environments due to the radiation levels causing radiation damage.
In all these cases the implemented systems need to be designed to withstand the effects of high energetic particles on the material. Depending on the purpose of a system it might be possible to protect the sensitive electronics by shielding it with lead or other dense materials. In the case of radiation sensors it becomes unavoidable that the electronics gets close to the radiation source. As the radiation damage in the material accumulates over time it eventually causes a degradation or a failure of the component. Due to different restrictions it is not always possible to simply replace damaged devices. Therefore it becomes unavoidable to develop radiation hard devices to assure the operation over a long period of time after the exposure of high levels of radiation. The development of these devices can be based on simulations and on aging studies by artificial irradiation. With an increasing number of particles a device is exposed to, it becomes more and more difficult to simulate the device properties. Thus after a certain fluence level only the option to test artificially irradiated devices remains to assure the operation.

The need for high event rates in High Energy Physics (HEP) experiments creates a constant demand for high luminosity at high energies. Particle detectors as in the ATLAS Experiment at the LHC are build to be operated for several years without having the opportunity to replace damaged electronics or sensors. Radiation hard sensors and electronics are the only way to endure the desired operation periods [1]. To cope with the increase in radiation and

longer operation periods radiation hard technologies need to be enhanced or new technologies have to be developed [2, 3, 4]. Due to these restrictions unprecedented fluence levels are expected by the LHC experiments in the coming years. As a result simulations can not be used as basis to select a sensor technology to be implemented in a detector. Correspondingly devices need to be artificially irradiated and tested to assure the proper operation up to the expected fluence levels.
So far planar silicon was mainly used as material for pixel and strip sensors in HEP applications. This is partially related to the success of silicon in general microelectronic products which accelerated the research in this field. Due to a long history with planar sensors lots of know-how was accumulated concerning the properties of this sensor technology which assures a high quality and reproducibility. An upcoming sensor technology known as 3D sensors uses vertical electrodes penetrating the bulk material to form read-out cells with short electrode distances which is correlated with high radiation hardness [5]. A further material for radiation hard sensors is artificial diamond fabricated by means of a chemical vapor deposition process [6]. Single- and poly-crystalline diamonds are already used for different applications in HEP and might be a possible option for the application as pixel sensors.

This work is focusing on the testing and the evaluation of radiation hard pixel sensor modules for future applications in the ATLAS Experiment. Upcoming upgrades of the experiments in 2013 and 2022 are going to set new and unprecedented design fluences and doses for sensors and read-out chips. The first upgrade will increase the levels up to $5 \cdot 10^{15}\ n_{eq}\ cm^{-2}$ and 250 Mrad while it is going to further increase to more than $10^{16}\ n_{eq}\ cm^{-2}$ and 500 Mrad during the next upgrade step. Different designs of the three sensor technologies silicon planar, silicon 3D and diamond planar before and after irradiation were tested to analyze their properties in terms of radiation hardness.
Chapter 1 gives an overview of CERN, the LHC, the ATLAS Experiment and the foreseen upgrade steps of the ATLAS Experiment. These focus on the Insertable B-Layer (IBL) and Diamond Beam Monitor (DBM) upgrade in 2013. A summary of the basic characteristics of semiconductor particle detectors is given in Chapter 2 summarizing the interaction with radiation and semiconductor principals. Chapter 3 describes the different parts and the fabrication of pixel detector modules used for the characterization before and after irradiation. The obtained results of the module characterization including measurements with radioactive sources and test beams are compared in Chapter 4. An overview of the first steps during the IBL module production and tests with the first prototype stave are given in Chapter 5. Chapter 6 summarizes the obtained results, compares the different sensor properties and gives an outlook for future radiation hard sensor technologies.

1 LHC and the ATLAS Experiment at CERN

The European Organization for Nuclear Research (CERN) in Geneva, Switzerland is a scientific research laboratory dedicated to work on fundamental physics. It was founded the 29 September 1954 after the "Convention for the Establishment of a European Organization for Nuclear Research" was ratified by the twelve founding member states: Belgium, Denmark, France, the Federal Republic of Germany, Greece, Italy, the Netherlands, Norway, Sweden, Switzerland, the United Kingdom of Great Britain and Northern Ireland, and Yugoslavia [7].

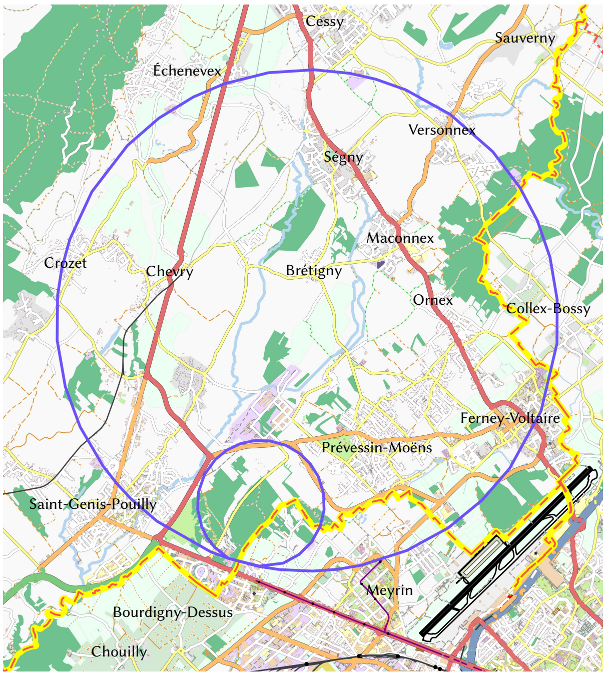

Figure 1.1: Map of the LHC at CERN crossing the franco-swiss border [8].

Since the start of the LHC in 2008 the public focus is directed towards the discoveries of the experiments attached to the collider. The most known are the two general purpose detectors ATLAS and CMS as well as the ALICE Experiment for heavy ion collision and the LHCb Experiment dedicated to b-physics. One of the recent findings was the discovery of a Higgs boson by the ATLAS and CMS collaborations [9, 10].

1.1 Large Hadron Collider - LHC

The LHC is a hadron collider build in the underground tunnel of its predecessor the Large Electron-Positron Collider at CERN. It has a circumference of about 27 km and is placed in a depth of 45 m to 170 m underground close to the Jura mountains. The LHC tunnel shown in Fig. 1.1 consists of eight straight parts and eight arcs and provides the necessary space for the four experiments ALICE, ATLAS, CMS and LHCb as well as the acceleration stages [11]. The first operation of the LHC started in September 2008 but was stopped after nine days due to an incident at an electrical connection between two magnets. After the restart in November 2009 the first collisions were performed at the injection energy provided by the Super Proton Synchrotron (SPS) which was then increased to reach the beam energy of 3.5 TeV in March 2010.
Proton bunches with an injection energy of 450 GeV are provided via two transfer tunnels from the CERN accelerator complex. LHC can store up to 2808 bunches per proton beam which are separated by a bunch crossing frequency of 40 MHz corresponding to 25 ns [11]. During the operation in 2010 and 2011 a beam energy of 3.5 TeV corresponding to collisions with a center of mass energy of 7 TeV was obtained. After reworks performed during the winter shut-down between 2011 and 2012 particles get accelerated up to 4 TeV creating collisions with a center of mass energy of 8 TeV [12]. A long shut-down period between 2013 and 2014 is used to prepare the collider for the operation under design conditions with an energy of 7 TeV per beam in order to reach the center of mass energy of 14 TeV for proton-proton collisions. To reach the design peak luminosity of $10^{34}\,\mathrm{cm}^{-2}\mathrm{s}^{-1}$ during proton-proton operation each bunch will hold up to $1.1 \cdot 10^{11}$ particles [13]. To keep the two proton beams in place the superconducting dipole magnets are operated at temperatures below 2 K to generate a peak dipole field of 8.33 T [11].

The existence of the Higgs boson as one of the missing particles in the standard model is one of the main questions physicists expect to answer with the results obtained during the operation of the LHC. In addition to other effects it is expected to observe new physics in the TeV range including supersymmetry or evidence of extra space-time dimensions [14].
From November 2009 till the winter shut-down in 2011 a total integrated luminosity of $5.61\,\mathrm{fb}^{-1}$ has been delivered with a beam energy of 3.5 TeV. Since the operation with 4 TeV started in 2012 till the end of the same year additional $23.3\,\mathrm{fb}^{-1}$ have been delivered to the ATLAS Experiment. With a rate of about 93.2 % recorded the ATLAS Experiment an integrated luminosity of $21.7\,\mathrm{fb}^{-1}$ and exceeded the expected $20\,\mathrm{fb}^{-1}$ for 2012 [13].

In order to overcome energy and intensity limitations of the LHC it was decided to perform three long shut-down periods including a maintenance and an upgrade program. The expected development of the integrated luminosity during the next years including the performance change related to the upgrade steps is shown in Fig. 1.2. The first LHC shutdown phase in 2013 will be used to upgrade the LHC for the operation at a center of mass en-

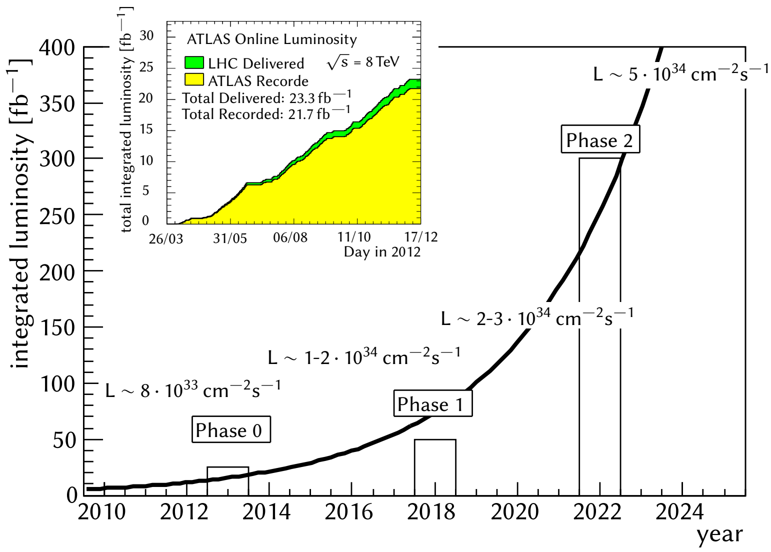

Figure 1.2: Expected development of the integrated luminosity and the luminosity over the three long shut-down periods till 2024 [13]. The recorded total integrated luminosity of the ATLAS Experiment in 2012 shown in the small plot is 21.7 fb^{-1} [15].

ergy of 14 TeV which will be constant during the upcoming years. The design luminosity of $1 \cdot 10^{34}\,cm^{-2}s^{-1}$ is expected to be reached in 2015 leading to a total integrated luminosity of 100 fb^{-1} until 2017. After the second shut-down in 2019 a luminosity increase of two to three times the nominal value will lead to a peak luminosity of $2 \cdot 10^{34}\,cm^{-2}s^{-1}$ to $3 \cdot 10^{34}\,cm^{-2}s^{-1}$ corresponding to additional 200 fb^{-1} until 2021. To reach this goal several modifications will be performed at the CERN accelerator complex including the connection of LINAC4 to the Proton Synchrotron (PS) and the Booster in order to replace LINAC2. For a further luminosity increase the High Luminosity LHC (HL-LHC) upgrade has been foreseen for the third shutdown around 2022. During this upgrade period LHC and the CERN accelerator complex will be enabled to handle enough particles to reach a peak luminosity of more than $5 \cdot 10^{34}\,cm^{-2}s^{-1}$ and delivering about 250 fb^{-1} per year. In total this will lead to an expected integrated luminosity of 3000 fb^{-1} in the twelve years of operation [13, 14].

1.2 ATLAS Experiment

The ATLAS Experiment (ATLAS) is one out of two general purpose experiments connected to the LHC. It was build in an about 80 m deep cavern at point 1 of the LHC tunnel. The experiment shown in Fig. 1.3(a) has a diameter of 25 m, a length of 44 m and an overall weight of about 7000 t. It consists of different components such as the Inner Detector shown in Fig. 1.3(b) surrounded by the solenoid magnet, the Calorimeters, the Muon Spectrometer with the toroidal magnets and the trigger and read-out system [16].

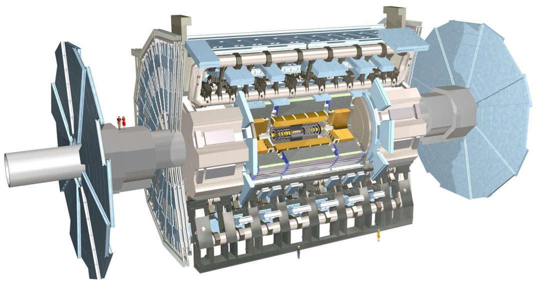

(a) Cross section of the ATLAS Experiment [16]

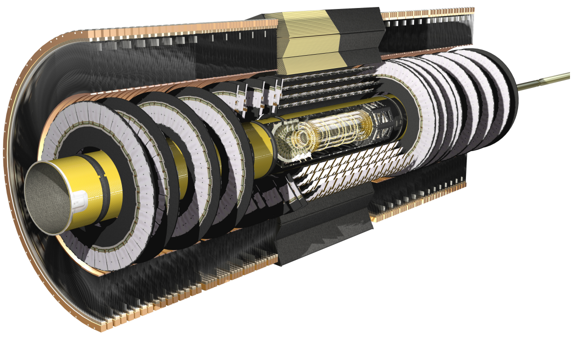

(b) Cross section of the Inner Detector [16]

Figure 1.3: The cross section of the ATLAS Experiment in Fig. 1.3(a) showing the Muon Spectrometer, Calorimeters and the Inner Detector. The three sub-detectors Transition Radiation Tracker, Semiconductor Tracker and Pixel Detector of the Inner Detector are shown in Fig. 1.3(b).

1.2.1 Inner Detector

The Inner Detector is dedicated to the track and vertex reconstruction of charged particles resulting from proton-proton interactions. Its diameter is about 230 cm with a length of 7 m housing three sub-detectors shown in Fig. 1.3(b). The Pixel Detector, the Semiconductor Tracker (SCT) and the Transition Radiation Tracker (TRT) are designed to operate at LHC luminosities of up to $10^{34}\,\mathrm{cm}^{-2}\mathrm{s}^{-1}$. Following the ATLAS design the Inner Detector covers an angular range relative to the beam axis corresponding to a pseudorapidity range of $|\eta| < 2.5$. To achieve the required momentum and vertex resolution high-precision measurements with a fine granularity are necessary. This is provided by three pixel and eight strip detector layers as well as up to 36 additional tracking points from the TRT. The implemented configuration assures a robust pattern recognition and high precision in ϕ and z. A magnetic field of 2 T parallel to the beam axis bends the path of charged particles to determine the particles transversal momentum and charge. Continuous tracking in the TRT additionally contributes to the momentum measurements of the particles and particle identification for electrons [17, 18].

Pixel Detector

The three layers of the pixel detector shown in Fig. 1.4 provide high-precision and fine granularity measurements close to the interaction point. It consists of three barrel layers with a nominal radius of 50.5 mm, 88.5 mm and 122.5 mm and three disks at each end of the pixel package. The three layers are build out of 112 staves holding 1456 pixel modules while the

48 endcap sectors hold additional 288 modules. These 1744 hybrid pixel modules with 46080 pixel read-out channels per module build together more than 80 million read-out channels. Each pixel module consist of a 250 µm planar n-in-n silicon pixel sensor with an active area of $16.4 \cdot 60.8\,\mathrm{mm}^2$ and 16 bump-bonded FE-I3 read-out chips. The nominal pixel size of 50 µm in ϕ-direction and 400 µm in z fits the corresponding front-end pixel cell. The chips provide amplification for each pixel and data storage until the arrival of the trigger decision [1].

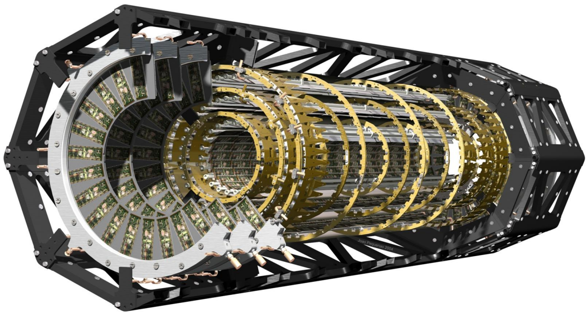

Figure 1.4: Cross section of the ATLAS Pixel Detector package showing the three barrel layers and three end-cap disks [16]

This detector configuration provides three high resolution space points for particles within the pseudorapidity range of $|\eta| < 2.5$. In ϕ-direction resolutions of about 12 µm and vertex reconstructions with z-resolutions of 100 µm can be achieved. The components implemented in the pixel detector correspond at a perpendicular incident angle to a radiation length of about 2.7 % per pixel layer [1, 17, 19, 20].
A radiation hard design was chosen for the modules to withstand a radiation dose of up to 50 Mrad and fluences of up to $1 \cdot 10^{15}\,\mathrm{n_{eq}\,cm^{-2}}$. The B-Layer as the innermost layer is expected to reach the dose of 50 Mrad after five years of operation. For the other two layers this limit will be reached after more than ten years of LHC operation [1].

Semiconductor Tracker (SCT)
The SCT contributes eight additional space points to the momentum measurement and the track reconstruction of the Inner Detector. It consists of four barrel layers at a radius of 300 mm, 373 mm, 447 mm and 520 mm and end caps with nine disks on both ends. Each of the 2112 SCT barrel modules is build out of four $63.6 \cdot 64.0\,\mathrm{mm}^2$ p-in-n silicon sensors holding two times 768 read-out strips with a 80 µm pitch. Two units of two daisy-chained sensor tiles building about 12 cm long strip sensors are glued back-to-back on a baseboard for cooling and mechanical support. To enable measurements in z-direction a rotation of 40 mrad between the modules is introduced during the gluing process. This sandwich design is also implemented in a wedge shape detector design for the end-cap modules to handle the space reduction at smaller radii. The read-out electronics of the barrel SCT modules is placed close to the center of the module where wire-bonds establish the connection to the individual

strips. In the experiment the strip modules in the barrel section are oriented parallel to the beam direction while the end cap strips point inwards. The SCT provides a resolution of 17 µm in the r-ϕ direction and 580 µm in z. Its contribution to the radiation length at $\eta = 0$ corresponds to $X/X_0 = 2.16\,\%$. Modules were irradiated and tested at bias voltages up to 500 V for the expected fluence of $2 \cdot 10^{14}\ n_{eq}\ cm^{-2}$ after 10 years of LHC operation [17, 19, 21, 22].

Transition Radiation Tracker (TRT)
The TRT design provides up to 36 additional track points for momentum measurements and pattern recognition with a distance of 559 mm to 1070 mm to the beam. It consists of a barrel part with 52544 axial and two end-caps with in total 245760 radial thin-walled proportional drift tubes. A film coating technology is used to build straws with a 35 µm thick multilayer wall to obtain the required mechanical and electrical properties. Low ohmic gold-plated tungsten wires with a diameter of 30 µm are used as anodes in the center of the straw. A gas mixture consisting of 70% Xe, 27% CO_2 and 3% O_2 was found to be an efficient transition radiation absorber and drift gas. The operation in high occupancy environments, electron identification due to the transition-radiation and an intrinsic radiation hardness are the advantages of the TRT. Drift time measurements provide the possibility to introduce a spacial resolution of 120 µm in the barrel and smaller than 100 µm in the endcap [17, 19, 23]. A total radiation dose of 10 Mrad at a fluence of $10^{14}\ n_{eq}\ cm^{-2}$ is expected in the TRT after 10 years of LHC operation [24].

1.2.2 Calorimeters

The calorimeters are dedicated to measure the energies of particles and jets in the ATLAS Experiment. The ATLAS calorimeter system is divided into the electromagnetic calorimeter and the hadronic calorimeter. Both systems implement a sampling technology using active detector and passive absorber material.

The electromagnetic calorimeter uses electromagnetic interactions to absorb and to measure photon and electron energies. It consists of a barrel and two end-caps covering a pseudorapidity range of $|\eta| < 3.2$. The electrodes and the absorber material are formed in an accordion design which provides full coverage in ϕ and fast signal extraction. The gaps between the absorber are filled with liquid argon (LAr) representing the active material of the detector. The lead absorber are glued to two stainless-steel sheets to increase the mechanical strength. Read-out electrodes formed out of patterned copper layers are used to create a segmentation in η. The signal in the read-out electrode is generated via capacitive coupling in the electrode at an operation voltage of 2000 V [16].

The hadronic calorimeter uses electromagnetic and nuclear interactions to measure the energies of hadrons which passed the electromagnetic calorimeter. It is divided in the tile

calorimeter parallel to the beam axis covering the pseudorapidity range for $|\eta| < 1.7$, the LAr hadronic end-cap calorimeter extending the pseudorapidity range from $1.5 < |\eta| < 3.2$ and the LAr forward calorimeter further increasing the range from $3.1 < |\eta| < 4.9$.
Steel and scintillator are used as absorber and active material in the tile calorimeter. It is divided in one barrel and two extended barrels surrounding the LAr hadronic end-cap calorimeter.
Both, the LAr hadronic end-cap calorimeter and the LAr hadronic end-cap calorimeter use liquid argon as active material. In case of the LAr hadronic end-cap calorimeter copper plates are implemented as absorber material using read-out electronics operated at 1800 V. The LAr forward calorimeter has to handle high particle fluxes due to the short distance to the beam pipe. As a result it implements smaller liquid argon gaps within the absorber material than the other calorimeters. The front part of the calorimeter implements an electromagnetic module with a copper absorber while the hadronic modules in the back use tungsten. The operation voltage of the modules varies between 250 V and 500 V [16].

1.2.3 Muon Spectrometer

The Muon Spectrometer is dedicated to measure muon tracks bend by the toroidal magnetic field to determine the muon momentum and charge. In addition provides the Muon Spectrometer a fast signal which is used as a Level-1 trigger in the ATLAS Experiment. Four different detector technologies are used to measure the muon trajectory and momentum with high precision. To reach a high accuracy the Muon Spectrometer spreads from a radius of about 4.25 m to the outermost part of the experiment at a radius of 11 m. The four detector technologies are used for two measurement purposes. While the Monitored Drift Tubes (MDT) and the Cathode Strip Chambers (CSC) are used for precision tracking the Resistive Plate Chambers (RPC) and the Thin Gap Chambers (TGC) handle the bunch crossing identification and provide the trigger function. In the pseudorapidity range of $|\eta| < 2.7$ provide the MDT and the CSC between 6 to 8 hits per track with a resolution of 100 μm. The RPC in the barrel or the TGC in the end cap region are the two detector parts providing a fast signal for the ATLAS trigger system [16, 25].

1.2.4 Trigger and Read-out system

To handle the enormous amount of data generated with a bunch crossing frequency of 40 MHz the trigger system of an experiment has to apply strong selection criteria to find interesting collisions. The ATLAS Trigger System is separated in Level-1 and Level-2 trigger which are followed by the event filter. Together the system is capable to reduce the trigger frequency to a rate of about 400 Hz representing the data storage limits.
The Level-1 trigger uses information from the muon chambers, calorimeters and forward detectors and is purely hardware based. Based on the data provided the Central Trigger Processor (CTP) takes the trigger decision with a latency of less then 2.5 μs. This first trigger level

reduces the rate of accepted events to 100 kHz. For the next level the data gets passed on to the Read-Out System. Here the software based Level-2 trigger performs a fast reconstruction process on regions of interest to refine the trigger decision. With an average processing time of 40 ms this trigger level reduces the event rate further to 3 kHz. The remaining events are then assembled by the event builder into a full event data structure and analyzed by the event filter. During this process the event rate drops down to about 200 Hz. With an average event size of 1.5 MB the ATLAS Trigger system reduced the amount of data by about seven orders of magnitude to 300 MBs^{-1} after the event filter [16, 26].

1.3 ATLAS upgrade

Following the upgrade efforts of the LHC the ATLAS Experiment is going to use the three long shutdown periods for maintenance and upgrade purposes. While the commissioning for Phase-0 in 2013-2014 is already taking place, letters of intend for Phase-1 and Phase-2 have been approved by the ATLAS Collaboration Board [27, 28].

Most relevant for the performance of the pixel detector is the development of the fluence and the total ionizing dose (TID) as the LHC upgrade progresses. The values given in Tab. 1.1 show an increase of one order of magnitude for the fluence and a more then 15 times higher TID from the ATLAS Pixel Detector to the ATLAS Inner Tracker (ITK) for the Phase-2 upgrade step. As the values given for the ITK are based on simulations and do not include a safety margin, higher design values will be defined.

	upgrade step	fluence	TID
ATLAS Pixel Detector		$1 \cdot 10^{15}\ n_{eq}\ cm^{-2}$	50 Mrad
ATLAS IBL	Phase-0	$5 \cdot 10^{15}\ n_{eq}\ cm^{-2}$	250 Mrad
ATLAS ITK	Phase-2	$1.4 \cdot 10^{16}\ n_{eq}\ cm^{-2}$	767 Mrad

Table 1.1: Development of the fluence and the TID for the different pixel detector upgrade steps. For the ATLAS Pixel Detector and the IBL the design values are given [1, 29]. The values for the ITK correspond to maximum values based on simulations for the ATLAS Phase-2 upgrade step [30].

1.3.1 Phase 0 - Insertable B-Layer Upgrade

During the first long shutdown several upgrade and maintenance points will be addressed in the ATLAS Experiment. One of the major activities is the Insertable B-Layer (IBL) upgrade with the intention to integrate a new innermost pixel layer in the Inner Detector. The challenge of the IBL is to develop a detector system radiation hard enough to be operated at a five times higher fluence and TID than the original pixel detector. To assure the operation

new and enhanced sensor designs are developed and tested. In addition a radiation hard front-end chip is needed to handle higher data rates in the future. To create the necessary space for this additional layer the present beam pipe will be replaced with a smaller one. The temporary removal of the current Pixel Detector from the Inner Detector provides the opportunity to replace the existing Service Quarter Panels (SQP) with new Service Quarter Panels (nSQP). An advancement to the diamond Beam Conditions Monitor (BCM) is the Diamond Beam Monitor (DBM) made out of eight three-layer diamond beam telescopes connected to the IBL read-out system.
Besides the upgrade efforts related to the IBL it is foreseen to perform a couple of additional upgrade activities. The development of new evaporative cooling plants is ongoing for SCT, Pixel Detector and IBL. The electronics of the calorimeters is following an additional upgrade procedure. A new neutron shielding is going to be introduced in the Muon Spectrometer and the outer part of the beam pipe made of stainless steal will be replaced with an aluminum beam pipe to reduce the background in the Muon Spectrometer [31].

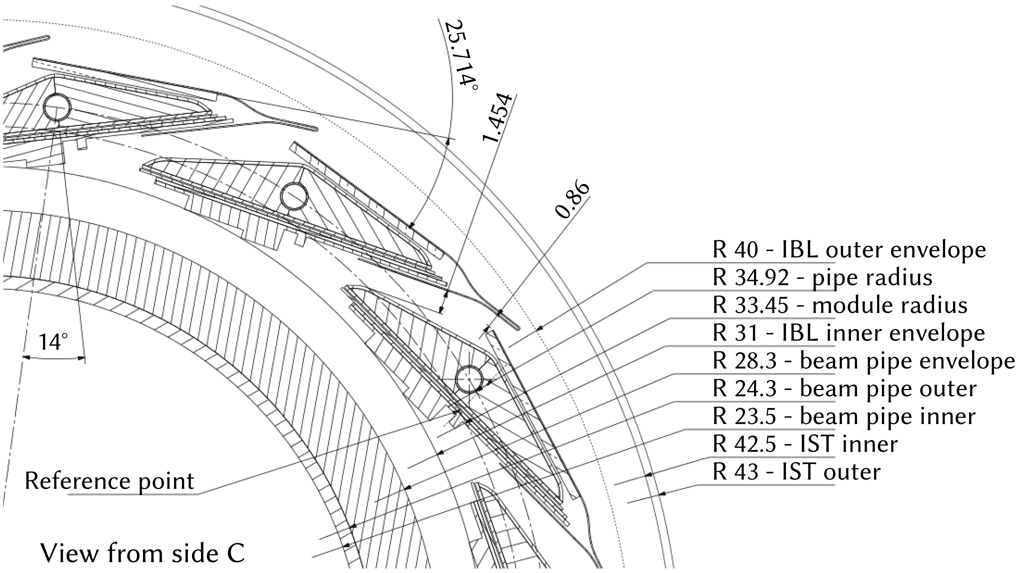

Figure 1.5: Cross section of the IBL layout showing the stave orientation, the IST and the dimensions of the new beam pipe [32].

The necessary space for the IBL shown in Fig 1.5 between the existing B-Layer and the beam pipe will be created by reducing the radius of the beam pipe by 4 mm to an outer beam pipe radius of 28.3 mm. The tasks for the IBL include an improvement of the vertex resolution, secondary vertex finding and b-tagging [29, 33]. At the same time it assures a continuous operation of at least three pixel layers to maintain the performance at high pile-up expected in the upcoming years.
The new layer consists of 14 staves surrounding the beam pipe, each tilted by 14° providing full coverage in ϕ-direction. A stave provides mechanical support and cooling for the IBL sensor modules and holds cables for module read-out and powering.

Boiling pipe, carbon-fiber-reinforced polymer (CFRP) skin and carbon foam are the three main parts of the IBL stave. The titanium boiling pipe with a diameter of 1.5 mm embedded in the carbon foam is part of the evaporative CO_2 cooling to reach temperatures below $-20\,^{\circ}C$ on the sensor. Properties as a high thermal conductivity and the low radiation length make carbon foam an ideal material providing uniform cooling combined with a low material budget. The CFRP skin is glued to the back of the stave to increase its structural stiffness. All 14 740 mm long staves are mounted on three mechanical support rings whereof the two outer rings are connected to the IST while the third ring stays floating in the center interconnecting the stave centers to minimize deformation due to gravity.
In the mixed sensor scenario each stave is equipped with 12 planar Double Chip Modules (DCMs) consisting of one sensor tile equipped with two read-out chips in the center and four 3D Single Chip Modules (SCMs) consisting of one sensor tile with one read-out chip on both ends. For this layout option 75 % and 25 % of the IBL modules are planar pixel and 3D pixel modules respectively. As there is not enough space to shingle the modules an inactive gap of about 205 µm is present between the modules.

The DBM is a spatially segmented detector to increase the possibilities of the ATLAS BCM providing luminosity and beam spot monitoring. Four three-layer diamond pixel beam telescopes on each side of the ATLAS Experiment will be attached horizontal and vertical to the beam axis for bunch-by-bunch luminosity monitoring. The telescopes will be installed at a distance of about 950 mm from the interaction point covering a pseudorapidity range between $3.0 < \eta < 3.4$. The 24 telescope planes consist of poly-crystalline Chemical Vapor Deposition (CVD) diamond sensors single chip modules with a sensor size of about $21 \cdot 18\,mm^2$. With a charge collection distance of 200 µm a most probable charge of $7200\,e^-$ is expected. The intrinsic radiation hardness and the low thermal resistance of diamond make the material an ideal solution for the application in high radiation regions as the forward direction of the ATLAS Experiment [33].
The purpose of the DBM is an improved bunch-by-bunch luminosity monitoring compared to the BCM. The high segmentation of the pixel module and the fast signal read-out in diamond sensors avoid the saturation of the material at high fluences. Three-layer telescopes enable tracking providing the capability to distinguish collision tracks from beam halo tracks.
The read-out of the telescopes will be implemented in the IBL read-out where the twelve modules on each side appear as one half stave. The modules will be operated at a threshold of $1100\,e^-$ with a maximum bias voltage of 1000 V.

1.3.2 Phase 1 Upgrade

During the second long shutdown the ATLAS Experiment is planing to prepare for an increased peak luminosity of $2 \cdot 10^{34}\,cm^{-2}s^{-1}$ or higher. This luminosity increase and the corresponding increase of interactions per bunch crossing at the design energy of 14 TeV needs to be handled by the detectors. The necessary upgrade efforts will mainly focus on the Muon

Spectrometer and the Calorimeter as well as the trigger and read-out system. To handle the luminosity increase after the upgrade a Fast Tracker (FTK) is proposed to provide fast track reconstruction. As part of the trigger upgrade the FTK will implement hardware based track finding and fitting algorithms to reduce the load on the ATLAS trigger system. The released resources of the trigger system can then be allocated to more sophisticated selection algorithms. The replacement of the muon small wheels at the beginning of the shutdown is the main priority during the phase 1 upgrade. In parallel the front-end electronics of both calorimeters will be upgraded to reduce high hit rates in the Level-1 trigger system [27, 34].

1.3.3 Phase 2 Upgrade

The dose and fluence collected in the Inner Detector by the time of the third long shutdown will have reached the design specifications of the individual sub-detectors. To be prepared for the high luminosity runs the ATLAS Collaboration is carrying out efforts to replace the Inner Detector with a new tracker. This new tracker needs to cope with peak luminosities of up to $5 \cdot 10^{34}\,\mathrm{cm^{-2}s^{-1}}$ and will collect an integrated luminosity of about $3000\,\mathrm{fb^{-1}}$. By then the number of interactions per bunch crossing will be more then 140 interactions with peak values exceeding 200 interactions. As a result the expected maximum fluence of the inner most pixel layer will exceed the design fluence of the IBL more than twice while the expected total ionizing dose will be more than three times higher. The increased fluence and total ionizing dose make it necessary to further increase the radiation hardness of the detector design. On the other hand a design based on the IBL detector design might be a suitable possibility for the application in the outer pixel layers and in the end caps of the pixel detector [28, 30].

The proposed layout of the future ITK implements a pixel and a silicon micro-strips sub-detector. The pixel detector consists of at least four barrel layers and six end-cap disks on each end. The two innermost pixel layer are mounted on a separate Inner Support Tube while the outer layers and the disks are mounted on the Pixel Support Tube. The silicon micro-strip detector is set up with five barrel layers and seven end-cap disks while the modules use a similar layout to the current SCT layout with two back-to-back sensors. A short strip and longer strip sensor design is going to be used in three and two of the layers respectively. The ITK design provides a minimum of 14 hits with a pseudorapidity range of $|\eta| < 2.5$ [28, 30].

Several sensor technologies for the pixel detector are currently tested to assure the operation up to fluences in the range of $10^{16}\,\mathrm{n_{eq}\,cm^{-2}}$. Possible candidate technologies are silicon n-in-n and n-in-p planar, silicon n-in-p 3D, HV-CMOS and diamond sensors. For the micro-strip detector a silicon n-in-p technology is proposed to provide good charge collection after irradiation without the effects of type inversion [35, 36].

2 Basic Characteristics of Semiconductor Particle Detectors

Semiconductor detector follow the basic principle of ionization counters which count the number of e/h-pairs produced by ionizing radiation. A bias voltage applied to both sides of the detector forms an electric field to separate the generated charges. The movement of the charge carriers induces a current pulse which is further processed in the attached read-out electronics. To increase the resolution of this kind of detector different electrode types are available to reach a high channel density.
The progress of silicon as semiconductor material in general purpose electronic products paved the way for the application of semiconductor material as particle detectors. More reliable large scale production at reasonable cost advanced the development of silicon read-out chips and different types of semiconductor sensor technologies. In the case of silicon as detector material it became even possible to build the read-out electronic and the sensor on the same wafer.
Advantages compared to predecessor technologies additionally accelerated the operation of semiconductor sensors in HEP applications. The low e/h-pair production energy in semiconductors results in an intrinsic high energy resolution enabling the implementation of thin sensors with a short radiation length. High mobility of electrons and holes leads to a fast responds time which is an important property for the application in experiments with high hit rates. The high spacial resolution related to the short range of knock-on electrons promotes the fabrication of small strip and pixel read-out electrodes.

This chapter describes semiconductor principles necessary for the application of silicon and diamond as radiation sensors. A comparison of different properties is given in Tab. 2.1 for the two materials. Later the different interaction mechanisms and effects of radiation on semiconductor materials are discussed. The focus of the discussion is directed towards the charge generation due to ionizing radiation and radiation damage in the semiconductor surface and bulk material. At last the implementation of semiconductor detectors is presented including signal amplification and noise effects related to the sensor and the read-out electronics.

2.1 Semiconductor Principles

Semiconductor detectors for the application in HEP experiments are used for particle tracking in the center of the experiments. A further application is to determine the amount of charge created by ionizing radiation in the sensor material. To avoid the recombination and the corresponding loss of information an electric field is used to separate the electron/hole-pairs (e/h-pairs). Depending on their charge the electrons and holes drift in opposite directions and induce a current pulse on top of the leakage current of the sensor. By integrating the induced current signal it becomes possible to determine the deposited charge in the sensor.
Sensor performance properties as the charge collection and the noise behavior strongly depend on the applied sensor material. These materials can be divided into groups with a high and a low specific intrinsic carrier concentration. While silicon is a representative of material with a high intrinsic carrier concentration represents diamond materials with a low intrinsic carrier concentration. Both sensor materials are under investigation for the application in future HEP experiments.

The intrinsic carrier concentration in a semiconductor is affected by the temperature and other material properties. This relation is defined by the Fermi-Dirac integral and can be simplified for non-degenerate semiconductor by the Boltzmann statistic given in Eq. 2.1. In non-degenerate semiconductor the number of thermally generated e/h-pairs dominates the number of impurities in the material. In addition the energy difference between the Fermi energy E_F and the energy of the conduction or the valence band E_C and E_V needs to be > 2 kT. These properties apply also to all intrinsic semiconductors which makes it possible to calculate the free electron n and free hole p concentration for these materials.

$$\begin{aligned} n &= N_C \cdot \exp\left(-\frac{E_C - E_F}{kT}\right) \\ p &= N_V \cdot \exp\left(-\frac{E_F - E_V}{kT}\right) \end{aligned} \tag{2.1}$$

Here, N_C and N_V represent the effective density of states in the conduction and valence band, k is the Boltzmann constant and T stands for the temperature [37]. For semiconductors which comply with these conditions the intrinsic carrier concentration can be defined by combining the mass action law $n_i^2 = n \cdot p$ and Eq. 2.1.

$$n_i = \sqrt{N_C \cdot N_V} \cdot \exp\left(-\frac{E_C - E_V}{2\,kT}\right) \tag{2.2}$$

Temperature increase in the semiconductor material leads to an exponential growth of thermally generated e/h-pairs. In addition shows Eq. 2.2 that the intrinsic carrier concentration also depends on the specific band gap energy of the applied material. This implies that semiconductors with wide band gap energies have a by several orders of magnitude lower

intrinsic carrier concentration than conventional semiconductor. In the case of silicon and diamond as detector material the intrinsic carrier concentration is $n_{i(Si,300\,K)} = 9.65 \cdot 10^{9}\,cm^{-3}$ and $n_{i(C,300\,K)} = 1 \cdot 10^{-27}\,cm^{-3}$ respectively [38, 39].
The conductivity of a semiconductor given in Eq. 2.3 is related to the intrinsic carrier concentration of the semiconductor material [37]. A higher e/h-pairs concentration leads to a higher conductivity, thus a higher current in the semiconductor. This current increase correlates with a rise of shot noise created by the increased number of electrons and holes in the material.

$$\sigma = \frac{1}{\rho} = q\,(\mu_n n + \mu_p p) \tag{2.3}$$

At room temperature the noise level of intrinsic semiconductors with a band gap energy in the range of 1 eV reaches up to the same order of magnitude as signals caused by ionizing radiation. This is not the case for wide band gap semiconductors which have much less intrinsic charge carriers, thus less noise. Depending on the band gap energy of the material different process steps need to be followed to fabricate a radiation sensor. For semiconductors with lower band gap energies it is necessary to build a pn-junction in the material while wide band gap semiconductor are directly operational.
In the following the implementations necessary for sensor materials with low and wide band gap energies are discussed. Radiation sensors made of silicon and diamond sensor material are used as examples representing the two types of band gap energies.

2.1.1 Silicon as Radiation Sensor

Silicon with a low band gap energies of 1.12 eV and a low creation energy for e/h-pairs of 3.6 eV shows the necessary requirements for the application as radiation sensor. Experience from developments of silicon applications in general purpose electronics contributed to the progress of several silicon sensor designs. Silicon doping techniques make it possible to build pn-junctions and to implement fine structures necessary to form read-out cells.
The high carrier concentration in intrinsic semiconductors with band gap energies of about 1 eV make them inoperable as radiation sensors without reducing the number of free charge carriers. A possibility to reduce this number is to build a pn-junction in the semiconductor. Impurity atoms with three or five valence electrons shown in Fig. 2.1 are introduced in the lattice to build p- and n-doped regions. As a result a space charge region without charge carriers forms at the junction between the two doped regions. This space charge region can be further increased by applying an external reverse bias voltage.
Doping atoms with three valence electrons e.g. B, Al, Ga and In in Fig. 2.1(a) leave one lose connection in the p-type semiconductor lattice. These acceptor form holes which represent free positive charge carriers in the valence band. Corresponding to the trivalent impurities, pentavalent doping atoms e.g. N, P, As and Sb in Fig. 2.1(b) introduce one additional electron in the n-type semiconductor lattice. These donor provide free negative charge carriers which

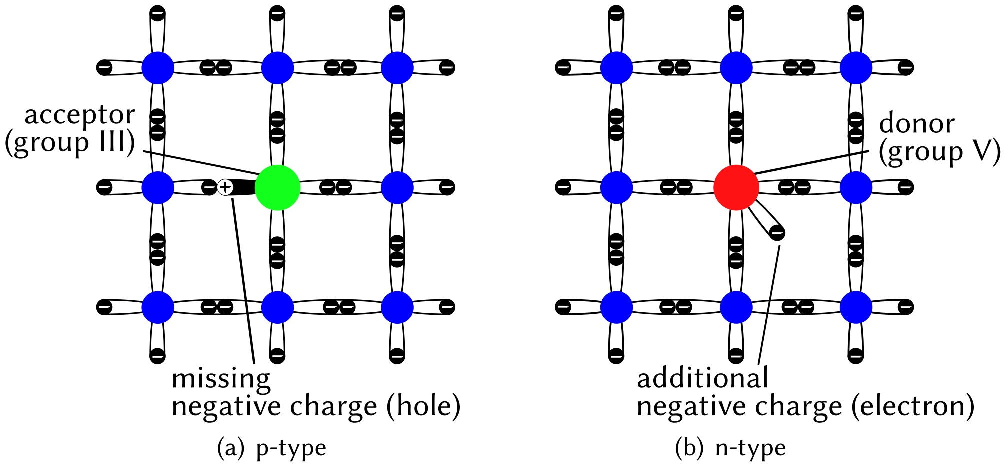

Figure 2.1: Doped silicon lattice forming p- and n-type semiconductors. P-type semiconductors in Fig. 2.1(a) uses acceptor elements from the III main group while n-type semiconductors in Fig. 2.1(b) use donor elements from the V main group [37].

can move in the conduction band. As a result of the doping the Fermi energy of p-doped material shifts towards the valence band and accordingly towards the conduction band for n-doped material.

For the formation of a pn-junction in the semiconductor, adjoin p- and n-doped regions shown in Fig. 2.2 a) need to be fabricated in a common material. The two corresponding free charge carrier close to the border of the junction diffuse across and leave fixed oppositely charged carriers building a space charge region. The expansion of the space charge width defined in Eq. 2.4 depends on the donor and acceptor concentration N_D and N_A and the dielectric constant ϵ of the semiconductor material. To simplify the discussion the space charge density in Fig. 2.2 b) can be approximated by two rectangular shaped space charge regions [37].

$$
\begin{aligned}
W_{Dn} &= \sqrt{\frac{2\,\epsilon_S \Psi_{bi}}{q} \frac{N_A}{N_D\,(N_A + N_D)}} \\
W_{Dp} &= \sqrt{\frac{2\,\epsilon_S \Psi_{bi}}{q} \frac{N_D}{N_A\,(N_A + N_D)}}
\end{aligned}
\tag{2.4}
$$

The resulting electric field in the space charge region shown in Fig. 2.2 c) can be determined by integrating the space charge density. Due to the abrupt change in the space charge density between the two zones, a maximum in the electric field E_{max} occurs at the junction.

An integration over the electric field distribution gives the potential distribution in Fig. 2.2 d). The built-in potential Ψ_{bi} which is proportional to the area under the electric field shown in Fig. 2.2 c) represents the potential difference between the borders of the space charge region shown in Fig. 2.2 d). In equilibrium condition without external voltage it is required that the

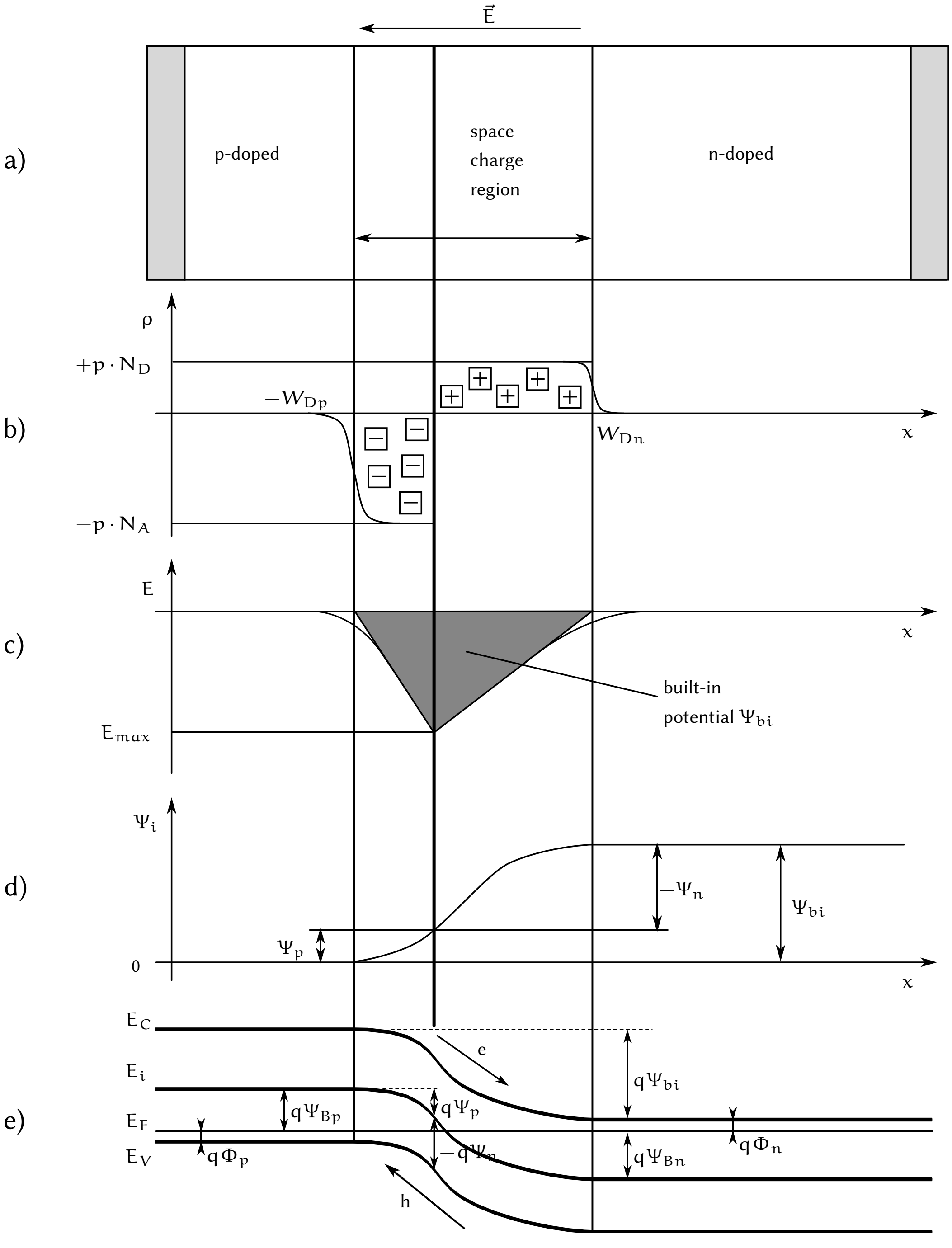

Figure 2.2: a) pn-junction, b) space charge distribution, c) electric field distribution, d) potential distribution, e) energy band diagram [37]

Fermi energy stays constant over the entire semiconductor. The shift of the Fermi energy between the doped regions creates a potential barrier $q\,\Psi_{bi}$ in the space charge region. This barrier is described by the curvature of the energy bands in Fig. 2.2 e).
For junctions with one dominating doping concentration as it is the case for silicon sensors used as particle detectors (n^+-p or p^+-n) Eq. 2.4 can be simplified to determine the total depletion width W_D in Eq. 2.5. Here, N corresponds to the dominating doping concentration given in Eq. 2.4 depending on the applied doping. In case of a n^+-p doped junction the donor concentration exceeds the acceptor concentration ($N_D \gg N_A$). As a result only a thin layer of the n-region is depleted while the depletion width in the p-region is orders of magnitude wider ($W_{Dn} \ll W_{Dp}$). Accordingly leads this behavior to a total depletion width corresponding to the depletion width in the p-region ($W_D \sim W_{Dp}$).

$$W_D = \sqrt{\frac{2\,\epsilon_S \Psi_{bi}}{q\,N}} \tag{2.5}$$

By replacing Ψ_{bi} in Eq. 2.5 with $\Psi_{bi} - V_{bias}$ it becomes possible to calculate the depletion width in function of the applied bias voltage. A positive bias voltage on the p-implant up to Ψ_{bi} reduces the depletion region and causes a strong current increase for higher values. On the contrary a negative bias voltage on the p-implant increases the depletion width and the electric field of the depletion region until the bulk material is fully depleted. The ideal leakage current behavior of a silicon diode in Fig. 2.3 shows the leakage current behavior corresponding to a negative bias increase. For low bias voltages the volume current increases up to the full depletion voltage followed by an additional surface current contribution. For increasing voltages a plateau region is formed which ends with a steep current increase when the breakdown voltage is reached [40].

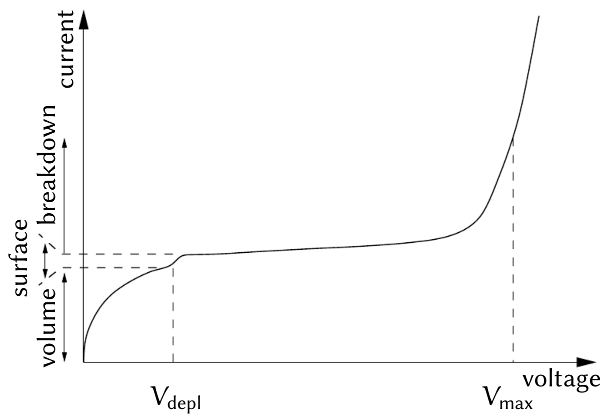

Figure 2.3: Ideal reverse leakage current behavior of a silicon diode showing the different depletion stages up to the breakdown voltage [40].

An effect of the earlier discussed temperature dependence of the charge carrier concentration can be directly observed by performing leakage current measurements for different temperatures. The measured silicon bulk current at a certain temperature T can be scaled with Eq. 2.6 to a reference temperature T_R.

$$\frac{I(T_R)}{I(T)} = \left(\frac{T_R}{T}\right)^2 \exp\left(-\frac{E_g}{2k_b}\left[\frac{1}{T_R} - \frac{1}{T}\right]\right) \tag{2.6}$$

Here, the band gap energy E_g corresponding to the specific band gap energy of silicon with 1.12 eV and the Boltzmann constant k_b are used [41].

Due to the electric field in the space charge region the majority charge carriers get flushed out of the depletion region. This behavior reduces the number of free charge carriers in the space charge region to a value below the intrinsic charge carrier concentration. The amount of the remaining charge carrier corresponds to the thermally stimulated minority carrier concentration in the depletion region. Depending on the doping type the minority carrier concentration can be calculated as $p_n = n_i^2/N_D$ and $n_p = n_i^2/N_A$ for n- and p-type silicon respectively [42]. For current ATLAS Pixel Detector sensors with an effective doping concentration of $1.7 \cdot 10^{12}\,\text{cm}^{-3}$ in the n-doped bulk and an intrinsic carrier concentration $n_{i(Si,300\,K)} = 9.65 \cdot 10^9\,\text{cm}^{-3}$ the minority charge carrier concentration of the bulk is in the order of $5.8 \cdot 10^7\,\text{cm}^{-3}$ [43, 44]. Due to the temperature dependence of the intrinsic carrier concentration in silicon an about two orders of magnitude reduced minority charge carrier concentration is obtained at a temperature of $-20\,°\text{C}$ [45]. This reduction of charge carriers in the depletion region also reduces the conductivity thus lower current and less shot noise in the sensor. Further enables this behavior the application of doped semiconductor material with low band gap energies as radiation sensors which is not the case for the intrinsic material.

To collect the maximum number of e/h-pairs generated by ionizing radiation it is desired to build a depletion region expanding over the entire semiconductor material. This full depletion configuration is typically achieved by using a low doped bulk material ($1.7 \cdot 10^{12}\,\text{cm}^{-3}$) with highly doped ($1 \cdot 10^{18}\,\text{cm}^{-3}$) p- and n-doped regions as electrodes. A high specific resistivity $> 2\,\text{k}\Omega\,\text{cm}$ is typically used to reach the full depletion of the entire sensor material [44]. For high reverse bias voltages applied to this sensor configuration the width of the depletion zone given in Eq. 2.5 extends over the whole low doped region but only penetrates the surface of the highly doped regions. The high concentration of charge carriers in the under-depleted regions keeps the ohmic characteristic of the semiconductor which is necessary to form the contact between the read-out electrodes and the metallization.

Substrate and Electrode Types

Based on the applied type of bulk material and read-out electrode four combinations of sensor types are available for the application as radiation detectors. These combinations implement highly n-doped or p-doped read-out electrodes in a n-doped or p-doped substrate.

Highly n-doped read-out electrodes in n- and p-doped bulk material are the two sensor types considered for high energy physics experiments with expected fluences higher than $3 \cdot 10^{14}\,\mathrm{n_{eq}\,cm^{-2}}$. Both sensor types based on n-doped read-out electrodes use the electron collection while the pn-junction is either formed around the read-out electrode or at the back side of the sensor. To assure the proper operation of these sensors certain layout features are required for both technologies. These features include the implementation of edge terminations to avoid a short circuit between the front and back side of the sensor as well as isolation structures between the read-out electrodes to avoid a short circuit between the channels. After type inversion due to radiation damage the n-in-n design starts to behave similar to the irradiated n-in-p design. As a result of this both sensor types show after irradiation an advantageous combination of the electric and the weighting field [46, 47]. Both designs are discussed in this work as possible sensor designs for future tracking detectors.
The remaining two sensor types implement highly p-doped read-out electrodes show different characteristics which dismiss them as tracking detectors for the application in future HEP experiments. The p-in-n design which is used as sensor design in environments with low fluences shows after type inversion a shift of the depletion region to the back side of the sensor. This corresponds to the behavior of the p-in-p design which can not be operated if the sensor is under-depleted. The hole collection at the segmented side of these sensor types is a further drawback after irradiation. This is due to the increased hole trapping probability as well as the disadvantageous combination of the electric and the weighting field [46]. As a result, both designs are not considered to be used in future tracking detectors [40].

An issue relevant for all combinations of sensor types is the surface damage in the silicon oxide. This damage leads to an accumulation of positive charges in the surface layer which change the electric field at the interface between the silicon oxide and the bulk material. Depending on the crystal orientation low oxide charge concentrations vary at about $10^{10}\,\mathrm{cm^{-2}}$ which increase after irradiation up to saturation values at about $3 \cdot 10^{12}\,\mathrm{cm^{-2}}$ [40]. Due to the changes in the electric field electrons start to pile up in the layer between read-out channels which eventually shortens several channels. To counteract this effect the p-stop and p-spray technique are used to form p-type implants between the channels to assure the isolation. The p-stop technique uses an additional photolithographic step to form a highly p-doped implant region between the read-out channels. The p-spray technique on the other hand forms a p-doped implant over the entire wafer surface. As the entire region between the read-out channels is p-doped a lower doping dose is typically applied using the p-spray technique. A combination of both techniques is the moderated p-spray where the p-region reaches the channels but additionally a higher doping concentration is build in the middle of the channels. An additional positive effect of these isolation techniques is the breakdown voltage increase after irradiation which is further explained in section 2.2.3 [48].

n-in-n sensor type

In case of the n-in-n sensor technology the pn-junction is located on the back side electrode of the sensor. The depletion zone in this configuration expands with increasing bias voltage towards the front side housing the read-out electrodes. This effect leaves the electrodes short circuited until the depletion zone reaches the front side and establishes the isolation between the implants. This property of n-in-n sensors makes it not possible to operate this technology before irradiation in an under-depleted state. An important feature of this technology is the type inversion of the bulk material after irradiation. This effect is caused by the accumulated radiation damage in the substrate further explained in section 2.2.3 which changes the sensor properties to behave similar to an irradiated n-in-p sensor. These properties especially include the shift of the space charge region towards the front side. As a result the space charge region extends after irradiation in direction of the sensor back side thus makes it possible to operate the sensor in an under-depleted state. To avoid a short-circuit across the pn-junction an edge termination consisting of several guard-rings surrounding the back side contact becomes unavoidable for the implementation of a n-in-n sensor type. Therefore a double sided production process needs to be applied [40, 49].

n-in-p sensor type

The space charge region in sensors using the n-in-p technology is formed around the read-out electrodes and extends with increasing bias voltage in direction of the back side electrode. An operation in an under-depleted state is possible as the read-out electrodes are intrinsically electrically isolated. This property is independent of the radiation damage as no type inversion occurs in the bulk material. As the pn-junction is build around the read-out electrodes it becomes possible to use a less costly single sided production process with less mask steps. The reduction in production cost comes with the disadvantage that the bias voltage reaches via the conductive edge the front side of the sensor housing the read-out channels. Electric sparks shorting the sensor and the electronics would destroy the read-out chip and need to be prevented. A common method to avoid this effect is to deposit a passivation layer between the read-out chip and the sensor. Further is a structure consisting of several guard rings implemented around the read-out electrodes. This multi-guard ring structure creates a potential drop for each of the guard rings to assure the isolation between the contacts [50, 51].

Advances on silicon sensor designs constantly support the wide application of silicon sensors in radiation detectors. The successful implementation of 3D-electrodes in the bulk material makes it possible to decouple the electrode distance from the sensors thickness [5]. New guard ring designs or the use of an active edge around the sensor are possibilities to reduce the inactive detector area [52]. Additional points as the high production quality for reasonable cost and good material properties endorse the application of silicon as active material in radiation detectors.

2.1.2 Diamond as Radiation Sensor

Diamond with its band gap energy of 5.47 eV comes with a low carrier concentration which makes it possible to use it as an intrinsic semiconductor. This property enables the application of diamond as radiation sensor with a homogeneous charge collection over the full sensor thickness. Additional properties as a high thermal conductivity, low leakage current and the high radiation hardness endorse its application in HEP experiments. Due to the lack of a pn-junction it can be operated for both polarities to collect either electrons or holes on the read-out side.

Artificial diamonds for industrial applications are generally fabricated by chemical vapor deposition (CVD) processes [53]. The hot-filament CVD (HFCVD) and the microwave CVD (MWCVD) process are two of the most common CVD processes for the fabrication of diamond material. To avoid the formation of graphite during the HFCVD process atomic hydrogen needs to be produced in the deposition chamber. A gas mixture of 1 vol-% methane (CH_4) and hydrogen (H_2) is decomposed by the heated tungsten wire in proximity to the substrate. A selective etch process introduced by the hydrogen runs at the same time as the deposition and reduces the growth rate. Deposition chamber pressures of up to 10 kPa and substrate temperatures between 700 °C and 1000 °C have been reported for this type of fabrication process. In case of the MWCVD process the process gas is introduced into the deposition chamber of the microwave-plasma reactor. When the microwave energy is introduced into the chamber the gas heats up and starts the diamond growth process on the substrate [53]. Typical substrate materials for the CVD process are cubic boron nitride, silicon carbide, silicon, nickel, platinum, iridium and diamond. The lattice mismatch between the applied substrate materials and single crystal diamonds lead to the formation of independent diamond seed crystals on the substrate. Regions with a uniform crystal structure build around the seeds and form a grain structure resulting in a poly-crystalline CVD (pcCVD) diamond. As the growth of single grains is highly irregular, slower grains can get pushed back and eventually disappear in higher deposition layers. To profit from this property thicker material is deposited on the substrate which is later thinned by a grinding process. By applying this grinding process to the substrate side of the grown material only the part containing the small grains is removed. For the formation of single-crystalline CVD (sCVD) diamonds the application of diamond single crystal substrates was demonstrated in the past. Due to the low availability of large-area single crystal diamond substrates it is only possible to produce sCVD diamonds with a size of about 1 cm^2. A further possibility for the formation of sCVD diamonds is the application of epitaxial iridium layers on $SrTiO_3$ as substrates which is currently under investigation [54].
Sensor properties and quality strongly depends on the fabrication technique and the substrate used during the growth process. The number of charge traps in the material is one of the main quality criteria for diamond sensors. Dangling bonds around the grain borders in pcCVD diamonds introduce additional trapping and recombination centers compared to

sCVD diamonds. A further effect is the possible formation of space charges related to impurities as nitrogen in the sensor material. This might result in lateral fields which would reduced the spacial resolution of the sensor [55]. Due to the absence of a grain structure in sCVD diamonds no additional trapping effects are introduced in this material.

For the application of diamonds as radiation detector electrodes need to be formed on both sides of the material to apply the bias voltage. Contrary to silicon and other doped semiconductors no electrode implantation is necessary for diamond sensors. Before the metal deposition the diamond surface needs to be polished and cleaned to remove residues from handling and the polishing process. Titanium-tungsten contact electrodes are build by a sputtering process on the diamond. Depending on the type of read-out electrode a second layer of gold or copper gets deposited as well. To cure surface damage created during the electrode deposition an annealing step at about 450 °C is performed with the detector [56].

Diamond as radiation detector material is mainly endorsed by its high radiation hardness, the small leakage current and the low capacitance. These properties related to the low noise compared to silicon also result in an about 2.2 times smaller charge signal. Comparisons of the Signal-to-Noise Ratio (SNR) for proton irradiated diamond and silicon sensors showed a better performance of diamond sensors for very high radiation fluences [57]. Additional properties as the high breakdown field and the good thermal conductivity support the application of diamond as radiation sensor. Furthermore spreads the electric field uniform in the diamond which corresponds to a scalable charge collection time in function of the applied bias voltage [55]. Recent measurements on proton irradiated diamond sensors confirmed the operation of this sensor material up to a fluence of $1.6 \cdot 10^{16}\ n_{eq}\ cm^{-2}$ [58].

property	units	silicon	diamond	reference
band gap	eV	1.12	5.48	
density	$g\ cm^{-3}$	2.33	3.52	
thermal conductivity	$W\ cm^{-1}K^{-1}$	1.48	>1800	
relative permittivity		11.7	5.7	
intrinsic carrier concentration	cm^{-3}	$9.65 \cdot 10^{9}$	$1 \cdot 10^{-27}$	[38, 39]
e/h-pair creation energy	eV	3.61	13.6	[59, 60]
carrier mobility electrons	$cm^2\ V^{-1}s^{-1}$	1450	1714	[61]
carrier mobility holes	$cm^2\ V^{-1}s^{-1}$	505	2064	[61]
saturation velocity electrons	$cm\ s^{-1}$	$24.0 \cdot 10^{6}$	$9.9 \cdot 10^{6}$	[62]
saturation velocity holes	$cm\ s^{-1}$	$7.5 \cdot 10^{6}$	$12.5 \cdot 10^{6}$	[62]

Table 2.1: Summary of material properties for silicon and diamond at 300 K [55, 56]

2.2 Interaction of Radiation in Semiconductor Material

When particles or photons penetrate semiconductor devices a multiplicity of desired and undesired interactions take place. The creation of e/h-pairs by ionizing radiation is one of the non-destructive effects and necessary for the particle detection in radiation sensors. In general the effects of ionizing radiation can be divided into interactions with photons and with charged particles.
In both cases e/h-pairs are created when an electron absorbs enough energy to move from the valence band to the conduction band. The necessary energy depends on the band gap energy of the semiconductor material. While the deposited energy creates e/h-pairs by ionization it also excites vibrations in the lattice by phonon emission. The energy dedicated to the phonon emission is lost for the e/h-pair production thus on average more energy than the band gap energy is necessary to create e/h-pairs. For silicon and diamond sensors pair-creation energies of 3.61 eV and 13.6 eV were determined respectively [59, 60].
Deterioration of the semiconductor due to radiation is considered as radiation damage in the bulk material or the surface layer. These damages influence the properties of the semiconductor by increased leakage current, type inversion and increased trapping effects which can be partially repaired by annealing.

2.2.1 Interaction of Photons with Matter

Photoelectric effect, Compton scattering and pair-production describe the three main interactions between photons and matter. With increasing energy the cross section changes first from the photoelectric effect to the Compton scattering and finally to the pair production which is shown in Fig. 2.4 for carbon and silicon.
During the passage of a photon beam through matter an attenuation of the intensity can be observed which is described by Eq. 2.7. The attenuation coefficient μ depends on the specific cross section, the density and the molecular weight of the traversed material σ, ρ and A as defined in Eq. 2.8 with the Avogadro constant N_A.

$$I = I_0 \, e^{-\mu x} \tag{2.7}$$

$$\mu = \frac{N_A \, \rho}{A} \left(\sigma_{\text{photo}} + \sigma_{\text{compton}} + \sigma_{\text{pair}}\right) \tag{2.8}$$

During the **photoelectric effect** the total energy $h\nu > E_{\text{binding}}$ of an incident gamma-ray gets absorbed by a bond electron. This electron subsequently leaves the atomic bond with a kinetic energy $E_{\text{kin}} = h\nu - E_{\text{binding}}$ corresponding to the binding energy subtracted from the incident energy of the gamma-ray. As the photon gets completely absorbed, a nucleus is necessary to absorb the recoil momentum in order to satisfy the conservation of energy and momentum. This is also the reason that the photoelectric effect does not appear at loose electrons. Figure 2.4 shows that the photoelectric cross section depends on the energy of the incident photon and the atomic number of the material. It implies that the cross section

increases for higher atomic numbers and decreases for higher gamma-ray energies.
With increasing photon energies $h\nu \gg E_{binding}$ the **Compton scattering** outranges the photoelectric effect. It describes an elastic scattering between a photon and a free electron which absorbs a part of the deflected photons energy. The resulting photon and electron energy is given in Eq. 2.9 and Eq. 2.10 respectively. The transformed energy depends only on the photons scattering angle Φ which defines the Compton edge at a maximal electron energy $E'_{e,max} = \frac{2\,(h\nu)^2}{m_e c^2 + 2\,h\nu}$ for $\Phi = 180\,°$.

$$E'_{\gamma} = \frac{h\nu}{1 + \frac{h\nu}{m_e c^2}\,(1 - \cos\Phi)} \tag{2.9}$$

$$E'_{e} = h\nu - \frac{h\nu}{1 + \frac{h\nu}{m_e c^2}\,(1 - \cos\Phi)} \tag{2.10}$$

The conversion of one photon in an electron-positron pair is described by the **pair production**. A photon energy $E_{\gamma} > 2\,m_e c^2$ is needed for the pair production which is the reason that it only takes place at higher energies. In the case of the production of an electron-positron pair a photon with an energy of more than 1.022 MeV is needed. For the conservation of momentum the pair production can only take place in the proximity of another particle.

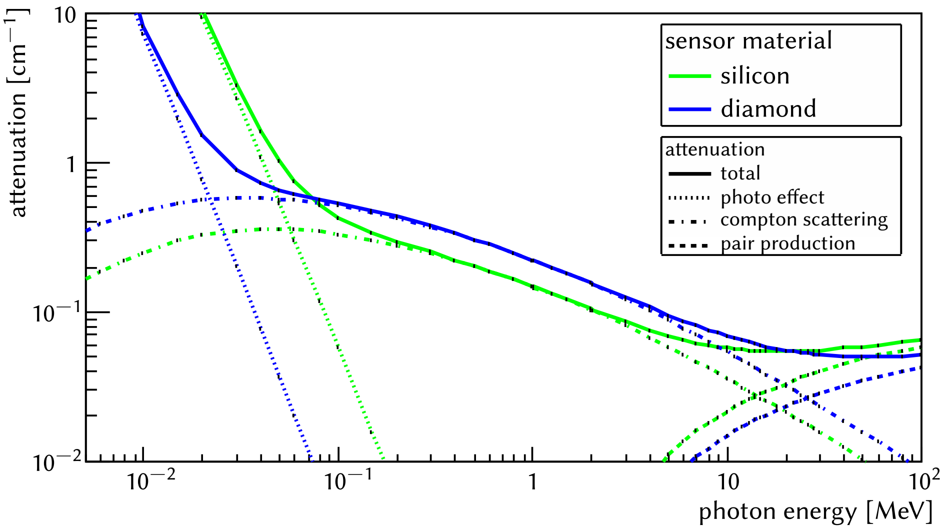

Figure 2.4: Attenuation of photons in silicon and diamond sensor material. For both materials three energy ranges dominated by the photoelectric effect, Compton scattering and pair production are visible [63].

Depending on the photon energy emitted by a radioactive source is a combination of the Compton spectrum and photoelectric peak visible. The photo electric peak measured with a semiconductor detector can be used for sensor and read-out calibration tests. The Compton scattering on the other hand is less useful for calibration purposes. Corresponding are sources with energies reaching the Compton scattering dominated part of the cross section less helpful as the photoelectric peak is less dominant.

2.2.2 Interaction of Charged Particles with Matter

Scattering between high energetic charged particles and electrons in the atomic shell can either excite or ionize an atom. In rare cases a strong energy transfer between the incident particle and the electron takes place creating a δ-electron which behaves as a free charged particle itself and traverses the detector.

$$-\left\langle \frac{dE}{dx} \right\rangle = Kz^2 \frac{Z}{A} \frac{1}{\beta^2} \left[\frac{1}{2} \ln \frac{2m_e c^2 \beta^2 \gamma^2 T_{max}}{I^2} - \beta^2 - \frac{\delta(\beta\gamma)}{2} \right] \tag{2.11}$$

The energy loss of charged particles within an intermediate energy range of $0.1 < \beta\gamma < 1000$ is described by the Bethe-Bloch formula in Eq. 2.11 [64]. The resulting stopping power for a muon in copper in function of $\beta\gamma$ is shown in Fig. 2.5.

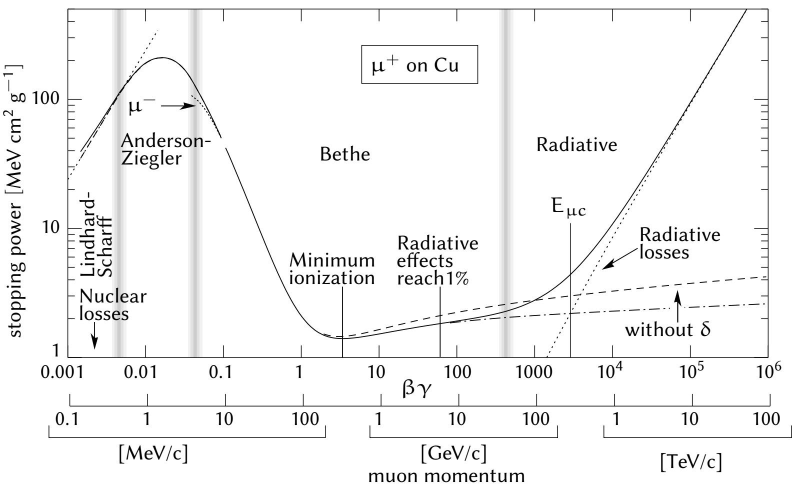

Figure 2.5: $\langle -dE/dx \rangle$ for positive muons in copper [64].

Minimum Ionizing Particles (MIPs) have a minimum stopping power and deposit the lowest energy in the sensor material. These MIPs or MIP like particles are commonly used to characterize the sensor performance as low energy depositions are harder to detect. The total stopping power of electrons and protons in silicon and diamond is given in Fig. 2.6 in function of the particle energy. Noticeable is the MIP energy shift depending on the type of particle.

The corresponding energy loss distributions can be described by a Landau-distribution. Here the most probably value of the distribution represents the most probable energy loss. Looking at the distributions for varying sensor thicknesses in Fig. 2.7 shows an increase of the most probable value in function of the sensor thickness. Noticeable is that the mean energy loss stays constant with the sensor thickness. Corresponding is the most probable value used to describe the energy loss of a single particle [64].

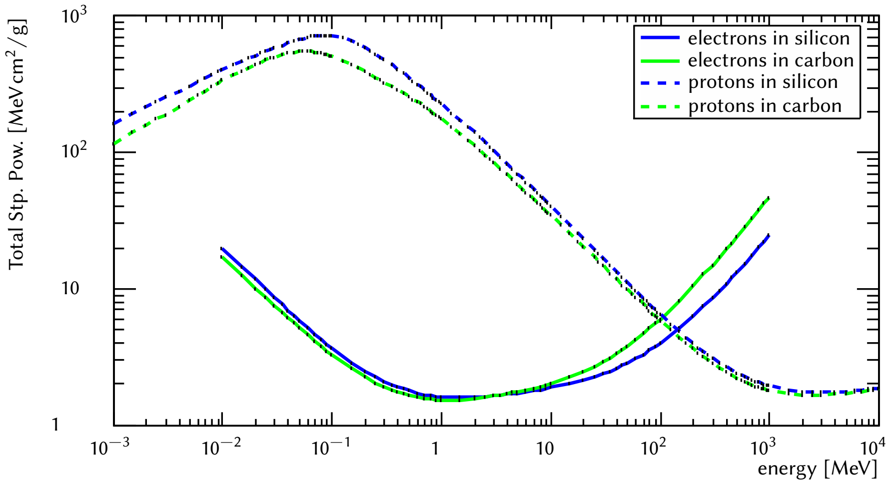

Figure 2.6: $\langle -dE/dx \rangle$ for electrons and protons in silicon and carbon [65].

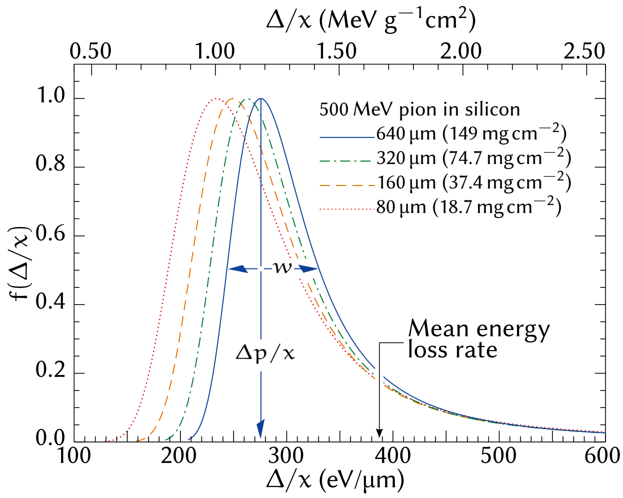

Figure 2.7: Normalized energy loss distributions of 500 MeV pions in 80 µm, 160 µm, 320 µm and 640 µm thick silicon [64]

2.2.3 Radiation Damage

The deterioration of semi-conductor detectors in HEP experiments is caused by radiation damage in the surface layer or the bulk material. While the surface damage is mainly caused by Ionizing Energy Loss (IEL) in the passivation layer, non Ionizing Energy Loss (NIEL) dominates the bulk damage effects. Depending on the kind of radiation damage different effects lead to property changes of the sensor material or the electronics. For hybrid pixel detectors consisting of a sensors bump-bonded to a read-out chip as they are used in the Pixel Detector of the ATLAS Experiment both effects need to be considered. In case of the read-out chip IEL dominates the property changes as NIEL becomes more relevant for the sensor.

Surface damage is typically related to electrons and holes created by ionizing radiation in the silicon oxide layer. The high electron mobility in silicon dioxide enables the electrons to leave the oxide where they get collected. The low hole mobility on the other hand prevents the holes from leaving the oxide layer leading to an accumulation of positive oxide charges. Those who reach the interface between the silicon dioxide and the silicon can build interface traps and trap electrons. This behavior increases linearly with the total radiation dose of the device. The distortion of the electric field caused by the fixed charges in the silicon dioxide changes the capacitance and depletion behavior of the device.
In silicon sensors the accumulation of positive charges in the interface region can alter the electric field resulting in conductive paths between read-out channels. Sensors using insulation techniques as p-spray, p-stop or a combination of both show a breakdown voltage increase after irradiation. In these cases the oxide charge increase creates a depletion zone between the electrode and the isolation region and reduces its potential. As a result the electric field profile between the high doped n-region and the isolation flattens out with a lower peak field at the junction. Hence, the breakdown voltage shifts to higher values until the peak field is high enough to trigger the avalanche [48]. This effect increases the lifetime of the sensor as higher bias voltages are needed to extend the electric field over the sensor thickness after irradiation.
Further radiation damage effects can be related to the rate of the delivered dose. The number of e/h-pairs created by ionizing radiation in the silicon substrate increases linear with the radiation rate. The charge carriers separated by electric fields in the device introduce an electrical current which can cause damage to the circuit if rates exceed $10^6\,\mathrm{rad\,s^{-1}}$ to $10^7\,\mathrm{rad\,s^{-1}}$ [66]. As dose rates this high do not appear in high energy physics experiments this radiation damage can be dismissed. An effect similar to the high dose rate but less severe is a Single Event Upset (SEU). During this events the current caused by the ionizing radiation exceeds the internal currents of the circuit. This can lead to faulty operation by altering memory cells or changing the logical state of the circuit [66].

Bulk damage in the sensor substrate is caused by an energy transfer of hadrons or high energetic leptons to a lattice atom. The transferred energy can lead to displacement damage by breaking the lattice bonds of an atom creating a Primary Knock-on Atom (PKA) corresponding to point defects of interstitials and vacancies. The displaced PKA and the remaining vacancy build a Frenkel defect which can migrate in the lattice where they build point defects with doping atoms. For the creation of these recoil atoms the energy transferred by the incident particle needs to exceed the displacement threshold of 25 eV in silicon. While the PKA migrates through the material it losses its energy by ionization or by displacing additional atoms on its path. This characteristic leads to the formation of damage tracks consisting of point defects through the silicon with shorter branches caused by secondary recoil atoms. When the atom lost most of its energy an increase in displacement damage takes place creating a disordered region also considered as a defect cluster.

Depending on the electronic properties of the defect the influence on the device can be described by additional donor and acceptor levels in the band gap. Defect parameters as the cross section, the ionization energy, the defect concentration and the defect type can change the electric field by introducing space charges, increase the trapping of electrons and holes and increase the leakage current of the device[67].
For temperatures higher than 150 K the created interstitials and vacancies have a very high mobility. This can lead to a self-healing effect when the Frenkel pairs recombine without leaving any damage. The point and cluster defects caused by the remaining interstitials and vacancies are the source for bulk damage deteriorating the material properties [41].

The non Ionizing Energy Loss (NIEL) hypotheses introduced a scale factor to compare the impact of radiation induced damage depending on the type of particle and the particle energy [68]. For this hypotheses a linear dependence between the induced displacement damage and the transferred energy during the collision is assumed. Here, the effects of the spatial distribution and the different annealing sequences are not considered for the changes related to displacement damages. Based on this assumption and knowing the amount of deposited energy the displacement damage cross section can be derived.

Depending on the radiation type and the related energy spectra a hardness factor κ is defined by using the displacement damage cross section. To compare the displacement damage of different samples the hardness factor in Eq. 2.12 is used to scale the obtained fluences. Typically the fluence is scaled to a neutron equivalent fluence (n_{eq} cm^{-2}) defined by the displacement damage caused by 1 MeV mono-energetic neutrons [41]. Hardness factors used to scale the fluence are given in Sec. 3.6 while introducing the irradiation facilities used during this work.

$$\Phi_{eq} = \kappa\Phi \tag{2.12}$$

Point defects created by displacement damage can be related to interstitials or vacancies in the sensor lattice. Vacancies in silicon can combine with acceptor and donor atoms but also with impurities in the material. In addition become pairs of two or more vacancies also possible. Mobility differences at low temperatures depending on the doping-type were discovered for silicon self-interstitials. Corresponding to vacancies can interstitials also form pairs with impurities and defects in the silicon. Following the Watkins replacement mechanism it is possible to replace impurities with silicon self-interstitials. This effect creates an undamaged silicon lattice with an electrical active impurity interstitial. A further possibility is the recombination with a vacancy reducing the radiation damage.
Depending on the energy state of the point defect new acceptor and donor energy levels get introduced in the band gap region. Based on the distance to the valence and conduction band defects are considered as shallow or deep level defects. These changes in the lattice structure change the sensor material and result in a property shift of the detector.

Defects in the band gap represent charge traps for electrons and holes. A charge carrier caught in a trap stays trapped for an effective trapping time τ_{eff} before it is detrapped again. The corresponding reduction in charge given in Eq. 2.13 causes a signal loss in the sensor if the trapping time exceeds the shaping time of the read-out system. The observed charge loss in the material increases with the number of defects thus the fluence. As the probability of trapping increases for higher fluences the mean free path and the mean lifetime of electrons and holes decreases.

$$Q_{e,h}(t) = Q_{0_{e,h}} \exp(-\frac{1}{\tau_{eff\ e,h}} \cdot t) \tag{2.13}$$

The introduction of new donor and acceptor states in the sensor bulk changes the effective doping concentration in the material. The donor removal in n-type material and the introduction of additional acceptor for low fluences reduces the effective doping concentration. In this case the doping dependent depletion width given in Eq. 2.5 explains a reduced full depletion voltage. For higher fluences the number of introduced acceptor states exceeds the number of donor states forming a p-type material. After this type inversion of the sensor bulk the depletion voltage increases again until it starts to rise in function of the fluence [41, 69].

New donor and acceptor states within the band gap region cause an increase of the leakage current in the bulk material. Measurements showed a linear dependence between the measured leakage current and the collected fluence. The current related damage rate α in Eq. 2.14 represents the influence of the annealing on the leakage current behavior [41, 70]. Here ΔI represents the current variation at a bias voltage V corresponding to a certain fluence Φ_{eq}.

$$\alpha = \frac{\Delta I}{V \cdot \Phi_{eq}} \tag{2.14}$$

During the annealing interstitials or vacancies forming point defects become active after a certain activation temperature is exceeded. These loose interstitials or vacancies migrate in the lattice where they can form new point defects or recombine. The recombination changes the effective doping concentration and with it the radiation damage effects. Depending on the sensor type and the fluence a decrease of the leakage current can be observed. With a lower number of defects the trapping is reduced causing a signal increase after annealing. On a long time scale a reverse-annealing effect appears causing an increase of the depletion voltage. The advancement of the reverse-annealing can be stopped for temperatures below $-10\,^{\circ}$C. To profit from the positive annealing effects the damaged sensors can be annealed for several minutes up to a few hours at increased temperatures at $60\,^{\circ}$C to $80\,^{\circ}$C and later stored at temperatures below $-10\,^{\circ}$C.

2.3 Implementation and Properties of Semiconductor Detectors

Semiconductor detector designs range from pad detectors with one read-out channel to strip and pixel detectors with several hundred, thousand and more read-out channels. Independent of the applied sensor design, material and technology the general functionality of all read-out channels is based on the same principles.

Ionizing particles passing through the detector create tracks of e/h-pairs in the active sensor material. These charge carriers get separated by the electric field creating an instantaneous current flow in the sensor. The resulting current pulse in the read-out channel corresponds to the induced current i_{ind} defined by Ramo's theorem given in Eq. 2.15 [71].

$$i_{ind} = -nq\,\vec{v} \cdot \vec{E}_Q \tag{2.15}$$

Here, n is the number of charge carrier with the charge q and the velocity v moving in the weighting field E_Q. The weighting field corresponds to the field of the measurement electrode set to unit potential in relation to all other electrodes set to ground level. Looking at one electrode the weighting field represents the coupling of the electrode and the moving charge. By integrating the induced current signal it becomes possible to calculate the deposited charge in the sensor.
Depending on the electrode layout the distribution of the weighting field changes in the sensor. As it behaves linear in the sensor material for large electrodes it starts to concentrate around smaller electrodes. This small pixel effect leads to an unequal distribution of the introduced current which means that the collected charge is mainly caused by the movement of charges close to the electrode. As the effect of charge trapping increases with irradiation the influence of the small pixel effect becomes more apparent when it leads to reduced charge collection.

For the later processing of the current pulse shapes from the sensor the pulses need to be amplified. For this purpose voltage-, current- and charge-sensitive amplifiers are typically used. As Charge-Sensitive Amplifiers (CSAs) are implemented in the pixel detector of the ATLAS Experiment the amplification process is described for this type of amplifier.
The schematic in Fig. 2.8 shows the general setup of a CSA connected to one sensor cell. It consists of an inverting voltage amplifier with a high input resistance and the feedback capacitance C_f. The voltage gain A of this type of inverting amplifier creates an inverted output signal $U_{out} = -A\ U_{in}$. The feedback capacitance C_f and the sensor capacitance C_s can be considered as a serial connection corresponding to the high input resistance of the amplifier. Charge up of the sensor capacitance C_s can be avoided by using a sufficient high feedback capacitance C_f also reducing signal loss [72].

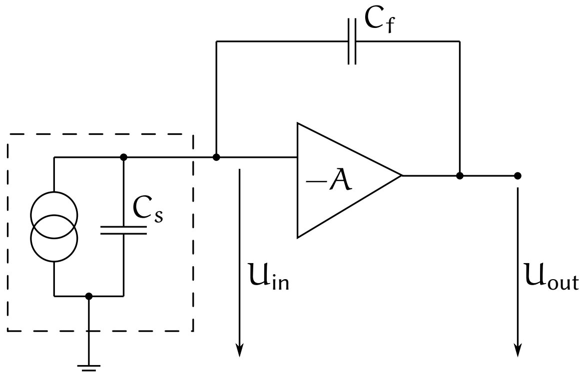

Figure 2.8: General layout of a CSA showing the equivalent circuit containing the sensor including the capacitance C_s, the amplifier and the feedback capacitance C_f [72].

In the case of pixel detectors CSAs are often used to preamplify the signal pulse. The output signal is then processed by a signal shaper and a discriminator to digitize the signal. This step becomes necessary to handle the huge amount of data generated during the operation of an experiment. The zero suppression is one of the methods used to reduce the data rate. This method uses the digitization of the signal to exclude all read-out channels with a signal below a certain threshold.
To improve the signal acquisition with CSAs typically a calibration and a leakage current compensation circuit are introduced at the input of the CSA. The calibration circuit consists of a test capacitance C_T which is used to inject charge signals into the preamplifier. By varying the voltage used to charge the capacitance it becomes possible to determine the signal responds of the amplification circuit in dependence of the injected charge. Data taken during the operation of the detector is stored and later converted and calibrated into charge [72]. A leakage current compensation at the input of the preamplifier becomes important when the leakage current increases after irradiation. The circuit automatically compensates the DC component of the leakage current at the amplifier input thus prevents interference with the discharge of the feedback capacitance C_f [73].

As discussed earlier introduces radiation damage, defects in the crystal lattice varying the charge collection properties of the material. Measurements on proton and neutron irradiated silicon n-in-p detectors at a bias voltage of 800 V showed an about 50 % reduced charge collection efficiency at a fluence of $3 \cdot 10^{15}\ n_{eq}\ cm^{-2}$ [74]. Similar results have been obtained for diamond pixel detectors irradiated with protons to a fluence of about $1.1 \cdot 10^{16}\ n_{eq}\ cm^{-2}$ [58]. Correspondingly decreases the signal level to values close to the noise level of the detector. As a result is the SNR reduced which makes it harder to distinguish signal pulses corresponding to hits in the sensor from noise hits. In case of an analogue read-out of the sensor both pulses are read out which results in an overlay of noise and signal hits. For detectors using a discriminator in the read-out chain all the signals which did not exceed the internal threshold are filtered out. As a result it becomes increasingly important to operate the detectors with low threshold settings to avoid data loss. On the other hand makes it this decrease more likely to read out noise signals. Thus, in order to compare different sensor materials and designs the SNR becomes an important factor.

Next to sensor modifications with the purpose to increase the signal a second approach is to decrease the noise of the detector. Therefore it becomes necessary to identify the different noise sources in a detector.
In the case of semiconductor detectors the dominating noise effects are related to baseline fluctuations. This fluctuations can be related to different sources whereas the electronic noise represents the fundamental limit. This noise effect can be described by fluctuations of a current passing through an electronic circuit. The current in a circuit is specified by the number of electrons n moving with a velocity v separated with a spacing distance s.

$$i = \frac{nev}{s} \tag{2.16}$$

The total differential of the current in Eq. 2.16 represents the current fluctuation and number fluctuation in Eq. 2.17 which is linked to the electronic noise. Based on this equation can the velocity and number fluctuation be distinguished as contributions to the electronic noise.

$$\langle di \rangle^2 = \left(\frac{ne}{s} \langle dv \rangle \right)^2 + \left(\frac{ev}{s} \langle dn \rangle \right)^2 \tag{2.17}$$

While velocity fluctuations are related to thermal motion thus considered as thermal noise, number fluctuations can be ascribed to shot noise and low frequency 1/f-noise [72].
Thermal noise corresponds to velocity fluctuations due to thermal motion in an electric conductor. As the power density spectrum of thermal noise is constant it is considered as white noise. To describe the spectral noise density of thermal noise in Eq. 2.18 typically the power in a resistance is used which corresponds to a temperature T and a resistance R dependency [72].

$$\begin{aligned} \frac{dv^2_{\text{thermal}}}{df} &= 4kTR \\ \frac{di^2_{\text{thermal}}}{df} &= \frac{4kT}{R} \end{aligned} \tag{2.18}$$

Noise depending on the fluctuation of the carrier flow which is limited e.g. by the potential barrier in a reverse biased semiconductor diode is considered as **shot noise**. In case of a semiconductor diode the probability of passing the potential barrier for one charged carrier is independent of the other carriers which gives shot noise a constant power density spectrum. The spectral current noise density of shot noise in Eq. 2.19 correlates with the average current

I of electronic charges e [72].

$$\frac{di^2_{shot}}{df} = 2eI \tag{2.19}$$

The second noise source related to number fluctuation is the **low frequency 1/f-noise** which is related to carrier trapping. In case of the release of trapped carriers after a time constant τ a nonuniform noise contribution is added to the noise spectrum. The spectral voltage noise density of 1/f-noise is given in Eq. 2.20 with the 1/f noise coefficient K_F and α which varies between 0.5 and 2 [72, 56].

$$\frac{dv^2_{1/f}}{df} = K_F \frac{1}{f^\alpha} \tag{2.20}$$

The three discussed noise sources can be considered as the main noise contributions to semiconductor detectors. As one or more noise sources appear in different detector components it becomes necessary to determine the individual noise contributions of each component in order to analyze the overall noise behavior.

A further effect related to low SNR is an increase of the noise occupancy in the detector. This effect becomes especially important in experiments which use a zero suppression to reduce the amount to transmitted data. In case of an increased noise occupancy additional data is generated by read-out channels which show continues hits due to electronic noise. As uninterrupted operations of one pixel cell can increase the noise in neighboring pixel cells a noise occupancy threshold is generally set to decide if a read-out channel needs to be switched off. In the current ATLAS Pixel Detector this noise occupancy threshold is set to $5 \cdot 10^{-5}$ meaning that pixel which show a higher ratio of hits to random trigger are excluded from the data taking.

3 Pixel Detector Modules for the ATLAS Upgrade

Different pixel detector technologies are considered to be used in the upcoming ATLAS IBL upgrade and later upgrade efforts of the ATLAS Experiment. These technologies include enhanced read-out chips as well as new silicon and diamond pixel sensor designs.
Hybrid pixel detector modules as they are used in the ATLAS Pixel Detector consist of three parts: sensor, front-end chip and front-end - sensor interconnections. The front-end read-out chip provides read-out channels for each pixel cell to amplify and digitalize the signal. The interconnections between the front-end chip and the sensor are necessary to provide the high density of electrical connections necessary for the communication between sensor and amplifier. The sensor tiles represent the active material to ionizing radiation where the e/h-pairs get separated to create the signal.

This chapter summarizes the different components used to build the pixel detector modules investigated in this work. The applied techniques to form the interconnections the two front-end chip designs and the different sensor designs are discussed. In addition an overview of the two read-out systems as well as the techniques to perform measurements with radioactive sources and in a Test-Beam (TB) environment are given. The different irradiation facilities used to introduce radiation damage to the modules are also presented. Finally the C++ based Cluster Analysis tool developed to be used for the analysis of source measurements is introduced.

3.1 Front-End - Sensor Interconnection

Bump-bond interconnections are used to form electrical connections between the pixel matrix of the sensor and the front-end chip. For the fabrication of ATLAS Pixel Detector modules bump-bonding processes using indium and solder are available. The indium process is used by Alenia Marconi Systems which became SELEX Sistemi Integrati S.p.A. (SELEX)[1] in 2005. The solder bump-bond process on the other hand is provided by the Fraunhofer-Institut für Zuverlässigkeit und Mikrointegration (IZM)[2]. The layout of both types of interconnection

[1]SELEX Sistemi Integrati S.p.A. (Rome, Italy)
http://www.selex-si.com/
[2]Fraunhofer-Institut für Zuverlässigkeit und Mikrointegration (Berlin, Germany)
http://www.izm.fraunhofer.de/

shown in Fig. 3.1 was adapted from the current module design to be also used for future modules as the ones investigated for the IBL upgrade.

For the indium bump-bond process a photoresist layer is applied to the front-end chip and the sensor wafer. A photolithography process follows to pattern the photoresist and to create openings for the bump-pads. These openings are then used to deposit an under bump metalization (UBM) on the exposed bump-pads. To clean the deposited UBM a plasma etching process is applied to the wafers before the indium is deposited on the front-end chip and the sensor wafer. For the deposition an electron beam evaporates an indium target in the chamber at a vacuum of about 10^{-6} Torr. After the removal of the photoresist about 8 µm high indium cylinders remain on the bump-pads. The diced chips and the sensor are then aligned, flipped and bump-bonded in an automated process. To form the bump-bonds a thermocompression process heats the module for several minutes to 90 °C while a force of 25 N is applied. The distance between sensor and front-end chip is about 10 µm after the connections are formed. To assure the quality of the connections an accurate alignment and homogeneous distribution of the force is necessary for this process [75].

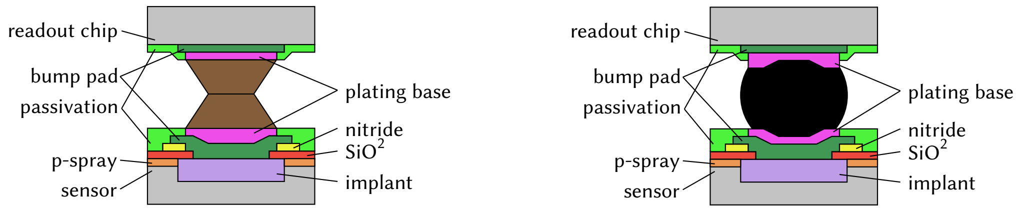

(a) indium bump bond connection (b) solder bump bond connection

Figure 3.1: The two bump bond connection techniques to establish the electrical contact between the sensor and the read-out chip used to fabricate the modules characterized in this work [75, 76].

The solder bump-bond process of the IBL pixel detector modules uses an eutectic tin silver SnAg3.5 mixture for the bump-bond formation. For the electroplating process a 200 nm thick adhesion layer of TiW and a 300 nm thick Cu plating base is sputtered on the sensor and the electronics wafer. A photoresist deposited on the wafer provides openings on top of the bump-pads for the electroplating process. Contacts to the plating base at the wafer edge are used to apply the voltage during the electroplating to form the UBM layer. This layer consists of a 5 µm thick copper layer which is directly connected to the plating base. Contrary to the indium process the bump-bond material is only deposited on the electronics wafers. The electroplated solder mixture forms several µm thick cylinders on top of the UBM. After the electroplating process the photoresist, the plating base and the adhesion layer are removed. Before the wafers are prepared for thinning and dicing the electronics wafer pass through a reflow step at 250 °C to transform the cylindrical form into a ball-shaped bump. The diced chips and sensors are then adjusted and flipped in a bonding machine followed by a second reflow process. At a peak temperature of 250 °C the connections between the sensor and the read-out chip are formed. Self alignment due to surface tension in the solder material eases the bump-bond formation. As part of the quality assurance process X-ray measurements are performed at the end of the bump-bond process to identify modules with missing or bridged bumps [75, 76, 29, 77].

The higher bump-bond density and the bigger chip size used for IBL modules made it necessary to adjust the processes to the new requirements. While the solder bump-bond process was chosen to be the baseline technology for IBL also tests on IBL modules using the indium process were performed. Apart from the deposition process an additional glass carrier wafer is bonded to the back side of the thinned IBL electronics wafer before dicing. The additional material eases the handling of the chips and avoids thermal induced bowing during the reflow process. This was observed to be one reason for disconnected bumps at the edges of FE-I3 chips which would increase for FE-I4 chips due to the bigger size and reduced thickness. The glass support is removed after the flip-chipping by breaking the adhesion layer by exposing it to a laser beam [29].

3.2 Front-End Electronic Chips

The two front-end electronic chips designs FE-I3 and FE-I4 have been available for the sensor characterization performed in this work. The FE-I3 chip is the front-end chip used for the fabrication of ATLAS Pixel Detector modules. The chip features a $18 \cdot 160$ pixel matrix with a pixel size of $50 \cdot 400\,\mu m^2$. The FE-I4 chip design was developed as radiation hard read-out chip for the ATLAS IBL upgrade. While the FE-I4A a prototype version of the FE-I4 was used for the module characterization the improved FE-I4B version is going to be used for the ATLAS IBL upgrade. Specific properties of the FE-I3 and FE-I4 read-out chips are summarized in Tab. 3.1.
Both front-end chip designs implemented similar analog pixel cell layouts shown in the block diagram in Fig. 3.2 consisting of a 2-stage amplifier followed by a discriminator. For the digital part the FE-I3 design implements a column-drain architecture while the FE-I4 chip uses a 4-pixel digital region for hit storage and recording.
An analog injection circuit used for artificial charge injection in Fig. 3.2 is build in both pixel designs using two capacitances. With the help of a pulse generator controlled by a digital to analog converter (DAC) the capacitances are charged and used to inject specific charges in the analog pixel cell. This charge injection offers the possibility to perform scans and tunings to determine and to adjust the pixel threshold and feedback current. Furthermore the implementation of calibration scans to convert the digital signal into the corresponding charge becomes possible. Variations between the implemented injection capacities and the calibration voltage compared to the design values are expected to be in the order of 15 % and 20 % for the current ATLAS front-end chip and the IBL front-end chip respectively [78].
For both designs the induced current signal reaches the input of the preamplifier through

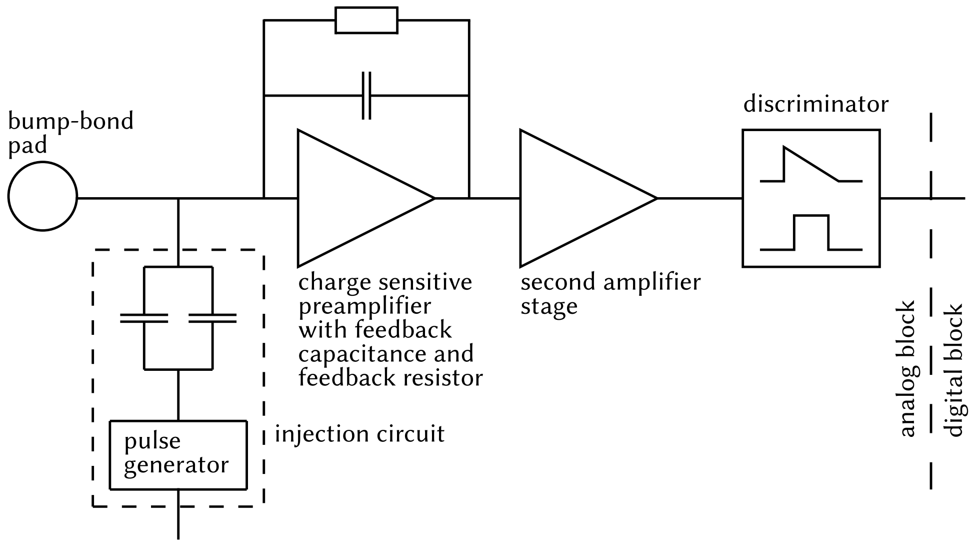

Figure 3.2: Block diagram of an analog front-end pixel layout with a 2-stage amplifier, discriminator, injection circuit and bump-bond pad [72].

the bump-bond connection between the sensor pixel and the read-out channel. The feedback capacitance in the charge sensitive preamplifier described in Sec. 2.3 charges up and creates a triangular pulse shape during its discharge. The width of this signal corresponds due to the nearly linear discharge of the feedback capacitance to the injected charge. The second stage amplifier provides additional signal amplification before the signal reaches the discriminator. Here an output signal is created when the amplified signal exceeds the pixel threshold. The output signal width is measured in units of time-over-threshold (ToT) and coded in 25 ns units following the LHC bunch crossing frequency of 40 MHz. Next to the injected charge also the threshold level and the feedback current slop shown in Fig. 3.3 affect the length of the discriminator output signal. Both front-end chips feature the possibility to adjust the output signal by controlling the threshold level and the feedback current slope with dedicated DACs.

The pixel threshold is extracted from a S-curve fit corresponding to an error function given in Fig. 3.4. This value represents the signal charge necessary to determine a hit signal with a probability of 50 %. The charge range corresponding to the slope between 30 % and 70 % is defined to be used for the approximation of the pixel noise representing the equivalent noise charge (ENC). The ENC itself is the input signal necessary to reach a SNR = 1 and corresponds to the standard deviation of the error function [72]. In case of an untuned module the threshold dispersion over all pixel can reach up to several hundred of electrons. A threshold tuning implemented in the control software adjusts the individual pixel baseline to obtain an uniform threshold level over the entire sensor. Another property correlated to the threshold settings is the noise occupancy meaning the number of noise signals wrongfully considered as hit signals. This noise occupancy decreases with increasing threshold settings thus limits the minimum threshold of a sensor module. For irradiated samples showing a

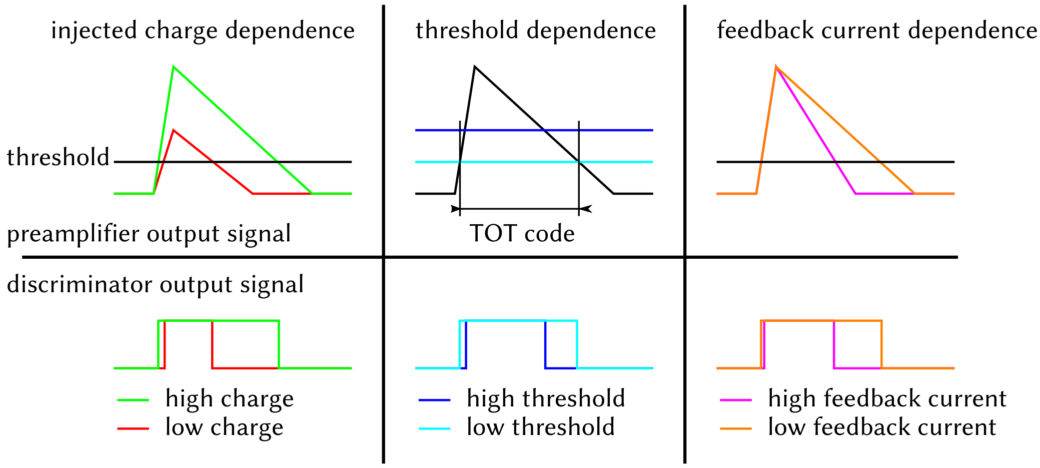

Figure 3.3: Relation between the signal after the preamplifier and the discriminator output signals for the injected charge, the threshold and the feedback current [75].

reduced charge collection this minimum threshold level could exceed the deposited charge which would result in an inefficient pixel [79].
Similar to the threshold tuning individual pixel DACs controlling the feedback current slope are used to create an uniform response of the feedback current. This provides the possibility to adjust the ToT response to the expected charge in the sensors. For both front-end chip designs the ToT tuning is set by changing the corresponding DACs until an injected charge corresponds to a specific ToT responds [79].

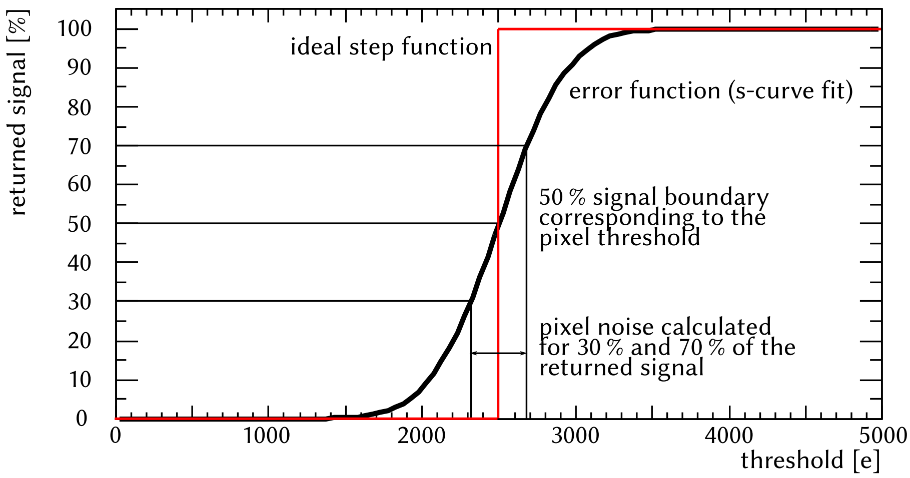

Figure 3.4: Ideal step function including an error function used to determine the pixel threshold and the pixel noise during a threshold scan [75].

After the tuning procedure a calibration scan is performed to obtain the calibration parameters for the ToT to charge calibration. For this scan a range of several charges gets injected in each pixel while the corresponding ToT response is measured. The result is an individual ToT to charge calibration graph which is later used to determine the charge values. Examples of these calibration graphs for a FE-I3 and a FE-I4 chip are shown in Fig. 3.5(a) and Fig. 3.5(b) respectively. The reason for the variation between the two read-out chips is the transition from a 8-bit ToT resolution in the FE-I3 chip to a 4-bit resolution in the FE-I4 chip. Different offline calibration procedures have been implemented to cope with the variation of the ToT range in the two read-out chips.

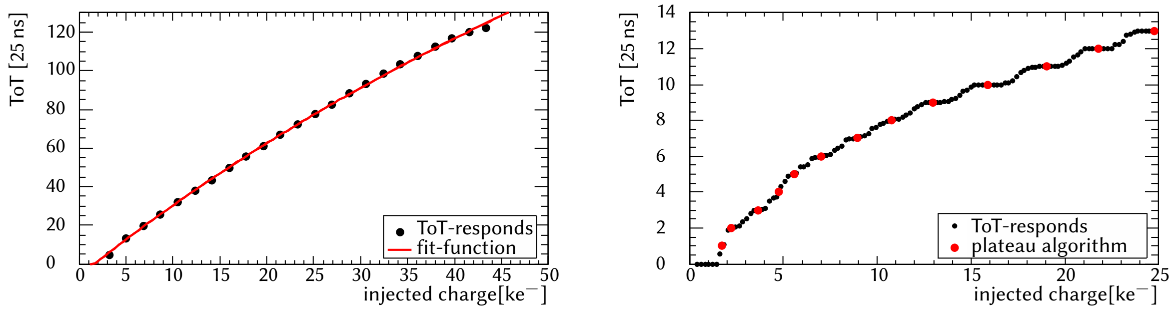

(a) FE-I3 (b) FE-I4

Figure 3.5: Example of the calibration scan results of a FE-I3 and a FE-I4 read-out chip. For the FE-I3 chip in Fig. 3.5(a) the fit-function defined in Eq. 3.1 is used to determine the calibration parameters. In case of the FE-I4 chip shown in Fig. 3.5(b) a plateau finding algorithm is used to extract the ToT and charge values corresponding to each plateau.

In case of the FE-I3 chip the ToT to charge calibration is based on a fit-function to represent the calibration scan. Depending on the read-out system two fit-functions both using three calibration parameters A, B and C are used [80]. While Eq. 3.1 is used in the TurboDAQ[3] [80] read-out system is Eq. 3.2 used in the current ATLAS Pixel Detector and in the USBPix[4] [79] read-out system. In order to reduce the amount of parameters for the calibration in the ATLAS Experiment a set of three values is extracted for each front-end chip. This becomes possible due to the tuning procedure introducing uniform pixel behavior.

$$\mathrm{ToT} = A + \frac{B}{C+Q} \tag{3.1}$$

$$\mathrm{ToT} = A \cdot \frac{B+Q}{C+Q} \tag{3.2}$$

The 4-bit ToT resolution of the FE-I4 read-out chip is the reason for the formation of the step function shown in Fig. 3.5(b). Instead of using a fit-function to determine the calibration parameters a look up table (LUT) containing 13 charge values with corresponding ToT values for each pixel is used for the charge calibration. These values are determined by a plateau finding algorithm and correspond to the center of each step shown in the calibration graph in Fig. 3.5(b). A distribution of the determined charge for the available ToT values of a whole

[3]TurboDAQ: http://physik2.uni-goettingen.de/~jgrosse/TurboDAQ/
[4]USBPix: http://icwiki.physik.uni-bonn.de/twiki/bin/view/Systems/UsbPix

front-end chip is shown in Fig. 3.6. To reduce the size of the LUT the mean charge value of each distribution is used to convert the measured ToT value into a charge value. This effectively reduces the LUT to 13 charge and 13 ToT values for each front-end chip.

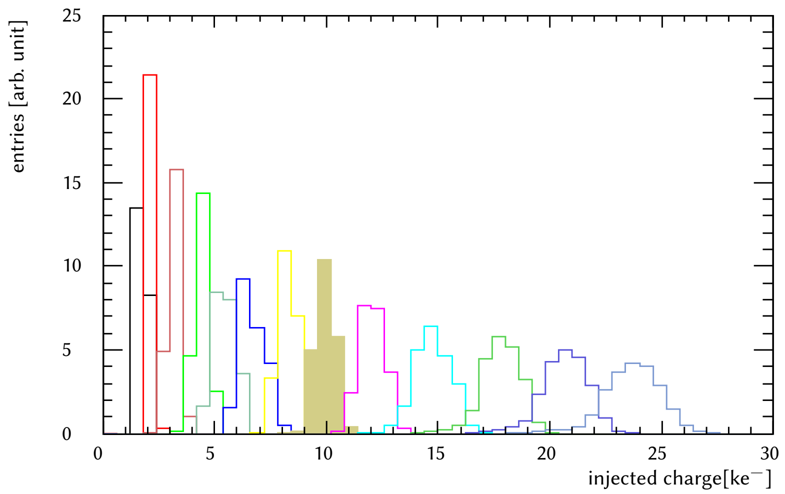

Figure 3.6: Charge distribution for the 13 ToT values in an entire FE-I4 chip. A tuning with a threshold of 1600 e^- and a gain of 8 ToT for 10 ke^- was used. Both tuning parameters are represented by the solid distribution in the plot. Furthermore, a concentration around specific values for each ToT can be observed.

3.2.1 FE-I3

The FE-I3 read-out chip implements a $18 \cdot 160$ pixel matrix with $400 \cdot 50\,\mu m^2$ read-out cells fitting the sensor pixel layout. Figure 3.7 shows the diagram of the analog read-out block cell and its connection to the digital part. Double columns build out of two neighboring pixel columns are connected to the same end of column region where the hit information is processed. The 2880 pixel cells and the logic region on the bottom of the chip form an active area of $7.2 \cdot 10.8\,mm^2$. A 250 nm deep sub-micron CMOS process with six process layers is used to fabricate about 3.5 M transistors.

The analog pixel block uses a charge sensitive folded cascode preamplifier with a 5 fF feedback capacitance. To reduce noise effects caused by high leakage currents through the sensor a leakage current compensation circuit is integrated in the preamplifier stage of each read-out pixel. The two transistors building the compensation circuit are able to cope with a pixel leakage current of up to 100 nA. A global DAC connected to the preamplifier of each pixel controls the global feedback current behavior. In addition the pixel DAC (FDAC) regulates the feedback current slope of each pixel individually to obtain the triangular discharge. Furthermore an injection circuit with a 8 fF and a 32 fF capacitance is connected in parallel to the sensor pixel to the preamplifier input [81].

The DC-coupled second amplifier stage uses a differential pair amplifier followed by the discriminator. To control the threshold a global DAC (GDAC) controls the reference input of the second stage. In addition the pixel DAC (TDAC) further adjusts the individual reference input to reach an uniform threshold distribution in the read-out chip. To avoid efficiency decrease but also noise increase a threshold of $4000\,e^-$ is used in the experiment. The most probable charge for a MIP exceeds this threshold more than twice even after irradiation.
To measure the ToT the discriminator output pulse triggers the storage of the time stamp for the leading and trailing edge in a 8-bit SRAM cell. In parallel the discriminator output pulse is used for the hitbus signal which is sent to the end of column logic. This signal triggers the read-out of the hit information stored in the column. The column extractor unit starts the read-out of the time stamps which are used to calculate the ToT later stored in the end of column (EOC) buffer [3].

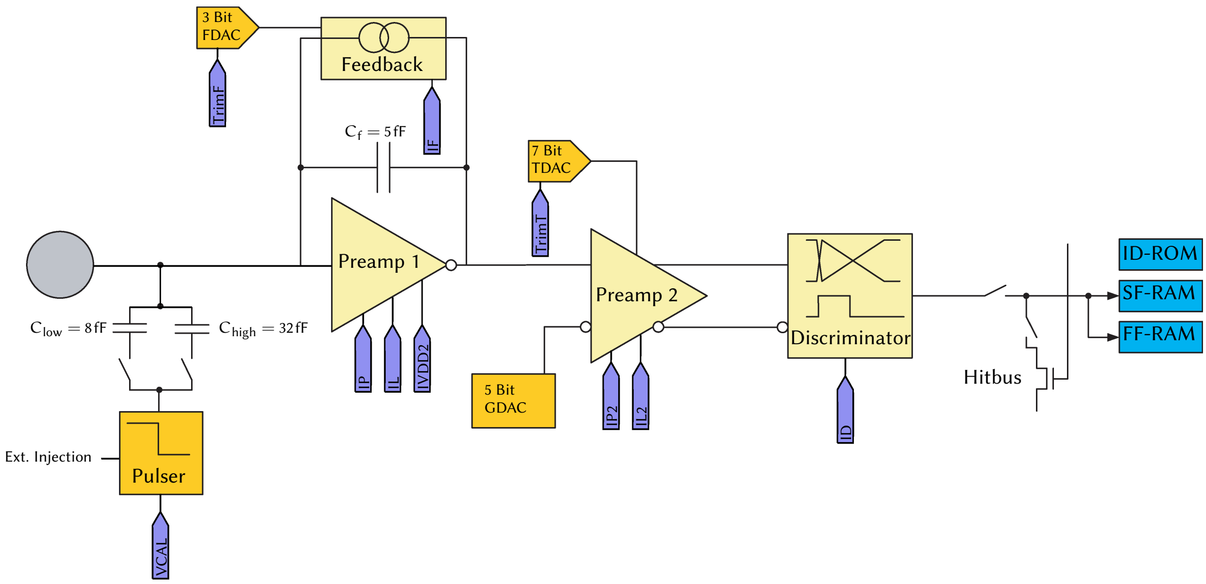

Figure 3.7: Analog front-end pixel layout of a FE-I3 pixel cell [81, 3].

In order to assure the Pixel Detector operation of several years a radiation hard design was used for the FE-I3 read-out chip. A total radiation dose of 50 Mrad corresponding to a fluence of $1 \cdot 10^{15}\,n_{eq}\,cm^{-2}$ was determined as the lifetime dose for FE-I3 modules. Irradiation tests with FE-I3 modules showed that the chip is still operational after radiation damage corresponding to about 100 Mrad and 150 Mrad for a proton irradiation with 24 GeV and 25 MeV respectively.

3.2.2 FE-I4

The FE-I4 front-end chip has been developed as radiation-hard pixel sensor read-out chip for the application in the ATLAS IBL and future ATLAS Pixel Detector upgrades. During the ATLAS IBL upgrade in 2013 the chip will be used for the read-out of the new B-layer. A second aim is to use the FE-I4 chip in the outer pixel detector layers after the replacement of the ATLAS Inner Detector during the phase-2 upgrade [82]. In order to be fully functional during its application period the performance requirements of the chip geared towards the expected luminosity increase following the LHC upgrade program. This included the operation at higher hit rates expected for a higher luminosity and a smaller distance from the interaction point. Reduced pattern recognition and the operation close to the full capacity of the read-out band-width are two of the main effects the new electronic chips have to handle. To cover a bigger surface with pixel detector modules it will be important to reduce the fabrication cost of the modules. By increasing the chip size the flip chipping cost will be reduced as less modules would be necessary to cover the same area. To take this point into account a larger chip size became a further requirement for the new design. In order to use the new read-out chip in the present detector but also in future upgrades the chip had to be compatible with the current and future read-out scheme [82, 83]. To comply with these requirements a redesign of the present front-end chip FE-I3 layout was used as a starting point for the development of the FE-I4. Based on the expected luminosity in the HL-LHC environment a minimum radiation tolerance of 250 Mrad for a fluence of $5 \cdot 10^{15}\ n_{eq}\ cm^{-2}$ was defined as basic specification for the FE-I4 read-out chip. The higher radiation hardness of the FE-I4 was mainly achieved by applying the 130 nm CMOS process on a pixel design similar to the one which was already used for the FE-I3. The reduction of the gate oxide thickness caused by the new process showed to be less effected by radiation damage than its predecessor technology [84]. To increase the performance at higher hit rates the pixel size was reduced to $250 \cdot 50\ \mu m^2$. This reduction of the long pixel side reduces the probability of shared clusters thus improves the pattern recognition properties. A further advantage is the increased spacial resolution along the beam axis. The new read-out chip design features a $80 \cdot 336$ pixels matrix with 26 880 read-out channels on a chip size of $20.0 \cdot 19.0\ mm^2$ [29, 78]. The hit information transfer from the pixel to the EOC region via the double column used in the FE-I3 was identified to be the main inefficiency at high hit rates due to a bottleneck in the column read-out band-width. To assure the operation at high hit rates a new read-out architecture using a 4-pixel digital region was developed for the FE-I4 chip. A prototype version of the FE-I4 using the 4-pixel region the so-called FE-I4A became available at the beginning of 2011 and was used for the sensor characterization in this work. The FE-I4B a debugged version of the FE-I4A is going to be used for the production of the sensor modules which are going to be used in the IBL upgrade [29].

The circuit diagram in Fig. 3.8 shows the analog read-out block of a FE-I4 pixel cell. Each pixel cell features a two-stage charge sensitive amplifier followed by a discrimination stage. The DC-coupled preamplifier with a feedback capacitance of 17 fF creates the triangular shaped feedback current signal. In order to adjust the ToT resolution the slope of the feedback current can be regulated with a local 4-bit DAC set in the front-end configuration. The chip design was build for a maximum input capacitance of 400 fF. An injection circuit with two capacitances C_{inj1} and C_{inj2} is available to inject specific charge values during the tuning procedure. To increase the range of the injected charge the two capacitances can be used either individually or in parallel. A leakage current compensation at the input of the preamplifier is able to handle a pixel leakage current of up to 100 nA. The second amplifier stage is AC-coupled with a 52 fF capacitance to the preamplifier which provides a further signal gain. The output signal of the second stage and the DAC controlled threshold are directly compared in the following discriminator. The discriminator output signal is then feed to the hitbus and the 4-pixel digital region [57].

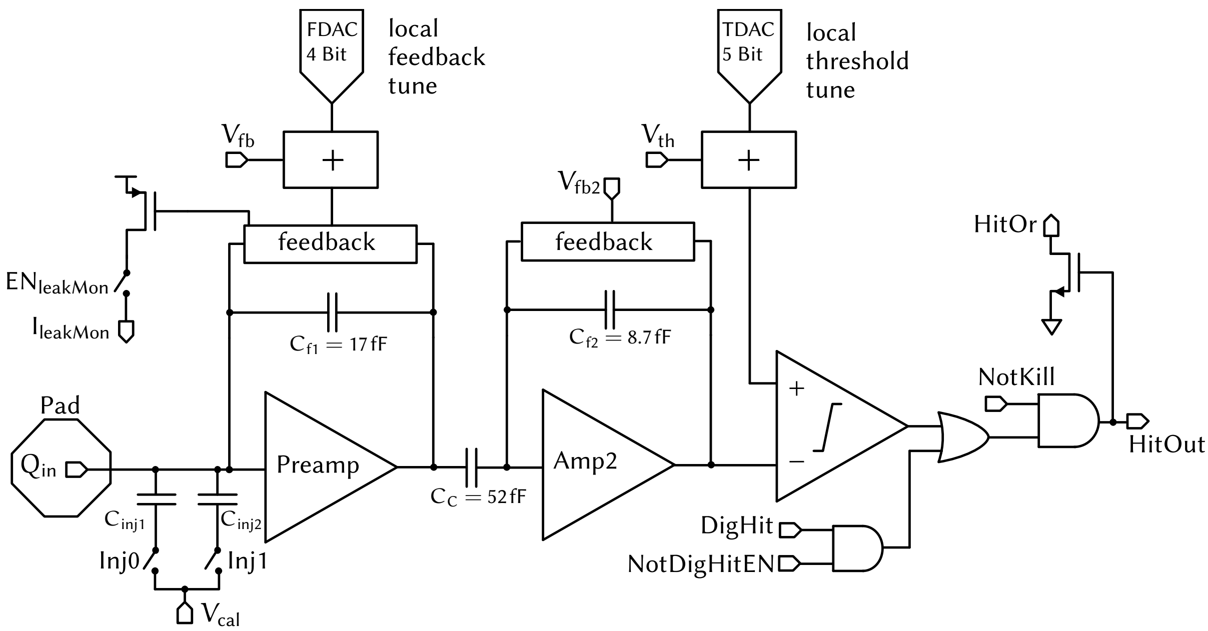

Figure 3.8: Analog front-end pixel circuit layout of a FE-I4 pixel cell [78].

The 4-pixel digital region shown in Fig. 3.9 consists of $2 \cdot 2$ pixels sharing a common digital block. This design was chosen to overcome FE-I3 inefficiencies at high hit rates. Each pixel features a hit processing unit to handle the time-stamping and the calculation of the ToT. An additional digital discriminator in each pixel can be used to distinguish small and large hits. Large hits exceeding the digital threshold are used as seeds to assign the time information while small hits which do not exceed the digital threshold use the timing information of one of the neighboring pixel. The purpose of this procedure is to reduce time-walk effects by associating small hits to large hits from an earlier bunch crossing. Furthermore if a hit is detected in one of the four pixels a common latency counter is assigned to store the four ToT values. The close proximity between the pixel and the hit processing increases the efficiency at high luminosity. A reduction of the power dissipation comes with the new design as hits get only transferred to the periphery after a trigger signal occurred [85, 83].

The FE-I4A version of the FE-I4 read-out chips was used for the sensor characterization during the IBL upgrade and to test the new 4-pixel digital read-out logic. In addition were

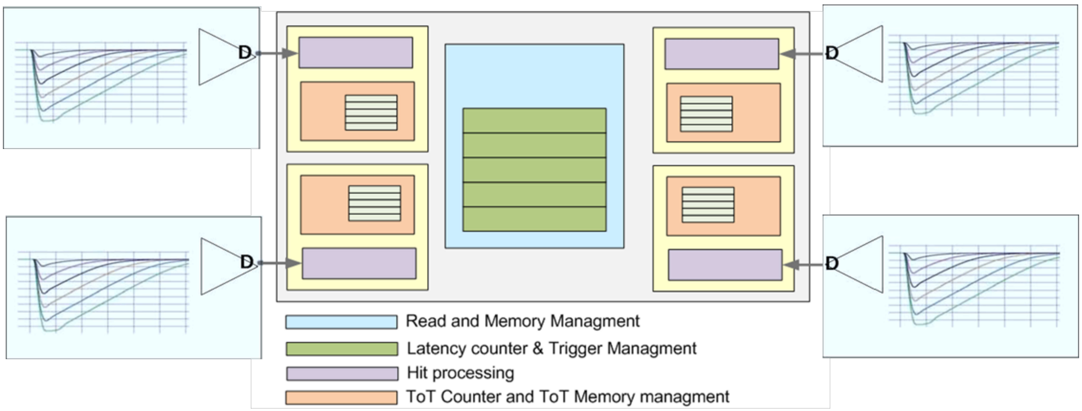

Figure 3.9: Digital 4-pixel region as it is implemented in a FE-I4 read-out chip [78].

different pixel variations implemented in several double columns to test other feedback capacitors, low power discriminators and single event upset hard pixel memory cells. As the FE-I4A is not equipped with a circuit to measure the injection capacitance the design values of $C_{inj1} = 1.9\,fF$ and $C_{inj2} = 3.9\,fF$ were used during the module tuning [78].
In the FE-I4B version only one pixel design was implemented in all double columns to provide an uniform behavior during the operation of the IBL. Next to other changes this new pixel design uses only metal-to-metal feedback capacitors, low-power injection transistor switches and DICE latches implementing an interleaved layout and a guard-ring. Calibration tests measuring the hit rate of four x-ray sources in function of the threshold showed a mismatch of the parallel calibration capacitance of about 1 fF in the FE-I4A chip. To reduce possible calibration uncertainties during the operation in IBL the FE-I4B holds a circuit to measure the injection capacitance. To cope with new DAQ requirements a slight redesign of the end of chip logic became necessary which included amongst others an user-programmable event size limit function, an event count reset and a possibility to suppress duplicated hits. The chip also features a powering scheme using the internal powering nets as well as the possibility to use the two in-chip low drop out voltage regulators [86]. Furthermore is an additional general purpose ADC and a temperature sensor included in the new design [78, 87].

As signal height decreases after irradiation it becomes more and more important to operate the detector modules at a low threshold. In this context the module noise as well as the noise occupancy become relevant parameters to characterize the module performance. Tests concerning this low threshold operation of the FE-I4A read-out showed a noise and noise occupancy increase for decreasing threshold values. A threshold in the range of $1600\,e^{-}$ was discovered to mark the minimum threshold for silicon sensors before the noise occupancy increased together with the number of noisy pixel. In diamond modules due to the lower noise properties a reduced threshold is expected. Further tests concerning the global threshold and feedback current settings showed an additional connection between these values and the electronic noise of the read-out chip. Noise increases were observed for decreasing threshold and increasing feedback current settings of the FE-I4 chip [78, 77].

To estimate the noise behavior of FE-I4 read-out chip modules a simplified noise model of the FE-I4 chip was used [57]. This simplified noise model focused on the main noise sources discussed in Sec. 2.3 adjusted to the FE-I4 read-out cell. The influence of the second amplifier stage of the pixel cell was due to the low noise contribution neglected. As expected were thermal-noise, shot-noise and 1/f-noise found to be the main noise sources in four regions of the read-out pixel. The transistor channel at the preamplifier input is considered as a combined source of thermal-noise and 1/f-noise while the leakage current of the sensor is the main source of shot-noise in the pixel circuit. Furthermore appears thermal noise in the transistors of the leakage current compensation and in the feedback loop. The different noise contributions of the simplified model are summarized in Eq. 3.3 representing the equivalent noise charge (ENC) of the pixel cell [57, 56]. For diamond modules a further simplified model can be used as the leakage current contribution can be neglected. This simplified model is used in Sec. 4.1.2 to determine temperature properties of the FE-I4 chip.

$$\begin{aligned}
\langle \mathrm{ENC}^2 \rangle &= A_{\text{parallel}} \cdot \left[\frac{\tau_b^2}{\tau_b + \tau_c} \right] + A_{\text{serial}}^{\text{thermal}} \cdot \left[\frac{1}{\tau_c} + \frac{\tau_a^2}{2\tau_c^3} \right] + A_{\text{serial}}^{\frac{1}{f}} \cdot \left[\frac{\tau_a^2}{2\tau_c^2} + \ln\left(\frac{\tau_b}{\tau_c} \right) \right] \\
&\text{with} \\
A_{\text{parallel}} &= \frac{2i_{leak} + i_{fb}}{2q} \\
A_{\text{serial}}^{\text{thermal}} &= \frac{C_D^2}{q^2} \frac{kT}{2g_m} \\
A_{\text{serial}}^{\frac{1}{f}} &= \frac{C_D^2}{q^2} \frac{K_F}{C_{ox} W L}
\end{aligned} \tag{3.3}$$

Here, the width W and the gate length L of the oxide capacitance C_{ox} of the MOSFET transistor on the preamplifier input and the 1/f-noise coefficient K_F are used to calculate the 1/f-contribution to the ENC. The time constants $\tau_a = C_f/g_m$, $\tau_b = C_f/g_{ds,fb}$ and $\tau_c = C_D/g_m$ contain the drain output conductance of the feedback transistor $g_{ds,fb}$ and the transconductance of the preamplifier input transistor g_m. The Boltzmann constant $k = 1.38 \cdot 10^{-23}\,\mathrm{JK^{-1}}$ and the elementary charge $q = 1.602 \cdot 10^{-19}\,\mathrm{C}$ are the two constants of the equation. The developed ENC model of the FE-I4 read-out chips revealed a dependence between the module noise and the four parameters leakage current i_{leak}, preamplifier input capacitance C_D, temperature T and the shaping time constant τ_b which is linked to the feedback current i_{fb}. To predict the influence of the preamplifier input capacitance on the noise behavior special effort concentrated on the determination of its formation. The contribution of the sensors capacitance C_D^{sensor} to the input capacitance was measured with a capacitance measurement chip (PixCap) specifically designed for this measurement. The remaining parallel capacitance of the input transistor itself was determined to be $C_D^{\text{transistor}} = 32.1\,\mathrm{fF}$ [57, 56].

Calculations based on the ENC model and simulations on the original FE-I4 chip layout were performed in function of leakage current, preamplifier input capacitance and shaping time constant to understand the ENC behavior for different sensor technologies. In the end the obtained results were used to determine the ENC in function of the irradiation fluence in order to calculate the SNR depending on the fluence for different sensor material [56, 57].

property	units	FE-I3	FE-I4
CMOS production process	nm	250	130
chip size	mm^2	$7.6 \cdot 10.8$	$20.0 \cdot 18.6$
active fraction	%	74	89
pixel array		$18 \cdot 160$	$80 \cdot 336$
read-out channels		2880	26 880
pixel size	μm^2	$50 \cdot 400$	$50 \cdot 250$
DC leakage current tolerance	nA	100	100
design radiation tolerance	Mrad	100	250
analog current	µA/pixel	16	10
digital current	µA/pixel	10	< 10
analog supply voltage	V	1.6	1.4
digital supply voltage	V	2.0	1.2
ToT resolution		8-bit	4-bit
output data rate	Mbit/s	40	160

Table 3.1: Properties of FE-I3 and FE-I4 read-out chips [3, 81, 1, 88, 29, 78]

3.3 Pixel Sensor Technologies

Several pixel sensor technologies are available for the application in high energy physic experiments. In the framework of this work three technologies have been investigated focusing on their properties before and after irradiation to fluences expected after several years of LHC operation. The tested technologies are planar silicon pixel sensor, 3D silicon pixel sensor and diamond pixel sensor fitting the FE-I3 and FE-I4 read-out chip design. Planar pixel sensor and 3D pixel sensor are using silicon as sensor material while diamond pixel sensor use single- and poly-crystalline diamond as active material.

3.3.1 Planar Pixel Sensors

Planar Pixel Sensor (PPS) use shallow pixel implants penetrating the front side of the silicon. The electric field spreads perpendicular to the sensor surface in the space charge region between the pixel implant and the common bias implant on the sensor back side. Two technologies using n-doped implants as read-out electrodes are investigated as candidates for future tracking detector applications. The n-in-n technology used in the current ATLAS

Pixel detector implements a n-doped bulk silicon while the n-in-p technology uses a p-bulk material. Both design use a highly p-doped back side implant as a common bias contact. A layout showing both technologies is given in Fig. 3.10 also including the electric field within the sensor.

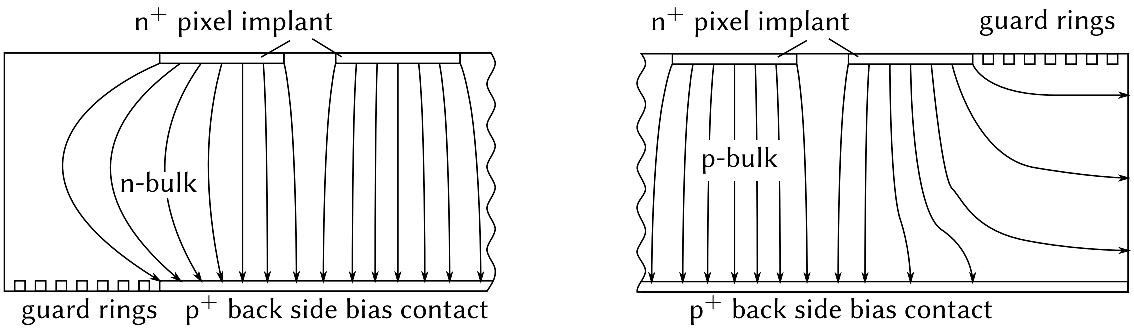

(a) n-in-n (b) n-in-p

Figure 3.10: Layout of the planar pixel sensor designs showing the distribution of the electric field within and on the edge of the sensor. The n-in-n design in Fig. 3.10(a) is using n^+-doped pixel implants in n-doped bulk material with a p^+-doped back side implant. The guard rings are build on the back side of the sensor. In case of the n-in-p design in Fig. 3.10(b) n^+-doped pixel implants are build in a p-doped bulk material with a p^+-doped back side implant. The guard rings are build on the front side of the sensors.

High resistivity silicon wafers are used for the sensor fabrication to keep the full depletion voltage of the sensor at a low value. The sensor capacitance of planar pixel sensors and with it the noise of the device is due to the sensor design correlated to the sensor thickness.
Planar n-in-n and n-in-p pixel sensors were produced by CiS Forschungsinstitut für Mikrosensorik und Photovoltaik GmbH (CiS)[5] and Hamamatsu Photonics K.K. (HPK)[6]. Modules on FE-I3 and FE-I4 read-out chips were tested in the framework of the Planar Pixel Sensors collaboration[89]. Lists containing the planar pixel modules used in this work are given in Tab. 3.2 and Tab. 3.3 for FE-I3 and FE-I4 read-out chips respectively. In case of irradiated modules also the fluence in $n_{eq}\,cm^{-2}$, the corresponding TID and the irradiation facility is included. Four planar pixel sensor designs have been characterized in this work varying the bulk material and the read-out chip. The n-in-n design on a FE-I3 read-out chip produced by CiS corresponds to the design of the current ATLAS pixel modules. The successor design fit to the FE-I4 read-out chip was fabricated in different thicknesses and used varying guard-ring designs. The CiS production of n-in-p sensors is derived from the current ATLAS pixel design and fits the FE-I3 read-out chip. The FE-I4 production of n-in-p sensors from HPK has a thickness of 150 µm and implements different biasing and isolation techniques.

[5]CiS Forschungsinstitut für Mikrosensorik und Photovoltaik GmbH (Erfurt, Germany)
http://www.cismst.org
[6]Hamamatsu Photonics K.K. (Hamamatsu, Japan)
http://www.hamamatsu.com

ID	thickness	fluence	TID	facility
Planar n-in-n silicon FE-I3 sensors from CiS				
CiS-I3-n-#1	250 µm	—	—	—
CiS-I3-n-#2	250 µm	—	—	—
CiS-I3-n-#2-p-irrad	250 µm	$1.6 \cdot 10^{15}\, n_{eq}\, cm^{-2}$	81 Mrad	CERN Set 1472
Planar n-in-p silicon FE-I3 sensors from CiS				
CiS-I3-p-#1	285 µm	—	—	—
CiS-I3-p-#2	285 µm	—	—	—
CiS-I3-p-#3	285 µm	—	—	—
CiS-I3-p-#4	285 µm	—	—	—
CiS-I3-p-#4-p-irrad	285 µm	$3.1 \cdot 10^{15}\, n_{eq}\, cm^{-2}$	156 Mrad	CERN Set 1471
CiS-I3-p-#5	285 µm	—	—	—
CiS-I3-p-#5-p-irrad	285 µm	$2.8 \cdot 10^{15}\, n_{eq}\, cm^{-2}$	141 Mrad	CERN Set 1473
CiS-I3-p-#6	285 µm	—	—	—
CiS-I3-p-#6-p-irrad	285 µm	$1.6 \cdot 10^{15}\, n_{eq}\, cm^{-2}$	81 Mrad	CERN Set 1472
CiS-I3-p-#7-p-irrad	285 µm	$1 \cdot 10^{15}\, n_{eq}\, cm^{-2}$	145 Mrad	KIT
CiS-I3-p-#8-p-irrad	285 µm	$1 \cdot 10^{15}\, n_{eq}\, cm^{-2}$	145 Mrad	KIT

Table 3.2: Table of planar silicon FE-I3 samples implementing the n-in-n and n-in-p sensor technologies considered in this work. In case of an irradiated sensor the collected fluence and the TID is given corresponding to the irradiation facility.

A commonality in all planar pixel sensor designs is the implementation of a biasing and a guard ring structure. While the biasing structure is used to test the sensor properties before the bump-bonding is the guard ring structure important to protect the sensor from a conductive connection across the sensor edge.

The **biasing structure** in the planar pixel sensor design is build in the form of a bias grid connecting all pixel with the bias ring surrounding the pixel region. This structure is used for leakage current measurements before bump-bonding to survey the sensor quality. To form the electrical contact between the bias grid and all pixel cells two methods are available to be implemented in planar pixel sensors. Punch through-dots build of an additional n^{+}-implant in the p-spray close to the pixel implant create a connection between the bias grid and the pixel when the depletion zone under the punch though dot reaches the pixel implant. A second possibility is a poly-silicon bias resistance surrounding the pixel structure to establish the same potential on the pixel as on the bias grid. The three sensor designs fabricated by CiS implement the punch though option by placing one punch through dot per pixel. A part of the HPK production also uses a punch through option while the other part implements the poly-silicon bias resistance in order to investigate and to compare the properties of both techniques. Both punch though and bias resistance makes it possible to perform leakage current measurements on the bare sensor thus to find damaged devices before bump-bonding [43, 90, 91, 92].

Guard ring structures are necessary to avoid a short circuit between the back side contact and the read-out electrodes on the front side. As shown in Fig. 3.10 are the guard rings typically fabricated on the sensor side holding the pn-junction. In case of the n-in-n design this causes additional production steps as the wafer back side needs to be processed as well. For the n-in-p designs the guard rings are fabricated around the active pixel region resulting in a less complex single sided process. This design introduces on the other hand the risk of sparks between the conductive sensor edge and the read-out chip which would damage or even destroy the electronics chip.

ID	thickness	design	fluence	TID	facility
		CiS n-in-n FE-I4			
CiS-I4-n-#01	250 µm	cons.	—	—	—
CiS-I4-n-#02	200 µm	SE	—	—	—
CiS-I4-n-#03	200 µm	SE	—	—	—
CiS-I4-n-#04	200 µm	SE	—	—	—
CiS-I4-n-#05	200 µm	SE	—	—	—
CiS-I4-n-#06	200 µm	SE	—	—	—
CiS-I4-n-#07	200 µm	SE	—	—	—
CiS-I4-n-#08-n-irrad	250 µm	cons.	$5 \cdot 10^{15}\,n_{eq}\,cm^{-2}$	5.43 Mrad	JSI
CiS-I4-n-#09-n-irrad	250 µm	cons.	$5 \cdot 10^{15}\,n_{eq}\,cm^{-2}$	5.43 Mrad	JSI
CiS-I4-n-#10-n-irrad	200 µm	SE	$5 \cdot 10^{15}\,n_{eq}\,cm^{-2}$	5.43 Mrad	JSI
CiS-I4-n-#11-p-irrad	200 µm	SE	$5.1 \cdot 10^{15}\,n_{eq}\,cm^{-2}$	257 Mrad	CERN Set 1533
CiS-I4-n-#12-p-irrad	200 µm	SE	$5.1 \cdot 10^{15}\,n_{eq}\,cm^{-2}$	257 Mrad	CERN Set 1533
CiS-I4-n-#13-p-irrad	150 µm	SE	$5.1 \cdot 10^{15}\,n_{eq}\,cm^{-2}$	257 Mrad	CERN Set 1533
CiS-I4-n-#14-p-irrad	200 µm	cons.	$5 \cdot 10^{15}\,n_{eq}\,cm^{-2}$	725 Mrad	KIT
		HPK n-in-n FE-I3			
HPK-I4-p-#1	150 µm	poly-silicon	—	—	—
HPK-I4-p-#2-p-irrad	150 µm	poly-silicon	$2 \cdot 10^{15}\,n_{eq}\,cm^{-2}$	290 Mrad	KIT
HPK-I4-p-#3-p-irrad	150 µm	poly-silicon	$2 \cdot 10^{15}\,n_{eq}\,cm^{-2}$	290 Mrad	KIT
HPK-I4-p-#4-p-irrad	150 µm	PT	$2 \cdot 10^{15}\,n_{eq}\,cm^{-2}$	290 Mrad	KIT

Table 3.3: Table of planar silicon FE-I4 samples implementing the n-in-n and n-in-p sensor technologies considered in this work. The conservative (cons.) and the slim-edge (SE) design are supported in the n-in-n sensor technology while n-in-p sensor feature a poly-silicon and a punch through (PT) biasing structure. In case of an irradiated sensor the collected fluence and the TID is given corresponding to the irradiation facility.

Planar n-in-n pixel sensors

The FE-I3 pixel layout of a planar n-in-n sensor shown in Fig. 3.11 is fabricated on 250 µm thick silicon wafers. The figure shows four pixel rows and two columns. While the inner pixel have a pixel size of $400 \cdot 50\,\mu m^2$ overlap the pixels on the short edge the front-end pixel matrix corresponding to a pixel size of $600 \cdot 50\,\mu m^2$. The entire pixel matrix is surrounded by the bias ring connected to the bias grid and the attached punch through dots. The metalization on the back side is surrounded by a 600 µm wide multi-guard ring structure consisting of 16 guard rings and additional 500 µm safety margin to the dicing edge [49].

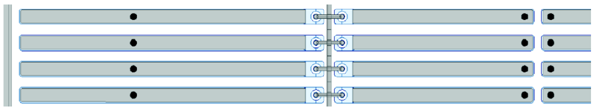

Figure 3.11: Pixel layout of a planar n-in-n pixels sensor adapted to the FE-I3 pixel matrix. The clipping shows four rows and two columns whereof the left column is an edge column and the right one corresponds to a center column. The bias grid shown between the two columns connects the punch through dots of the pixel with the bias ring which is visible on the left edge. The bump pads are placed at the opposing side of the pixel. As the edge column overlaps the front end pixel matrix the bump pad of this column needed to be shifted more to the center of the pixel [77].

To increase the active area for future planar pixel sensors tests and simulations with reduced safety margin and reduced number of guard rings have been performed [50, 51, 49]. Based on the achieved results two advanced designs featuring a pixel size of $250 \cdot 50\,\mu\text{m}^2$ and 13 guard rings have been developed to fit to the FE-I4 read-out chip. The so-called 'conservative' design corresponds to the FE-I3 design with pixel implants overlapping the back side metalization. The surrounding guard rings and the reduced safety margin leave a roughly 450 µm wide inactive area at the pixel edge. This inactive area consists of a 90 µm safety margin while the remaining 360 µm are covered by the 13 guard rings. To reduce the inactive area a 'slim edge' design shown in Fig. 3.12 was proposed extending the length of the edge pixel to a pixel size of $500 \cdot 50\,\mu\text{m}^2$. As a result the edge pixels overlap the guard ring structure increasing the active area of the sensor. Depending on the applied bias voltage the space charge region reaches about 200 µm in the area which would be inactive in the conservative design [90]. Both designs have been produced and tested on 150 µm, 200 µm and 250 µm thick wafer. The Planar Pixel Collaboration proposed the slim edge design implemented on 200 µm wafer as candidate for the production of the IBL upgrade. During the wafer probing of the IBL production a depletion voltage in the range of 50 V was measured. To assure the full depletion of the sensor a safety margin of 30 V was introduced corresponding to an operation voltage of 80 V for unirradiated modules [93].

Planar n-in-p pixel sensors

A planar n-in-p pixel sensor designed by the Max-Planck-Institut für Physik[7] and the Max-Planck-Institut Halbleiterlabor[8] adapted the sensor layout of FE-I3 n-in-n sensors for a p-bulk material. The sensors were fabricated at CiS following the same procedure used for

[7] Max-Planck-Institut für Physik (München, Germany) http://www.mpp.mpg.de

[8] Max-Planck-Institut Halbleiterlabor (München, Germany) http://hll.mpg.de

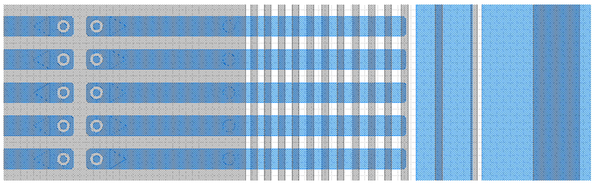

Figure 3.12: Pixel layout of the planar n-in-n slim edge sensor design proposed for the IBL upgrade. The overlapping region of the edge pixel and the guard ring region of the design reduces the inactive edge down to 200 µm. The punch through dots of the edge pixel and the neighboring pixel in the next column is also visible [77].

FE-I3 n-in-n sensors. The layout of one pixel cell in Fig. 3.13 shows the pixel implant with the bump contact as well as the punch-through dot including the connection to the bias grid. The 285 µm thick sensors implement the $400 \cdot 50\,\mu m^2$ pixel size of the FE-I3 read-out chip as well as the extended edge pixel size with $600 \cdot 50\,\mu m^2$ and the ganged and inter-ganged pixel at the top part of the sensor. For this sensor design the guard ring structure got placed on the pixel side reducing the number of process steps. Different multi-guard ring structures using 8, 15 and 19 guard rings surround the pixel region with an additional safety margin. The inactive edge of 1040 µm for 19 guard-ring got reduced to 610 µm for 8 and 15 guard rings. While the safety margin for the 15 guard ring design was reduced by about 60 µm leaving about 550 µm for the guard-ring structure the inactive edge was kept constant for the 8 guard-ring design leaving a wider safety margin. As the fully metalized high p-doped back side is in contact with the conductive sensor edge it becomes possible that the high voltage potential reaches the front side of the sensor. A passivation layer on the read-out chip protects the modules from sparks crossing the gap between the grounded chip and the biased sensor edge. This 3 µm thick passivation layer of benzocyclobutene (BCB) increases the dielectric strength which prevents the chip from destruction. Punch through dots similar to the n-in-n design are used for leakage current measurements before bump-bonding. Bump-bonding and the deposition of the passivation layer has been performed by IZM [94, 95, 96, 97, 98].

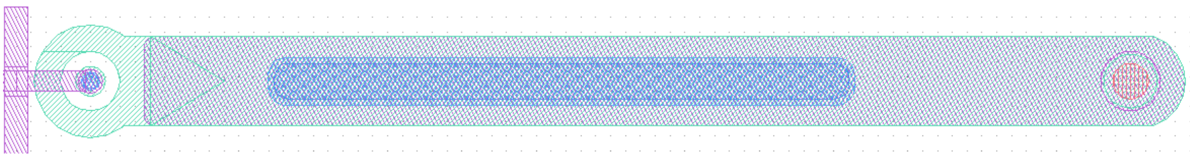

Figure 3.13: Layout of a n-in-p pixel cell with a pixel size of $400 \cdot 50\,\mu m^2$ fit to the FE-I3 read-out chip. The bump contact on the right side provides the contact between sensor pixel and the front-end pixel cell. The punch through dot on the left side is connected to the bias grid to perform leakage current measurements on the wafer level as well as after dicing [98].

A further planar n-in-p pixel sensor design fitting the FE-I4 pixel matrix was fabricated by HPK. The sensors have been produced on 320 µm thick 6 inch-wafer. To reach the sensor thickness of 150 µm the pixel side was produced first before the back side was thinned and further processed. To test different bias and isolation techniques the sensors implement punch through dots and poly-silicon resistance as bias structure as well as a p-spray, common and individual p-stop to isolate the pixel. The punch through dots shown in Fig. 3.14 are placed at the pixel corner connecting four pixel at a time. To further decrease the number of punch through dots it would be also possible to alternate between the corners. The poly-silicon bias resist shown in Fig. 3.14 surrounds the pixel region to form a long trace. The contact between the punch through dots and the poly-silicon resistance is provided by the bias grid which is connected to the bias ring surrounding the pixel matrix. The common and individual p-stop as well as the p-spray are used to isolate the pixel cells from each other. While the two p-stop techniques use a mask step to deposit a p-implant between the pixel cells the wafer for the p-spray technique already implement an overall p-implantation at the surface. Leakage current measurements on the wafer level showed a stable operation up to 1000 V with a leakage current in the range of 200 nA. After dicing an inactive area of 450 µm to the end of the short pixel edge was left while an area of 1175 µm was left to the long pixel edge. Next to the bias ring one guard ring was implemented in the inactive area. The modules have been bump-bonded at IZM using the solder bump-bonding technique. In order to avoid sparks between the conductive sensor edge and the front-end chip which were observed at a bias voltage at about 500 V a silicone adhesive encapsulation was applied to the modules. The encapsulation covered the sensor edge close to the wire-bonds as it was seen on test structures that sparks appear mainly on this edge [91, 92].

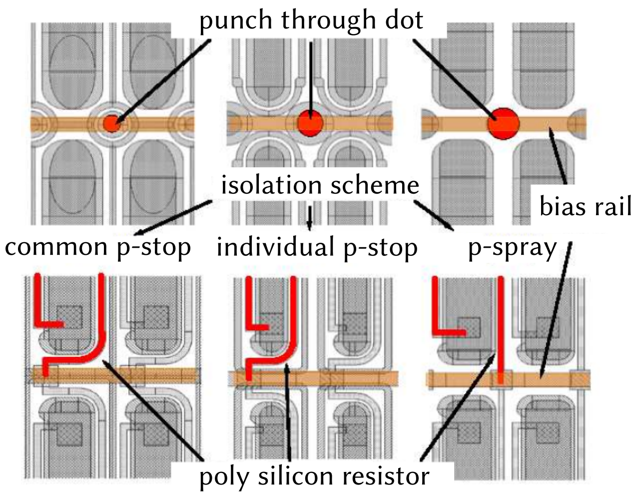

Figure 3.14: The layout of the planar n-in-p pixel sensor fabricated for the FE-I4 read-out chip features two biasing techniques and three isolation techniques. For the biasing the design features a poly-silicon bias resistance surrounding each pixel or a punch through dot at the corner between four pixel. To isolate the pixel cells from each other a p-spray as well as a common and an individual p-stop got implemented [91].

3.3.2 3D Pixel Sensors

A 3D sensor design using conductive columns as electrodes penetrating the bulk material was proposed in 1995 to decouple the electrode distance from the sensor thickness [5]. For the column formation a Deep Reactive Ion Etching (DRIE) process is used while the columns in the silicon wafer are later filled with doped poly-crystalline silicon to form the electrodes. During the development different designs have been tested and enhanced resulting in a single sided and a double sided process.

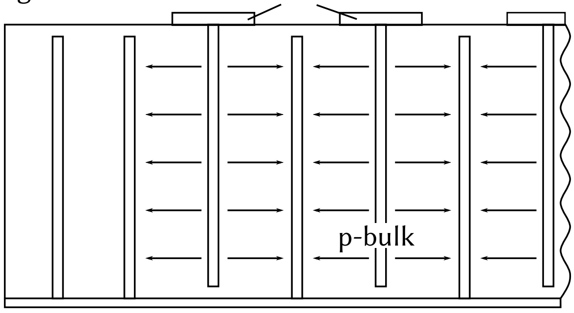

Figure 3.15: Layout of a 3D silicon sensors produced with a double sided process. The n^+-doped electrodes penetrating from the pixel side of the sensor are used as read-out electrodes. The p^+-doped columns are in contact with the back side metalization to bias the sensor. The two columns to the sensors edge are part of the slim-edge design and build a guard-fence structure to reduce the leakage current contribution of the conductive sensor edge.

The single sided process uses a support wafer to fabricate the electrodes entirely from one wafer side [99]. The double sided process on the other hand forms the electrodes from both sides which causes additional alignment efforts. The layout of a 3D sensor produced with a double sided process in Fig. 3.15 shows the different electrodes penetrating the sensor material and the electric field in the sensor. The column overlap which is related to the depth of the column can vary in the double sided process.
The slim-edge approach shown in Fig. 3.15 which can be implemented in a double sided process uses several rows of ohmic columns surrounding the pixel matrix. This fence like structure prevents the depletion region to spread to the conductive sensor edge thus reduces its leakage current contribution [100]. A further possibility is the formation of an active-edge extending the sensitive sensor area. Here the etching process would be used to form a trench which would be later filled with doped poly-crystalline silicon. To hold the individual sensors in place a support wafer is necessary which favors a single sided process. As a result the electric field in the sensor could spread up to the sensor edge reducing the inactive area to only few micro meters [101, 102].

Silicon 3D pixel sensors characterized in this work were fabricated by Fondazione Bruno

ID	thickness	design	fluence	TID	Facility
			FBK FE-I3		
FBK-I3-2E-#1	200 µm	2E400	—	—	—
FBK-I3-2E-#1-p-irrad	200 µm	2E400	$1.6 \cdot 10^{15}$ n_{eq} cm^{-2}	81 Mrad	CERN Set 1472
FBK-I3-4E-#2	200 µm	4E400	—	—	—
FBK-I3-4E-#2-p-irrad	200 µm	4E400	$1.6 \cdot 10^{15}$ n_{eq} cm^{-2}	81 Mrad	CERN Set 1472
FBK-I3-2E-#3-p-irrad	200 µm	2E400	$1 \cdot 10^{15}$ n_{eq} cm^{-2}	145 Mrad	KIT
FBK-I3-3E-#4-p-irrad	200 µm	3E400	$1 \cdot 10^{15}$ n_{eq} cm^{-2}	145 Mrad	KIT
FBK-I3-4E-#5-p-irrad	200 µm	4E400	$1 \cdot 10^{15}$ n_{eq} cm^{-2}	145 Mrad	KIT
			FBK FE-I4		
FBK-I4-2E-#1	230 µm	2E250	—	—	—
FBK-I4-2E-#2-p-irrad	230 µm	2E250	$2 \cdot 10^{15}$ n_{eq} cm^{-2}	290 Mrad	KIT
FBK-I4-2E-#3-p-irrad	230 µm	2E250	$5 \cdot 10^{15}$ n_{eq} cm^{-2}	725 Mrad	KIT
FBK-I4-2E-#4-p-irrad	230 µm	2E250	$2 \cdot 10^{15}$ n_{eq} cm^{-2}	290 Mrad	KIT
			CNM FE-I4		
CNM-I4-2E-#1	230 µm	2E250	—	—	—
CNM-I4-2E-#2	230 µm	2E250	—	—	—
CNM-I4-2E-#3	230 µm	2E250			
CNM-I4-2E-#4-p-irrad	230 µm	2E250	$5 \cdot 10^{15}$ n_{eq} cm^{-2}	725 Mrad	KIT
CNM-I4-2E-#5-n-irrad	230 µm	2E250	$5 \cdot 10^{15}$ n_{eq} cm^{-2}	5.43 Mrad	JSI
CNM-I4-2E-#6-n-irrad	230 µm	2E250	$5 \cdot 10^{15}$ n_{eq} cm^{-2}	5.43 Mrad	JSI

Table 3.4: Table of 3D silicon sensors for the FE-I3 and FE-I4 read-out chip layout considered in this work. In case of an irradiated sensor the collected fluence and the TID is given corresponding to the irradiation facility.

Kessler (FBK)[9] and Centro Nacional de Microelectrónica - Instituto de Microelectrónica de Barcelona (CNM)[10] using a double sided production process. The columns were build in p-doped wafer using n^{+}-doped read-out electrodes in p-bulk corresponding to the n-in-p technology. Due to the low operation voltage necessary to reach full depletion no additional steps are necessary to avoid sparks between the sensor edge and the read-out chip. A summary of the modules used in this work is given in Tab. 3.4 showing the sensor thickness and column configuration. For irradiated modules also the fluence, the corresponding TID and the irradiation facility are given. Depending on the front-end chip and the producer three different 3D sensor designs are characterized in this work. The naming of the modules corresponds to the number of junction columns per pixel and the pixel length. The 2E400, 3E400 and 4E400 sensor designs from FBK matching the FE-I3 read-out chip feature two, three and four read-out columns per pixel. The two 2E250 sensor designs from FBK and CNM for the

[9] Fondazione Bruno Kessler (Trento, Italy)
http://www.fbk.eu/

[10] Centro Nacional de Microelectrónica - Instituto de Microelectrónica de Barcelona (Barcelona, Spain)
http://www.imb-cnm.csic.es/

IBL upgrade fit the FE-I4 read-out chip while using two read-out electrodes per pixel.

FE-I3 3D pixel sensors

The Double Side Double Type (DDTC) 3D sensor design was proposed in 2008 by FBK and fabricated in two batches on 4 inch wafers [103]. The pixel layout in Fig. 3.16 shows the schematics of the three types of 3D-DDTC sensors featuring two, three and four columns per pixel. The DRIE process of the two batches was performed by Ion Beam Services (IBS)[11] and FBK. The column geometry in Fig. 3.16 represents the partial column overlap of the first production batch. Here the total overlap in the 200 µm thick wafer is about 90 µm to 100 µm. This corresponds to a column depth of 100 µm to 110 µm and 180 µm to 190 µm for the junction and the ohmic column respectively. The column diameter is about 10 µm. To establish the pixel isolation p-spray and p-stop implants are used. The sensors of both batches were bump-bonded at SELEX to FE-I3 read-out chips using the indium bump technique. An early breakdown has been observed in sensors from the second batch which was attributed to a contamination during the sensor production [104, 105]. Due to this effect only modules from the first production batch are discussed.

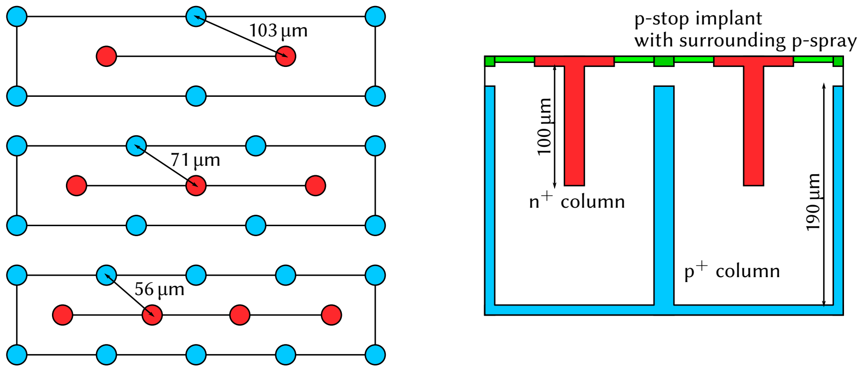

Figure 3.16: Pixel layout of the 3D DDTC sensor design showing the two, three and four read-out column per pixel configuration. The column geometry shows the penetration depth of the junction and ohmic column resulting in a column overlap of 90 µm to 100 µm in the 200 µm thick sensor. The implemented pixel isolation is based on a combination of p-stop and p-spray [106].

Depending on the sensor type the electrode distance changes from 103 µm to 71.2 µm and 56 µm from two to three and four read-out electrodes [106]. To compare the FE-I3 design with the FE-I4 design it ought to be noted that the electrode distance of the 3E400-type corresponds roughly to the 2E250-type sensor design matching the FE-I4 read-out chip.

FE-I4 3D pixel sensors

The two 2E250 n-in-p 3D pixel sensor designs in Fig. 3.17 fabricated by FBK and CNM for the

[11]Ion Beam Services, (Peynier, France)
http://www.ion-beam-services.com/

IBL upgrade are following the same design principles. Both designs are fabricated on 230 µm thick high resistivity wafers and implement two read-out columns per pixel. The slim-edge design in Fig. 3.18(b) surrounding the pixel matrix results in an inactive area of about 200 µm on the short pixel side housing the guard fence structure. Both sensor types were solder bump-bonded to FE-I4 read-out chips at IZM.

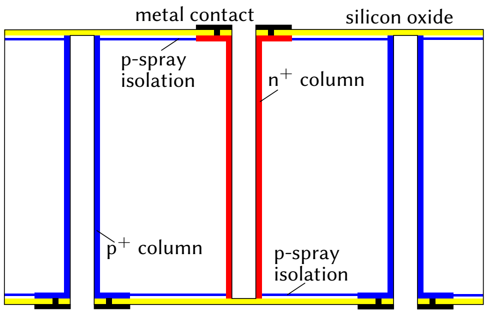

(a) FBK 3D sensor design

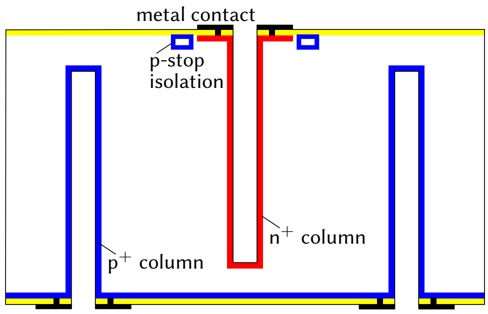

(b) CNM 3D sensor design

Figure 3.17: Sensor layout of the 'full-3D' design in Fig. 3.17(a) fabricated by FBK and the 'partially through 3D' design in Fig. 3.17(b) fabricated by CNM. Both designs feature the 2E250 pixel layout but feature a different column depth and a different inter pixel isolation technique [77].

The production technique applied by FBK results in a 'full-3D' column configuration shown in Fig. 3.17(a) with columns traversing the entire wafer thus forming a column overlap corresponding to the sensor thickness. For the isolation between the pixel cells FBK implements a p-spray which needs to be applied on both sides of the wafer as the read-out columns penetrate the entire wafer. The guard fence structure in Fig. 3.18(a) used by FBK consist depending on the sensor edge of more than three rows of ohmic columns surrounding the pixel matrix. In order to perform leakage current measurements on the wafer level FBK deposits temporary metal lines on each column to short all pixel. The measurement is then performed for each column individually and later summed up to determine the sensor leakage current. After the measurement the temporary metal is removed to have the sensor ready for the module fabrication [107].
The CNM design on the other hand implements the 'partially through 3D' design shown in Fig. 3.17(b). Here the columns penetrate the bulk material and stop a few micro meter before the opposite side is reached. The column overlap in this design is less than the wafer thickness but still more than 200 µm. A p-stop surrounding the n^+-doped columns is used on the front side of the sensor to establish the inter pixel isolation. The pixel matrix of the 3D sensor design fabricated by CNM in Fig. 3.18(b) is surrounded by one n^+-doped 3D guard ring followed by the ohmic guard fence structure. As the sensor design does not include a bias structure the only possibility to perform a leakage current measurements on the wafer level is the 3D guard ring surrounding the pixel area [107].

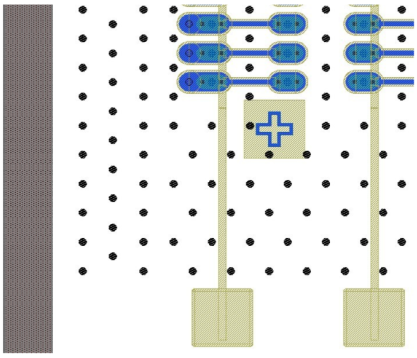

(a) FBK 3D sensor layout

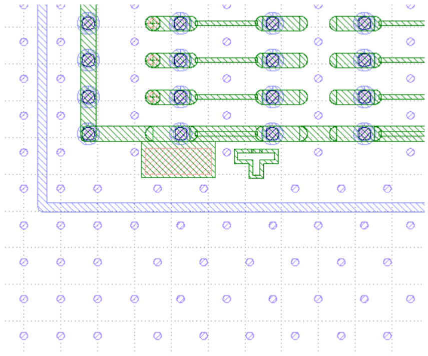

(b) CNM 3D sensor layout

Figure 3.18: Layout of the 3D sensors fabricated by FBK and CNM. The pixel matrix of the FBK design in Fig. 3.18(a) is surrounded by the guard fence structure. Pads of the temporary metal for leakage current measurements are also visible. The pixel matrix of the CNM design in Fig. 3.18(b) is surrounded by one guard ring. The pad connected to the guard ring is used for leakage current measurements. The guard ring itself is surrounded by the guard fence structure [108]

3.3.3 Diamond Pixel Sensors

The pixel structure in diamond pixel sensors is not defined by implants in the material but by its metalization. Depositing the metalization on the surface of the sensor material thus makes it possible to fabricate a sensor with a planar field configuration. The pixel layout in Fig. 3.19 shows the metalization of two pixel columns including the pads used for the formation of the bump connection. In this case the electric field spreads perpendicular through the material until it reaches the back side of the sensor. Depending on the application single- and poly-crystalline diamonds can be used as sensor material.

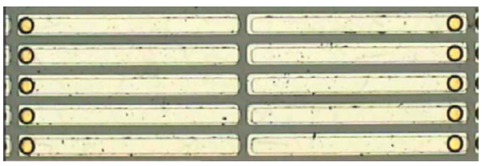

Figure 3.19: Pixel metalization on the surface of a diamond detector. The bump-pads on the pixel edge are used to connect the sensor to the read-out electronic chip [55].

The diamond structures in Tab. 3.5 use a surface metalization fitting the FE-I3 and FE-I4 read-out chip. The table also shows the crystal structure of the material and the thickness. In case of irradiated material also the obtained fluence and the irradiation facility are given. The diamond materials used to produce the FE-I3 modules is single-crystal diamond. Poly-crystal diamond material is used for the fabrication of the FE-I4 modules as this is the proposed material for the DBM.

The single-crystalline diamonds used for the fabrication of the FE-I3 diamond modules are produced by Diamond Detectors Ltd. (DDL)[12]. The seed crystal used to build the diamond material had a size of $4.7 \cdot 4.7\,\text{mm}^2$ thus smaller than the FE-I3 read-out chip. In total the sensor material covers an area corresponding to 85 columns and 11 rows of the read-out chip. Measurements of the sensor thickness of the three modules showed a variation between 513 µm and 570 µm. The pixel metalization was placed on the growth side of the diamond consisting of diamond material with less lattice defects than the back side. Pixel and back side metalization were deposited at IZM which also took care of the bump-bonding to the front-end chip. To avoid a connection between the back side and the conductive edge an unmetalized region surrounding the edge was formed.

ID	crystal structure	thickness	fluence	facility
		FE-I3 DDL		
single-I3-#1	single	560 µm	—	—
single-I3-#2	single	513 µm	—	—
single-I3-#2-p-irrad	single	513 µm	$1.08 \cdot 10^{15}\,\text{n}_{\text{eq}}\,\text{cm}^{-2}$	PSI Set 1412
single-I3-#3	single	570 µm	—	—
single-I3-#3-p-irrad	single	570 µm	$1.08 \cdot 10^{15}\,\text{n}_{\text{eq}}\,\text{cm}^{-2}$	PSI Set 1412
		FE-I4 DDL		
poly-I4-#1	poly	750 µm	—-	—
poly-I4-#2	poly	750 µm	—-	—
poly-I4-#3	poly	750 µm	—-	—
poly-I4-#4	poly	500 µm	—-	—

Table 3.5: Table of single and poly crystal diamond sensors for the FE-I3 and FE-I4 read-out chip layout considered in this work. In case of the irradiated sensor the collected fluence is given corresponding to the hardness factor of silicon for the irradiation facility.

The poly-crystal diamond modules are build from diamond wafers fabricated by DDL. The sensor tiles cut out of these wafers cover the entire read-out chip. The metalization and the bump-bonding was performed at IZM. The first module batch containing modules with a thickness of 750 µm had the back side metalization deposited up to the sensor edge. Due to that the modules could not be operated at bias voltages higher than 300 V. The metalization of the following batch does not reach the sensor edge but shows strong variations on the edge of the metalization. In addition to the metalization limited a defect in the PCB design the maximum bias voltage of the modules.

[12] Diamond Detectors Ltd. (Dorset, United Kingdom)

3.4 Read-out system

For the module characterization of FE-I3 and FE-I4 modules the TurboDAQ and the USBPix read-out system have been available. The TurboDAQ system was developed for the testing and the commissioning of FE-I3 modules for the ATLAS Pixel Detector thus only supports the read-out of FE-I3 modules. The USBPix read-out system on the other hand was developed as laboratory test system supporting the read-out of the FE-I3 and the FE-I4 chip. Both systems provide the possibility to perform scans and tuning steps to configure the DAC values of the module. Furthermore they support the input of a trigger signal which makes it possible to use the system for the read-out during source scans and test-beam measurements with an external trigger system.

3.4.1 TurboDAQ

The TurboDAQ software was implemented during the ATLAS Pixel Detector production phase to characterize pixel modules. The communication between the computer and the pixel module is established via a PC-to-VME interface connected to a set of custom made printed circuit boards (PCBs).
The setup consists of a VME-crate to houses the VME controller board and the Turbo Pixel Low Level (TPLL) board. The controller board establishes the connection between the computer and the VME system and controls the VME bus. The TPLL board handles parts of the data taking and takes care of the communication with the Turbo Pixel Control Card (TPCC). This includes the generation of the clock signal, the trigger input and the data handling with encoding and histogramming. The TPCC provides the communication between the system and up to four single chip modules [80]. For the testing of single chip modules no additional hardware is necessary. In the case of full ATLAS pixel modules an additional Module Adapter Card (MAC) is connected in between the TPCC and the module. This technique is also used for test-beam measurements to operate several modules at the same time.

3.4.2 USBPix

The USBPix system was developed as a general purpose read-out system by the SiLAB group in Bonn. It consists of a multipurpose input-output (Multi-IO) board for the communication with the computer and an adapter board for the connection to the sensor board.

The Multi-IO board enables the communication with the computer and provides sufficient input/output channels for different sensor adapter cards. It features a micro controller with an USB2.0 interface, a programmable Xilinx Spartan3 FPGA and a 2 MB SRAM memory block. The operational voltage for the system can be alternatively provided via the USB connection or an external power supply. In both cases DC/DC-converters are used to adjust the input voltage to the operation voltage of the read-out chip. An Ethernet connector as well as six

LEMO connectors on the board are available for the communication with external trigger systems [79].
The micro controller provides the communication between the computer and the system. In particular it establishes the communication to the FPGA and offers an interface to the Serial Peripheral Interface (SPI) and the Inter-Integrated Circuit (I^2C) bus. The firmware for the micro controller is loaded during the power-up of an EEPROM which is connected to the I^2C bus. A clock generator connected to the I^2C bus and the FPGA provides a clock signal between 80 kHz and 150 MHz. The FPGA chip is programmed to provide the necessary functions for the communication between the Multi-IO board and the connected adapter card. This includes the front-end configuration, the charge injection and the supply of a level 1 trigger signal. A SRAM cell is connected directly to the FPGA to increase the available memory. Raw data coming from the sample can be either stored directly in the SRAM or gets filled in a histogram which than gets stored in the SRAM.

The FE-I3 adapter card establishes the communication between the read-out system and the FE-I3 front-end chip. A set of three LVDS drivers and receivers provide the necessary communication lines to and from the front-end chip. The connector for the analog and digital powering of the samples is also mounted on the adapter card. Furthermore provides the adapter card a connector for a flat ribbon cable for single chip modules and a type0 connector for the communication with entire ATLAS pixel modules [79].

For the communication with the FE-I4 chip the FE-I4 adapter card is used with the Multi-IO board. The adapter card features four power regulators to generate the digital and analog voltages necessary for the operation of the front-end chip. The input voltage is provided via a connector on the board. A LVDS chip and five CMOS level shifter chips provide the communication lines for input/output and shift the supply voltage for the front-end chip. The communication to the front-end chip can be established via a flat ribbon or an Ethernet cable. In case of the flat ribbon cable the analog and digital voltage is distributed via the cable. For the Ethernet communication an additional board to board powering or a direct powering of the front-end chip is necessary.

A C++ based software package was developed to operate the USBPix system. This package included the implementation of a DLL to provide an interface between the computer and the read-out system. The corresponding library USBPixdll offers all necessary functions to implement the communication between the read-out system and different software tools. One of these tools is STControl which is also used for the control of the ATLAS Pixel Detector. For the application in the experiment it implements the PixLib library which is necessary for the communication to the Pixel Detector read-out. Both software tools have been adjusted to handle the functions provided by the USBPixdll in order to perform scans with the USBPix read-out system [79].

3.5 Source and Test-Beam measurements

In order to determine the performance of a sensor technology the module responds to photons and charged particles needs to be measured. Typically these measurements are performed with radioactive sources or with accelerated particles from a test-beam. In case of the radioactive sources a variety of sources can be used emitting different particles at different energies. This kind of measurement is normally performed in the environment of a laboratory which is equipped with the radioactive source. Test-beam measurements on the other hand rely on an acceleration facility which provides access to a beam line.
Measurements done in the context of this work were performed with radioactive photon and electron sources as well as with test-beams of pions and positrons. In general photon source measurements are used to determine the sensor calibration while charged particles simulate the sensor performance in responds to a MIP.

3.5.1 Photon and Electron Source measurements

The measurements with photon and electron sources have been performed with the available sources at CERN. A summary of the sources available during this work is given in Tab. A.1 also providing the source ID, the isotope, the activity and the emitted radiation.

Photon Source measurements
The interaction between photons and the active sensor material depends on the energy of the photon. As described in Sec. 2.2.1 shifts the main interaction from photoelectric effect to Compton scattering and pair production with increasing photon energies. The photon

roentgen fluorescent target	energy [keV] K_α	K_β
Copper (Cu)	8.04	8.91
Rubidium (Rb)	13.37	14.97
Molybdenum (Mo)	17.44	19.63
Silver (Ag)	22.10	24.99
Barium (Ba)	32.06	36.55
Terbium (Tb)	44.23	50.65

Table 3.6: Energies emitted by the different roentgen fluorescent targets of the X-ray sources.

sources available during this work are a Cd-109, a Am-241 and a X-ray source containing an Am-241 core with different roentgen fluorescent targets. The energy range of the X-ray source shown in Tab. 3.6 can be adjusted between 8.04 keV and 50.65 keV while the energy

of the Cd-109 and the Am-241 source is 22 keV and 59.5 keV respectively. The spectra corresponding to the different sources are shown in Fig. A.1(a) and in Fig. A.1(b). Based on the provided photon energies the expected interactions in the sensor are the photoelectric effect and Compton scattering. For energies at the lower end of the range a dominating contribution of interactions related to the photoelectric effect is expected.
For sensor measurements with photon sources the contribution of the photoelectric effect can be used to confirm the sensor calibration. This is possible as the photon energy is well known and because of the deposition of the entire energy during the photoelectric effect. Of course this behavior is only correct for unirradiated and fully depleted sensors assuming that no charge trapping takes place.
To perform the measurement the source is placed on top of the module with a solid angle wide enough to irradiate the entire sensor. The internal hit-bus of the front-end chip is used to trigger the read-out. Depending on the pixel size and the position where the interaction takes place the cluster size changes between single and double hit cluster. For low threshold settings also cluster with three pixel can be observed. The Cluster Analysis software described in Sec. 3.7 provides the possibility to cluster the hits and plot the obtained spectra.

Electron Source measurements

Common practice to perform source measurements with charged particles in a laboratory environment is the application of a Sr-90 electron source. The decay process from Sr-90 to Y-90 and Zr-90 emits beta-particles with energies in the range of 546 keV and 2.3 MeV respectively. As shown in Sec. 2.2.2 this energy is already in the MIP range of electrons in

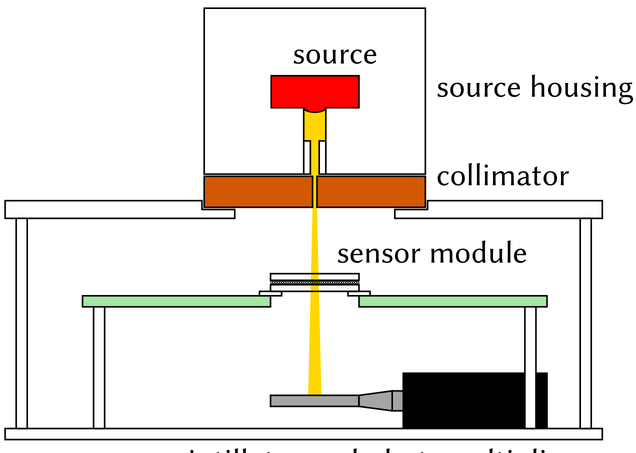

Figure 3.20: Measurement setup for source measurements with electron sources. The electron beam is collimated with a 1 mm bras collimator to create 'beam-like' condition. A scintillator connected to a PMT is placed under the sensor to create a trigger signal.

silicon and diamond material. The layout in Fig. 3.20 illustrates the measurement setup dedicated to perform electron source measurements. By collimating the beta particles 'beam like' condition can be created corresponding to an approximately uniform incident angle for

all electrons penetrating the device. The used bras collimator has a thickness of 10 mm with a 1 mm wide hole. Based on the geometry the electrons pass the sensor placed about 15 mm under the collimator with an angle between 84° and 90°. The electrons with an energy high enough to penetrate the entire module and to reach the scintillator placed under the device cause a signal at the output of the PMT. This signal is used as an external trigger signal in order to read-out the module hit information generated by the electron. The expected charge distribution for this measurement corresponds as described in Sec. 2.2.2 to a Landau distribution. The angular distribution related to the collimator causes a smearing in the measured spectrum which can be described by a convolution of a Gaussian and a Landau distribution. The peak of the Landau distribution is considered as the most probable charge loss in the material. Due to charge sharing in the sensor a clustering process becomes necessary to obtain the deposited charge. As for the photon source measurements this function is also integrated in the Cluster Analysis program described in Sec. 3.7.
The trigger signal generated either by the hit-bus or the external trigger is due to the radioactive decay of the source caused by a stochastic process. The internal clock of the read-out system on the other hand is set to 40 MHz. As the two signals are not correlated it is not possible to determine at what time within the 25 ns bunch-crossing window the particle hit the sensor. As a consequence the signals arriving late in a bunch-crossing window might be attributed to the next window.

3.5.2 Pion and Positron Test-Beam measurements

Test-beam measurements with accelerated particles provide the possibility to perform sensor characterization under similar conditions as in a HEP experiment. The application of a beam telescope makes it possible to determine the particle track through the device under test with a resolution of several micro meter. This information is necessary to determine the spatial resolution of the device and to see the effects of radiation damage within the pixel structure at a high precision.
The test-beam measurements considered in this work are related to several test-beam periods which took place between 2010 and 2012 at the DESY II as well as at the CERN SPS H6 and H8 beam-lines. The beam provided by the DESY test-beam facility consists of positrons within the energy range of 4 GeV to 6 GeV. To avoid multiple scattering related to the low energy not more than two devices were tested at the same time. The CERN SPS test beam facility on the other hand provides high energetic pions whereof beam energies of 120 GeV or 180 GeV were chosen. Due to the high momentum of the particles several devices can be measured at the same time neglecting the effects of multiple scattering.

In order to reach a high spatial resolution within the device under test the EUDET telescope[13] was used to track the particles passing through the devices [109]. The six telescope planes

[13] EUDET Joint Research Activity "DESY Testbeam and Pixel Telescope" http://www.eudet.org/e13/e21/

whereof three are mounted on each side of the DUTs are equipped with Mimosa26 pixel sensors. These sensors come with an active sensor area of $21.2 \cdot 10.6\,\mathrm{mm}^2$ holding rectangular pixel with a length of 18.4 µm. For the sensor read-out a rolling-shutter technique is used which needs 112 µs to read the sensor data [110]. The DUTs are mounted in a cooling box to perform measurements on irradiated devices which are placed between or behind the two telescope arms. While different designs of cooling boxes and techniques were applied at the beginning the most practical option was provided by implementing a dry ice cooling. To apply this technique the cooling box was divided into two compartments whereof one was used to mount the DUTs and the other one provided space for the dry ice slices. Copper strips connected to the back side of the DUTs are guided to the second compartment to provide a thermal contact to the dry ice. As the cooling box compartments are independently accessible it is possible to refill the dry ice without accessing the Device Under Test (DUT) compartment. To avoid short circuits due to condensation either dry air or nitrogen was used to flush the box during the cooling and heating phase. The over pressure due to evaporated carbon dioxide prevents humidity from entering the box thus avoiding condensation during the measurement. To track the temperature during the ongoing measurement several PT1000 resistance temperature detectors are mounted on the inside of the box and on the DUTs. Depending on the position of the DUT the estimated spacial resolution of the telescope varies between 2 µm and up to 10 µm for DUTs between the telescope arms and behind them respectively. The trigger signal for the read-out systems is provided by two $2\,\mathrm{cm}^2$ scintillators in coincidence mounted at the front and the back of the telescope. Adapted versions of the two read-out systems described in Sec. 3.4 are used to configure and to communicate with the DUTs. Due to the different read-out methods used for the telescope and the DUTs it is possible to miss the hit information in the sensors. To cope with this effect it was decided to consider only telescope tracks for the analysis which also show at least one hit in one of the DUTs. To maximize the number of considered tracks an unirradiated sensor module was always added to the DUTs as an efficiency close to 100 % is expected in this kind of device [111, 112].

The data obtained by the telescope and the DUT is stored together after a preliminary analysis procedure was applied to the telescope data. The following reconstruction process contains several exclusion criteria which are necessary to associate DUT hits with the corresponding telescope tracks. The reconstructed data files containing the hit information of the DUT and the associated telescope tracks are then analyzed by different analysis algorithms to determine the detector properties. In general these algorithms included analysis procedures to determine the cluster size distribution, the residuals, the charge collection, the charge sharing probability and the hit efficiency of the DUT.

3.6 Module Irradiation

To determine the sensor characteristics after irradiation sensor modules are irradiated with protons, pions and neutrons. Irradiated modules used in this work have been irradiated during different irradiation campaigns at the Jožef Stefan Institute (JSI) in Ljubljana/Slovenia, the Karlsruher Institut für Technologie (KIT) in Karlsruhe/Germany, the Paul Scherrer Institut (PSI) in Villigen/Switzerland and in the CERN PS irradiation facility. The target fluence chosen for the different campaigns was adjusted to the properties of the front-end chip and the future applications. In case of FE-I3 modules which are designed to withstand a total ionizing dose of 50 Mrad measurements were possible up to the dose range between 100 Mrad and 150 Mrad depending on the particle energy. For FE-I4 module the IBL design fluence of $5 \cdot 10^{15}\,n_{eq}\,cm^{-2}$ at the end of lifetime was used to test the module performance. The relation between the target fluence and the collected dose given in Tab. 3.7 summarizes the total ionizing dose for the different irradiation facilities for fluences typically used in this work.

NIEL fluence	TID [Mrad]		
[$n_{eq}\,cm^{-2}$]	KIT	CERN PS	JSI
$1 \cdot 10^{15}$	145	50	1.1
$2 \cdot 10^{15}$	290	101	2.2
$5 \cdot 10^{15}$	725	252	5.4

Table 3.7: Total ionizing dose for irradiation campaigns at KIT, CERN PS and JSI for fluences used for the characterization of ATLAS Pixel sensor modules [113, 114, 115].

To reduce annealing after irradiation the samples are stored and transported at sub-zero temperatures. Modules irradiated in Geneva, Ljubljana and Villigen are taken off the printed circuit board to avoid activation of the electronic components. During the gluing and wire-bonding procedure necessary for the following sensors characterization the samples stayed for several hours at room temperature. The FE-I4 samples used for the IBL sensor characterization are annealed for 120 min at 60 °C to cure the glue and to reach a similar annealing state.

The TIGRA Mark II research reactor of the JSI in Ljubljana/Slovenia is used for **neutron irradiation** with thermal, epithermal and fast neutrons. For the irradiation the samples are placed in plastic bags which are lowered in one of the seven about 5 m deep irradiation channels leading into the reactor core. Depending on the selected column the energy ratio changes between thermal ($< 0.625\,eV$), epithermal (0.625 eV-0.1 MeV) and fast ($> 0.1\,MeV$) neutrons. In order to normalize the obtained fluence to mono-energetic 1 MeV neutrons the hardness factor $\kappa_{JSI} = 0.75\,n_{eq}\,neutrons^{-1}$ is applied to Eq. 2.14. As there is no cooling available during the irradiation and due to the heat in the reactor core annealing can not be avoided during the irradiation [113].

A low energy **proton irradiation** is provided by the Irradiation Center of the KIT in Karlsruhe/Germany. During the irradiation the samples are placed in an insulated box mounted on a xy-table which moves the samples in 1 mm spaced rows through the beam. The beam generated by a compact cyclotron has a diameter between 4 mm and 8 mm with a beam energy in the cyclotron of about 25 MeV. The energy of the protons after extraction is about 23 MeV with a corresponding hardness factor $\kappa_{KIT} = 2.0\,n_{eq}\,\text{protons}^{-1}$. The proton current of about 1.5 μA makes it possible to reach a fluence of $1 \cdot 10^{15}\,n_{eq}\,\text{cm}^{-2}$ in a $10 \cdot 10\,\text{mm}^2$ in about 15 min. An aluminum shielding plate with openings for the sensors covers the printed circuit board to protect the electronic components from activation. The box with the mounted devices is cooled to −40 °C during the irradiation procedure to avoid heating of the sample and annealing. As the samples are already mounted on the PCB no additional thermal cycling for gluing and wire-bonding is necessary before the sensor characterization [114].

facility	set number	year	error	reached fluence	normalized fluence
CERN	1472	2010	±7.8 %	$2.58 \cdot 10^{15}$ protons cm^{-2}	$1.6 \cdot 10^{15}\,n_{eq}$ cm^{-2}
CERN	1473	2010	±7.7 %	$4.48 \cdot 10^{15}$ protons cm^{-2}	$2.8 \cdot 10^{15}\,n_{eq}$ cm^{-2}
CERN	1471	2010	±7.6 %	$4.99 \cdot 10^{15}$ protons cm^{-2}	$3.1 \cdot 10^{15}\,n_{eq}$ cm^{-2}
CERN	1533	2011	±7.0 %	$8.16 \cdot 10^{15}$ protons cm^{-2}	$5.1 \cdot 10^{15}\,n_{eq}$ cm^{-2}
PSI	1412	2010	±20.0 %	$9.81 \cdot 10^{14}$ pions cm^{-2}	$1.08 \cdot 10^{15}\,n_{eq}$ cm^{-2}

Table 3.8: Fluences reached in the different proton and pion irradiation campaigns performed in 2010 and 2011 at CERN and PSI. The normalized values are calculated with respect to the corresponding silicon hardness factors [115].

The high energy **proton irradiation** of the PS Irradiation Facility in the CERN East Hall provides a proton beam with an energy of 24 GeV. The two beam-lines "Irrad1" and "Irrad3" are both connected to the PS ring which accelerates the protons. "Irrad1" is equipped with a scanning beam which makes it possible to perform uniform irradiations on samples which are bigger than the actual beam spot. A vortex tube cooler is attached to the irradiation table to cool the samples to avoid annealing during the irradiation. The full width half maximum (FWHM) of about 10 mm in "Irrad3" is not enough to perform uniform irradiations on FE-I3 and FE-I4 samples. To avoid a partial irradiation the samples can be tilted to a low angle until they are completely in the beam line. By applying this method on FE-I3 modules it also becomes possible in "Irrad3" to obtain an uniform irradiation. Due to the larger size of FE-I4 modules it is only possible to irradiate a stripe of about 10 mm. As there is no cooling available in "Irrad3" the samples experience a certain degree of annealing during the irradiation. The high energy of the beam makes it possible to irradiate several samples at the same time by placing the samples behind each other. For the normalization the hardness factor $\kappa_{CERN} = 0.62\,n_{eq}\,\text{protons}^{-1}$ is used. The results shown in Tab. 3.8 summarize the different irradiation campaigns corresponding to samples irradiated for this work [115].

The **pion irradiation** is carried out in the PiE1-beam line of the PSI in Villigen/Switzerland. As during the proton irradiation at the PS Irradiation Facility the samples can be stacked behind each other to irradiate several modules at the same time. During the pion irradiation campaign two diamond samples but no silicon samples have been irradiated. The beam energy of about 300 MeV corresponds to a hardness factor for silicon of $\kappa_{\mathrm{PSI}} = 1.11\,\mathrm{n_{eq}\,pions^{-1}}$. Due to the lack of an corresponding hardness factor for diamond the silicon hardness factor will be applied. This is done while keeping in mind that the expected hardness factor for diamond is smaller than for silicon thus reducing the collected fluence. The values in Tab. 3.8 summarize the obtained irradiation results based on the silicon hardness factors.

3.7 Cluster Analysis

The Cluster Analysis software developed as part of this work provides data handling, cluster finding, analysis and plotting of source measurement data. The data analysis process with Cluster Analysis consists of two steps. During the conversion step the data is clustered and stored in a cluster file holding all the hit information. For the analysis step the clustered data is converted into charge, plotted and used to extract different values.

To handle the different read-out systems and chips dedicated functions are included to convert the raw files in a common cluster file which in addition reduces the file size. Independent of the read-out system and the front-end chip all raw data files consist of a number of trigger windows corresponding to the number of trigger send to the read-out system during the scan. Each of these trigger windows contains between 1 and 16 consecutive bunch crossings holding the hit-data. Depending on the position in the trigger window a hit gets allocated to a specific bunch crossing with a time resolution of 25 ns. In addition the hit-data contains the row and the column as well as the measured charge in ToT.
During the data conversion each trigger window is read in separately and clustered. The algorithm extracts the information for each hit in the trigger window and forms cluster depending on the geometrical and temporal relation. For the cluster formation a cluster seed hit is compared to the remaining hits and added to the cluster if they occurred within a variable time or geometrical distance. Default values for the row, column and time distance used in this work have been chosen to be 2 rows, 1 column and 3 bunch crossings. Using these default settings for the clustering only adds hit pixel which are direct neighbors on the short pixel side or at least next to a neighbor on the long pixel side. These settings also provide the possibility to merge cluster even though one neighbor on the long pixel side is masked or due to a missing bump-bond connection not connected to the read-out channel. The read-out of up to 16 consecutive bunch crossings provides the possibility to merge hit pixel not only in relation to the geometrical distance but also to the hit time in bunch crossings. Due to this feature hit pixel with low charge which shifted due to time-walk to a later bunch crossing can be combined with a seed pixel from an earlier bunch crossing. A second reason for the

implementation of this feature is the work with radioactive sources. Here the trigger appears random compared to the 25 ns clock cycle of the read-out electronics widening the time distribution of the hits. In case of remaining unclustered hits a second seed pixel is chosen to form a further cluster corresponding to the same trigger window. The obtained clusters are stored in the cluster file based on the root-file format containing the data in form of a root-tree[14].

For the analysis the clustered data is extracted from the root-file and a ToT to charge calibration as described in Sec. 3.2 is used to determine the corresponding charge of each pixel. To reduce noise effects only trigger windows with one cluster are used for the analysis. All other trigger windows containing more than one cluster after the available cuts have been applied are rejected for the analysis. The pixel showing the highest charge in each cluster is considered as seed pixel to fill the hitmap and the row and column histogram. The pixel corresponding to the earliest bunch crossing is used to determine the timing of the cluster. A Level-1 distribution showing the 16 bunch crossings in a trigger window is filled with the cluster timing. The total cluster charge and ToT is used to fill the charge and ToT histogram. Depending on the applied radiation source either a Gaussian or a Landau function convoluted with a Gaussian (LanGau) fit is applied to the distribution [116]. While the mean charge available from the Gaussian fit is the relevant value for photon-sources the most probable charge can be extracted from the LanGau fit for charged particles. To differentiate the effects of the cluster size on the collected charge dedicated histograms are filled for clusters with one, two and three pixel while the general histograms are filled with all cluster sizes. To understand the distribution of the different cluster sizes a cluster size histogram is filled at the end of the analysis.
Different cuts can be applied for the analysis to dismiss certain kind of clusters. To concentrate the analysis on a specific region minimum and maximum rows and columns can be set. Similar to the spacial cut a timing cut can be used to consider only clusters within a bunch crossing range. To reduce noise effects pixel with a high occupancy can be also excluded from the analysis. The ToT range can be used to identify regions with high and low ToT appearance.

Noise occupancy scan
For noise occupancy scans the obtained raw-data files can also be read in with the Cluster Analysis program to determine the mean noise occupancy of a module. Here either a randomized external trigger with low threshold settings to trigger on noise in the PMT or a trigger signal form a pulse-generator can be used.

At first the program determines the number of hits in each pixel as well as the number of triggers send and the number of level-1 triggers read out. Based on the noise occupancy

[14] ROOT - A Data Analysis Framework: http://root.cern.ch

threshold described in Sec. 2.3 and Eq. 3.4 it is determined if a pixel is considered as a noisy or a good pixel. By building the sum of all hits in the good pixels of the module shown in Eq. 3.5 the mean noise occupancy of the module is determined.

$$\text{If: } \frac{\#\,\text{pixel hits}}{\#\,\text{trigger}\cdot\#\,\text{LVL1}} \geqslant 5\cdot 10^{-5} \Rightarrow \text{noisy pixel} \tag{3.4}$$

$$\text{mean NOcc} = \frac{\Sigma\text{pixel hits}}{\#\,\text{trigger}\cdot\#\,\text{LVL1}\cdot\#\,\text{good pixel}} \tag{3.5}$$

As it is not possible to distinguish noise hits from a muon hit a mean noise occupancy contribution from muons needs to be taken into account for the measurements. Assuming a muon rate of $1\,\text{cm}^{-2}\,\text{min}^{-1}$ a rate of about $50\cdot 10^{-15}$ hits pixel^{-1} BC^{-1} caused by muons can be attributed to the measured hit rate. Depending on the number of triggers used for the measurement the sensitivity of the measurement has to be taken into account as well. As the number of triggers used for the measurements in this work corresponds to a sensitivity of about $1\cdot 10^{-12}$ hits pixel^{-1} BC^{-1} it becomes possible to neglect the muon contribution.

4 Pixel Module Characterization

The performance of pixel detector modules in the future ATLAS Pixel Detector will be crucial for the operation and the performance of the Inner Detector within the experiment. Especially the impact of radiation damage on the modules needs to be understood to assure the high tracking efficiency of the system. For the proper operation of the pixel modules in the experiment extensive measurements need to be performed in order to get to know the properties of the individual components as well as the properties of the pixel module as a whole. The characterization of pixel modules in this work focuses on measurements related to the performance of the two front-end chip designs and the analysis of silicon and diamond based sensor technologies. Measurements concerning the front-end chips provide insight into the noise, threshold and temperature properties of the read-out electronics. The sensor analysis aims to determine the properties of the different sensor technologies. This analysis also includes the sensor responds to ionizing radiation before and after irradiation. Looking at the interaction between the chip and the applied sensor technology the obtained results will be useful to determine the operation condition and limitations in future experiments.

In order to achieve reproducible condition all measurements were performed in a climate chamber providing temperature control combined with a desiccant dryer to avoid condensation on the samples. At the beginning of this work a minimum operation temperature of $-20\,^{\circ}\mathrm{C}$ was feasible while a second cooling system with a minimum temperature of $-50\,^{\circ}\mathrm{C}$ was added later. If not otherwise marked are the given temperatures the set temperatures of the climate chamber. This temperature does not necessarily represent the actual temperature of the device under test.

4.1 Front-end performance

The front-end performance is strongly related to the noise contribution of the front-end chip and its relation to different operation parameters. Especially the operation threshold of future pixel modules becomes more important with longer detector lifetimes when the collected charge decreases after radiation damage. The operation temperature of $-20\,^{\circ}\mathrm{C}$ foreseen for the IBL is a further parameter influencing the noise contribution of the read-out chip.

Prior to the front-end characterization a sequence of tests and scans needs to be performed to assure the proper operation of the module. These scans usually including a test of the

analog and the digital part of the chip. Non-working pixel can be identified with these tests giving a first impression on the bump-bonding quality and possible front-end damage in the analog or digital part. During the measurements the sensor is biased providing the opportunity to perform a leakage current scan which is also used to identify sensor defects evident from high leakage currents or early breakdown voltages. After the communication is established and the sensor is biased the module is ready for the front-end characterization. This includes front-end tunings to different threshold and feedback current settings in order to adjust the ToT gain.
To compare the results of the front-end characterization the injection signal of the chip needs to be calibrated. As described in Sec. 3.2 both injection circuits consist of two injection capacitances and the calibration voltage. In case of the FE-I3 read-out chip both injection capacitances and the slope of the calibration voltage are measured. Due to the missing test capacitances in the FE-I4A chip it is not possible to determine individual values for each chip. Therefore only the offset and the slope of the calibration voltage is measured while the injection capacitances are set to the design values. Despite of the calibration are errors expected to be in the order of 15 % and 20 % for the FE-I3 and FE-I4 chip respectively.

4.1.1 Tuning analysis

During the front-end tuning process all pixel get set to a uniform threshold and a ToT value corresponding to a specific charge. The tuning procedures used by the two available read-out systems TurboDAQ and USBPix follow the algorithms described in Sec. 3.4.1 and Sec. 3.4.2 respectively.

Tuning of FE-I3 chips

Typically the threshold dispersion of an untuned FE-I3 module is in the range of about 400 e^-. After the tuning process this value is reduced to 60 e^- and 20 e^- shown in Fig. 4.1(a) for the TurboDAQ system and in Fig. 4.1(b) for the USBPix system. The corresponding noise distributions for both systems in Fig. 4.1(c) and Fig. 4.1(d) show dispersions below 10 e^-. Concerning the dispersion of the ToT value, a reduction from 5 ToT to 2 ToT is typical for both systems.
Tunings performed with the TurboDAQ system show an about 150 e^- higher threshold than the target threshold. The threshold distribution of a bare FE-I3 chip tuned with the TurboDAQ system to a threshold of 3200 e^- in Fig. 4.1(a) illustrates this effect. This behavior is related to the threshold tuning algorithm implemented in the TurboDAQ system. The different implementation of the tuning process in the USBPix system prevents the appearance of this threshold offset. As shown in Fig. 4.1(b) for the same bare FE-I3 chip tuned with the USBPix system this algorithm leads to better agreement between the target and measured threshold value.
By comparing the noise results obtained for both systems shown in Fig. 4.1(c) and Fig. 4.1(d) a differences in the order of 30 e^- can be observed. A similar behavior has been observed during the production of the ATLAS Pixel Detector where two systems using the TurboDAQ

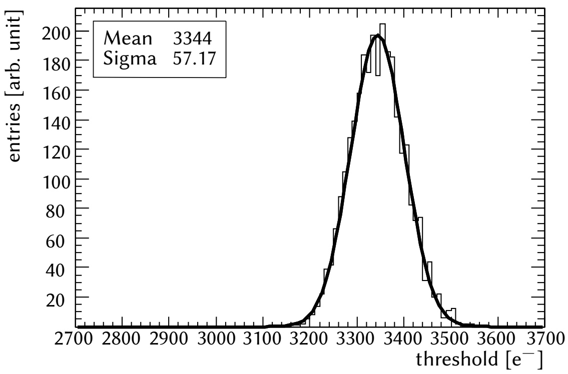

(a) Threshold distribution with TurboDAQ

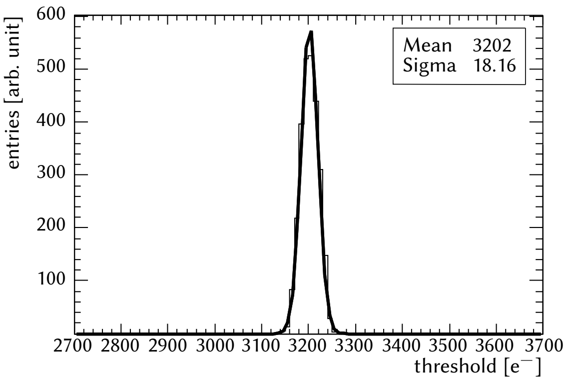

(b) Threshold distribution with USBPix

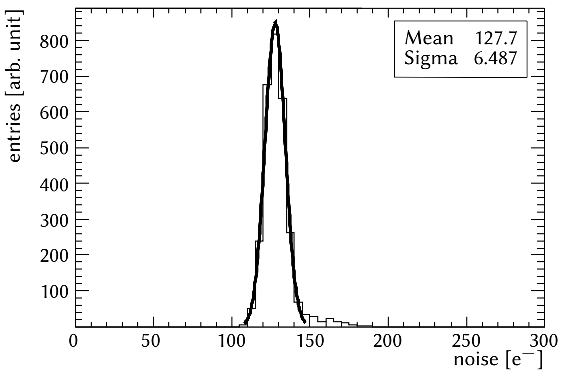

(c) Noise distribution with TurboDAQ

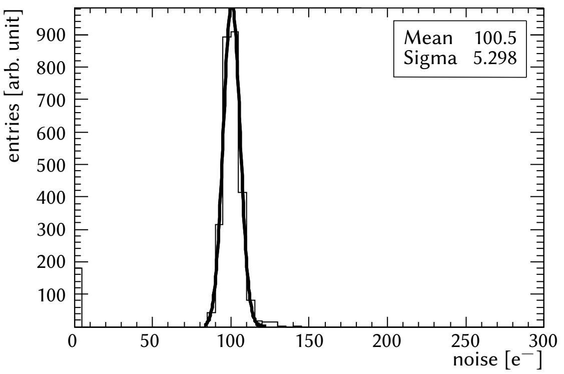

(d) Noise distribution with USBPix

Figure 4.1: Threshold and noise distributions of a bare FE-I3 read-out chip tuned to a threshold of 3200 e^- using the TurboDAQ and the USBPix system. The threshold distribution in Fig. 4.1(a) shows a threshold offset of about 150 e^-. This effect is not present for the tuning in Fig. 4.1(b) performed with the USBPix read-out system. The observed threshold offset is related to the tuning algorithm implemented in the TurboDAQ systems. Fig. 4.1(c) and Fig. 4.1(d) show the corresponding noise distribution for the two read-out systems.

and the USBPix algorithm were used. As measurements show that this noise offset is not related to common mode noise [117] the origin can only be explained by intrinsic properties of the system. To avoid systematic errors introduced by the system it was decided to compare only results obtained with the same software as well as the same scan parameters [80].

To better understand the correlation between the target threshold and the measured threshold a set of tunings to different target threshold values was performed for both systems. Modules using different sensor technologies were part of the study to determine variations between the technologies. In addition a bare front-end chip was also included to distinguish effects related to the sensor.

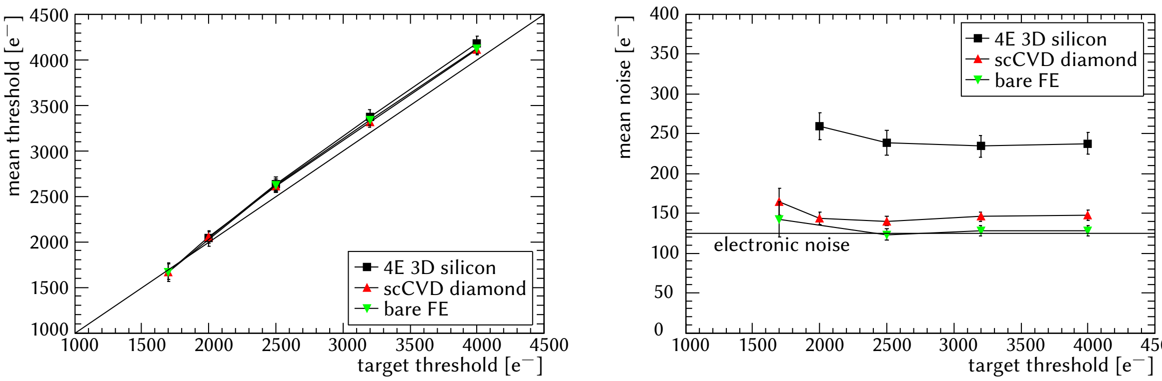

(a) mean threshold

(b) mean noise

Figure 4.2: Measured threshold and noise depending on the target threshold value for FE-I3 modules tuned with the TurboDAQ system. The measured threshold in Fig. 4.2(a) shows an offset of about 150 e^- for target threshold values higher than 2500 e^-. For target threshold values higher than 2500 e^- the mean noise in Fig. 4.2(b) stays constant while a noise increase can be observed for lower threshold values. Measurements on a bare FE-I3 chip show a noise contribution of about 125 e^-.

Tuning results of FE-I3 modules tuned with the TurboDAQ system shown in Fig. 4.2 illustrate the measured threshold and module noise depending on the target threshold. For the bare FE-I3 chip and the diamond sample tunings with a minimum target threshold of 1700 e^- where feasible while a target threshold of 2000 e^- was the minimum threshold obtained with the 3D sample. Increased noise values for low threshold settings in Fig. 4.2(b) related to non-linear properties of the front-end electronics make it impossible to reach lower threshold values. The measured threshold offset of about 150 e^- shown in Fig. 4.2(a) stays stable for target threshold values higher than 2500 e^-. In this region the fitting algorithm implemented in the tuning procedure overestimates the threshold settings. For lower target threshold values this overestimation is due to the non-linear behavior of the chip reduced even causing an underestimation for low values.
The corresponding measurements of the threshold and the module noise of FE-I3 modules

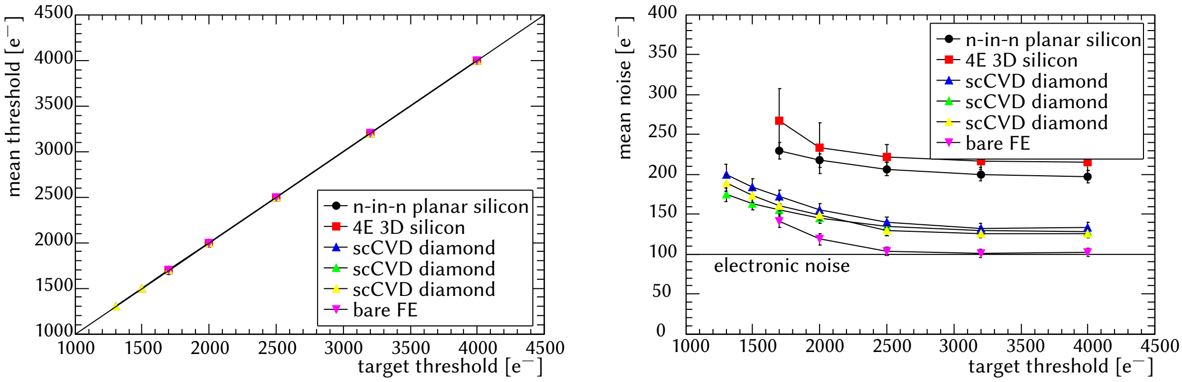

(a) mean threshold

(b) mean noise

Figure 4.3: Measured threshold and mean noise depending on the target threshold value for FE-I3 modules tuned with the USBPix system. The measured threshold in Fig. 4.3(a) shows a good correlation to the target threshold value. For threshold values higher than 2500 e^- the mean noise in Fig. 4.3(b) stays constant while a noise increase can be observed for lower threshold values. Measurements on a bare FE-I3 chip show a noise contribution of about 100 e^-.

tuned with the USBPix system are shown in Fig. 4.3. Due to the lower noise in the USBPix system about 300 e^- lower threshold values than with the TurboDAQ system can be reached. The noise measurements in Fig. 4.3(b) also show increased noise for threshold values below 2500 e^- while a constant noise is measured above. Contrary to the results obtained with the TurboDAQ system show the results in Fig. 4.3(a) a good correlation between the measured threshold and the target threshold.

For the noise analysis it is assumed that the total noise of a sensor module consists of the noise of the front-end chip and the sensor noise. The results obtained in Fig. 4.2(b) and Fig. 4.3(b) show that the module noise of FE-I3 modules is constant for threshold values exceeding 2500 e^-. For lower threshold values the non-linear behavior of the front-end chip increases the sensor noise and with it the total noise. Based on the measurements taken with the bare FE-I3 module and provided that the threshold is higher than 2500 e^- a front-end noise of 125 e^- and 100 e^- is assumed for the FE-I3 modules tuned with TurboDAQ and USBPix respectively.
Rough values of the sensor contribution to the module noise can be derived from the results shown in Fig. 4.2(b) and Fig. 4.3(b). The single crystal CVD diamond sensors show a sensor noise contribution of about 25 e^- while the planar and 3D silicon pixel sensor designs show a sensor noise contribution of about 100 e^- and 115 e^- respectively. Comparing the results for the different sensor technologies and looking at the noise contributions discussed in Sec. 2.3 shows that the front-end and sensor noise contribution can not be considered as independent entities. Thermal noise in Eq. 2.18 and low frequency 1/f-noise in Eq. 2.20 are both linked to

the transistors used in the amplifier or more specific to the voltage fluctuation on the amplifiers input. While the feedback capacitance in the amplifier is an intrinsic value of the circuit is the sensor capacitance related to the sensor technology and material [80]. A further variable to the thermal noise is the temperature set to 20 °C during the measurements. The shot noise in Eq. 2.19 as remaining noise contribution is related to the temperature dependent leakage current of the sensor thus also linked to the sensor technology and material.
While the temperature was set to the same value for all measurements show the leakage current and the sensor capacitance variations related to the sensor material and sensor technology. For the two silicon sensor technologies the noise offset of the 3D design can only be explained by the variation of the sensor capacitance as the leakage current of both designs is comparable at about 100 nA. The short column distance of the measured 4E design further increases the impact of the sensor capacitance compared to a 2E or 3E design [118]. Comparing the diamond and silicon designs shows that the sensor capacitance as well as the leakage current of diamond sensors are both at least one order of magnitude lower than in silicon. Based on the measurement and the discussed noise sources is the noise contribution in diamond sensors due to the lower sensor capacitance and the lower leakage current reduced compared to silicon sensors. Concerning the operation of the different sensor technologies this offers the possibility to operate diamond modules at lower threshold settings than silicon modules. Due to the similar noise behavior in both silicon technologies also similar operation setting need to be chosen.

Tuning of FE-I4 chips

As for untuned FE-I3 modules is the threshold dispersion of an untuned FE-I4 module in the range of about 400 e$^-$. The tuning with the USBPix system shown in Fig. 4.4(a) reduces this

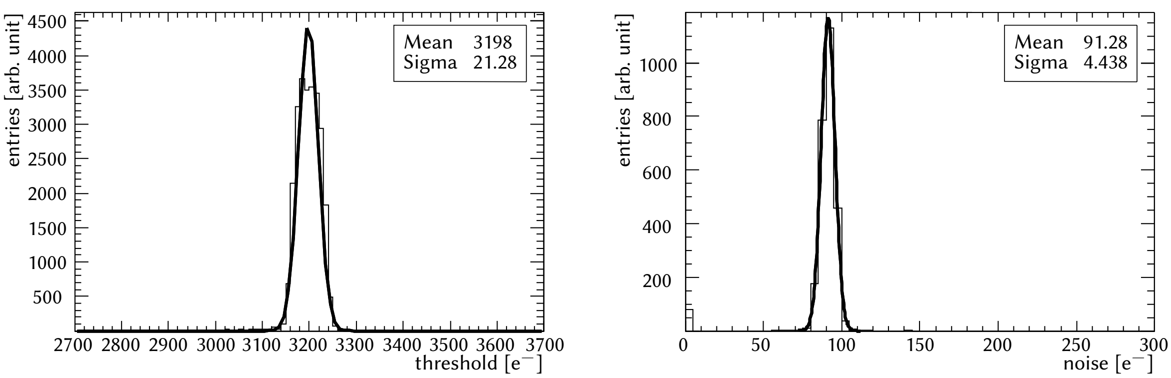

(a) Threshold distribution of a bare FE-I4 chip

(b) Noise distribution of a bare FE-I4 chip

Figure 4.4: Threshold and noise distributions for a bare FE-I4 read-out chip tuned with USBPix to a threshold of 3200 e$^-$. The threshold distribution in Fig. 4.4(a) shows a good correlation with the target threshold value. Fig. 4.4(b) shows the corresponding noise distribution for the bare FE-I4 module.

value to a dispersion below 30 e^-. The measured threshold obtained with the USBPix system tuning algorithm for FE-I4 modules varies only by a few electrons from the target value. The different design used in the FE-I4 chip compared to the FE-I3 chip leads to reduced noise behavior shown in Fig. 4.4(b). Similar to the measurements performed with the FE-I3 modules several samples were tuned to different threshold values to understand the threshold and noise behavior depending on the target threshold. As TurboDAQ is not capable to communicate with FE-I4 modules no comparisons between systems is possible.
A bare FE-I4 module as well as modules using diamond and silicon sensors shown in Fig. 4.5 have been tested in the target threshold range from 500 e^- up to 3200 e^-. Due to the different charge collection in diamond and silicon sensors a different feedback current gain was used to tune the modules. The silicon sensor modules and the bare FE-I4 module were set to a gain of 8 ToT for 10 ke^- while the diamond module was tuned to 8 ToT for 5 ke^-. It needs to be remarked that several iterations of the tuning procedure have been necessary to reach threshold values below 1000 e^-. The minimum threshold tuning of the silicon sample at 1000 e^- already showed an increase of untuned pixel correlated to the noise increase. The bare FE-I4 chip was only tested to a threshold value of 1000 e^- which can not be considered as the minimum threshold value for FE-I4 modules. Independent of the sensor technology show the measured threshold values in Fig. 4.5(a) a strong correlation with the target threshold value.

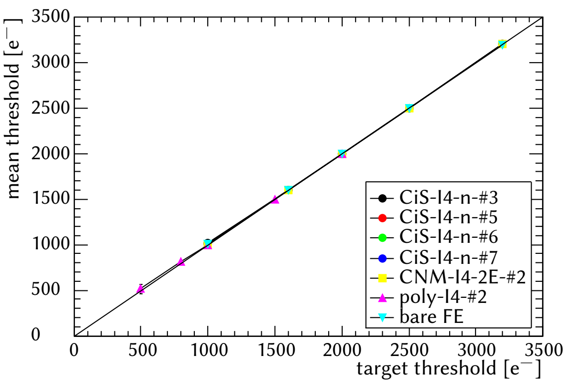

(a) Threshold

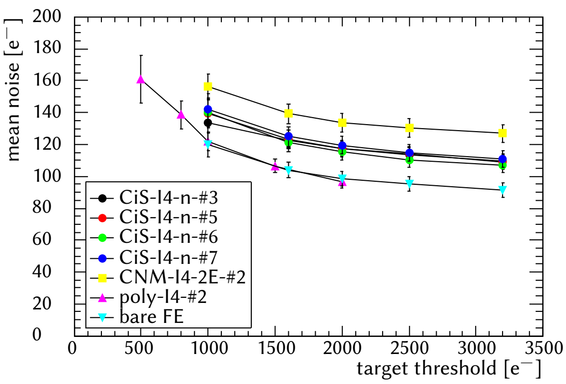

(b) Noise

Figure 4.5: Measured threshold and noise depending on the target threshold value for FE-I4 modules tuned with the USBPix system. The measured threshold in Fig. 4.3(a) shows a strong correlation with the target threshold value. A noise decrease is visible in Fig. 4.5(b) for increasing target threshold values. The feedback current gain of the bare module and the silicon modules was tuned to 8 ToT for 10 ke^- while the diamond sample was tuned to 8 ToT for 5 ke^-.

The noise distribution in Fig. 4.5(b) shows a noise decrease with increasing target threshold. Results obtained with the bare FE-I4 module indicate that the increased noise for lower threshold settings is related to the noise from the front-end chip. Additional noise measure-

ments focusing on the feedback current gain and the threshold settings of FE-I4 chips found that the front-end noise contribution is connected to both settings [77]. Similar to the FE-I3 sensors show the planar sample a smaller noise offset than the 3D sample. In numbers this offset corresponds to about 35 e^- and 70 e^- for the planar and the 3D samples respectively. Noticeable is the high uniformity between the four planar sensors especially knowing that the samples were produced in two different batches. The noise contribution of the poly crystal diamond shows due to the variation of the feedback current gain similar values as the bare front-end chip. For the same operation conditions an increased noise contribution in the diamond module would be expected.
As for the FE-I3 modules the noise contribution of the silicon sensors is expected to be caused by the sensors capacitance. Contrary to earlier measurements an about four time higher leakage current is present in the 3D module. This current offset causes an additional shot noise contribution to the noise in the 3D module. The more than 50 times lower leakage current in the diamond module explains that the shot noise contribution can be neglected. In addition is the diamond sensor capacitance due to a lower permittivity and a wider sensor width reduced compared to the silicon modules. As a result the thermal noise and the low frequency 1/f-noise are also reduced in diamond modules.

Tuning of FE-I4 chips after irradiation

To understand the impact of radiation damage on the front-end chip similar measurements as before irradiation have been performed with irradiated silicon planar and 3D sensor modules. The results shown in Fig. 4.6 were performed with the USBPix read-out system at a temperature of −20 °C and −30 °C for 3D and planar samples respectively. Due to the lower temperature settings necessary to control the increased leakage current after irradiation it is not possible to compare the results from before and after irradiation. As expected show the threshold measurements of the irradiated samples the same strong correlation with the target threshold as unirradiated samples.
Due to radiation damage the parameters influencing the noise properties of sensor modules sensor capacitance, leakage current and temperature are extended by the fluence increasing the leakage current and radiation dose. Bare FE-I4 chips irradiated with 800 MeV protons to radiation doses of about 6 Mrad, 75 Mrad and 200 Mrad showed a noise increase on the order of 15 % to 25 % [84].
In case of irradiated planar modules in Fig. 4.6(a) three combinations of fluence and radiation dose are displayed. Here, the modules irradiated with high energy protons to a fluence of $5 \cdot 10^{15}$ n_{eq} cm^{-2} corresponding to a dose of about 252 Mrad show the highest noise. Neutron irradiated samples reaching the same fluence but a low radiation dose of about 5 Mrad on the other hand show the lowest noise. Planar n-in-p samples irradiated with low energy protons to a fluence of $2 \cdot 10^{15}$ n_{eq} cm^{-2} collected a radiation dose of 290 Mrad show noise values within the same range. The leakage current increase after irradiation of more than two orders of magnitude despite the applied cooling corresponds to a shot noise increase in

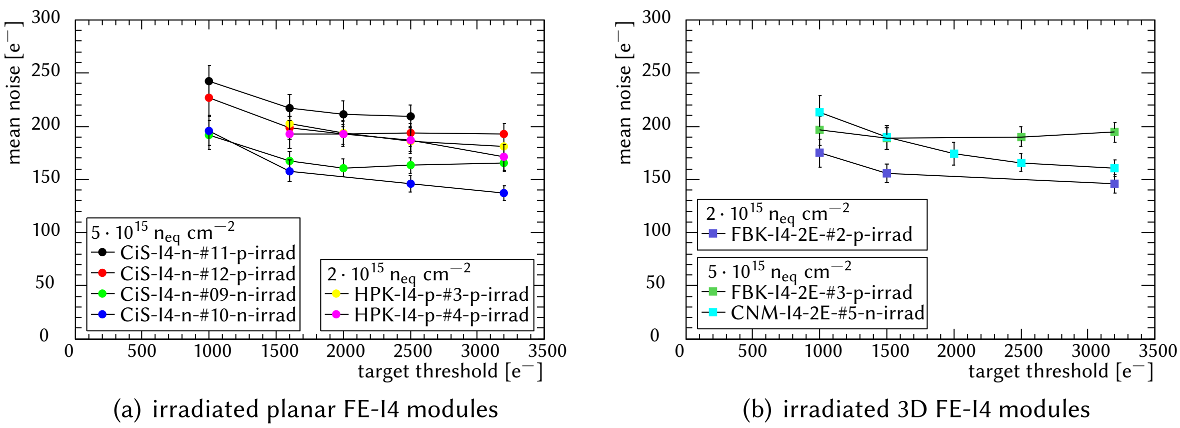

Figure 4.6: Noise behavior depending on the target threshold value for irradiated planar and 3D FE-I4 modules. Measurements on planar modules in Fig. 4.6(a) have been performed at a temperature of −30 °C while the corresponding 3D module measurements in Fig. 4.6(b) have been performed at −20 °C.

all modules. This effect alone does not explain the noise of the $2 \cdot 10^{15}$ n_{eq} cm^{-2} irradiated n-in-p modules with an about five times smaller leakage current than the irradiated n-in-n modules. A possible explanation for this behavior is the varying noise contribution caused by the collected radiation dose. Compared to the proton irradiated n-in-n samples collected the n-in-p samples an about 15 % higher radiation dose causing the increased noise in these samples. In addition are the n-in-p samples 50 µm thinner which increases the sensor capacitance.
Results of irradiated 3D samples in Fig. 4.6(b) on the other hand also show a shot noise increase correlated with the higher leakage current. A with low energy protons to a fluence of $2 \cdot 10^{15}$ n_{eq} cm^{-2} irradiated module shows an about three times lower leakage current and also the lowest noise. The two samples irradiated with protons and neutrons to a fluence of $5 \cdot 10^{15}$ n_{eq} cm^{-2} show despite the varying radiation dose of about 725 Mrad similar noise behavior. This noise behavior can be also related to the sensor layout as the samples are based on different 3D designs.

Tuning impact on operation and performance

The obtained results for FE-I3 and FE-I4 modules show that the tuning algorithm in the ATLAS Experiment leads to a strong correlation between target and measured threshold. Even though that a noise increase is visible for low target threshold settings with both chips show the FE-I4 chips a higher robustness. This robustness of FE-I4 modules is still present after irradiation. For the operation in the experiment even irradiated pixel modules can be operated at lower threshold settings preserving the detector sensitivity after radiation damage reduced the charge collection in the sensors. Concerning the noise contribution a shift from the sensor capacitance before irradiation to the leakage current after irradiation as dominating factor becomes visible. Before irradiation silicon modules can be operated at room temperature showing noise values below 250 e^- and 160 e^- using typical operation settings for FE-I3 and FE-I4 chips respectively. Diamond modules on the other hand show reduced noise contribution compared to silicon. After irradiation the noise contribution in FE-I4 modules increases up to about 210 e^-. This behavior depends on the cooling to control the leakage current as well as the fluence and radiation dose. For a stable operation before and after irradiation the modules need to be temperature controlled to avoid increased leakage current associated with shot noise. In addition show the obtained results that the communication as well as tuning properties of the FE-I4 chip are not affected after exceeding the design radiation dose up to three times. This feature promotes the application of the chip also for future experiments exceeding the expected radiation dose of the IBL.

4.1.2 Temperature dependence of the ENC in the FE-I4

The ENC model discussed in Sec. 3.2.2 shows the noise dependency on the leakage current i_{leak}, the preamplifier input capacitance C_D, the shaping time constant τ_b and the temperature T. Measurements and simulations based on the model have been used to understand the influence of the leakage current, the preamplifier input capacitance and the shaping time constant on the noise [56, 57]. The temperature which especially after irradiation strongly influences the sensor leakage current was however not part of the analysis. In order to investigate the temperature properties of the front-end chip an unirradiated poly-crystal diamond module was used to avoid noise contributions related to leakage current and sensor capacitance.

For diamond modules the discussed ENC model in Eq. 3.3 can be reduced to the influence of the thermal noise of the feedback transistor, the thermal noise and the 1/f-noise of the preamplifier. This reduction is possible by assuming that the noise sources related to the leakage current can be neglected due to the low leakage current in diamonds. Simulations focusing on the leakage current showed that the contribution of the thermal noise of the feedback transistor and the 1/f-noise of the preamplifier can be also neglected for low leakage current values [56, 57]. For these simplifications of the ENC in Eq. 3.3 represents the thermal noise of the preamplifier $ENC_{thermal}$ given in Eq. 4.1 the main noise contribution of the module. Following these assumptions makes it possible to analyze the influence of the temperature on the thermal noise in the FE-I4 read-out chip independent of the other noise contributions.

$$ENC_{thermal} = \sqrt{\frac{(C_D^{sensor} + C_D^{transistor})^2}{q^2} \frac{kT}{2g_m} \cdot \left[\frac{1}{\tau_c} + \frac{\tau_a^2}{2\tau_c^3}\right]} \tag{4.1}$$

Noise measurements in Fig. 4.7 show the module noise in function of the threshold and the temperature for an about 750 µm thick diamond module at a bias voltage of 300 V. As earlier discussed shows the diamond module in Fig. 4.7(a) the threshold noise correlation known from other FE-I4 modules (see Fig. 4.5(b)). The noise temperature behavior in Fig. 4.7(b) shows a linear behavior in function of the temperature tested in the range from −20 °C to 20 °C. For the target threshold of 500 e^- the sensor noise approaches the tuning limitations causing a wide noise deviation amongst the pixel. The reason for this noise increase is the threshold dependent transconductance of the preamplifier g_m in Eq. 4.1 also affecting the time constants τ_a and τ_c [56].

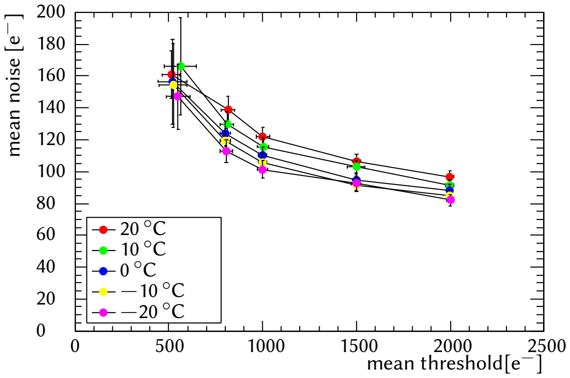

(a) Noise in function of the threshold

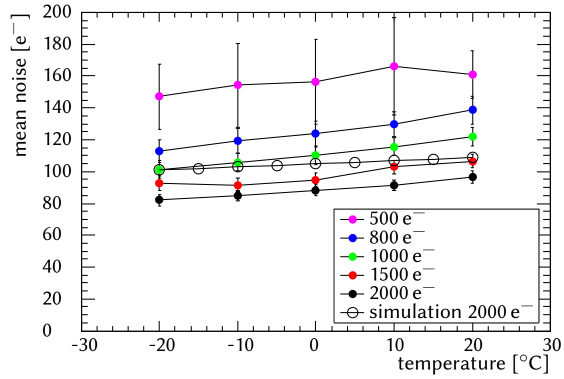

(b) Noise in function of the temperature

Figure 4.7: Noise measurements of an unirradiated 750 nm thick poly-crystal CVD diamond FE-I4 module at a bias voltage of 300 V in function of the target threshold and the temperature at a current gain of 8 ToT and an injected charge of 5 ke^-. Measurements in Fig. 4.7(a) show the typical noise distribution in function of the target threshold. The noise distribution in Fig. 4.7(b) shows the temperature dependence for different target threshold values. In addition the ENC based on the model in Eq. 4.1 for a threshold of 2000 e^- is also included in the plot.

To calculate the thermal noise contribution in dependence of the temperature the input capacitance C_D in Eq. 3.3 was substituted by the contribution of the diamond sensors capacitance $C_D^{diamond}$ and the transistor capacitance $C_D^{transistor}$ to obtain Eq. 4.1. As the diamond sensors capacitance of the tested diamond sensor are not available it was decided to use the sensors capacitance of a 450 µm diamond module. Results for a dedicated PixCap chip to measure the sensor capacitance determined a diamond sensor capacitance for a 450 µm sensor of 35 fF [56]. Due to the thickness variation a lower sensor capacitance is expected in the measured module corresponding to a lower ENC for the module. The diamond capacitance in parallel to the transistor capacitance $C_D^{transistor} = 32.1$ fF results in a total input capacitance of $C_D = 67.1$ fF which is used for the analysis. The remaining time constants $\tau_a = 0.075$ ns, $\tau_b = 21.25$ ns and $\tau_c = 0.15$ ns as well as the transconductance of the preamplifier $g_m = 225$ µS have been extracted from the simulation based on a threshold tuning to 2000 e^- [56].

The results obtained based on the simplified ENC model in Eq. 4.1 for a threshold setting of 2000 e^- in Fig. 4.7(b) show an overestimation of the calculated noise. This overestimation can be explained by the higher sensor capacitance used for the calculations. Independent of the offset show the calculated noise and the measurement noise at a target threshold of 2000 e^- a similar noise gradient. Further can neglected noise effects and temperature variations due to self heating of the module also influence the measured noise causing a variation between the measured and calculated value.

The obtained results confirm that it is advantageous to operate FE-I4 modules at lower temperatures to reduce the thermal noise contribution of the module. For the operation of irradiated silicon modules this property comes as an intrinsic feature of FE-I4 modules as it is also necessary to cool the irradiated sensor. In the case of irradiated diamond modules which do not require cooling after irradiation front-end cooling might become a possibility to reach a better signal to noise ratio at the end of lifetime.

4.2 Sensor analysis

The sensor analysis focuses on the sensor responds to ionizing radiation but also includes the analysis of sensor properties related to the operation in the experiment. These sensor properties become due to the interaction of the sensor and the front-end chip relevant for the module operation. The leakage current in function of the bias voltage as a sensor property also passes through the front-end chip thus effects noise and noise occupancy behavior of the module. Concerning the sensor responds to ionizing radiation measurements with radioactive photon and electron sources as well as test beam measurements with charged particles are performed. Scans with photon sources are commonly used to test the front-end calibration and the interconnections between the front-end and the sensor. Measurements with electron sources are a possibility to create 'beam-like' conditions useful to determine the charge collection in the sensor. The application of a beam telescope during test-beam measurements makes it possible to track the path of a particle through the device under test. This test allows further analysis on the charge collection and efficiency within the pixel region as well as an evaluation of the edge efficiency and the spacial resolution of the sensor. Finally the obtained results are used to analyze the charge collection properties and sensor efficiency for different conditions.

4.2.1 Leakage current analysis

Leakage current measurements are a common method used for the sensor characterization of silicon devices. During the testing of individual modules results can be used to determine the full depletion voltage and the breakdown voltage. Acceptance tests of sensors also include leakage current measurements to determine the production yield based on electrical

specifications.
Defects introduced due to radiation damage change the leakage current characteristics in sensor materials described in Sec. 2.2.3. Therefore leakage current measurements on irradiated samples are also used to determine the operation values but also to estimate the damage factor in the material.

Planar Pixel Sensors on FE-I3

Leakage current measurements before and after irradiation of planar FE-I3 pixel sensors based on the n-in-n and n-in-p design are summarized in Fig. 4.8.

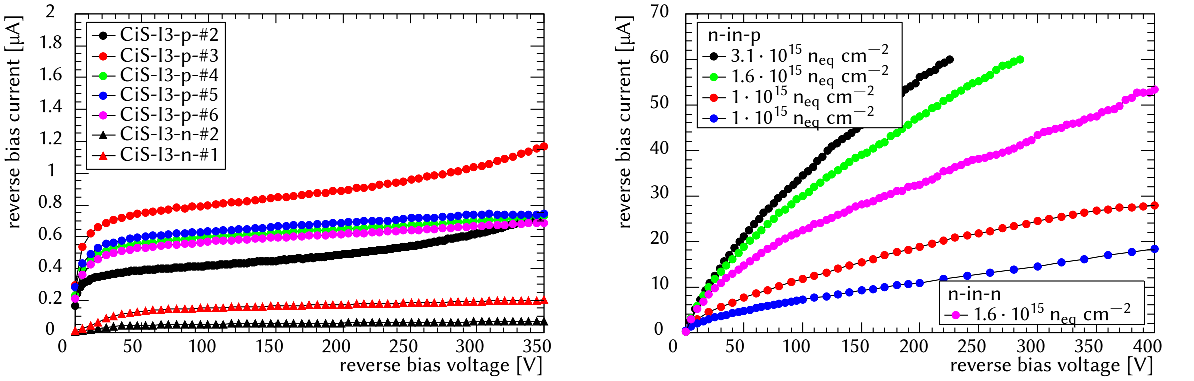

(a) before irradiation (b) after irradiation

Figure 4.8: Leakage current measurements on planar FE-I3 n-in-n and n-in-p modules before and after irradiation. Measurements before irradiation in Fig 4.8(a) show the current increase for voltages below full depletion and the plateau region. The current increase after irradiation in Fig. 4.8(b) scales with the collected fluence. All measurements were performed at 20 °C and −20 °C before and after irradiation respectively.

While the full depletion voltage of the n-in-p design was determined to be in the range of about 60 V the operation voltage was set to be 150 V [94]. Measurements on unirradiated modules in Fig. 4.8(a) show leakage currents below 0.8 µA at the operation voltage. These results are slightly higher than results obtained during the electrical characterization before bump-bonding [94, 96]. This increase is explained by mechanical stress on the sensor during the bump-bonding process but also temperature variations can cause this behavior. The breakdown voltage for n-in-p samples implementing the 15 and 19 guard-ring design exceeds for most sensors 400 V [95]. Measurements with up to $3.1 \cdot 10^{15}\,n_{eq}\,cm^{-2}$ proton irradiated modules in Fig. 4.8(b) show the expected leakage current increase after irradiation. Thermal runaway of the leakage current due to insufficient cooling in the climate chamber made it impossible to reach the full depletion voltage after irradiation. Despite of the insufficient cooling the expected leakage current increase depending on the collected fluence is clearly visible. Additional measurements at lower temperatures and scaled with Eq. 2.6 to −20 °C confirm the obtained results [95, 97]. In addition a breakdown voltage shift exceeding 1000 V

was observed for fluences higher than $5 \cdot 10^{15}\,n_{eq}\,cm^{-2}$ [97].
For quality testing and assurance of the ATLAS Pixel Detector the operation voltage V_{op} of planar n-in-n sensor modules was set to 150 V to exceed the depletion voltage. During the testing of the ATLAS pixel modules the condition $I(V_{op})/I(V_{op} - 50\,V) < 2.0$ was introduced to identify slow breakdown effects around the operation voltage [4]. Both unirradiated n-in-n modules in Fig. 4.8(a) behave accordingly to this condition. In addition do they show an enlarged plateau region with a leakage current below 0.2 µA up to 350 V. The with high energetic proton irradiated n-in-n sample in Fig. 4.8(b) shows the expected leakage current related to radiation damage. Due to the insufficient cooling it was not possible to reach stable conditions for voltages exceeding 400 V. Charge collection measurements on irradiated samples using the same design showed that voltages exceeding 600 V are necessary for the operation after irradiation [119].
Handling during and after irradiation made it impossible to obtain the same annealing time for the individual planar n-in-n and n-in-p samples. Nevertheless correspond the calculated damage factors to the expected range of $2 \cdot 10^{-17}\,A\,cm^{-1}$ to $5 \cdot 10^{-17}\,A\,cm^{-1}$.

3D Pixel Sensors on FE-I3

Leakage current measurements of FE-I3 3D-DDTC samples implementing 2E, 3E and 4E columns show that the breakdown voltage for most samples is around 70 V with a full depletion voltage of about 12 V [118]. These results are confirmed by the measurements shown in Fig. 4.9(a) for unirradiated 2E and 4E sensor modules from the same batch. It is noticeable

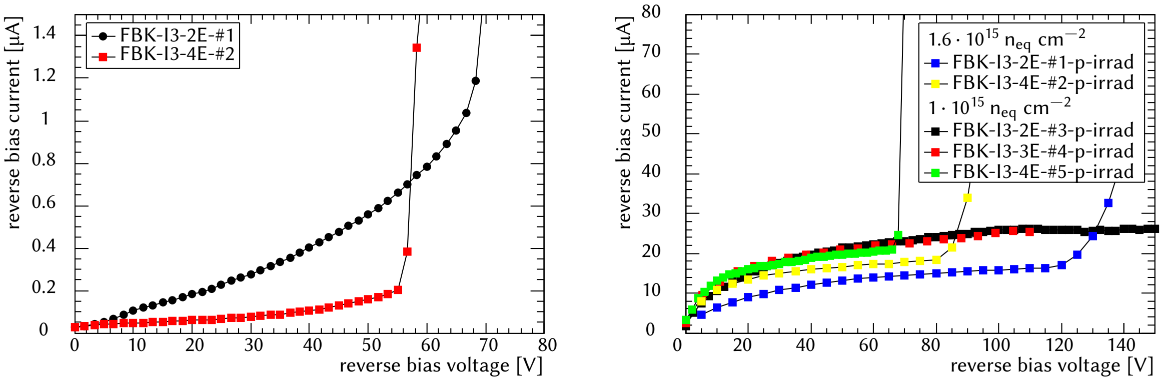

(a) before irradiation (b) after irradiation

Figure 4.9: Leakage current measurements on 3D FE-I3 modules before and after irradiation. Measurements before irradiation in Fig. 4.9(b) show low leakage current below 1 µA up to the breakdown voltage for a 2E and a 4E module. Two sets of samples irradiated at KIT and CERN PS at a temperature of −20 °C are shown in Fig. 4.9(b).

that the leakage current of the 4E sample forms a wide plateau region while a steady current increase takes place in the 2E sample. Due to this effect a duplication of the leakage current in the 2E sample compared to the 4E sample can be observed at an operation voltage of 30 V.

To further investigate on this effect measurements were performed in the temperature range between −20 °C and 20 °C. The results of both samples in Fig. 4.10(a) and Fig. 4.11(a) show the expected leakage current decrease for lower temperatures. After scaling the measurements with Eq. 2.6 to 20 °C a noticeable current variation becomes present for the 2E module in Fig. 4.10(b) while the 4E module in Fig. 4.11(b) shows an uniform current. As only the bulk current contribution is scaled by Eq. 2.6 the results suggest that a non-negligible surface current is part of the measured leakage current. Nevertheless were both modules operational and later irradiated with high energetic protons. Leakage current results for sensor modules

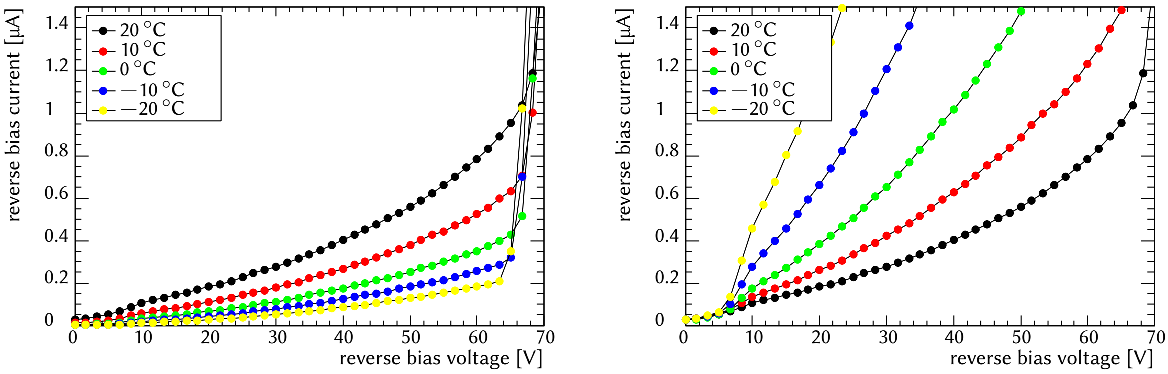

(a) measured leakage current

(b) scaled leakage current

Figure 4.10: Leakage current measurements of FBK-I3-2E-#1 in the temperature range between −20 °C and 20 °C. The leakage current decrease for low temperatures is shown in Fig. 4.10(a). After scaling the leakage current to 20 °C a surface current contribution becomes visible in Fig. 4.10(b).

irradiated in two irradiation campaigns measured at a temperature of −20 °C are summarized in Fig. 4.9(b). The two sets of proton irradiated samples show the expected leakage current increase and breakdown voltage shift to higher values [106]. In case of the 2E and 3E devices this breakdown shift let to voltages exceeding 100 V. For the two 4E-sensors the shift is less strong. The three $1 \cdot 10^{15}\,n_{eq}\,cm^{-2}$ irradiated samples show an uniform leakage current behavior. This effect is less noticeable for the two $1.6 \cdot 10^{15}\,n_{eq}\,cm^{-2}$ irradiated sample. This behavior can be explained by annealing effects caused by be missing cooling during the irradiation at the CERN PS. To confirm the behavior of the samples additional measurements in the temperature range between −20 °C and −5 °C have been performed. The measurements of the $1 \cdot 10^{15}\,n_{eq}\,cm^{-2}$ irradiated samples show that the uniform behavior is independent of the temperature and that no surface current contribution is visible after irradiation (Fig. A.3). In case of the two $1.6 \cdot 10^{15}\,n_{eq}\,cm^{-2}$ irradiated samples confirms the scaling to −20 °C that the radiation damage increases the bulk current but not the surface current contribution (Fig. A.2). This is especially relevant for module FBK-I3-2E-#1 which showed before irradiation in Fig. 4.10(b) an increased surface current. A further result of the more than tenfold increase of the leakage current after irradiation is that the surface current

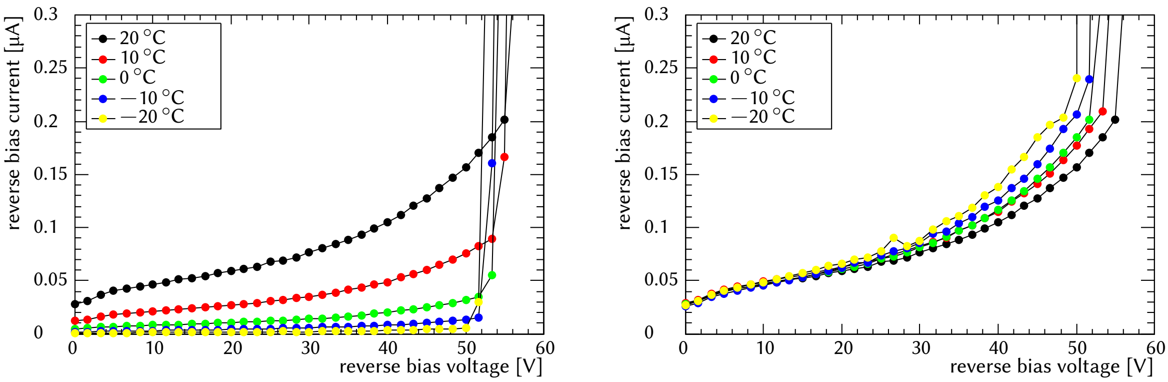

(a) measured leakage current

(b) scaled leakage current

Figure 4.11: Leakage current measurements of FBK-I3-4E-#2 in the temperature range of −20 °C and 20 °C. The leakage current decrease for low temperatures is shown in Fig. 4.11(a). After scaling the leakage current to 20 °C an uniform current becomes visible in Fig. 4.11(b) indicating only a bulk current contribution.

contribution observed before irradiation vanishes.

Leakage current measurements on FE-I4 modules

Measurements on FE-I4 modules have been carried out with powered and non-powered front-end chips. The purpose of this measurement procedure was to understand the temperature increase in the sensor due to the power dissipation in the FE-I4 chip. The measurements have been performed in a climate chamber with a constant air temperature. Assuming that the sensor temperature in case of a non-powered front-end chip is equal to the air temperature makes it possible to determine the temperature increase for powered front-end chips. For this the measured leakage current on powered modules was scaled with Eq. 2.6 in steps of 1 °C to compare the scaled values with the measurements of the non-powered module (Anx. A). To compensate for the increased power dissipation of irradiated sensors the determination of the temperature offset was based on low bias voltages.

Planar Pixel Sensors on FE-I4

In case of the unirradiated planar modules in Fig. 4.12(a) and Fig. 4.12(c) temperature offsets between 5 °C and 9 °C have been measured at an air temperature of 20 °C. Apart from different chip configurations which can influence the power dissipation in the chip also different PCB layouts have been used which explains the wide temperature range.
The leakage current measurements agree with the results obtained during the quality control of the planar n-in-n sensors [93]. The three 200 µm thick as well as the 250 µm thick sensors in Fig. 4.12(a) show a stable plateau region with a leakage current below 1 µA. The breakdown voltage around 300 V or higher is more than double the operation voltage of the samples. Measurements on an unirradiated powered n-in-p sample in Fig. 4.12(c) shows a

leakage current below 0.4 µA at a bias voltage of 1000 V. The leakage current of 0.2 µA measured in the non-powered case confirms the results obtained during the wafer probing [91].

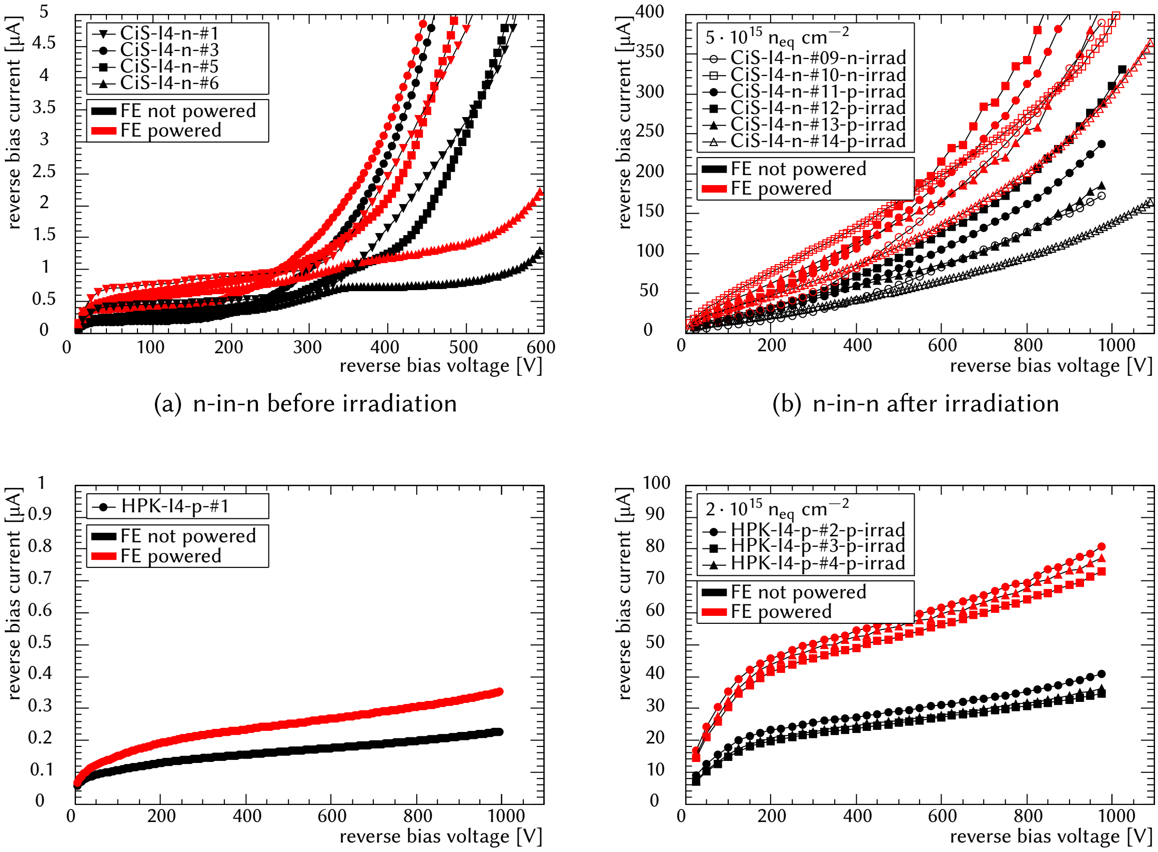

(a) n-in-n before irradiation (b) n-in-n after irradiation

(c) n-in-p before irradiation (d) n-in-p after irradiation

Figure 4.12: Leakage current measurements on planar n-in-n and n-in-p sensors on FE-I4 chips before and after irradiation with powered and non-powered front-end chip. Measurements before irradiation in Fig. 4.12(a) and Fig. 4.12(c) performed at 20 °C show leakage currents below 1 µA. In case of the unirradiated n-in-p module a bias voltage of 1000 V was reached. After irradiation the samples were cooled to −30 °C to avoid effects of thermal runaway. Irradiated n-in-n modules in Fig. 4.12(b) were biased up to 1000 V. For n-in-p modules in Fig. 4.12(d) a powered biasing of up to 1000 V is possible with leakage currents below 100 µA.

After irradiation both sensor designs show a temperature offset between 5 °C and 7 °C to the air temperature of −30 °C.
All $5 \cdot 10^{15}\ n_{eq}\ cm^{-2}$ irradiated n-in-n modules in Fig. 4.12(b) have been biased up to the operation voltage of 1000 V. The power dissipation in the front-end chip and in the sensor itself increases the temperature of the sensor. This heating brings the sensor close to the point of thermal runaway when the cooling is not sufficient enough and an uncontrolled leakage current increase takes over. The breakdown voltage of all $5 \cdot 10^{15}\ n_{eq}\ cm^{-2}$ irradiated samples

moved beyond 1000 V allowing the operation at the foreseen operation voltage of the IBL. The three $2 \cdot 10^{15}\,\mathrm{n_{eq}\,cm^{-2}}$ irradiated n-in-p modules in Fig. 4.12(d) show a leakage current of about 40 µA and 90 µA at a bias voltage of 1000 V for non-powered and powered front-end chips respectively. The expected breakdown voltage shift to higher values could not be observed as the breakdown voltage already exceeded 1000 V before irradiation. The measurements confirm that the biasing of the sensor is after an irradiation of $2 \cdot 10^{15}\,\mathrm{n_{eq}\,cm^{-2}}$ still possible [91, 92]. The low leakage current variation of around 10 µA in the samples shows that the varying bias and isolation structures implemented in the three n-in-p sensor designs do not effect the leakage current properties after irradiation.

3D Pixel Sensors on FE-I4

During the leakage current measurements of unirradiated FE-I4 3D modules from FBK and CNM a temperature offset of about 4 °C to the air temperature of 20 °C has been determined for a powered front-end chip.

An unirradiated FBK module from the IBL pre-production in Fig. 4.13(a) shows a leakage current below 1 µA up to the breakdown voltage of 40 V. Similar results have been obtained during the wafer probing of sensor tiles from the same production batch [77].

Due to the guard fence leakage current measurement technique applied at CNM it is not possible to compare the results from the wafer probing before flip-chipping with the results of bump-bonded modules. Measurements on two unirradiated modules in Fig. 4.13(c) show a leakage current below 2 µA at the operation voltage of 10 V. In addition provides the breakdown voltage at about 70 V a wide safety range for the operation. The measured currents are below results obtained for sensors from the same batch which is explained by temperature variations during the measurements [77].

Similar to the unirradiated case show the irradiated 3D modules with powered front-end chip a temperature offset of 4 °C to 5 °C at an air temperature of −20 °C.

The irradiated 3D module FBK-I4-2E-#4-p-irrad in Fig. 4.13(b) was part of a FBK production prior to the IBL pre-production. Earlier measurements on devices from this production revealed a high leakage current behavior combined with a low breakdown voltage. Mechanical stress during the production is considered as reason for the high leakage current while the low breakdown voltage is attributed to the high p-spray concentration [100]. The observed device properties did not change after irradiation. Especially the breakdown voltage stayed at a low value of about 20 V to 30 V which made it impossible to operate the device at full depletion.

The two FBK 3D modules FBK-I4-2E-#2-p-irrad and FBK-I4-2E-#3-p-irrad from the IBL pre-production also shown in Fig. 4.13(b) performed according to the expectations. For both proton irradiated samples a leakage current increase and breakdown voltage shift is visible which is in agreement with the obtained fluence. With a breakdown voltage between 70 V and 80 V leans the $2 \cdot 10^{15}\,\mathrm{n_{eq}\,cm^{-2}}$ irradiated samples towards a operation voltage around 60 V. Due to the voltage drop on the resistance in series to the sensor this operation voltage

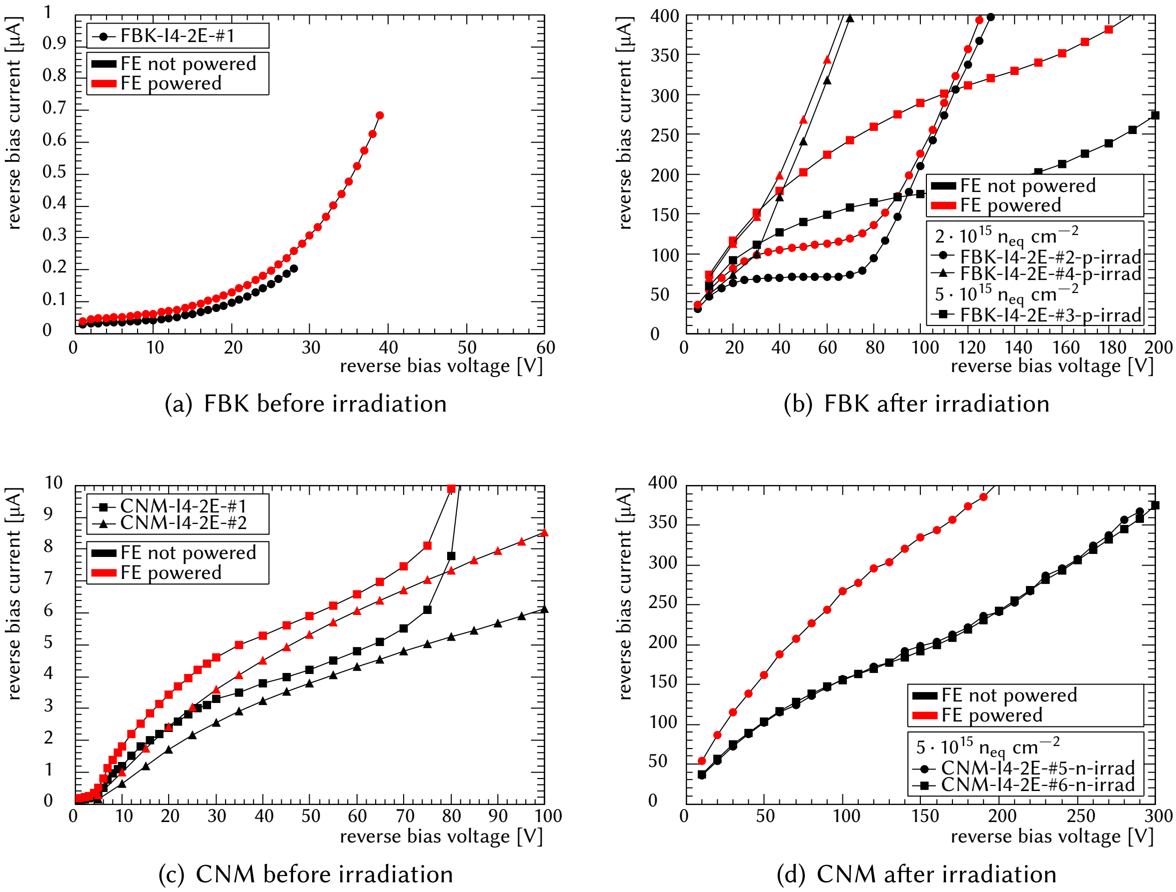

(a) FBK before irradiation

(b) FBK after irradiation

(c) CNM before irradiation

(d) CNM after irradiation

Figure 4.13: Leakage current measurements on 3D sensors on FE-I4 chips before and after irradiation with powered and unpowered front-end chip. Measurements before irradiation in Fig. 4.13(a) and Fig. 4.13(c) performed at 20 °C show at 10 V a leakage current below 0.1 μA and 2 μA respectively. Irradiated FBK and CNM modules in Fig. 4.13(b) and Fig. 4.13(d) show the expected current increase and breakdown shift.

corresponds to about 50 V on the sensor. The breakdown voltage shift of the $5 \cdot 10^{15}$ n$_{eq}$ cm^{-2} irradiated samples lead to a value exceeding 160 V. To assure a stable operation and to reach a sensor voltage of 120 V an operation voltage of 150 V has been considered [77].

Neutron irradiated CNM modules in Fig. 4.13(d) show the expected leakage current increase and breakdown shift at a fluence of $5 \cdot 10^{15}$ n$_{eq}$ cm^{-2}. To compensate the voltage drop on the serial resistance an operation voltage between 190 V and 200 V has been chosen [120]. Due to the serial resistance and corresponding to the measured leakage current the actual sensor bias is about 160 V.

Diamond Pixel Sensors on FE-I4

During long biasing periods of diamond sensors other experiments observed erratic currents.

Measurements of these currents which increase erratically for a certain period by an order of magnitude have shown to be correlated with the direction of electric fields [121]. This behavior is going to be investigated with DBM samples as the results could affect the orientation of the DBM.
To investigate the current stability of a diamond module a long term stability test was included in the leakage current measurements shown in Fig. 4.14. To avoid temperature effects the measurements were performed at 20 °C. The leakage current in Fig. 4.14(a) shows a stable plateau region at about 10 nA. During the long term stability test in Fig. 4.14(b) the samples was biased at 500 V for about 120 min. During the bias increase current peaks in the range of 1 nA can be observed which could be reduced by using smaller voltage steps. After reaching the bias voltage of 500 V a stable current between 10 nA and 9 nA is observed during the tested time of about 120 min.

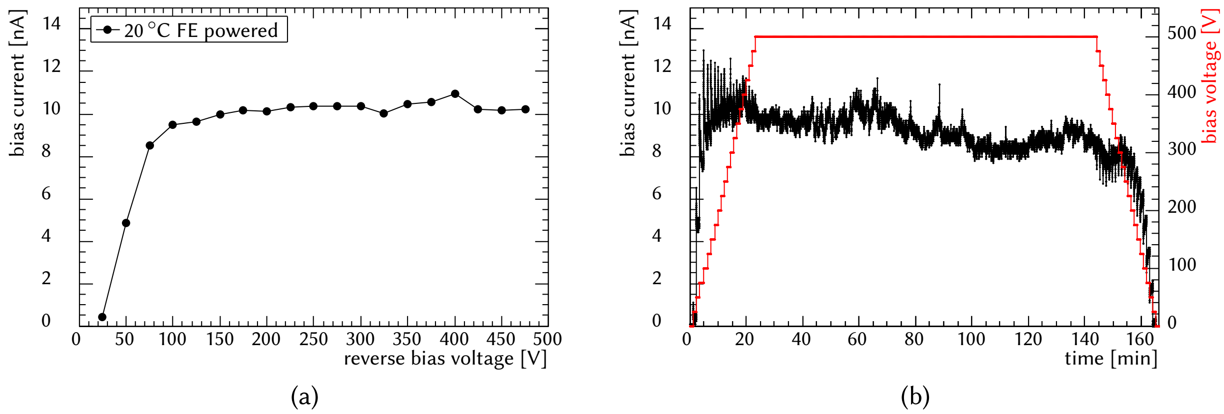

Figure 4.14: Leakage current measurements up to 500 V on an unirradiated diamond FE-I4 module. At bias voltages higher than 100 V a plateau region with a leakage current of about 10 nA can be observed in Fig. 4.14(a). A long term measurement for about 120 min in Fig. 4.14(b) shows a stable leakage current over the measurement period.

Leakage current impact on operation and performance

The performed leakage current measurements on modules implementing the three considered sensor technologies confirmed the sensor type specific expectations. For planar modules additional effort concerning the cooling becomes necessary to assure the operation after irradiation. Especially the power dissipation of the front-end chip needs to be taken into account as the additional heat increases the sensor temperature by several degrees. Due to the lower operation voltages applied at irradiated 3D sensors a more tolerant cooling system can be implemented. On the other hand are 3D sensors due to the lower operation voltage more sensitive to the voltage drop at the serial resistance. For the operation in the experiment a compared to the single chip boards reduced serial resistance could be used to avoid high voltage drops. The tested diamond module shows a good reliability during the stability test.

Despite of the more than one order of magnitude lower leakage current in diamond sensors it might become necessary to introduce a cooling system to compensate the temperature increase introduced by the front-end chip.

4.2.2 Noise analysis

Noise contributions related to the front-end chip discussed in Sec. 4.1.1 were performed at the operation voltage of the connected sensor. To further understand the noise contribution related to the sensor, measurements are also performed at different bias voltages. Sensor parameters as leakage current, depletion width and sensor capacitance change with the applied bias voltage thus change the noise behavior. Intrinsic sensor properties as the sensor technology, the material and the electrode design are further parameters which affect the noise contribution of the sensor. An example is the formation of the bias voltage dependent depletion zone in silicon sensors changing the sensor capacitance. Due to the missing depletion zone in diamond sensors is this effect only relevant for silicon sensors.
After irradiation the effective doping concentration increases due to the introduced radiation damage in the material. As a result the full depletion voltage shifts to higher values and the sensor capacitance gradient is reduced. As a result is the variation of the sensor capacitance after irradiation reduced which corresponds to an approximately constant sensor capacitance [122]. With an approximately constant sensor capacitance in function of the bias voltage also the noise contribution related to the sensor capacitance stays constant. On the other hand increases the leakage current of the sensor with the fluence also increasing the to the leakage current linked shot noise contribution.
As the measurements are performed on a sensor module includes the measured noise also the front-end noise contribution discussed in Sec. 4.1.1. In the case of irradiated FE-I4 modules an additional noise of 15 % to 25 % from the chip is expected for radiation doses up to 200 Mrad [84].
For the operation in the experiment the noise before and after irradiation becomes also relevant as the introduced radiation damage changes sensor properties. Here, the shift from the sensor capacitance dominated noise before irradiation towards the leakage current dominated noise after irradiation becomes most relevant.

Planar Pixel Sensors on FE-I3

Results of planar n-in-n and n-in-p sensors on FE-I3 read-out chips before irradiation in Fig. 4.15(a) confirm the expected dependence between sensor capacitance and noise. Both technologies show the expected noise saturation for voltages exceeding the full depletion voltage. Below that voltage more than 50 e^- higher noise values can be observed. The results also show the design features related to the different formation of the depletion zone in n-in-n and n-in-p sensors. While the depletion zone in n-in-p sensors starts to form around the pixel implants only small voltages are necessary to build a depletion region to isolate the pixels from each other. For n-in-n sensors the depletion zone develops from the back side of the sensor shorting all pixel with each other until the depletion zone reaches the pixel implants at a voltage of about 50 V.

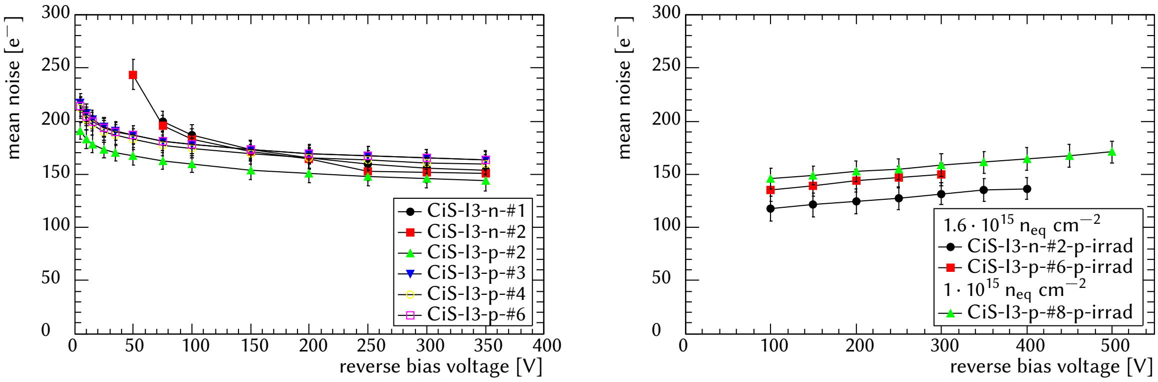

(a) before irradiation (b) after irradiation

Figure 4.15: Noise behavior in function of the applied bias voltage for planar n-in-n and n-in-p sensor modules on FE-I3 chips. Results before irradiation in Fig. 4.15(a) show the saturation region for voltages exceeding the full depletion voltage. For low voltages the different depletion region formation between the two technologies can be distinguished. Results after irradiation in Fig. 4.15(b) show a shot noise rise caused by the high leakage current.

After irradiation this property of the n-in-n design disappears as the n-bulk starts to behave as p-bulk material caused by the type inversion of the material. Apart from the effects of the type inversion show the results in Fig. 4.15(b) a noise increase for higher bias voltages. This shot noise contribution is related to the leakage current increase after irradiation. It is noticeable that the $1 \cdot 10^{15}$ n$_{eq}$ cm^{-2} irradiated module shows a higher noise than both $1.6 \cdot 10^{15}$ n$_{eq}$ cm^{-2} irradiated modules. To explain this behavior it needs to be pointed out that the modules were irradiated at different facilities. As a result the $1 \cdot 10^{15}$ n$_{eq}$ cm^{-2} irradiated module collected a radiation dose of about 145 Mrad while both $1.6 \cdot 10^{15}$ n$_{eq}$ cm^{-2} irradiated sample collected about 81 Mrad. Due to this variation is the noise contribution of the $1 \cdot 10^{15}$ n$_{eq}$ cm^{-2} irradiated chip expected to be higher, explaining the increased total noise. Furthermore exceeds the dose of about 145 Mrad the design specifications of the FE-I3 read-out chip. The variation of the collected radiation dose and the fluence make it difficult to compare the obtained results. Due to the insufficient cooling capabilities the test on the irradiated sensors could not be performed up to the expected operation voltage.
Measurements at lower temperatures on neutron irradiated n-in-p sensors from the same production show the same noise increase for higher voltages [98]. Furthermore is a noise increase dependent on the collected fluence visible. Due to the low radiation dose caused by the neutron irradiation is it possible to neglect the front-end noise contribution [98].

3D Pixel Sensors on FE-I3

The mean noise of two unirradiated FE-I3 3D sensors implementing the 2E and 4E column design in Fig. 4.16(a) differs by about 40 e^-. This effect can be attributed to the variation of the column pitch in the two designs which results in a different electrode distance thus a different capacitance. The application of n-doped read-out electrodes in a p-bulk material makes it possible to operate the sensors in an under-depleted state. While lateral depletion of the sensor is reached at 3 V to 4 V a full depletion voltage between 10 V to 15 V is necessary to deplete the part of the sensor without column overlap [118]. This behavior is related to the particular column design in Fig. 3.16 featuring an overlap of about 90 µm. The remaining 110 µm of the sensor thickness feature an enlarged electrode distance thus a higher depletion voltage. In addition leads the circular expansion of the electric field in the rectangular pixel to an inhomogeneous behavior further effecting the sensor capacitance.

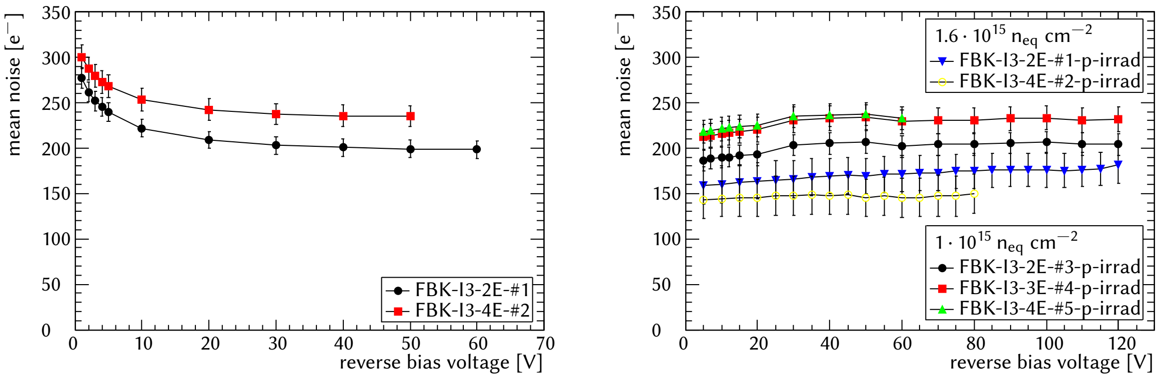

(a) before irradiation

(b) after irradiation

Figure 4.16: Noise behavior in function of the applied bias voltage for 3D-DDTC sensor modules on FE-I3 chips. Results before irradiation in Fig. 4.16(a) show the expected noise decrease. Furthermore is a noise offset in the 4E sensor visible which is related to the shorter electrode distance thus higher sensor capacitance. Noise measurements of proton irradiated samples from Karlsruhe and CERN in Fig. 4.16(b) show a shot noise rise caused by the increasing leakage current.

All irradiated 3D modules in Fig. 4.16(b) show a noise increase in function of the applied bias voltages. As discussed earlier for the irradiated planar FE-I3 modules show also the irradiated 3D samples a shot noise rise corresponding to the increased leakage current. Also in this case is the collected radiation dose of about 145 Mrad for the $1 \cdot 10^{15}\ n_{eq}\ cm^{-2}$ irradiated samples higher than for the $1.6 \cdot 10^{15}\ n_{eq}\ cm^{-2}$ irradiated samples with about 81 Mrad. Corresponding to the higher radiation dose show the $1 \cdot 10^{15}\ n_{eq}\ cm^{-2}$ irradiated samples a higher front-end noise contribution leading to a higher total noise despite of the lower fluence. On the other hand is the noise contribution related to the sensor capacitance almost constant due to the high resistivity of the sensor substrate [122, 106].

Noise measurements on FE-I4 modules

Measurements on bare FE-I4 read-out chips showed a strong dependence between the module noise and the threshold and feedback current settings [77]. Due to this dependence it is only possible to compare noise measurements of modules tuned to the same target values.

Planar Pixel Sensors on FE-I4

As expected show planar n-in-n and n-in-p modules before irradiation in Fig. 4.17(a) a noise decrease in function of the bias voltage until they reach the saturation region. The observed noise decrease between under-depleted and full-depleted FE-I4 sensors before irradiation is in the range of 20 e^-. For planar IBL single chip modules a threshold tuning to 1600 e^- was chosen. To investigate the feedback current tuning impact on the module noise settings for 5 ToT and 8 ToT for an injected charge of 10 ke^- were selected. Following earlier measurements on a bare FE-I4 read-out chip decreases the module noise in function of the feedback current [77]. In case of the tested values in Fig. 4.17(a) the noise decreases by about 25 e^- when the gain is changed from 5 ToT to 8 ToT for 10 ke^-. Remarkable is the high noise uniformity between the four IBL modules which use sensors fabricated in two different production batches. Next to the 200 µm thick n-in-n modules one 150 µm thick n-in-p module was also tuned to a threshold of 1600 e^- with a feedback current gain of 5 ToT for an injected charge of 10 ke^-. The increased sensor capacitance due to the reduced sensor thickness causes a higher sensor noise compared to the IBL modules.
Measurements on irradiated modules in Fig. 4.17(b) were performed at a temperature of

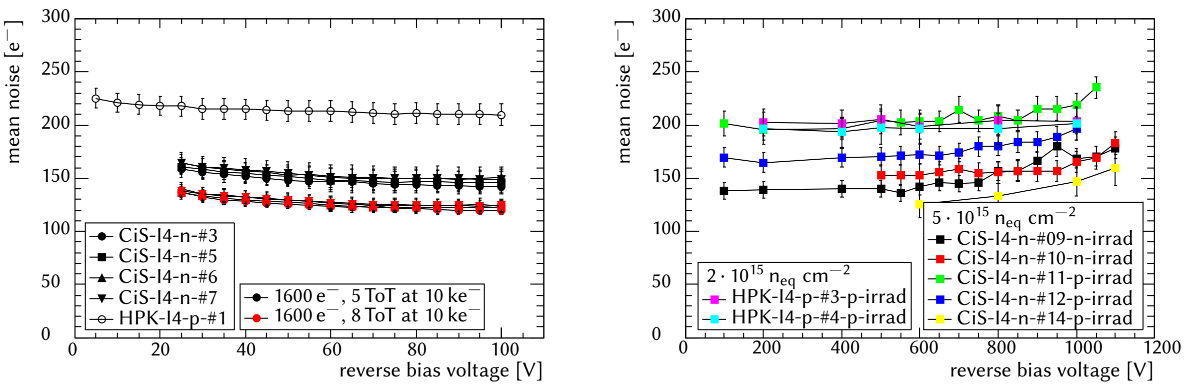

(a) before irradiation (b) after irradiation

Figure 4.17: Noise behavior in function of the applied bias voltage for planar n-in-n and n-in-p sensor modules using the FE-I4 read-out chip. Measurements before irradiation in Fig. 4.17(a) show the expected noise decrease for higher voltages. Furthermore is the noise behavior of modules for different feedback current setting visible. Noise measurements of n-in-n samples irradiated at KIT, CERN PS and JSI in Fig. 4.17(b) show a shot noise increase at higher voltages. Irradiated n-in-p modules show a stable noise behavior correlated with the smaller leakage current increase.

$-30\,^{\circ}$C. In order to avoid introducing further parameters a threshold of 1600 e^{-} with a feedback current gain of 5 ToT for an injected charge of 10 ke^{-} was chosen. Noticeable for the $5 \cdot 10^{15}$ n_{eq} cm^{-2} irradiated n-in-n modules is the noise increase at voltages approaching the operation voltage of 1000 V. Independent of the radiation source this increase varies between 20 e^{-} and 40 e^{-}. Looking at the leakage current measurements in Fig. 4.12(b) these results fit the expected noise increase of $2\sqrt{i_{leak}}$ [56]. Based on the simulation the noise consists of the shot noise contribution as well as the thermal noise contribution caused by the leakage current compensation [56]. The low leakage current increase of the $2 \cdot 10^{15}$ n_{eq} cm^{-2} irradiated n-in-p modules in Fig. 4.12(d) on the other hand explain the stable noise behavior of these samples. A further effect visible in Fig. 4.17(b) is the noise increase caused by the collected radiation dose in the front-end chip. As expected show the $5 \cdot 10^{15}$ n_{eq} cm^{-2} neutron irradiated samples with a radiation dose of about 5 Mrad the lowest noise contribution. Based on radiation studies of bare chips the electronic noise contribution due to neutron irradiation of the chip is expected to be below 1 % thus can be neglected [84]. Looking at the samples irradiated with high energy protons from CERN PS corresponding to a radiation dose of 252 Mrad a front-end noise increase between 15 % and 30 % is measured. For the n-in-p samples which collected a radiation dose of about 290 Mrad an noise increase of about 30 % is measured. For these samples it needs to be pointed out that the sensors are 50 µm thinner thus cause in addition a higher noise contribution due to the sensor capacitance. The exception is sample CiS-I4-n-#14-p-irrad irradiated with low energetic protons which was tested with an early software version which did not implement all factors necessary for the front-end calibration. As a result the measured noise of the sample represents an underestimated value which can not be compared. Due to the high radiation dose of 725 Mrad a front-end noise contribution exceeding the other values would have been expected.

3D Pixel Sensors on FE-I4

Noise measurements on a CNM module before irradiation tuned to a feedback current gain of 5 ToT for an injected charge of 10 ke^{-} in Fig. 4.18(a) show a stable noise behavior for voltages higher than 5 V. With a depletion voltage below 10 V no noise decrease caused by the variations of the sensor capacitance becomes visible. Tests for threshold values between 1000 e^{-} and 3200 e^{-} show that the noise distribution stays stable within the tested target threshold range. The obtained results are in agreement with the measurements shown in Fig. 4.5(b) for different bias voltages. Furthermore are the results also in agreement with the measurements concerning the correlation between the noise and threshold on bare FE-I4 chips [77]. For the specific tuning configuration used in Fig. 4.18(a) the expected noise decrease followed by a noise saturation in function of the applied bias voltage can be seen.

Measurements on irradiated modules in Fig. 4.18(b) were performed at a temperature of $-20\,^{\circ}$C. A front-end tuning to 1500 e^{-} with a feedback current gain of 8 ToT for an injected charge of 20 ke^{-} was chosen to avoid the introduction of further parameters. The $5 \cdot 10^{15}$ n_{eq} cm^{-2} irradiated modules show in the tested voltage range a noise increase below

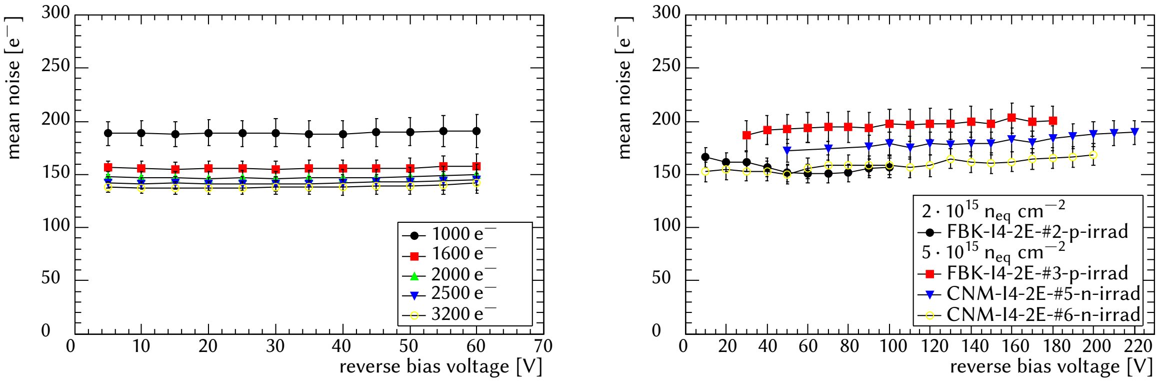

(a) before irradiation (b) after irradiation

Figure 4.18: Noise behavior in function of the applied bias voltage for 3D sensor modules from CNM and FBK using the FE-I4 read-out chip. Measurements on an unirradiated CNM module in Fig. 4.18(a) show the noise saturation for voltages exceeding the full depletion voltage. Furthermore is the noise behavior of the modules for different threshold settings with a feedback current gain of 5 ToT for an injected charge of 10 ke^- visible. Noise measurements on FBK and CNM modules irradiated at KIT and JSI in Fig. 4.18(b) tuned to a threshold of 1500 e^- with a feedback current gain of 8 ToT for an injected charge of 20 ke^- show a shot noise increase in function of the applied bias voltage.

20 e^-. Looking at the leakage current results in Fig. 4.13(b) and Fig. 4.13(d) the obtained results fit the expected noise contribution of shot noise and thermal noise from the leakage current compensation [56]. The noise decrease at low voltages of the $2 \cdot 10^{15}$ n_{eq} cm^{-2} irradiated module promotes a variation of the sensor capacitance in function of the applied bias voltage. Due to the shallow leakage current increase in Fig. 4.13(b) a shot noise increase of only few electrons becomes visible at about 80 V. The noise shift of the two FBK modules is explained by the variation of the collected radiation dose. While the $2 \cdot 10^{15}$ n_{eq} cm^{-2} irradiated module with a dose of 290 Mrad is still close to the expected dose for the chip, exceeds the $5 \cdot 10^{15}$ n_{eq} cm^{-2} irradiated module with a dose of 725 Mrad more than twice the design values. The two irradiated CNM modules were tested with an early software version which did not implement all factors necessary for the front-end calibration. As a result the measured noise offset of the sample does not represent absolute values which prevents a comparison between modules.

Diamond Pixel Sensors on FE-I4

As expected show noise measurements on unirradiated diamond sensors in Fig. 4.19 the for diamond sensors typical low noise behavior. The bias voltage increase on the sensor only leads to a higher electric field in the sensor material but does not change the sensor capacitance thus has no effect on the sensor noise. The measurements confirm the expectation that the sensor noise is independent of the applied bias voltage. Due to the compared to silicon reduced noise it is possible to reach low threshold configurations with diamond modules down to 800 e⁻. While the noise in the threshold range between 2500 e⁻ and 1500 e⁻ only varies by about 20 e⁻ a stronger increase is visible for the tested lower threshold values. The variation of the sensor thickness between the tested modules which changes about 250 µm can due to the low sensor noise not be distinguished.

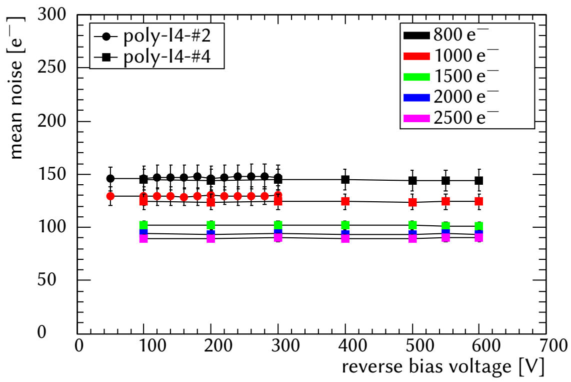

Figure 4.19: Noise measurements of unirradiated diamond FE-I4 modules in function of the bias voltage. Furthermore is the noise behavior of the modules for different threshold setting visible.

Noise impact on operation and performance

The performed noise measurements on unirradiated silicon modules implementing a planar- or a 3D-sensor technology confirm the expected noise behavior in function of the applied bias voltage. Below the full depletion voltage the noise decreases with the sensor capacitance until a saturation is reached at the full depletion voltage. The shift from the sensor capacitance to the leakage current as dominating factor of the noise contribution caused by radiation damage introduces a further factor influencing the sensor noise. While the sensor capacitance is an intrinsic value of the sensor design is the leakage current related to the temperature. To reduce the noise impact during the sensor operation it is interesting to use sensors with a low sensor capacitance at low temperatures. Whereas the operation at low temperatures become important after irradiation. Concerning the sensor capacitance the 3D design features the advantage of a linear relation between the sensor thickness and capacitance. Further is the leakage current of the 3D design after irradiation lower than in the planar design which reduces the cooling necessary to reach the same noise performance. Diamond sensors on the other hand have due to intrinsic diamond properties a low sensor capacitance and low leakage current thus before and after irradiation a low sensor noise contribution.

The front-end noise properties show a development towards low threshold operation for the FE-I4 chip down to 800 e⁻ and 1600 e⁻ for diamond and silicon sensors. The total noise is expected to be below 200 e⁻ also after irradiation. The noise increase caused by the collected radiation dose also needs to be taken into account during the operation of the experiment. During the measurements a dose of 725 Mrad was reached at which the operation of the FE-I4 chip was still possible. In the experiment it will become necessary to adjust the front-end settings for an operation at low threshold with an adequate feedback current gain depending on the fluence while aiming for a low front-end noise contribution. Also the noise occupancy in the experiment will become relevant to reduce noise hits in the data.

4.2.3 Noise Occupancy-Analysis

The noise occupancy is next to the intrinsic module noise a further important factor for the determination of the minimum operation threshold. For decreasing threshold settings the probability increases that noise charge exceeds the threshold and gets considered as hit information. During the detector operation in the experiment these noise hits increase the amount of data to read out which could in extreme cases result in data loss. In addition corrupt the noise hits the collected data which makes it more difficult to analyze the measurements. To reduce the contribution from noisy pixels a noise occupancy threshold of 10^{-5} hits pixel^{-1}BC^{-1} is used in the current ATLAS pixel detector. Based on this threshold it is decided if a pixel is noisy and should be masked.

In order to investigate the noise occupancy an external signal with a rate in the range of 9 kHz to 10 kHz was used to trigger the read-out of the modules hit information. As the rate is much lower than the operation rate in the LHC enough time is provided to process and read-out the data without influencing the properties of the module. A total amount of one million trigger was send for each tested condition corresponding to a read-out of 16 consecutive level-1 trigger. Based on the amount of triggers send for each operation condition a sensitivity in the order of 10^{-12} hits pixel^{-1} BC^{-1} could be obtained. As the expected muon hitrate of about $50 \cdot 10^{-15}$ hits pixel^{-1} BC^{-1} is three orders of magnitude smaller than the sensitivity it is not expected to contribute to the measurements. To process the raw data the noise occupancy analysis implemented in the Cluster Analysis software described in Sec. 3.7 is used. The number of noisy pixel per module and the mean noise occupancy of the module are calculated by the software corresponding to Eq. 3.4 and Eq. 3.5 respectively.
To determine the noise occupancy behavior $5 \cdot 10^{15}$ n_{eq} cm^{-2} irradiated planar modules shown in Fig. 4.20 were tested at a bias voltage of 600 V.
In both cases a decrease of the number of noisy pixel can be observed in Fig. 4.20(a) before it stabilizes at a threshold value of about 2500 e^{-}. While the slope for threshold settings below 2500 e^{-} indicates a threshold dependence of the number of noisy pixel indicates the plateau a threshold independent contribution. The effect that the probability of noise charge exceeding the threshold rises with lower threshold settings explains the threshold dependent noise contribution. The threshold independent contribution on the other hand could be represented by a fix number of damaged pixel. The offset between the neutron and the proton irradiated module is probably related to the variation of the collected dose during the ir-

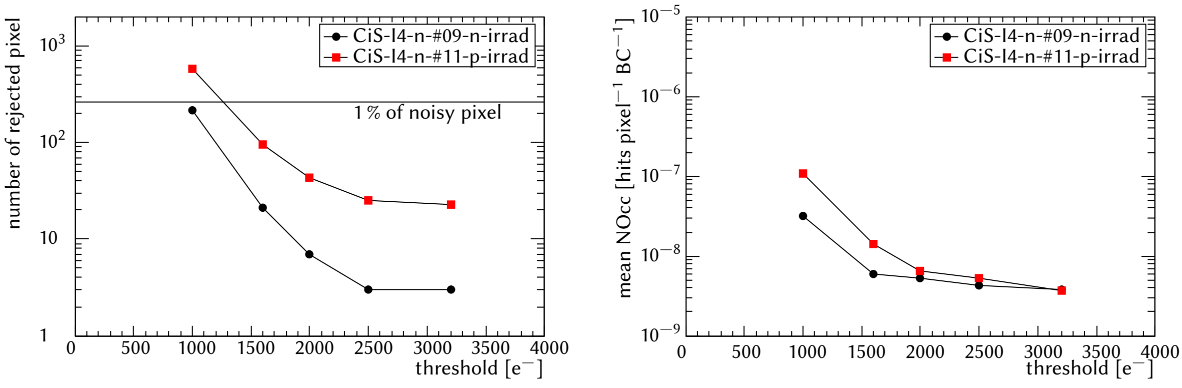

Figure 4.20: Noise occupancy measurements on $5 \cdot 10^{15}\,n_{eq}\,cm^{-2}$ irradiated planar pixel modules at a bias voltage of 600 V. The number of noisy pixel in function of the threshold decrease in Fig. 4.20(a) with the threshold before it stabilizes around 2500 e^-. The mean noise occupancy in Fig. 4.20(b) shows a plateau region beginning at threshold values between 1500 e^- and 2000 e^- indicating a threshold independent noise contribution.

radiation. Here, the neutron irradiated sample collected a dose of about 5 Mrad while the proton irradiated sample collected a dose of 252 Mrad which is close to the design dose of the FE-I4 chip. Looking at the percentage of noisy pixel per module the 1 % line is reached for threshold values between 1000 e^- and 1300 e^-.
The mean noise occupancy of the modules in Fig. 4.20(b) also show a threshold dependent part for threshold settings below 2000 e^- with an independent contribution for higher threshold values. Also here is the threshold dependence explained by the Gaussian noise distribution reducing the probability to exceed the threshold thus creating noise hits in function of the module threshold. Ionizing radiation as candidate for a threshold independent noise contribution explains the plateau region for threshold values above 2000 e^-. As the rate contribution from muons is lower than the sensitivity of the measurements a further source must be the reason for the increased noise occupancy. A possible explanation is the activity of the sensor modules them self generating hits in the sensor which would be considered as noise hits. An example is Ta-182 generated during the neutron irradiation with thermal neutrons with a half lifetime of three to four months emitting β-particles.

Measurements performed with irradiated planar and 3D sensor modules showed a similar noise occupancy increase for threshold values below 1600 e^-. An unirradiated bare front-end chip on the other hand showed a constant noise occupancy corresponding to the measurements sensitivity down to a threshold value of 500 e^- [78]. Based on these results the Planar Pixel and 3D Pixel collaboration decided to operate the modules at a threshold of 1600 e^- and 1500 e^- respectively. The diamond pixel collaboration on the other hand decided to use a threshold of 1100 e^- to compensate for the smaller charge generated in diamond sensors.

4.2.4 Photon Source

Measurements with photon sources have been performed with planar and 3D silicon pixel sensors mounted on FE-I3 and FE-I4 read-out chips. The analysis was performed with the Cluster Analysis program described in Sec. 3.7. If not otherwise indicated only single hit cluster were used for the analysis. This way the cluster threshold corresponds to the threshold set in the module. In the case of clusters containing more than one hit pixel the module threshold needs to be exceeded by each pixel. This effect increases the cluster threshold linearly with the cluster size thus making it impossible to measure small charges.
To avoid noise triggers caused by noisy channels a masking was applied during the measurement. The increased noise occupancy after irradiation made it impossible to distinguish if hits are generated by a photon or by noise. As a result measurements with FE-I3 modules were only possible up to a fluence of $1 \cdot 10^{15}\ \mathrm{n_{eq}\ cm^{-2}}$.
Measurements on FE-I3 modules were performed at a threshold of $3200\,\mathrm{e^-}$ with a current gain of 60 ToT for an injected charge of $20\,\mathrm{ke^-}$. For FE-I4 modules on the other hand different front-end settings were used to look at the module operation at low threshold settings.
The application of photon sources with different photon energies discussed in Sec. 3.5.1 makes it possible to determine calibration curves for FE-I3 and FE-I4 modules. The results for both front-end chips are summarized in Fig. 4.25 following the individual results for the different sensor technologies.

Planar Pixel Sensors on FE-I3

The results in Fig. 4.21 show the responds of planar n-in-n and n-in-p FE-I3 modules to measurements with varying photon energies and bias voltages. The charge distributions of a n-in-n module at a bias voltage of 150 V in Fig. 4.21(a) correspond to different photon energies. Noticeable is the overlap of the spectrum of the Am-241 source and the copper roentgen fluorescent target spectrum. This behavior is explained by the energy emitted by the copper target which is not high enough to exceed the module threshold. The photons directly emitted by the Am-241 source on the other hand exceed the threshold of the module thus are the only contribution to the charge distribution. Corresponding become measurements with the copper roentgen fluorescent target only relevant for threshold settings below $2000\,\mathrm{e^-}$. Overall show the measured charge distributions the expected shift of the photo peak according to the emitted photon energy. By comparing the charge of the measured photo peak with the expected charge it becomes clear that a reduced charge value is measured. The offset between the two values shown in Fig. 4.25(a) further increases for higher energies.
Photon source measurements of an unirradiated planar n-in-p module with an Am-241 source in Fig. 4.21(b) show the influence of the bias voltage on the sensor responds. As expected does the charge distribution not change after exceeding the full depletion voltage between 50 V and 100 V. For values below the full depletion voltage the number of hits with energies below the photo peak increases. This behavior is related to the reduced space charge region in case of an under-depleted sensor. While the space charge region shrinks it increases the

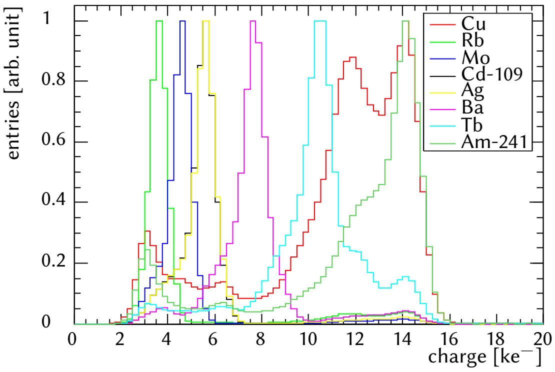

(a) planar n-in-n

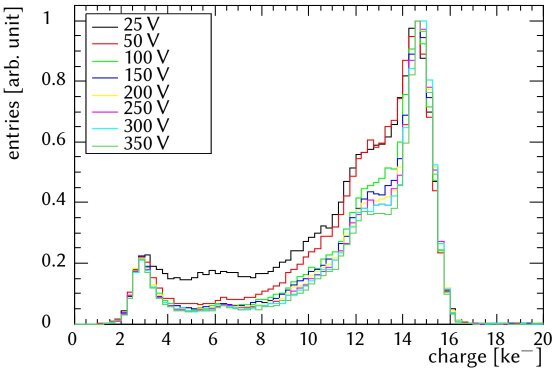

(b) planar n-in-p

Figure 4.21: Photon source measurements of unirradiated planar n-in-n and n-in-p pixel sensor modules on FE-I3 read-out chips. The charge distributions in Fig. 4.21(a) correspond to measurements with photon energies ranging from 8 keV to 60 keV for a n-in-n module at 150 V. The sensor response to an Am-241 source in Fig. 4.21(b) shows the influence of the bias voltage on the charge distribution measured with a n-in-p module.

probability that photo electrons move out of the active sensor area. As a result only a part of the deposited energy can be measured thus an increased contribution to the spectrum at lower energies appears. Similar to the n-in-n module also a reduced charge than the expected photon energy is measured.

3D Pixel Sensors on FE-I3

Results of photon source measurements with an Am-241 source on irradiated 3D sensor modules using the 2E-, 3E- and 4E column design are shown in Fig. 4.22. The modules were irradiated with low energy protons to a fluence of $1 \cdot 10^{15}\, n_{eq}\, cm^{-2}$. The corresponding charge distributions for the 2E-, 3E- and 4E sensors are shown separately in Fig. 4.22(a), Fig. 4.22(b) and Fig. 4.22(c). The distribution of the photo peak in Fig. 4.22(d) shows a similar charge increase for the 2E- and 3E sensors while the increase is less strong in the 4E sensor. This effect is related to the mean free path of the electrons and holes in silicon after irradiation. In case of the 2E- and 3E sensor the minimum electrode distance is about 103 µm and 71 µm respectively. The mean free path of $1 \cdot 10^{15}\, n_{eq}\, cm^{-2}$ proton irradiated silicon with about 100 µm is in the same range as the electrode distance [57]. On the other hand is the mean free path about twice as long as the electrode distance of the 4E sensor. As a result is the probability of charge trapping in the 2E- and 3E-type sensor higher than in the 4E-type sensor. In case of the 4E sensor only the maximum electrode distance reaches the length of the mean free path thus shows the sensor only small charge trapping effects. The same effect contributes partially to the offset of the photo peak between the 2E- and the 3E-type as the minimum electrode distance is still below the mean free path length. In addition is the electric field due to the shorter electrode distance in the 3E sensor stronger than in the 2E sensor.

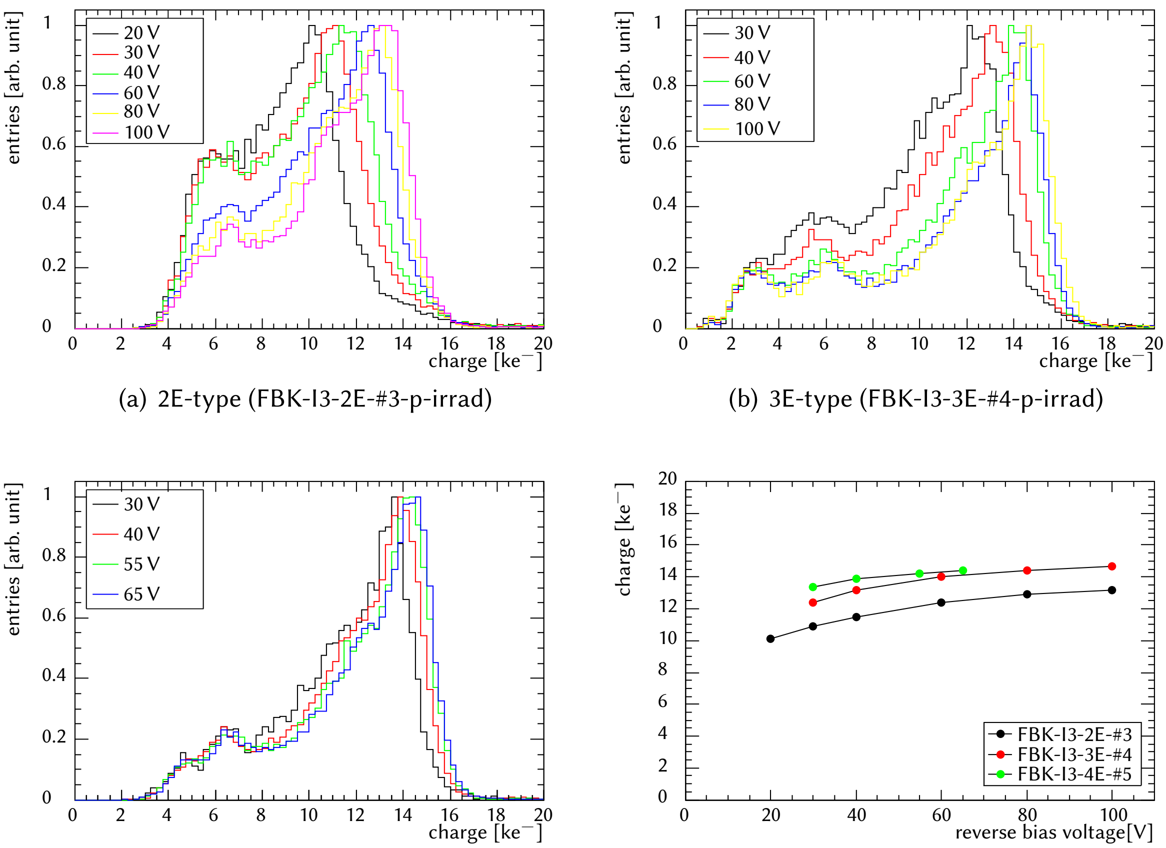

(a) 2E-type (FBK-I3-2E-#3-p-irrad)

(b) 3E-type (FBK-I3-3E-#4-p-irrad)

(c) 4E-type (FBK-I3-4E-#5-p-irrad)

(d) measured photo peak

Figure 4.22: Photon source measurements of 3D pixel sensor modules on FE-I3 read-out chips irradiated with protons to a fluence of $1 \cdot 10^{15}\,n_{eq}\,cm^{-2}$ at KIT. The individual charge distributions for the 2E-, 3E- and 4E-column type are shown in Fig. 4.22(a), Fig. 4.22(b), Fig. 4.22(c) respectively. The behavior of the photo peak in function of the applied bias voltage in Fig. 4.22(d) shows a saturation for high bias voltages and the influence of the column distance.

Planar Pixel Sensors on FE-I4

The sensor responds of unirradiated planar modules on FE-I4 read-out chips to photon sources is shown in Fig. 4.23. The influence of the threshold on the charge spectrum is shown in Fig. 4.23(a) for a n-in-n sensor module. The measured photo peak of the charge distributions corresponds to the expected value of an Am-241 source. Also noticeable is the noise increase for threshold settings below 2000 e^-. The charge distribution in Fig. 4.23(b) shows the sensor responds of a n-in-p modules to different photon energies. The measured photon energies correspond to the expected values emitted by the photon source. A more detailed discussion of the relation between photon energy and measured energy in FE-I4 modules follows later (see Fig. 4.25(b)).

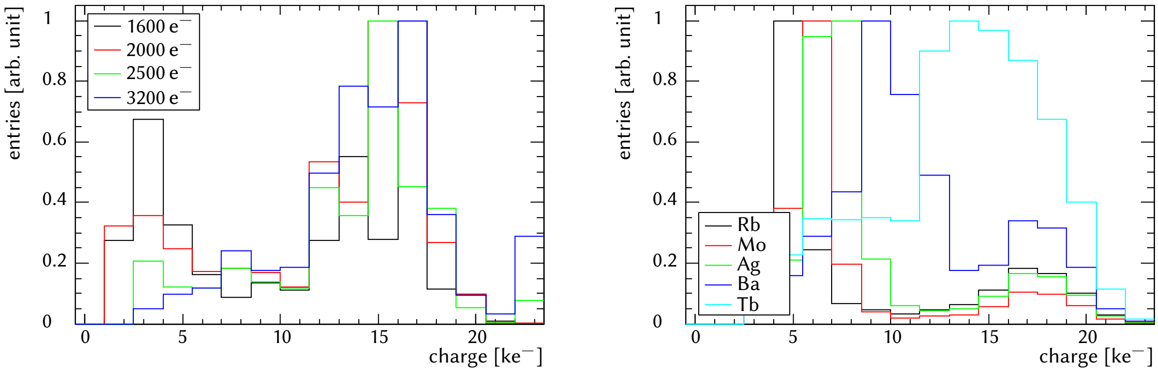

(a) planar n-in-n (b) planar n-in-p

Figure 4.23: Photon source measurements of unirradiated planar n-in-n and n-in-p sensor modules on FE-I4 read-out chips. Measurements in Fig. 4.23(a) show the sensor response to an Am-241 source for a n-in-n module in function of the module threshold. The charge distributions in Fig. 4.23(b) show the sensor responds to different photon energies measured with a n-in-p module at a threshold of 3200 e^-.

3D Pixel Sensors on FE-I4

Photon source measurements of 3D modules using sensors fabricated by CNM and FBK are shown in Fig. 4.24. The responds of an unirradiated 3D pixel sensor from CNM for different threshold settings in Fig. 4.24(a) confirms the results obtained with planar sensors. Also here the photo peak corresponds to the expected charge of an Am-241 source. In case of

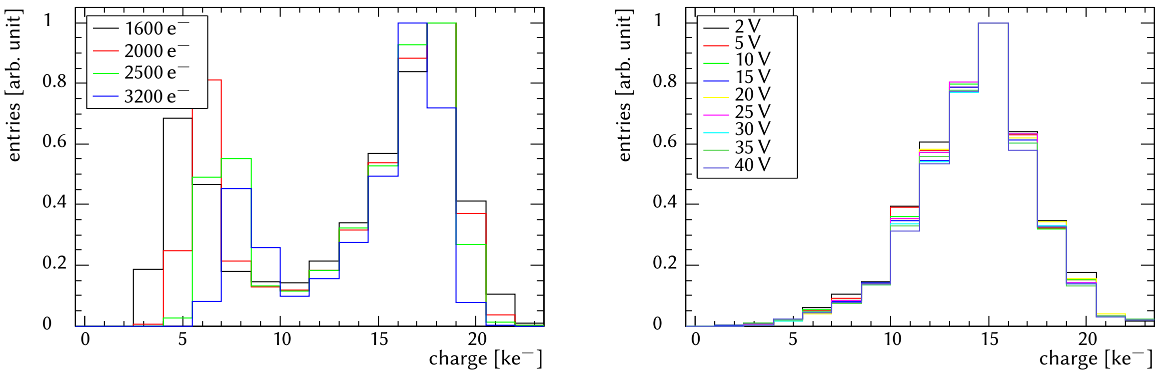

(a) CNM design (b) FBK design

Figure 4.24: Photon source measurements with an Am-241 source of unirradiated 3D sensor modules on FE-I4 read-out chips. Measurements of the CNM module in Fig. 4.24(a) shows the sensor response for different threshold settings at a bias voltage of 20 V. The sensor response of the FBK module in Fig. 4.24(b) shows the influence of the bias voltage considering only double hit cluster.

the FBK module in Fig. 4.24(b) the influence of the bias voltage on the sensor responds is shown for double hit clusters. With a module threshold of 1500 e⁻ the total cluster threshold corresponds to 3000 e⁻. This means that the charge collected in both cluster hits and the total cluster exceeded the module threshold and the cluster threshold respectively. As a result hits introducing a signal below the cluster threshold are excluded from the analysis preventing the contribution of noise hits. The remaining Am-241 photo peak and the high energetic part of the Compton spectrum behave uniform in the tested bias voltage range.

Calibration results for FE-I3 and FE-I4 modules

The calibration curves in Fig. 4.25 show the measured photo peak charge of unirradiated FE-I3 and FE-I4 modules in function of the injected photon energy. In case of the FE-I3 modules in Fig. 4.25(a) the divergence between the expected and measured value increases for higher charges. This behavior is related to the applied tuning method using only the small injection capacitance. Due to this effect measurements with charged particles are expected to underestimate the injected charge.

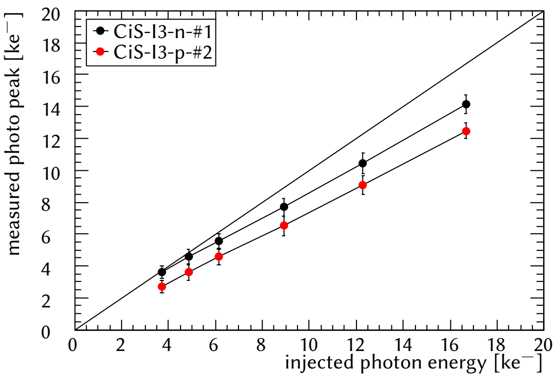

(a) FE-I3 modules

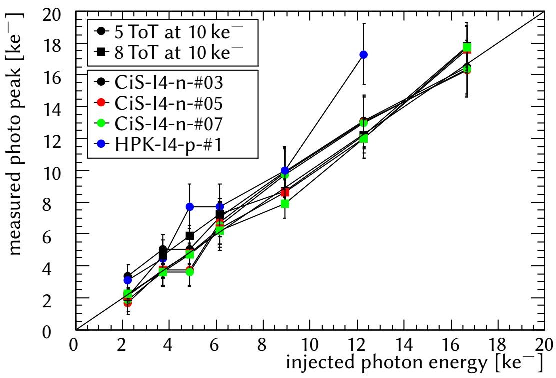

(b) FE-I4 modules

Figure 4.25: Calibration curves for unirradiated FE-I3 and FE-I4 silicon modules. The tested FE-I3 modules in Fig. 4.25(a) show an increasing deviation between the measured and expected charge value for higher charges. The results for FE-I4 modules in Fig. 4.25(b) show a good correlation between the expected and the measured value at a threshold of 1600 e⁻ and different feedback current settings.

For FE-I4 modules in Fig. 4.25(b) on the other hand a correlation between the injected and measured charge is visible. Both tested feedback current configurations lead to uniform results for the tested planar n-in-n modules. The planar n-in-p module on the other hand shows an overestimated value at 12 ke⁻. The tested charge range is below charge values expected for unirradiated sensors. Nevertheless it is assumed that the correlation is also present for higher values. On the other hand covers the tested range the charge range expected for irradiated sensors. This information will help to interpret the collected charge after irradiation.

4.2.5 Electron Source

The charge distribution related to the interaction of charged particles with the sensor material is described by a Landau-distribution. For measurements with a collimated electron source the angle of the incident particles usually varies up to a certain degree changing the path length through the sensor. To take this effect into consideration the Landau-distribution is convoluted with a Gaussian forming the so-called LanGau distribution. The most probable charge deposited in the material is then defined by the most probable value of the Landau-distribution. Source measurements with electrons provide the possibility to measure the charge distribution and to compare charge collection properties of different sensor technologies.

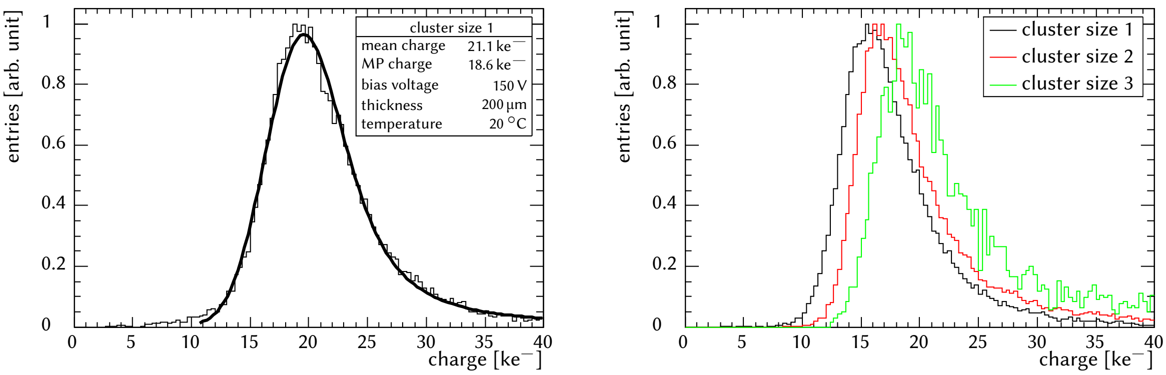

(a) Planar n-in-p sensor module

(b) planar n-in-n sensor module

Figure 4.26: Electron source measurement results for unirradiated planar sensor modules on FE-I3 read-out chips. The charge distribution shown in Fig. 4.26(a) corresponds to single hit clusters including the LanGau fit. The impact of the cluster size on the charge distribution in Fig. 4.26(b) increases with bigger clusters.

Measurements of unirradiated planar and 3D sensors on FE-I3 read-out chips in Fig. 4.26 and Fig. 4.27 show typical results of electron source measurements. The Cluster Analysis software described in Sec. 3.7 implements the necessary functions for the analysis. The LanGau fit function in Fig. 4.26(a) is used to determine the most probable charge value of the measured charge distribution [116]. Parameter as the cluster size in Fig. 4.26(b) or the operation voltage in Fig. 4.27(a) influence the charge distribution. In case of the cluster size the most probable charge shifts towards higher values with increasing cluster size. This behavior is favored by charge sharing between read-out cells. In the case that the charge in a neighboring pixel stays below the threshold this pixel is not read out thus not available for the analysis. As a consequence does the cluster size not increase and the charge in the neighboring pixel is not added to the total cluster charge. Corresponding show clusters containing more pixel a higher charge as less charge is lost to neighboring pixel. A further effect is that delta electrons tend to move perpendicular to the incident particle. As a result the additional

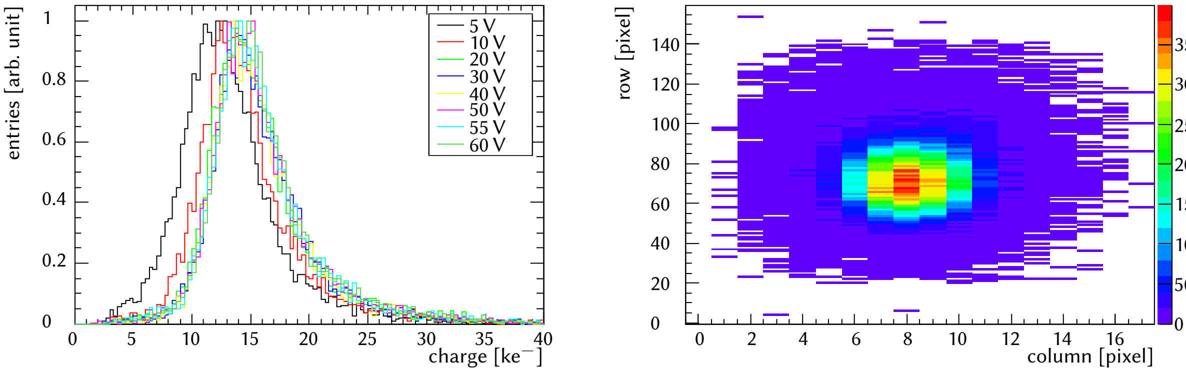

(a) FBK-I3-2E-#1 3D sensor module (b) FBK-I3-4E-#2 3D sensor module

Figure 4.27: Electron source measurement results for unirradiated 3D sensor modules on FE-I3 read-out chips. The influence of the bias voltage on the charge distribution in Fig. 4.27(a) shows an increase with higher bias voltages until the sensor is fully depleted. The hit map in Fig. 4.27(b) shows the beam spot corresponding to the collimated source.

charge introduced by the delta electron then further increases the cluster charge. Looking at the cluster size distribution about 90 % off all cluster contain one or two pixel while the distribution of the remaining 10 % rapidly decreases for higher cluster sizes. In order to reach sufficiently high statistic for the analysis a default value of one million trigger was chosen per measurement step corresponding to a measurement time of about 2 h per step. Looking at the charge collection in function of the bias voltage in Fig. 4.27(a) an increase of the most

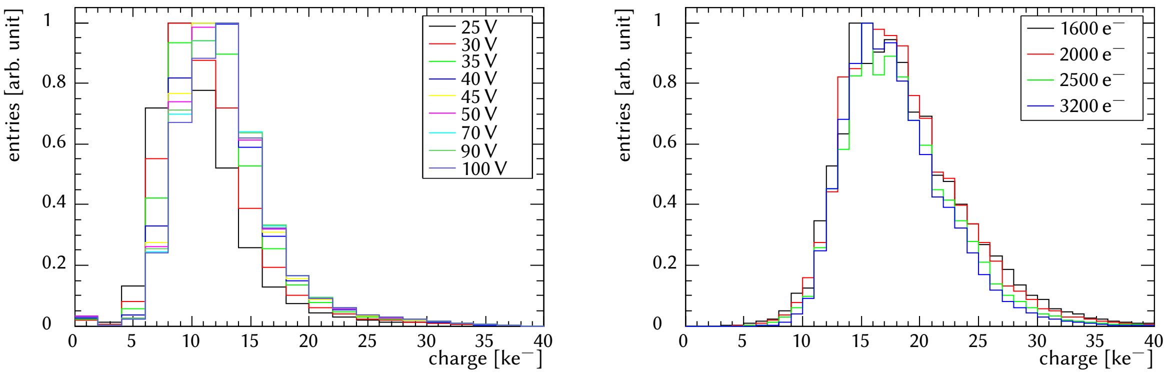

(a) Planar n-in-p sensor module (b) 3D sensor module CNM design

Figure 4.28: Electron source measurement results for unirradiated sensor modules on FE-I4 read-out chips. The influence of the bias voltage on the collected charge in Fig. 4.28(a) shows an increase with the bias voltage until the 150 µm thick sensor is fully depleted. The results for different threshold settings in Fig. 4.28(b) show similar behavior in a 230 µm thick 3D sensor.

probable charge appears corresponding to the depletion width of the sensor. The hit map in Fig. 4.27(b) confirms the correlation between the measurements and the collimated beam.

The charge distributions in Fig. 4.28 correspond to unirradiated modules using the FE-I4 read-out chips. Due to the reduced number of ToT-counter in the FE-I4 read-out chip a charge resolution of 2000 e^- and 1000 e^- is chosen for single and double hit cluster receptively. The bias voltage scan in Fig. 4.28(a) shows the charge increase up to the full depletion voltage at about 50 V. For double hit cluster in Fig. 4.28(b) an increased charge resolution becomes possible. The results confirm that the charge collection is independent of the threshold setting. As the collected charge decreases after irradiation it becomes more difficult to chose the correct resolution. In order to cope with this effect in FE-I4 modules the charge corresponding to the ToT showing the most entries is used instead of the most probable charge value from the fit.

Measurements of FE-I3 modules

While measurements of unirradiated FE-I3 modules were performed at an air temperature of 20 °C was the temperature for irradiated modules set to −20 °C. The relative humidity in the test environment is reduced to a value below 3 % to avoid condensation at low temperatures.

Planar Pixel Sensors on FE-I3

Next to the bulk materials used to fabricate the planar sensor types for the FE-I3 read-out chips is the sensor thickness the most relevant parameter affecting the properties of the designs. Due to the thickness variation from 250 μm to 285 μm for the n-in-n and n-in-p design respectively an about 14 % higher charge is expected in n-in-p modules. Results for both designs in Fig. 4.29 show the most probable charge value for single hit clusters before and after irradiation in function of the applied bias voltage. As expected show the unirradiated n-in-p modules in Fig. 4.29(a) due to the increased thickness a higher charge collection than the n-in-n modules. Comparing the measured and the expected charge for both sensor designs shows that about 5000 e^- less than expected are measured. Extrapolating the calibration results in Fig. 4.25(a) to the expected values shows that the observed offset correlates with the calibration offset. Therefore the offset between measured and expected charge can be mainly attributed to the miscalibration of the charge in FE-I3 modules. A further effect is the charge loss due to charge sharing related to the analysis of single hit clusters. An analysis of the n-in-p sensor measurements considering all cluster sizes showed as expected an increased most probable charge of 19 ke^- [95]. Also noticeable is the variation of the collected charge between the designs for voltages below 100 V. Similar behavior was already observed in Fig. 4.15(a) while analyzing the noise properties. As for the noise is the charge variation related to the formation of the depletion zone in the devices. As the unirradiated sensors will be operated above the depletion voltage are the charge collection properties below full depletion not relevant for the sensor operation.

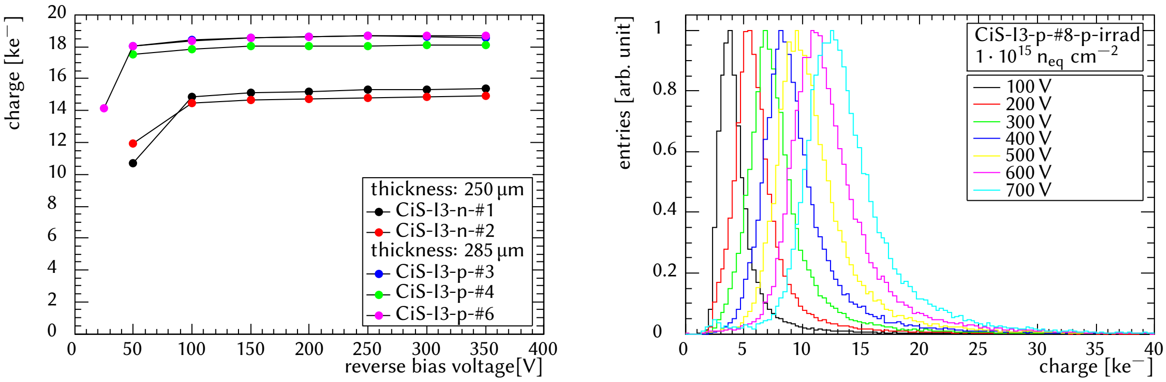

(a) before irradiation

(b) proton irradiated n-in-p module

Figure 4.29: Electron source measurements of planar n-in-n and n-in-p silicon sensors on FE-I3 read-out chips using single hit clusters. The charge collection offset in Fig. 4.29(a) is related to the thickness variation of the sensor material. The increase of the charge distribution in Fig. 4.29(b) shows the influence of the bias voltage on the charge collection after irradiation.

Despite of the fluence of $1 \cdot 10^{15}\ n_{eq}\ cm^{-2}$ and the temperature was it still possible to operate the proton irradiated n-in-p module in Fig. 4.29(b) up to 700 V. The charge distributions in function of the bias voltage show an increase of the most probable charge. Assuming a similar calibration offset observed for unirradiated modules in Fig. 4.25(a) a most probable value of about 16 ke^- would be expected at 700 V. This result could be even further increased by applying a higher bias voltage. Measurements on samples irradiated in different irradiation campaigns confirmed the successful operation of the n-in-p sensor design at higher fluences up to $10 \cdot 10^{15}\ n_{eq}\ cm^{-2}$ [95, 98]. For sensors using the n-in-n design the even operation at a fluence of $2 \cdot 10^{16}\ n_{eq}\ cm^{-2}$ has been demonstrated [119].

3D Sensors on FE-I3

A selection of 3D silicon sensors in Fig. 4.30 using two, three and four read-out columns per pixel was tested on FE-I3 read-out chips before and after irradiation. Measurements of unirradiated modules using the 2E400 and 4E400 design in Fig. 4.30(a) show a similar charge collection after full depletion. These results confirm the expectations as only the electrode distance changes while the sensor thickness is kept at 200 µm. Due to the expanded electrode distance in the 2E design a higher bias voltage is necessary to reach full depletion. Corresponding to this behavior increases the collected charge over a wider voltage range before it reaches the saturation region. Comparing the measured and the expected charge reveals a charge loss of about 3000 e^-. Similar to the planar modules discussed earlier is this behavior explained by the charge calibration in Fig. 4.25(a) and charge sharing between neighboring pixels.

As mentioned during the discussion of photon source measurements shown in Fig. 4.22 be-

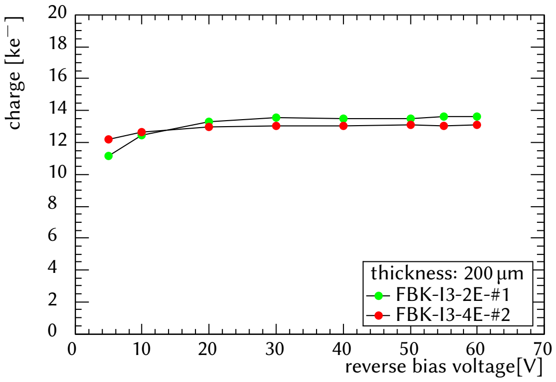

(a) before irradiation

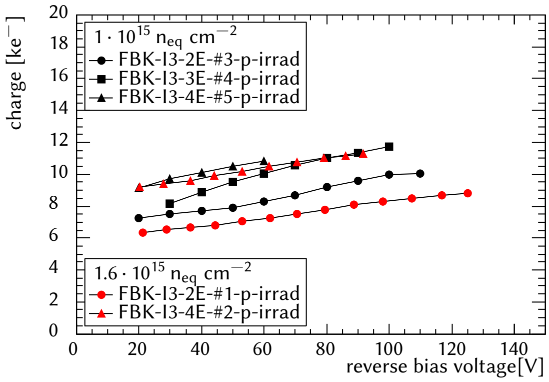

(b) after irradiation

Figure 4.30: Electron source measurements of 3D silicon sensors on FE-I3 read-out chips using single hit clusters. The charge collection in Fig. 4.30(a) before irradiation shows uniform behavior after full depletion independent of the number of read-out columns. Results after irradiation up to $1.6 \cdot 10^{15}\ n_{eq}\ cm^{-2}$ in Fig. 4.30(b) show the charge collection in function of the bias voltage.

comes the electrode distance relevant for the charge collection after irradiation. As expected show both batches of irradiated samples in Fig. 4.30(b) a charge collection increase with increasing number of read-out electrodes. As discussed earlier is this effect related to the mean free path after irradiation. In case of the 4E400 modules was argued that the length of the mean free path after irradiation up to $1 \cdot 10^{15}\ n_{eq}\ cm^{-2}$ would be still in the range of the electrode distance thus full charge collection should be possible. The fact that this is not the case for the electron source measurements is related to the column overlap in the sensor. While the overlap region is expected to show full charge collection this is not the case for the regions on top and bottom of the sensor where the electrode distance is longer than the mean free path. Corresponding to the geometrical configuration of the DDTC 3D sensor is a part of the deposited charge in the top and bottom region lost. The same effects can be also observed in the $1.6 \cdot 10^{15}\ n_{eq}\ cm^{-2}$ proton irradiated sample. Due to the higher fluence the mean free path is further decreased even reaching the maximum electrode distance of the 4E400 sensors. As a result is the collected charge further reduced compared to the lower irradiated sensors. The higher charge collection caused by the shorter electrode distance in the 4E400 design is compensated by an increased operation voltage of the 3E400 design. In case of the $1 \cdot 10^{15}\ n_{eq}\ cm^{-2}$ irradiated 3E sensor the combination of electrode distance and maximum bias voltage seem to be especially advantageous as it exceeds the charge collection of the other design even after a fluence of $1.6 \cdot 10^{15}\ n_{eq}\ cm^{-2}$.

Measurements of FE-I4 modules

For the analysis of charge measurements with FE-I4 modules the charge corresponding to the peak ToT-value is considered as the most probable value. The error bars are used to

indicate the charge resolution of the FE-I4 chip. Due to the non-linearity of the calibration a higher charge resolution is possible for lower charge values. As the resolution varies between 1000 e^- and 4000 e^- it is not possible to determine small variations of the signal. Nevertheless is it still possible to see the general charge development of a module.
Measurements of unirradiated FE-I4 modules were performed at an air temperature of 20 °C. While irradiated 3D modules were measured at −20 °C, was the temperature decreased to −30 °C for irradiated planar modules. Following the discussion in Sec. 4.2.1 corresponds this to a sensor temperature in the range of −25 °C to −23 °C for irradiated planar modules and −16 °C to −15 °C for irradiated 3D modules. All measurements were performed at a relative humidity below 3 %.

Planar Pixel Sensors on FE-I4

Charge collection measurements with an electron source of planar n-in-n and n-in-p modules on FE-I4 read-out chips are shown in Fig. 4.31 before and after irradiation. For all electron source measurements with planar modules a front-end tuning with a threshold of 1600 e^- and a feedback current gain of 5 ToT for 10 ke^- is used.

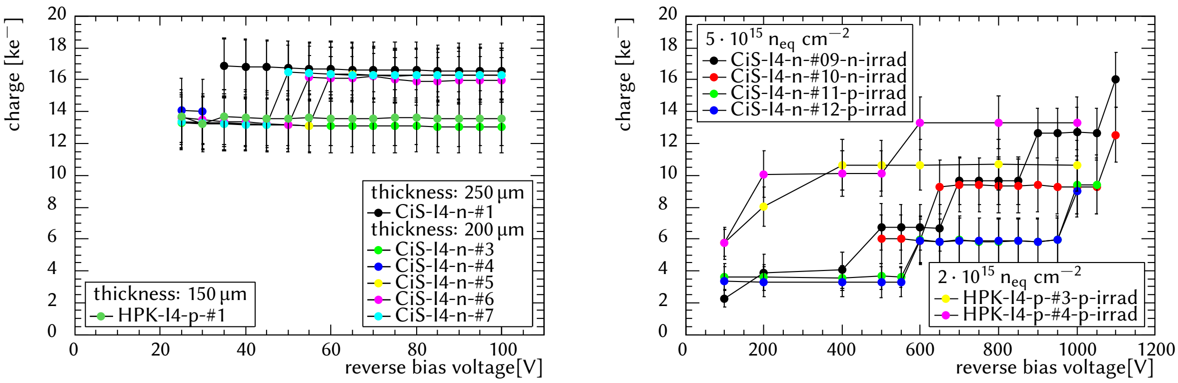

(a) before irradiation

(b) after irradiation

Figure 4.31: Electron source measurements of planar n-in-n and n-in-p silicon sensors on FE-I4 read-out chips using single hit clusters. Before irradiation in Fig. 4.31(a) the collected charge stays stable within two ToT-bins. After irradiation in Fig. 4.31(b) the collected charge increases in function of the bias voltage.

In case of the unirradiated modules in Fig. 4.31(a) the collected charge stays within one or two ToT-bins. Despite of the low charge resolution is it possible to distinguish variations depending on the sensor thickness. The 150 µm thick n-in-p sensors show a stable charge collection in the expected charge range. The 200 µm thick n-in-n sensors show a charge increase at about 50 V which fits the full depletion voltage. While one of the modules shows an early breakdown below the full depletion stays another sample even above full depletion below the expected charge. Looking at the individual ToT-distributions shows only a small charge offset between the samples. A similar behavior is observed for the 250 µm thick n-in-n

sensor which underestimates the expected charge due to the same effect.
Sets of two modules have been irradiated in the KIT, JSI and the CERN PS irradiation facilities. The n-in-p modules irradiated at KIT reached a fluence of $2 \cdot 10^{15}\,n_{eq}\,cm^{-2}$ while the n-in-n modules irradiated at JSI and CERN PS reached up to $5 \cdot 10^{15}\,n_{eq}\,cm^{-2}$. The charge collection results obtained for these modules are shown in Fig. 4.31(b). While the two modules irradiated at CERN show similar charge properties in the tested bias voltage range a variation is visible between the neutron irradiated modules. This behavior is explained by the thickness variation between the two sensors. At an operation voltage of 1000 V foreseen in the IBL the CERN PS and JSI irradiated modules show a charge in the range of 8 ke^- to 10 ke^-. The irradiated n-in-p modules on the other hand seem to reach a charge saturation at about 400 V while the charge in one of them still moves up to the next ToT-bin. The collected charge at an operation voltage of 1000 V is close to 12 ke^- which corresponds to results obtained before irradiation.

3D Pixel Sensors on FE-I4

Most probable charge distributions of the 3D silicon sensor designs from FBK and CNM on FE-I4 read-out chips are shown in Fig. 4.32 before and after irradiation. For all electron source measurements with 3D modules a front-end tuning with a threshold of 1500 e^- and a feedback current gain of 8 ToT for 20 ke^- is used.

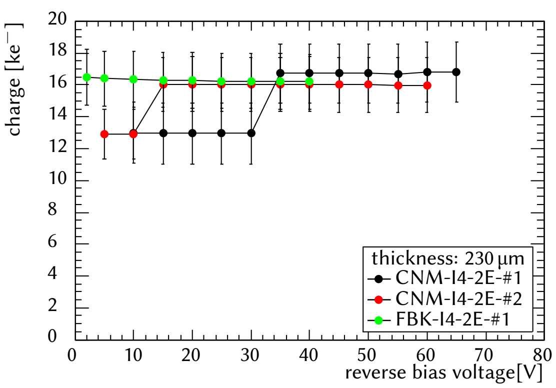

(a) before irradiation

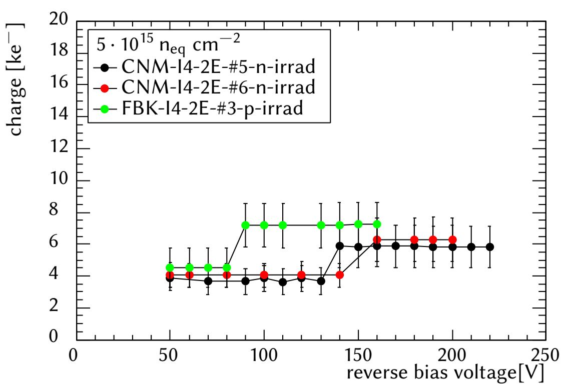

(b) after irradiation

Figure 4.32: Electron source measurements of 3D silicon sensors modules on FE-I4 read-out chips using single hit clusters. Before irradiation in Fig. 4.32(a) the collected charge stays stable within two ToT-bins. After irradiation in Fig. 4.32(b) the collected charge increases in function of the bias voltages.

The unirradiated FBK module in Fig. 4.32(a) shows a stable charge collection over the tested bias voltage range. The CNM modules on the other hand show a charge shift to the next ToT-bin. The late charge increase observed for CNM-I4-2E#1 is explained by the missing offset calibration which was not available at the time of the measurement. Corresponding is the measured charge underestimating the expected value. Comparing the measured and

the expected charge shows that the measured charge of all modules is below the expected value. As the expected value is close to the next ToT-bin this behavior can be explained with variations in the calibration. Unfortunately were the applied front-end settings not tested with a photon source as the ones shown in Fig. 4.25(b).
Modules using 3D sensors have been irradiated up to $5 \cdot 10^{15}\ n_{eq}\ cm^{-2}$ at the JSI and CERN PS irradiation facilities. The charge collection results after irradiation are shown in Fig. 4.32(b). The two neutron irradiated CNM modules show a similar charge collection between 5 ke$^-$ to 7 ke$^-$ at a bias voltage of 200 V. The proton irradiated FBK module shows a slightly higher charge collection in the range of 6 ke$^-$ to 8 ke$^-$ at 150 V.

Electron source measurement impact on operation and performance
Electron source measurement of planar and 3D silicon sensor technologies on FE-I3 and FE-I4 read-out chips are summarized in Tab. 4.1. The different operation conditions of the sensor modules make it difficult to compare the obtained results. Nevertheless are the results in Tab. 4.1 useful to identify the operation conditions for the different sensor technologies. These conditions might become later challenging points for the operation in an experiment.

technology	bias voltage	temperature	fluence	threshold	collected charge
			FE-I3		
planar n-in-p	700 V	−20 °C	$1 \cdot 10^{15}\ n_{eq}\ cm^{-2}$	3200 e$^-$	13 ke$^-$
3D FBK	100 V	−20 °C	$1 \cdot 10^{15}\ n_{eq}\ cm^{-2}$	3200 e$^-$	12 ke$^-$
			FE-I4		
planar n-in-n	1000 V	−30 °C	$5 \cdot 10^{15}\ n_{eq}\ cm^{-2}$	1600 e$^-$	9 ke$^-$
planar n-in-p	1000 V	−30 °C	$2 \cdot 10^{15}\ n_{eq}\ cm^{-2}$	1600 e$^-$	12 ke$^-$
3D FBK	150 V	−20 °C	$5 \cdot 10^{15}\ n_{eq}\ cm^{-2}$	1500 e$^-$	7 ke$^-$
3D CNM	150 V	−20 °C	$5 \cdot 10^{15}\ n_{eq}\ cm^{-2}$	1500 e$^-$	6 ke$^-$

Table 4.1: Summary of electron source measurement results for planar and 3D silicon sensor technologies using FE-I3 and FE-I4 read-out chips.

Noticeable for the three IBL sensor designs is that the charge collection of all designs exceeds the chosen threshold settings by more than four times. In case of the planar sensor design the high bias voltage and low temperature are the two main issues for the operation after irradiation. With a collected charge of about 9 ke$^-$ at 1000 V a sufficient high charge offset to the threshold is available to register even smaller charges. For the 3D sensor design on the other hand the high leakage current restricting the maximum operation voltage limits the charge collection properties. This behavior might improve during the operation in the ATLAS Experiment as the modules will be operated at a lower temperature which will decrease the leakage current compared to the measurements. The reduced leakage current would then promote a higher operation voltage further increasing the charge collection.

Diamond Pixel Sensors

Charge collection measurements with an electron source have been also performed with single and poly-crystal diamond sensors using FE-I3 and FE-I4 read-out chips. Measurement results of both crystal types are shown in Fig. 4.33. The measurements were performed at 20 °C in a dry air environment.

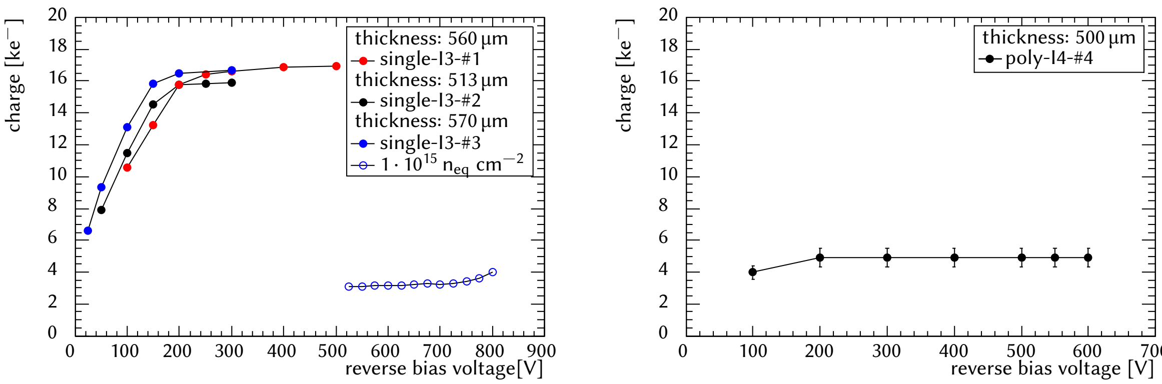

(a) single-crystal diamond on FE-I3 (b) poly-crystal diamond on FE-I4

Figure 4.33: Electron source measurements of diamond sensors on FE-I3 and FE-I4 read-out chips. The charge collection of single-crystal sensors before and after irradiation on FE-I3 chips in Fig. 4.33(a) illustrates the charge decrease after pion irradiation to $1 \cdot 10^{15}\,n_{eq}\,cm^{-2}$. Charge collection measurements of a poly-crystal diamond sensor on a FE-I4 chip tuned to a threshold of $1000\,e^{-}$ in Fig. 4.33(b) shows a charge collection distance of about 140 µm in the saturation region.

The charge collection measurements of single-crystal diamond sensors before irradiation in Fig. 4.33(a) show a saturation for bias voltages above 200 V. Due to a shift in the cluster size distribution from single hit towards double hit clusters it was decided to use all cluster sizes for the analysis. The shift in the cluster size distribution is correlated to the increased sensor thickness. With higher thickness increases the possibility of charge sharing due to the penetration angle and multiple scattering thus the number of clusters with more hit pixel also increases. The obtained results for single-crystal diamond sensors correspond to a charge collection distance between 440 µm and 470 µm assuming a charge generation of $36\,e^{-}\,\mu m^{-1}$. Comparing these results to the expected charge collection a charge loss of about $3\,ke^{-}$ is observed. It is not possible that the charge loss corresponds entirely to the miscalibration observed for single hit clusters in Fig. 4.25(a) as all cluster sizes are used for the analysis. During the investigation of this charge loss it was found out that the graphitization process prior to the electrode deposition was changed and the reason for this behavior. Next to the observed charge loss a temporal component was also discovered which further increased the charge loss over time. During the ongoing investigation were two modules irradiated at PSI with pions to a fluence of $1 \cdot 10^{15}\,n_{eq}\,cm^{-2}$. Measurements after irradiation in Fig. 4.33(a) show a most probable charge value of about $4\,ke^{-}$ at a bias voltages of 800 V. Compared to

the expected value for the collected charge the results correspond to a charge loss of more than 50 %. It is assumed that this charge loss is related to the fabrication process of the electrodes. This assumption is confirmed by modules from the same production mounted on FE-I4 read-out chips using a revised graphitization process and irradiated with protons. Source measurements with these modules did no show the charge loss observed with the FE-I3 modules [56]. The next research step with these modules is the removal of the read-out chip to form pad or strip detectors in order to confirm that the observed charge loss is related to the graphitization process.
Source measurements of an unirradiated poly-crystal diamond modules for the DBM project are shown in Fig. 4.33(b) for a bias voltage up to 600 V. While a small charge increase can be observed between 100 V and 200 V a saturation region is reached above this bias voltage. The corresponding charge collection distance is about 140 μm. In order to determine a suitable threshold configuration for the operation of the diamond modules the measurement has been performed for different threshold settings. The tested threshold range between 800 e^- and 2500 e^- showed comparable charge collection properties. As the operation range is reduced for high threshold settings but also the noise occupancy increases for low threshold settings a threshold configuration of 1100 e^- is considered as a compromise for the operation of diamond modules used in the DBM.

4.2.6 Test-Beam

Several modules have been tested before and after irradiation with charged particles from a test-beam in order to study further sensor properties as the charge collection and the efficiency within the pixel region or at the edge of the sensor. Measurements with FE-I3 modules oriented towards the general sensor characterization for future sensor applications. Modules using the FE-I4 read-out chip with planar n-in-n and 3D sensors focus on the module characterization for the IBL performance review and performance studies for the IBL.

FE-I3 test beam results
Measurements of the planar FE-I3 modules have been performed up to $1 \cdot 10^{16}\,n_{eq}\,cm^{-2}$ and $2 \cdot 10^{16}\,n_{eq}\,cm^{-2}$ for the planar n-in-p and n-in-n sensor designs respectively. Bias voltage scans on irradiated sensors show a linear charge increase which flattens out for high fluences. While the bias range for measurements on the n-in-p design reached up to 1000 V, this limit was pushed to 1500 V during the measurement of the $2 \cdot 10^{16}\,n_{eq}\,cm^{-2}$ irradiated modules. For both sensor designs a decreased efficiency has been observed within the pixel region at the position of the punch-through dot which is not connected to the pixel implant. Overall a hit efficiency in the planar n-in-n design of 98.8 % and 95.4 % has been determined for fluences of $5 \cdot 10^{15}\,n_{eq}\,cm^{-2}$ and $1 \cdot 10^{16}\,n_{eq}\,cm^{-2}$ with perpendicular incident angle. The hit efficiency of 98.6 % and 97.2 % obtained with planar n-in-p modules confirms a similar efficiency behavior for both sensor technologies after irradiation [112, 98]. Both sensor designs showed based on the obtained results that they are possible candidates for the implementa-

tion in future sensor applications of the ATLAS Experiment and other HEP experiments.

Test-beam measurements on the DDTC 3D modules from FBK fitting the FE-I3 read-out chip were performed up to fluences of 10^{15} n_{eq} cm^{-2}. Additional measurements have been performed in an electric field of 1.6 T to simulate the conditions created by the solenoid field in the ATLAS Inner Detector. Efficiency studies on modules before irradiation showed regions of inefficiency at the position of the ohmic and the read-out columns. This effect is related to the perpendicular incident angle of the particle. Further studies showed that these inefficient regions disappear for small variations of the incident angle in the order of 5° and 10°. Tests on proton and neutron irradiated 3E400 3D modules have been performed at a perpendicular incident angle and at 15°. As expected is the shape of the columns visible for measurements with perpendicular incident angle. After tilting the sensor the shape of the column is less dominant as the particles only partially penetrate the inactive column region. This result also corresponds to an efficiency change from 97.6 % to 98.1 % for the neutron irradiated modules and 99.0 % to 99.9 % for the proton irradiated module [123, 124]. The reduced charge collection observed after irradiation is related to the partial column overlap in the sensor design. This effect promotes the implementation of a higher column overlap in future 3D sensor designs as it is used in the 'full 3D' and 'partial through' design proposed for the IBL modules.

FE-I4 test beam results

The planar n-in-p pixel sensor from HPK were irradiated up to $2 \cdot 10^{15}$ n_{eq} cm^{-2} to determine the performance of the implemented bias and pixel isolation structures. Efficiency studies after irradiation concentrating on the center region of the pixel showed an efficiency of about 99 %. Considering the entire pixel region the efficiency decreased to 95.6 % for the design using the poly silicon bias resist with a common p-stop and 94.2 % for the design connected to the punch-through dot and the individual p-stop. While inefficient regions of the first design are mainly at the corners close to the bias grid are the inefficient regions of the later design in all corners visible. As the design using the individual p-stop shows inefficient regions in all corners this effect indicates a relation to the applied isolation technique. The further extension of the punch-through dot compared to the bias resist leads in addition to a wider inefficient region at the edge close to the bias grid [92, 91]. Nevertheless to the low efficiency regions show the sensors an overall good efficiency. The tests of different isolation and bias techniques is leading to an advanced pixel sensor design suitable for applications in future experiments.

Planar and 3D silicon sensor technologies for the IBL have been characterized during test-beam measurements performed at CERN and DESY. In total 17 test-beam periods dedicated to either one of the sensor technologies or to the IBL module characterization took place between 2011 and 2012. The test-beam runs used for the sensor characterization in this work are summarized in Tab. A.2. The modules were mainly irradiated up to a fluence of

$5 \cdot 10^{15}\,n_{eq}\,cm^{-2}$ as this is the maximum fluence defined for the IBL sensor qualification. The charge measurements performed during the test-beam use only the ToT-values and not the converted charge as the ToT-to-charge calibration data is not available for most of the measurements.

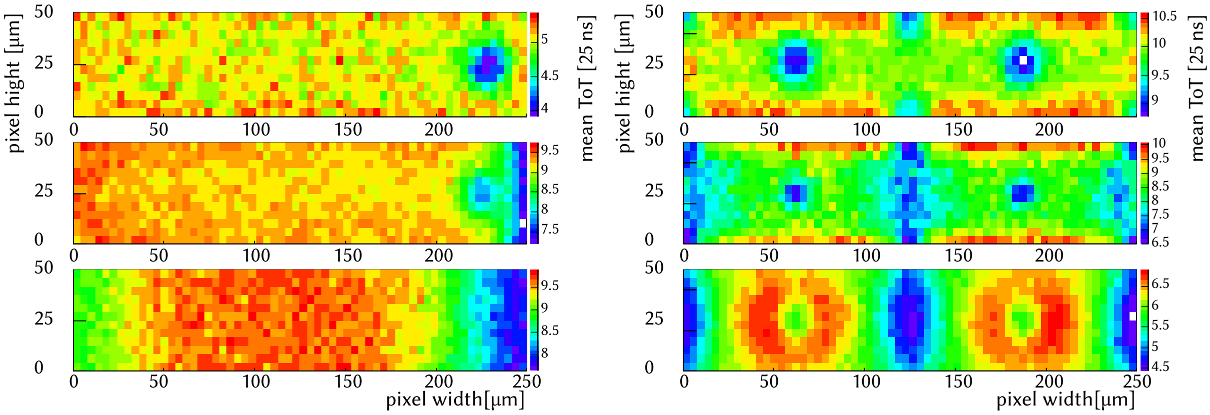

(a) planar sensors

(b) 3D sensors

Figure 4.34: Charge collection properties within a single pixel for planar and 3D sensors. The planar results in Fig. 4.34(a) show an unirradiated module (top) at a perpendicular incident angle and two $5 \cdot 10^{15}\,n_{eq}\,cm^{-2}$ irradiated modules. The neutron irradiated (JSI) module (center) is also at a perpendicular incident angle while the proton irradiated (CERN PS) module (bottom) is set to an incident angle of 15°. The 3D modules in Fig. 4.34(b) are all set to a perpendicular incident angle. The FBK module (top) and the CNM module (center) are unirradiated while the CNM module (bottom) is neutron irradiated (JSI) to a fluence of $5 \cdot 10^{15}\,n_{eq}\,cm^{-2}$.

The accuracy of about 4 µm provided by the telescope makes it possible to reconstruct the path of a particle through the sensor. With this information a characterization within the pixel cell can be used to identify regions with varying charge collection properties. The results in Fig. 4.34 show examples of these variations for planar and 3D modules. The planar results in Fig. 4.34(a) show an unirradiated (top) as well as a neutron (JSI) (center) and a proton (CERN PS) (bottom) irradiated module. For the unirradiated module a bias voltage of 100 V was used while both irradiated modules were operated at 1000 V. The unirradiated module as well as the neutron irradiated module show the position of the punch-through dot on the right side of the pixel. The proton irradiated module is oriented with an angle of 15° to the beam corresponding to the inclination of the modules in the IBL. This inclination distorts the shape of the punch-through dot to a region with reduced charge collection at the short pixel edge. While the charge collection of the proton irradiated sample is bigger on the inside of the pixel cell an increased charge collection is observed at the border of the neutron irradiated sample. This effect is also explained by the variation of the incident angle for the measurements. In case of the unirradiated 3D modules in Fig. 4.34(b) the region with higher charge collection can be found between the p-doped columns at the pixel edge.

Comparing the FBK module (top) with the CNM module (center) reveals a strong variation of the charge collection within the pixel cell of the CNM module. For the neutron irradiated CNM module (bottom) operated at a bias voltage of 160 V is the increased charge collection region shifted to form a circular structure around the read-out columns. Due to the different module configurations used during the measurements it is not possible to compare the results obtained for different modules. Nevertheless exceeds the collected charge in the pixel region even after irradiation for all modules the threshold settings by several ToT.

The spatial resolution of FE-I4 sensors is expected to be at about 72 µm for the long and 14 µm for the short pixel direction assuming that the spatial resolution corresponds to about $1/\sqrt{12}$ of the pitch [40]. The residual analysis for planar and 3D sensors shown in Fig. 4.35 and Fig. 4.36 confirms this assumption. It also shows that the resolution does not significantly decrease after irradiation to a fluence of $5 \cdot 10^{15}\,n_{eq}\,cm^{-2}$. In case of the planar sensors the residual distribution of the unirradiated and the neutron irradiated module corresponds to

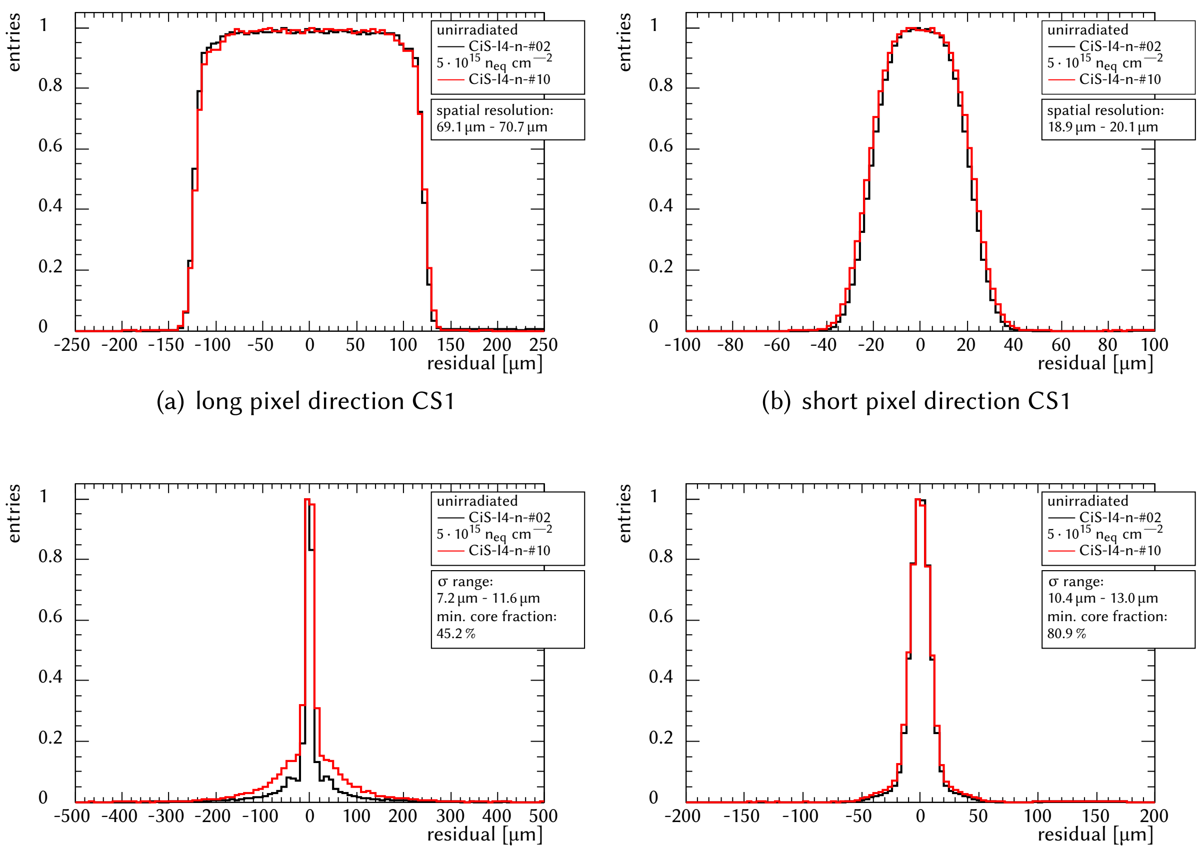

(a) long pixel direction CS1

(b) short pixel direction CS1

(c) long pixel direction CS2

(d) short pixel direction CS2

Figure 4.35: Residual of planar pixel sensor modules. While the two figures in the top row show the residuals for single hit clusters in the short and long pixel direction show the two figures in the bottom row the results for double hit clusters.

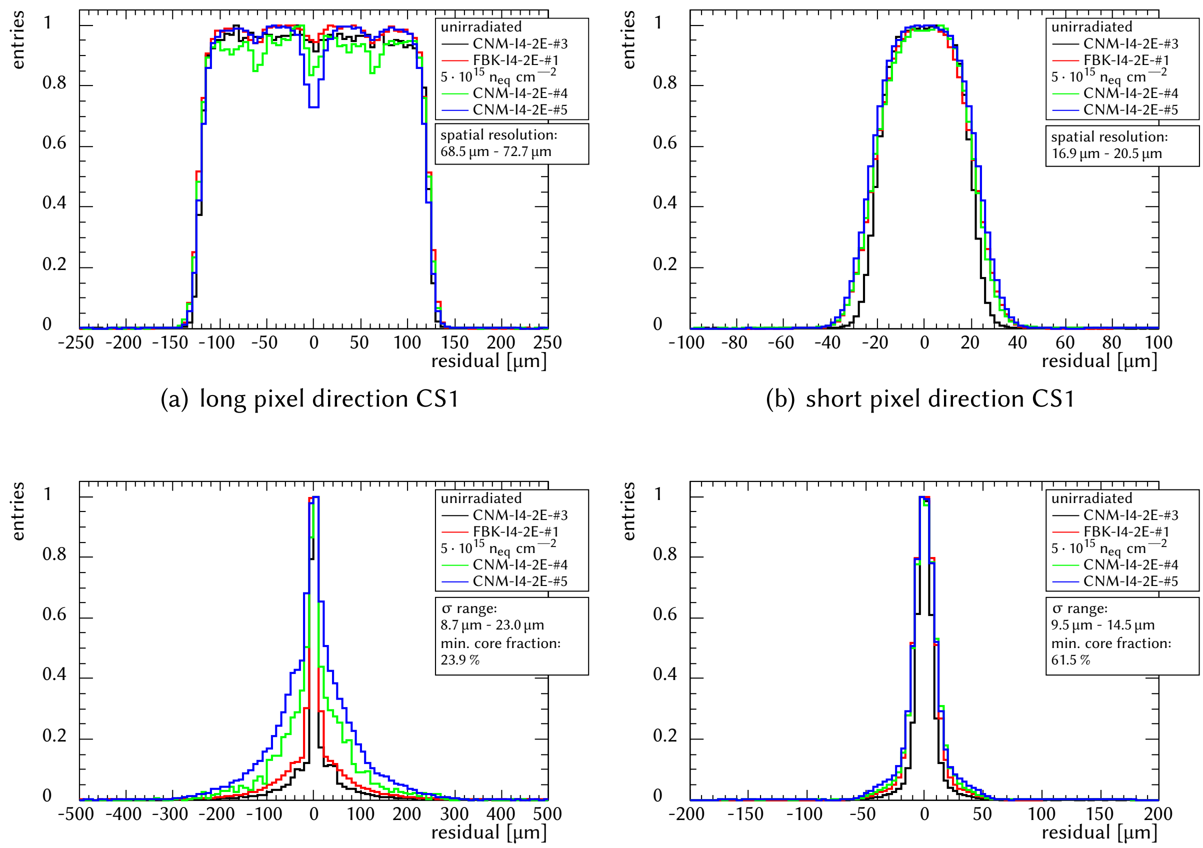

(a) long pixel direction CS1 (b) short pixel direction CS1

(c) long pixel direction CS2 (d) short pixel direction CS2

Figure 4.36: Residual of 3D pixel sensor modules. While the two figures in the top row show the residuals for single hit clusters in the short and long pixel direction show the two figures in the bottom row the results for double hit clusters.

each other. Only a decrease of the core fraction in Fig. 4.35(c) indicates a reduced amount of well reconstructed hits along the long pixel direction. Nevertheless does this behavior not affect the residual. Similar residual distributions are shown for 3D sensor modules in Fig. 4.36 comparing unirradiated modules with neutron (JSI) and proton (KIT) irradiated modules. Noticeable is a reduction of the distribution within the pixel region after irradiation corresponding to the columns position in the pixel. Similar to the planar results is a decrease of the core fraction in Fig. 4.36(c) visible. In case of the neutron irradiated module this effect becomes so strong that the resolution decreases up to 23.0 μm. The proton irradiated module however does not show a significant residual increase compared to the unirradiated modules.

The edge efficiency analysis of planar pixel sensors in Fig. 4.37 focuses on the characterization of the slim edge design proposed for the planar sensor design used in the IBL upgrade. For the 3D sensor designs implementing the guard fence technique the analysis is focusing on the spread of the electric field at the sensor edge.

The results in Fig. 4.37(a) show the efficiency increase at the edge of an irradiated planar silicon sensor for different bias voltages. For a bias voltage of 400 V the edge efficiency of the 500 µm long edge pixel stays below 40 %. Increasing the bias voltage up to 800 V shows a flatter efficiency profile with a small slope towards the pixel edge. At a bias voltage of 1000 V the slope flattens out and the edge efficiency spreads over the entire edge pixel. As the obtained results correspond to a 250 µm thick sensor a further efficiency increase is expected for 200 µm thick sensors which are used for the IBL upgrade. The results also show that the slim edge design is a viable option to reduce the inactive edge of a planar silicon n-in-n sensor. In the case of the planar IBL sensor design this increases the active sensor area by 250 µm on both sides. In total this reduces the inactive sensor edge to about 200 µm consisting of 90 µm safety margin and about 110 µm of guard ring structure which is not overlapping with the pixel structure.

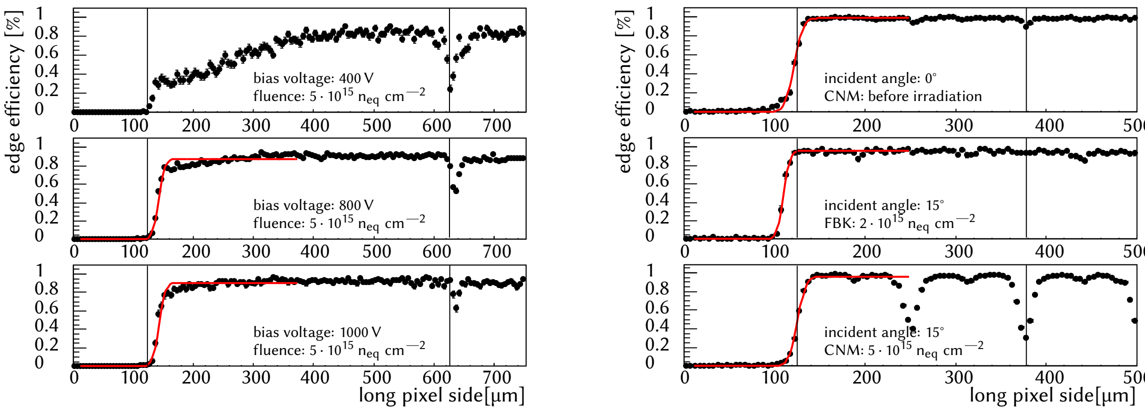

(a) planar sensors (b) 3D sensors

Figure 4.37: Edge efficiency profile of planar and 3D silicon sensors. The evolution of the edge efficiency with bias voltage is given in Fig. 4.37(a) for a neutron irradiated planar n-in-n sensor at an incident angle of 15°. In case of the 3D sensors in Fig. 4.37(b) results are shown for both sensor designs at different fluences and incident angles.

For 3D sensors the edge efficiency in Fig. 4.37(b) spreads up to the pixel edge defined by the p-doped edge columns. The guard fence structure surrounding the sensor suppresses the formation of an electric field which is necessary to avoid short circuits with the sensor edge but also prevents charge collection outside the pixel matrix. The unirradiated CNM module as well as the $2 \cdot 10^{15}$ n_{eq} cm^{-2} proton irradiated FBK module in Fig. 4.37(b) (top) and (center) show uniform efficiency up to the pixel edge. This behavior is also visible for the $5 \cdot 10^{15}$ n_{eq} cm^{-2} neutron irradiated CNM module Fig. 4.37(b) (bottom) with the difference that a reduced efficiency is observed around the ohmic-columns. Looking at the pixel efficiency studies of 3D sensors in Fig. 4.39 shows that this behavior might be intensified by the incident angle. The edge design of the 3D sensors for the IBL upgrade implements an area of about 200 µm to fabricate the guard-fence structure which as the edge efficiency measurements show also corresponds to the inactive sensor area.

The efficiency analysis of IBL modules is used to determine the hit efficiency of a sensor focusing especially on the performance after irradiation to a fluence of $5 \cdot 10^{15}\ n_{eq}\ cm^{-2}$. To calculate the hit efficiency only tracks are considered which penetrated the active sensor area. This information is provided by the reconstruction data of the beam telescope. The telescope resolution of about 4 µm makes it possible to determine the efficiency inside of a pixel cell and to identify areas with reduced efficiency.

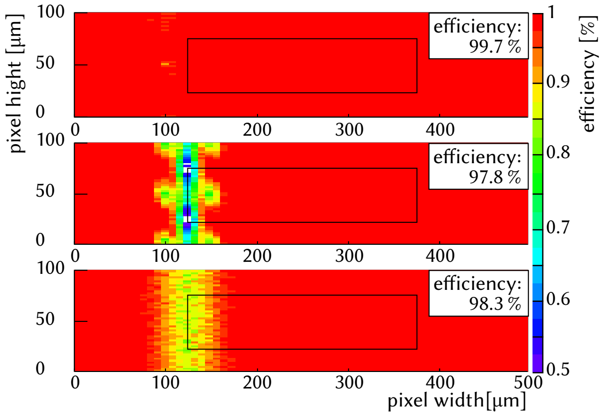

Figure 4.38: Pixel efficiency map of planar n-in-n silicon sensors. The unirradiated planar sensor (top) and the $5 \cdot 10^{15}\ n_{eq}\ cm^{-2}$ neutron (center) (JSI) sample were both tested at a perpendicular incident angle. The $5 \cdot 10^{15}\ n_{eq}\ cm^{-2}$ proton (bottom) (CERN PS) irradiated sample was tested at an incident angle of 15°. For both irradiated samples the bias grid region is clearly visible.

Measurements on planar pixel sensors in Fig. 4.38 show a hit efficiency for an unirradiated module of about 99.7 %. Despite of the lower charge collection at the punch-through dot observed in Fig. 4.34(a) (top) stays the efficiency uniform in the entire pixel area. After irradiation to a fluence of $5 \cdot 10^{15}\ n_{eq}\ cm^{-2}$ a reduced efficiency is observed at the punch-through dots and the bias grid. The neutron irradiated module which was tested at a perpendicular incident angle shows a hit efficiency of 97.8 %. The proton irradiated module on the other hand shows a slightly higher hit efficiency of 98.3 %. This is related to the incident angle of 15° resulting in a longer track thus higher charge deposition in the sensor. Both irradiated samples were operated at a bias voltage of 1000 V. The shape of the punch-through dots as well as the bias grid which are clearly visible in the perpendicular case wash out after changing the incident angle. The obtained efficiency results show that the planar pixel sensor design performs according to the IBL specifications. Additional measurements performed on irradiated modules show that similar results can be already obtained at an operation voltage of about 800 V [77]. The reduced efficiency around the punch-through dots and the bias grid already observed with planar FE-I3 modules led to different proposals for a re-routing of the bias grid which could represent a possibility to increase the overall hit efficiency of the sensor [112].

Efficiency measurements of an unirradiated FBK module at perpendicular incident angle in Fig. 4.39(a) show a hit efficiency of 98.7 %. The column structure of both column types which penetrate in this design the entire sensor thickness are visible as regions of reduced efficiency. Additional measurements performed with the same module at a 15° incident angle show an increased hit efficiency of 99.9 %. The two proton irradiated samples are both operated at a 15° incident angle. The $2 \cdot 10^{15}\,n_{eq}\,cm^{-2}$ irradiated module shows an efficiency of 98.4 % while the $5 \cdot 10^{15}\,n_{eq}\,cm^{-2}$ irradiated module shows an efficiency of 94.5 %. Due to the angled incident changes the observed column patter from before irradiation to a strip pattern whereof the read-out columns dominate the regions of reduced efficiency.

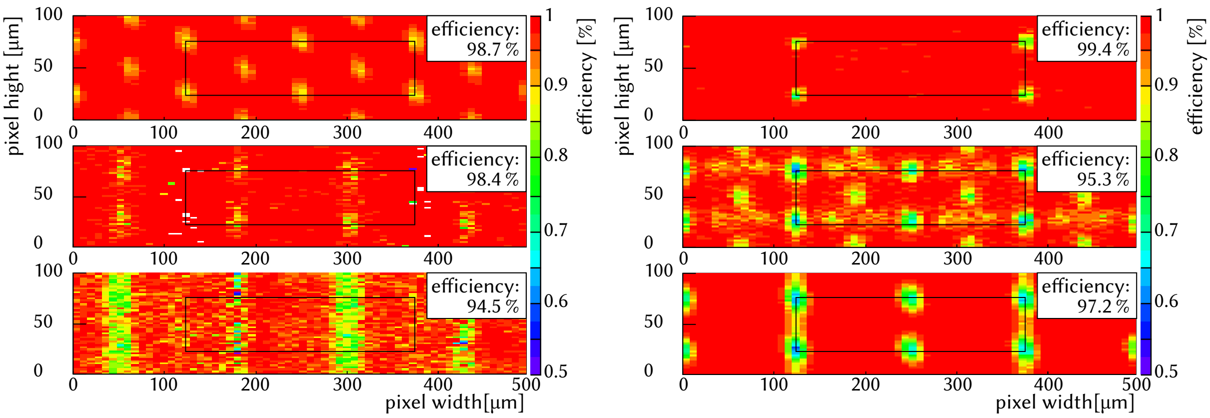

(a) FBK design (b) CNM design

Figure 4.39: Pixel efficiency map of 3D silicon sensors using the FBK and CNM design. The FBK design in Fig. 4.39(a) shows the results of an unirradiated module (top) at perpendicular incident angle and proton irradiated (KIT) modules at a fluence of $2 \cdot 10^{15}\,n_{eq}\,cm^{-2}$ (center) and $5 \cdot 10^{15}\,n_{eq}\,cm^{-2}$ (bottom) at an incident angle of 15°. The CNM design in Fig. 4.39(b) shows an unirradiated module (top) as well as a proton (center) (KIT) and a neutron (bottom) (JSI) irradiated module at a fluence of $5 \cdot 10^{15}\,n_{eq}\,cm^{-2}$ all at a perpendicular incident angle.

The efficiency measurements of the CNM design in Fig. 4.39(b) were performed with an unirradiated module as well as a proton and a neutron irradiated module at a fluence of $5 \cdot 10^{15}\,n_{eq}\,cm^{-2}$. The pixel efficiency maps in all cases show the column structure in the pixel cell which is related to the perpendicular incident angle. In case of the unirradiated module only the ohmic columns at the pixel corners are visible which is related to the reduced charge collection in the sensor region without column overlap. In case of the corner columns the increased charge sharing with the surrounding pixel reduces the hit efficiency. Despite the regions of reduced efficiency reaches the module a hit efficiency of 99.4 %. For the proton and neutron irradiated sample the hit efficiency is reduced to 95.3 % and 97.2 % respectively. The pixel efficiency maps of the irradiated modules show the impact of the irradiation type on the sensor. The proton irradiated module shows reduced efficiency at the position of both column types but also at the pixel edge which is also related to charge sharing. The neutron irradiated module on the other hand shows only the shape of the ohmic columns surrounding the pixel region. This effect is related to the formation of the electric

field which starts to form at the pn-junction at the read-out columns in the pixel region. In addition is the influence of the weighting field around the ohmic columns reduced which results in a reduced efficiency around these columns.
The efficiency results obtained for 3D modules show that both designs can be operated with a sufficient high hit efficiency at a bias voltage of 160 V after reaching a fluence of $5 \cdot 10^{15}\ n_{eq}\ cm^{-2}$.

Test-beam measurement impact on operation and performance
Test-beam measurement and operation conditions of planar and 3D silicon sensor technologies to be used in the IBL are summarized in Tab. 4.2. Concerning the charge collection for both sensor technologies a charge exceeding the threshold by several ToT-values was determined before and after irradiation. For the operation a bias voltage of 160 V was necessary for irradiated 3D sensors while irradiated planar modules need to be biased above 800 V. Despite the sufficient results show both technologies design areas of reduced charge collection enhanced by radiation damage.

	planar sensor		3D sensor	
	before irradiation	after irradiation	before irradiation	after irradiation
bias voltage	$\sim$ 100 V	$>$ 800 V	$\sim$ 20 V	$\sim$ 160 V
spatial resolution	18.9 µm	20.1 µm	16.9 µm - 19.8 µm	20.3 µm - 20.5 µm
inactive sensor edge	$\sim$ 200 µm	$\sim$ 200 µm	$\sim$ 200 µm	$\sim$ 200 µm
pixel efficiency	$\sim$ 99.7 %	97.8 % - 98.3 %	$>$ 98.7 %	94.5 % - 97.2 %

Table 4.2: Test-beam measurement results and operation conditions of planar and 3D silicon sensor technologies before and after irradiation to a fluence of $5 \cdot 10^{15}\ n_{eq}\ cm^{-2}$.

Comparing the spacial resolution of both sensor technologies does not show a significant variation. Also comparing the results before and after irradiation shows only an increase within the telescope accuracy. Due to the slim edge design used in the planar sensor design the inactive sensor edge was reduced to a width of about 200 µm corresponding to the inactive sensor edge of the 3D sensor design. While both unirradiated designs show a hit efficiency close to 100 % decreases the efficiency after irradiation. The considered measurements show an efficiency dependence to the fluence, the bias voltage, the incident angle and the module setting. For the operation in the experiment it will be therefore important to optimize the settings depending on the positioning of the sensor technology.

5 IBL Module quality assurance

Due to the rescheduling of the long shutdown periods of the LHC the originally foreseen installation date of the IBL at the end of 2015 was moved forward to 2013/2014. As a result of this schedule change the original plan considered in the IBL technical design report needed to be adjusted [29].
Especially the choice of the applied sensor technology was sped up in order to start the sensor fabrication in time. As a result of the acceleration only two of the originally considered sensor technologies were taken into account for a pre-production launched at the beginning of 2011. The planar n-in-n and the 3D slim edge design described in Sec. 3.3.1 and Sec. 3.3.2 were the technologies chosen to be fabricated in this pre-production. Qualification tests of these modules discussed in Chap. 4 were performed in the laboratory and with test-beams at CERN and DESY. An advantage of this procedure was the availability of 30 % to 50 % of the sensors necessary for the production of the IBL by the time of the sensor review. Based on the obtained results the sensor review committee recommended in July 2011 a mixed sensor scenario with 75 % or twelve planar Double Chip Modules (DCMs) in the center and 12.5 % or four 3D Single Chip Modules (SCMs) on each end of the stave [33].
A further proposal introduced with the schedule change of the IBL project was the DBM consisting of 24 CVD diamond modules as discussed in Sec. 3.3.3. The arrangement of four diamond pixel telescopes on each side of the experiment each consisting of three diamond modules are introduced as supplement to the existing ATLAS BCM. It is foreseen that the DBM will be used as spacial segmented bunch by bunch luminosity monitor [33, 125].

The following chapter summarizes the achievements reached between the rescheduling of the IBL project and the end of 2012. Special focus is directed on the Quality Assurance (QA) and Quality Control (QC) to assure proper functioning of each individual component and later the entire detector.
At first the production flow of the different parts is described to ease the understanding of the different process steps. This includes the assembling and testing of the modules as well as the preparation of the stave and the electronics. A first prototype stave equipped with FE-I4A modules was available in the middle of 2012 to be tested in a dedicated QA test bench at CERN. Statistics based on the results obtained during the production of the so-called stave-0A are summarized to give an overview of the yield at the beginning of the production. Measurements performed during the testing of the stave-0A are shown to introduce the testing procedure during the production of the IBL staves.

5.1 IBL stave production flow

The production of an IBL stave consists of several steps which are carried out by different groups to share the workload and profit from the localized knowledge of each group. The module fabrication and testing as well as the stave flex preparation and testing are the two main components necessary for the assembling of the stave. The preparation of both components is thus the first step in the production flow prior to the module loading. All production steps are followed by regular tests to determine production variations.

5.1.1 IBL module fabrication

The front-end chip, the sensor and the module flex are the three main components for the IBL module fabrication. The flow diagram in Fig. 5.1 shows the different steps of the three components before the assembly and testing of the flex module.

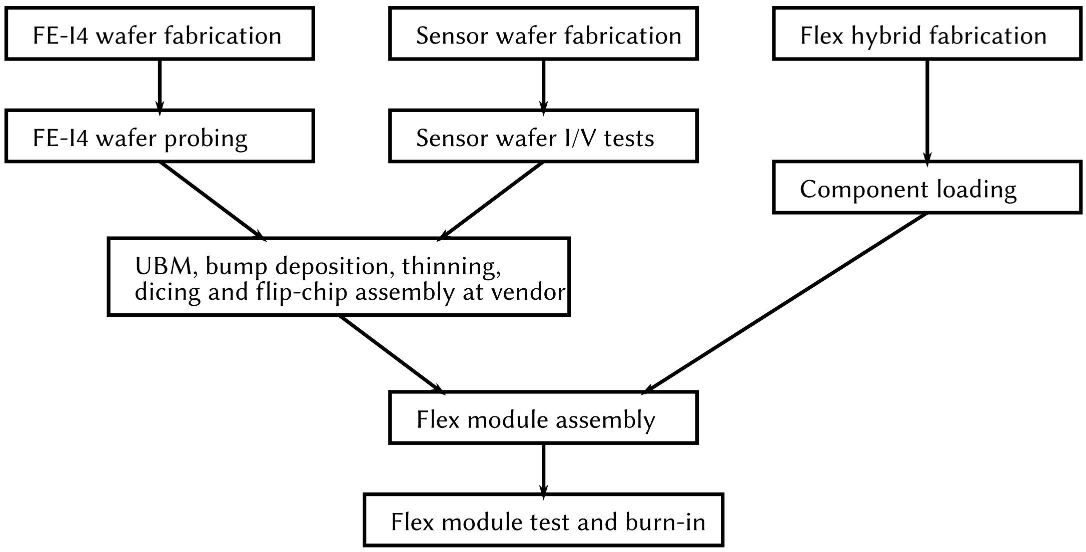

Figure 5.1: Flow diagram of IBL module production [33]

After the production of the front-end wafers all FE-I4 wafers have to pass through a wafer probing to test the basic properties of the chips. As a result the chips are categorized in three groups. Chips with full functionality are assigned to the green group while non functioning chips are moved to the red group. Chips with minor problems such as damaged double columns are marked as yellow which means that they are not suitable for the IBL production but could still be used for general sensor testing. After the probing the wafers are polished and glued to support wafers to avoid bending during the bump-bonding procedure.
In parallel the QC of both sensor technologies was performed by the appropriate institutes. These characterizations included a visual and mechanical inspection to identify scratches and unusual wafer bowing. Electrical tests as leakage current measurements were performed to determine if the sensors can be operated at the foreseen operation voltage. Based on these

measurements and the specification for the corresponding technologies a selection of sensors suitable for the production of IBL modules was made [126, 107].
Following the preliminary testing of the front-end chips and the sensor tiles the two parts are bump-bonded using the solder bump-bond technology to form bare modules. In case of the planar sensors two front-end chips are bump-bonded to one Double Chip Sensor (DCS) to form a bare DCM. For bare 3D SCMs only one front-end chip is bump-bonded to one Single Chip Sensor (SCS). The bump-bonding process it self follows the description of the solder bump-bond technology in Sec. 3.1 illustrating the formation of a front-end - sensor interconnection. Before the shipment to the module production sites in Bonn and Genova the remaining glass element of the support wafers on the front-end chip needs to be removed [29]. As IZM does not provide this process step the modules are send to an external company for the removal of this glass support.
At the production sites the bare modules are then assembled with the flex hybrid to form flex modules. The loading of the flex hybrid with its electrical components is done before this production step. The prepared flex modules are then ready for testing and the burn-in step. A configuration file is provided for each of the flex modules which are shipped to Geneva to perform the stave loading.
To assure the proper functioning on the stave all flex modules follow a module reception test. The provided configuration files are used to test the modules and to compare the results obtained at the production site. The reception tests include digital and analog tests of the front-end chip as well as a tuning. Noise and threshold properties are extracted from scans with and without applied bias voltage to check for disconnected bump-bonds. Part of the tuning procedure is a scan to verify the feedback current calibration and the pixel cross-talk. A leakage current scan is performed to verify the operation voltage and the leakage current specifications of the bump-bonded sensor. To test the resistivity against thermo-mechanical stress each module passes through a thermal cycling test consisting of ten cycles between $-40\,^{\circ}$C and $40\,^{\circ}$C. The earlier tests are repeated after the thermal cycling to identify samples which show damage due to the introduced stress. A source scan with an Am-241 photon source is performed with each module to confirm the operation of the module with a real charge signal [35, 127].

5.1.2 Stave loading and testing

The stave loading process is the final assembly step thus important for the fabrication of a high quality detector system. In order to reach a maximum number of working pixels per stave all parts are tested extensively before they are used for the stave production.
On the stave side the stave flex is tested during the preparation and before gluing to assure proper powering and communication with the sensor modules. In addition to the reception test are a visual inspection and basic electrical tests part of the procedure before the selected modules are attached to the stave. The loading process consists of 16 steps which ends with the transport of the stave to CERN for further testing and QA [35].

A test bench dedicated to the testing of IBL staves is set up at CERN to test the prepared staves. The QA after the production of the stave foresees a similar test program as it is used for the reception test of individual modules. This includes leakage current tests of the sensors and tuning tests of the front-end chips. The test bench also integrates the possibility to perform source tests by automatically moving a source over the complete length of the stave to test the performance of each module to real charge signal. Scintillators on top and on the bottom of the test bench provide the possibility to test the stave with an external trigger system based on cosmic radiation [127, 128].

5.2 Module production overview

The following summarizes the production of the two sensor technologies used for the IBL as well as the effects observed during the module production.

5.2.1 Summary of the Planar sensor production

A total number of 150 wafers was ordered for the IBL upgrade production campaign of planar pixel sensors. As each wafer provides space for four DCSs a total amount of 600 DCSs was fabricated. The sensor design follows the planar slim edge design in Sec. 3.3.1. Knowing that 224 DCSs would be necessary for a 100 % planar solution the production includes enough overhead to assure sufficient supply of planar pixel sensors for both sensor scenarios.
The agreement with the vendor included that all wafers containing more than one working DCS would be accepted as valid wafer. Leakage current and depletion voltage measurements on the wafer level have been performed by the vendor to verify the wafer quality. Leakage

batch	1	2	3	4	5	6	7	8	9	total
wafer	20	22	18	20	17	22	12	11	8	150
total DCS	80	88	72	80	68	88	48	44	32	600
good DCS	68	76	64	70	62	83	47	42	32	544
yield	85.0 %	86.4 %	88.9 %	87.5 %	91.2 %	94.3 %	97.9 %	95.5 %	100 %	90.7 %

Table 5.1: Production yield for DCSs of the nine batches fabricated in the planar pixel sensor production campaign. Together 544 DCSs have been fabricated with a total yield of 90.7 % [129].

current measurements have been cross-checked in Dortmund to verify the results and to confirm which of the wafers are considered as valid. In total 150 wafers produced during nine production batches were accepted for further processing. The production yield of the nine batches before UBM and dicing summarized in Tab. 5.1 is based on the measurements performed by the vendor and in Dortmund. Overall a total yield of 90.7 % was achieved with the nine batches resulting in 544 DCSs. As each wafer also houses three further SCSs a total of 409 additional SCSs has been fabricated which are available for further research purposes. A full depletion voltage of about 46 V was measured for the first six batches which is lower than the about 67 V measured for the last three batches [129]. Due to the high production yield in the first six batches it was decided that the DCSs with a low full depletion voltage are used for the IBL module production. Thus the 119 wafers from the first six batches were sent to IZM for further processing while the remaining 31 wafers are kept as backup in Dortmund. During shipping to and handling at IZM a total of 39 DCSs broke whereof 32 DCSs came from wafers which broke entirely and 7 DCSs were individual sensors from different wafers. These values correspond to a mechanical yield related to the wafer handling of about 91.8 %. The remaining 437 DCSs were tested after UBM and dicing to assure that the sensors properties still agree with the qualification values. Based on the characterization results before and after processing the sensors were categorized in four groups: 1.) Sensors which performed before and after processing according to the qualification values, 2.) Sensors which never performed according to the qualification values, 3.) Sensors which got worse after processing, 4.) Sensors which got better after processing.

Out of the 437 tested DCSs 366 and 37 were categorized in group 1.) as sufficient and 2.) as insufficient sensors for IBL modules respectively. The remaining 34 DCSs are grouped by 21 in group 3.) with sensors which got worse and 13 in group 4.) with sensors which got better after processing. By taking out the 37 DCSs of group 2.) which were never considered as sufficient sensors a total of 400 DCSs remains which performed at some point according to the IBL specifications. Combining the good sensors from group 1.) and the ones which got better in group 4.) a total of 379 DCSs is available after processing. These results correspond to a yield concerning the electrical properties after UBM and dicing of 94.8 %.

A total of 379 DCSs which perform according to the IBL specifications are available for the module production of planar DCMs for the IBL upgrade.

5.2.2 Summary of the 3D sensor production

For the IBL upgrade 3D sensor production a collection of 121 wafers was processed by the two vendors FBK and CNM. The production at FBK was divided into four batches containing 71 wafers while the production at CNM contained 50 wafers which were divided in three production batches. The wafer design used by both vendors holds eight 3D SCSs per wafer thus corresponding to 968 SCSs. Depending on the vendor the two 3D sensor designs described in Sec. 3.3.2 are fabricated. A total of 112 3D SCSs is necessary for the 25 % solution of the IBL upgrade the performed 3D sensor production provides sufficient overhead to assure the availability of 3D sensors.

Both vendors performed measurements on the wafer level to determine the production quality of the fabricated sensors. To reduce the production cost per SCS it was decided that only wafer with at least three 3D SCSs which perform according to the sensor specification should be selected for further processing. Due to the different designs used by FBK and CNM the leakage current measurements on the wafer level were performed in different ways. A temporary metal connecting all pixel cells in a column is used by FBK to measure the leakage current over the full sensor area. At CNM the leakage current is measured on the guard ring which surrounds each sensor but does not cover the inside of the sensor area. Based on the results provided by FBK and CNM the wafer selection summarized in Tab. 5.2 and Tab. 5.3 has been made respectively.

batch	FBK-A10	FBK-A11	FBK-A12	FBK-A13	total
produced wafers	21	22	17	11	71
SCSs on produced wafers	168	176	136	88	568
good SCSs on produced wafers	71	23	67	23	184
yield on produced wafers	42.3 %	13.1 %	49.3 %	26.1 %	32.4 %
selected wafers	12	4	13	4	33
SCSs on selected wafers	96	32	104	32	264
good SCSs on selected wafers	56	14	63	16	148
yield on selected wafers	58.3 %	43.8 %	60.6 %	50.0 %	56.1 %

Table 5.2: Production yield of 3D SCSs of the four FBK production batches fabricated during the 3D pixel sensor production campaign. A total of 148 SCSs has been produced on 33 selected wafers out of 71 produced wafers with a production yield on the selected wafers of 56.1 %

In the case of FBK 33 wafers have been selected to be used as IBL wafers corresponding to 264 SCSs in total. The 148 SCSs which perform according to the sensor specification represent a production yield of 56.1 % of the selected wafers. For test purposes three wafers of the production batch FBK-A10 were sent with the selected wafers to IZM. The three wafers contained one, two and three SCSs performing according to the sensor specification. All three wafers are not considered in the statistics of selected IBL wafers even though one contains three good SCSs. The overall production yield of the four FBK production batches considering all 71 wafers is about 32.4 %. By the end of 2012 a collection of 28 selected wafers fabricated in the three batches FBK-A10, FBK-A11 and FBK-A12 containing 130 SCSs following the IBL specification was sent to IZM for further processing. Damage during the shipment resulted in two broken wafers corresponding to a loss of 13 SCSs. As no further damage took place during UBM and dicing the mechanical yield of the FBK campaign is at 90 % providing 117 3D SCSs for the fabrication of FBK SCMs.

A total of 41 wafers of the CNM production has been selected holding 328 SCSs. The yield of the selected wafers is 71.3 % which corresponds to 234 SCSs. Taking all wafers into account an overall production yield of 61.3 % has been obtained.
In total 29 selected wafers fabricated in batch CNM-1 and CNM-2 as well as one wafer with only two good SCSs tiles from CNM-1 were sent for further processing to IZM. Together the wafers contained 152 3D SCSs which performed according to the IBL specifications. Damage during the transport caused one wafer holding 6 SCSs to break. Additional two wafers

batch	CNM-1	CNM-2	CNM-3	total
produced wafers	18	17	15	50
SCSs on produced wafers	144	136	120	400
good SCSs on produced wafers	86	85	74	245
yield on produced wafers	59.7 %	62.5 %	61.7 %	61.3 %
selected wafers	16	13	12	41
SCSs on selected wafers	128	104	96	328
good SCSs on selected wafers	84	81	69	234
yield on selected wafers	65.6 %	77.9 %	71.9 %	71.3 %

Table 5.3: Production yield of 3D SCSs of the three batches fabricated at CNM of the 3D pixel sensor production campaign. A total of 234 SCSs has been produced on 41 selected wafers out of 50 produced wafers with a yield on the selected wafers of 71.3 %

holding 9 SCSs and 4 individual SCSs broke during processing. Due to the damage during transport and handling a mechanical yield of 87.5 % has been obtained. The remaining 133 3D SCSs are available for the module fabrication process.
As no additional test have been performed after UBM and dicing it is not possible to determine if sensor tiles show electrical damaged caused by the processing. Overall 53 3D wafers have been processed and provided 250 3D SCSs which is more than twice the amount of 3D sensors necessary for the 25 % option of the IBL production.

5.2.3 Module production and reception test

To test the work flow during module and stave production the first sensor modules to be mounted on the stave-0A were build with FE-I4A read-out chips. Modules for the production of the later stave-0B and the staves for the IBL itself use the FE-I4B read-out chip.
In total 14 planar DCMs and nine 3D SCM with FE-I4A read-out chips were tested during the module reception test for the stave-0A. As the thermal cycling process of four planar modules and three 3D modules was already done in Genoa these seven modules could not be tested before the process. The remaining modules were first tested at the University of Geneva and then at CERN where the thermal cycling process was performed. After the process the samples were measured again at CERN before they went back to the University of Geneva for the final tests and stave loading.
Based on the reception tests eight planar modules were classified as green modules while four and two modules were rated as yellow and red respectively. In case of the 3D modules seven modules were classified as green modules while the remaining two modules was rated as yellow and red.
Leakage current results for the modules used to populate stave-0A are shown in Fig. 5.2 separately for the two sensor technologies. The measurements where performed with unbiased front-end chip to avoid additional heating of the sensor. Due to the different sensor size for

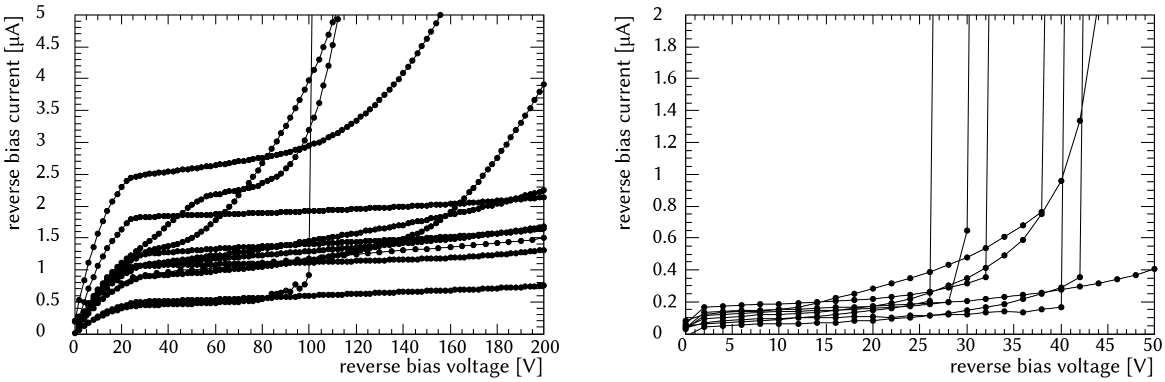

(a) Selected planar modules (b) Selected 3D modules

Figure 5.2: Leakage current measurements for the selected modules used for the population of stave-0A performed during the module reception test at the University of Geneva. Most of the planar modules in Fig. 5.2(a) show a breakdown higher than 100 V with a leakage current below 2 µA. Higher leakage current and lower breakdown voltages are observed in three of the planar modules. The breakdown voltage of most 3D modules in Fig. 5.2(b) varies between 25 V and 45 V with a leakage current below 1 µA.

the two technologies it is not possible to directly compare the leakage current performance. Most of the planar modules in Fig. 5.2(a) perform within the range specified for the sensor qualification of planar sensors on wafer level. The leakage current at an operation voltage of 60 V is for nine modules below 2 µA. While one of these modules shows a hard breakdown at about 100 V the breakdown voltage of the remaining modules exceeds in most cases 200 V. A higher leakage current and earlier breakdown can be observed in three of the modules. Nevertheless they were considered suitable for the fabrication of stave-0A as biasing to values above the operation voltage was still possible.
All the selected 3D modules in Fig. 5.2(b) show a leakage current below 1 µA up to the breakdown voltage varying between 25 V and 45 V. In one of the tested 3D modules the breakdown voltages exceeded 50 V. With an operation voltage below 25 V used for 3D modules all selected modules can be operated according to the specified range.

Threshold and noise measurements for the selected modules are summarized in Fig. 5.3 based on the later position on stave-0A. Measurements of the threshold in Fig. 5.3(a) show a constant threshold varying between 3000 e^- and 3200 e^-. The configuration files delivered from the production site were tuned to a threshold of 3000 e^- with a feedback current gain of 5 ToT for 20 ke^-. The increased threshold values for the two modules used at position A2 and C6 on stave-0A are related to the applied configuration file. The module at position A2 shows a shift of the individual pixel threshold DAC values to the maximum which is related to the global threshold DAC setting. As a result only a smaller range of the individual pixel threshold DAC can be used to tune the threshold of the module thus a higher deviation can be observed in

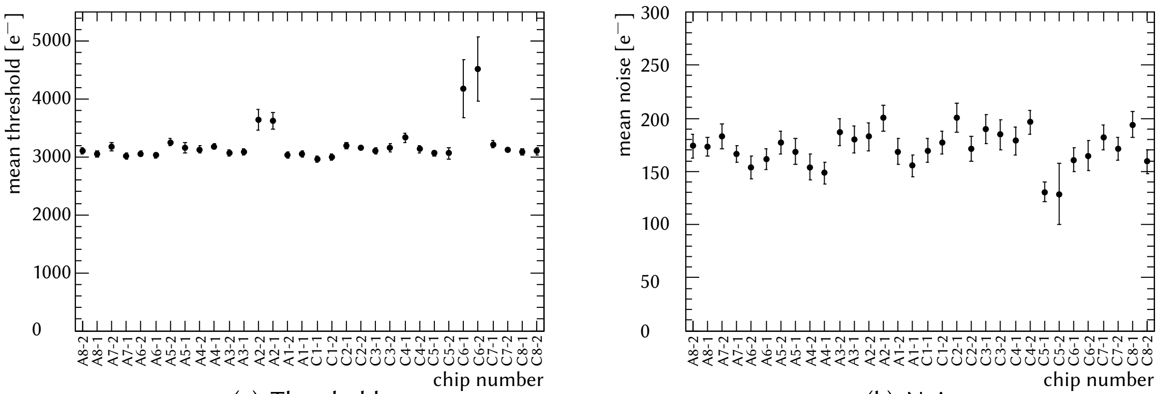

(a) Threshold (b) Noise

Figure 5.3: Threshold and noise measurements for the selected modules used for the population of stave-0A performed during the module reception test at the University of Geneva. The results are given in regards of the later position on stave-0A. Threshold results in Fig. 5.3(a) show a constant threshold for most modules varying between 3000 e^- and 3200 e^-. The noise distribution in Fig. 5.3(b) shows a noise variation for most modules between 150 e^- and 200 e^-.

the threshold. Pixel with a threshold offset exceeding this range can not be tuned to the target threshold which shifts the module threshold to higher values. This behavior can be fixed by retuning the modules which was not the purpose of the module reception test. In case of the module at position C6 the configuration did not contain tuning values which means that the module shows the wide threshold distribution of an untuned module. The results of the noise measurements in Fig. 5.3(b) show a noise distribution varying between 150 e^- and 200 e^-. The lower noise observed for the module at position C5 is related to communication problems, which classified this module as yellow. The noise offset of about 50 e^- compared to the measurements discussed in Sec. 4.1.1 is related to the different feedback current gain used for the tuning. These results are also in agreement with measurements performed on a bare front-end chip showing the same noise behavior [77].
Other reasons to classify a module as yellow are pixel with increased noise and merged or disconnected bump-bonds. The summary of the modules shown in Tab. 5.4 indicates the module position, label and sensor type also the classification made during the module reception test. The A-side of stave-0A holds only modules classified as green while there are four yellow planar DCMs and one yellow 3D SCM on the C-side of the stave.

5.3 Stave-0A testing

After module loading of the selected modules on stave-0A the stave was sent to CERN SR1 to be tested in the dedicated test setup for QA of the IBL staves. These tests included electrical tests to assure the communication with the modules but also module tests to assure the

chip	module number	sensor type	class	chip	module number	sensor type	class
A8-2	17-01-43	3D	green	C1-1	66-10-02	planar	yellow
A8-1	03-04-41	3D	green	C1-2		planar	
A7-2	13-03-37	3D	green	C2-1	66-11-02	planar	yellow
A7-1	17-04-28	3D	green	C2-2		planar	
A6-2	65-07-01	planar	green	C3-1	66-12-01	planar	yellow
A6-1		planar		C3-2		planar	
A5-2	66-06-01	planar	green	C4-1	66-12-02	planar	green
A5-1		planar		C4-2		planar	
A4-2	65-05-01	planar	green	C5-1	65-10-02	planar	yellow
A4-1		planar		C5-2		planar	
A3-2	66-03-02	planar	green	C6-1	65-10-01	planar	green
A3-1		planar		C6-2		planar	
A2-2	66-09-01	planar	green	C7-1	13-08-27	3D	green
A2-1		planar		C7-2	03-06-40	3D	green
A1-2	65-08-02	planar	green	C8-1	03-08-35	3D	green
A1-1		planar		C8-2	17-02-18	3D	yellow

Table 5.4: Labeling and positioning of the chosen modules for stave-0A. The A-side of the stave holds only modules classified as green while there are four yellow planar DCMs and one 3D SCM on the C-side of the stave.

proper functioning after the assembling process. These module tests included the module characterization consisting of tuning procedures, leakage current measurements and source scans with Am-241 sources. Furthermore the availability of stave-0A was used to improve the test setup and to develop a test procedure going to be used during the production stave testing [127].

The bias voltage circuit design provides only one bias voltage for four front-end chips. In case of the 3D modules the four SCM on each side of the stave are combined as M4A and M4C. For the planar modules always two DCMs are combined as M1, M2 and M3 for the A and C side [127].
Comparing the leakage current measurements of the individual 3D modules in Fig. 5.2(b) or separated for each group in Fig. A.9 confirms that the breakdown voltage of the group is defined by the module showing the lowest breakdown voltage. In case of the planar modules in Fig. 5.2(a) also separated for each group in Fig. A.6, Fig. A.7 and Fig. A.8 this behavior is less obvious. While one of the modules in M1A has a hard breakdown at 100 V it is surprising to see a current increase starting at about 60 V. The behavior of M1C agrees with the expectation as both DCMs showed a higher leakage current and an early breakdown. As the modules used to build M2 and M3 for both sides have their breakdown above 100 V a stable operation up to this voltage is expected. Solely the current increase at about 80 V observed in M2C does not correlate with the measurements performed on the individual modules. A

possible explanation for this unexpected breakdown behavior in M1A and M2C is the loading process of the stave. This behavior needs to be observed on the following staves in order to prevent possible module damage.

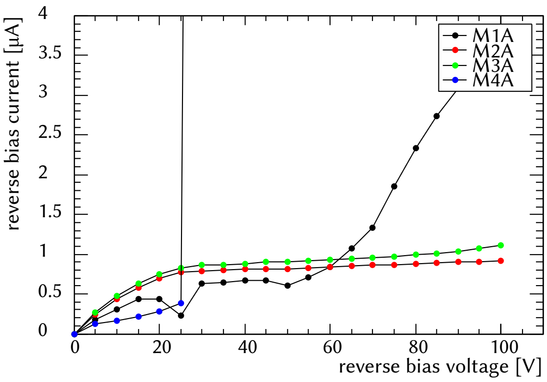

(a) A-side

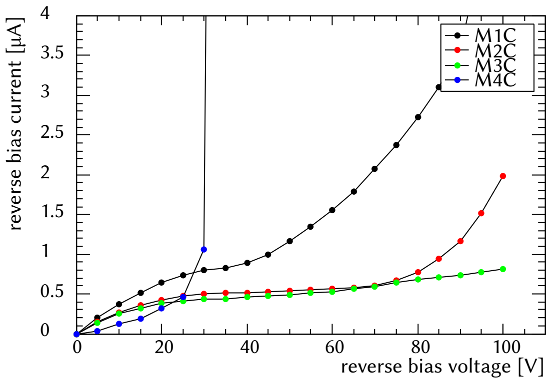

(b) C-side

Figure 5.4: Leakage current measurements of the modules setup on stave-0A. Planar DCMs M2 and M3 on both sides show a late breakdown at 80 V and higher while the two modules M1A and M1C show an earlier current increase. The leakage current of the 3D modules M4A and M4C is below 1 µA up to the breakdown voltage between 25 V and 30 V [127].

During the stave testing several tuning procedures have been performed to better understand the stave behavior depending on the front-end setting. As planar and 3D modules are mounted together on the stave the tuning needs to handle the different bias voltages and eventually consider sensor specific properties.

Measurements for different front-end settings shown in Fig. 5.5 show the overall threshold and noise performance of stave-0A. The tuning results for threshold values of 2000 e^-, 2500 e^- and 3000 e^- in Fig. 5.5(a) show an uniform threshold behavior over the entire stave. This behavior applies for both sensor technologies which were both tuned to the same target values. Comparing the results obtained for the different threshold settings a decrease of the standard deviation is observed for higher threshold values. For the tested modules on stave-0A the average standard deviation of the threshold increases by 10 e^- when the threshold is changed from 3000 e^- to 2000 e^-. Contrary to the threshold measurements an offset in the mean noise shown in Fig. 5.5(b) can be observed for the two sensor technologies. Independent of the applied threshold setting an about 50 e^- higher noise compared to the planar modules is observed for the 3D modules. The expected noise decrease for higher threshold values is also present for the two technologies. Considering the change of the threshold configuration from 2000 e^- to 3000 e^- a mean noise decrease of 14.6 e^- and 12.3 e^- is measured for planar and 3D modules respectively. The lower noise values compared to the measurements performed during the module reception and measurements discussed in Sec. 4.1.1 are related to the applied feedback current gain of 9 ToT for an injected charge of 16 ke^- [77].

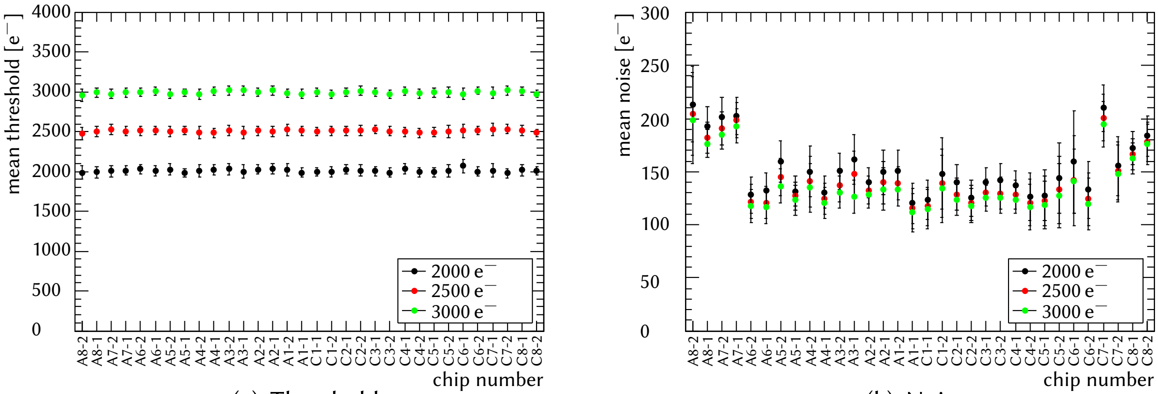

(a) Threshold (b) Noise

Figure 5.5: Threshold and noise measurements for different front-end settings to reach threshold values of 2000 e⁻, 2500 e⁻ and 3000 e⁻. The feedback current gain was tuned to 9 ToT for an injected charge of 16 ke⁻. The stave was operated at a temperature of 10 °C during the tuning and measurement procedure.

The QA-setup includes the possibility to perform source measurements to test the stave performance with charge generated in the sensor. For the production stave testing an automated procedure in the test setup is used to move a radioactive source over the length of the stave. This measurement makes it possible to test the charge collection properties of the sensor to analyze the pixel connections of the stave modules and in case of a photon source to calibrate the sensor [128]. Hit maps of an Am-241 source scan for a planar and a 3D module in Fig. 5.6 show an uniform hit distribution over the modules. Regions with lower occupancy are correlated with the position of electronic components mounted on the module flex.

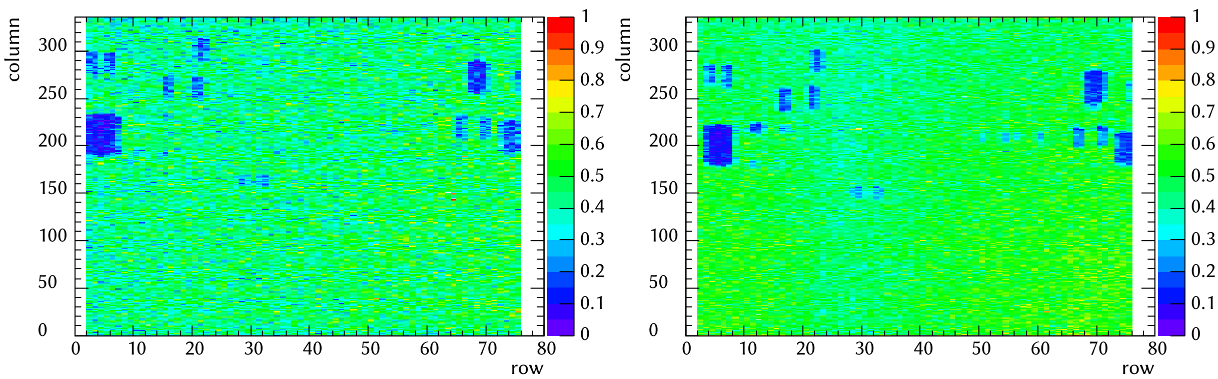

(a) Planar (b) 3D

Figure 5.6: Hit map of an Am-241 source scan of a planar and a 3D module mounted on stave-0A. The regions of lower occupancy are related to electronic components mounted on the module flex on top of the sensor.

6 Summary and Outlook

In the context of this work sensor technologies based on silicon and diamond sensor material have been tested before and after irradiation to fluences of up to $5 \cdot 10^{15}\,n_{eq}\,cm^{-2}$. The total ionizing dose collected by the attached front-end chips went up to 725 Mrad. While the analyzed fluence range covers the design values for the ATLAS IBL given in Tab. 1.1 reach dose rates close to the expected maximum values of the ITK. In addition covers the tested fluence range up to $5 \cdot 10^{15}\,n_{eq}\,cm^{-2}$ also the average fluence expected for outer layers and end cap disks of the ITK. The results also imply the operation of irradiated planar and 3D silicon pixel detectors up to five times higher fluences and more than 14 times higher total ionizing dose then the design values for the ATLAS Pixel Detector.
In addition to the characterization of sensor technologies used in the upcoming IBL upgrade also further possible technologies for future sensor upgrade programs in the ATLAS Experiment have been investigated. In total this includes the planar silicon technology implementing different designs based on the n-in-n and n-in-p pixel layout, the 3D silicon technology with varying column overlap and the planar diamond technology with single- and poly-crystal sensor material.

The **planar silicon sensor** technology which is due to its widespread application the most established technology is in many cases used as a baseline for comparisons to other technologies. In the context of this work several planar n-in-n sensors have been irradiated to fluences of up to $5 \cdot 10^{15}\,n_{eq}\,cm^{-2}$ to demonstrate the possible operation of this technology in the IBL upgrade. Further research even showed the operation of this technology up to a fluence of $2 \cdot 10^{16}\,n_{eq}\,cm^{-2}$ [119]. The slim-edge design implemented in the layout of the planar sensor modules for the IBL is an additional step to reduce the inactive area at the sensor edge. Further options as the application of an active edge would be also feasible with this technology but would complicate the production process. As the n-in-n sensor design is used in the IBL additional experience with this technology will be made in the upcoming years. Based on the obtained results it was demonstrated that planar n-in-n sensors could be implemented in the outer layers and end cap disks of future pixel detectors. For the implementation in the inner layers additional measurements need to confirm the operation in the expected fluence range.
In case of the n-in-p design the performed research is already directed towards the application as pixel sensor for detector upgrades after IBL. For the two proposed designs the operation was demonstrated up to $2 \cdot 10^{15}\,n_{eq}\,cm^{-2}$ and $1 \cdot 10^{16}\,n_{eq}\,cm^{-2}$ [91, 98]. These results confirm the possible operation in the outer layers and end cap disks of the ITK. As for

the n-in-n design the operation at higher fluences still needs to be demonstrated in order to deduce if this technology could also be used in the inner layers of the ITK. Due to the single sided processing in the n-in-p design it is assumed that the production costs are reduced compared to the n-in-n design. This assumption still needs to be confirmed on a sensor production corresponding to the amount of wafers necessary for the production of the pixel detector.
New biasing techniques to minimize the reduced charge collection and efficiency around the punch through dot are currently under investigation and might lead to a higher in-pixel efficiency. The application of thinner sensors down to a thickness of 150 µm was also demonstrated in this work and is expected to show a higher radiation hardness in the future. This increase of radiation hardness further raises the potential for the application of the planar silicon sensor technology as possible candidate for future pixel detectors. Issues related to the cooling and the high bias voltage necessary for the operation after irradiation are the two items which might limit the application of this technology at some point. Nevertheless shows the production yield of more than 90 % obtained during the IBL production how good this technology is controlled and understood.

The work performed on the **3D silicon sensor** technology showed a remarkable evolution over the last few years. The application of a double sides process to fabricate the sensors without a support wafer as it is used in the single sided process increased step by step the column overlap. In case of the 3D sensors used for the IBL this lead to the 'partial 3D' and 'full 3D' design. For the later the columns penetrate the entire wafer to form an overlap region corresponding to the entire wafer thickness. Different 3D sensor technology steps have been irradiated in the context of this work to fluences of up to $5 \cdot 10^{15}\ n_{eq}\ cm^{-2}$ to demonstrate the operation for the IBL upgrade. The guard fence design implemented in the 3D sensors for the IBL upgrade reduces the inactive edge of the sensor. The 3D silicon pixel sensors which are implemented in the IBL will demonstrate for the first time the application of 3D sensors in a HEP experiment. The experience from the operation in the experiment will provide inside on the behavior of this sensor technology under real conditions.
As the columns are already etched in the wafer the application of an active edge seems to be the next logical step to further reduce the inactive area. The lower operation voltage as well as the less strict temperature constraints compared to the planar sensor design are the advantages of this sensor technology for the operation at fluences after IBL. The more complex production process necessary for the fabrication of 3D sensor modules on the other hand makes it difficult to produce vast amounts of sensors within a short time. Although the IBL 3D sensor production fabricated more sensor tiles than necessary for the IBL an overall production yield of 32.4 % and 61.3 % is not enough for the fabrication of an entire detector. However, the 3D sensor technology might be a possible option for the application in the innermost layer of future detectors. In order to confirm the operation further tests in the expected fluence range need to be performed with a 3D sensor design.

The **poly-crystal diamond detectors** used for the DBM project of the IBL upgrade represent a further application using diamond detectors for particle tracking. The low leakage current before and after irradiation as well as the good thermal conductivity of diamond are interesting properties for the application as detector material. The low number of e/h-pairs generated per micro meter corresponds to a low charge collection. This disadvantage becomes less relevant if the SNR is taken into account. While the SNR of unirradiated silicon is higher than for diamond, the SNR changes to the advantage of diamond after irradiation. For high fluences the SNR is even inverted promoting diamond detectors as radiation hard material for fluences exceeding the IBL specifications [57]. The research performed with diamond sensors in this work showed that one of the issues with this technology is the proper electrode deposition. As the essential part to read-out the charge signal and to apply the bias voltage this issue plays an important role for future applications. The long fabrication process and the high cost of the sensor material is also a drawback for applications with a large sensor surface. Nevertheless offers this sensor material a wide range of possible applications including the application as sensor material in the innermost detector layers.

The prototype version of the FE-I4 read-out chip for the IBL exceeded the expectation concerning radiation hardness. Dose levels of 725 Mrad reached at irradiation campaigns at KIT nearly triple the expected operation dose. These results promote the application of a FE-I4 based read-out chip for the application in the outer pixel layers and the end cap disks of the ITK. Further tests at higher dose rates would be necessary to confirm if this front-end chip design could also be used for the innermost layer in future pixel detectors.

The results obtained in the context of this work lead to a further understanding of the latest sensor technology designs for the application in HEP experiments. In case of the planar and 3D silicon sensor technologies it was possible to contribute to the sensor characterization necessary for the upcoming IBL upgrade. In the long term sensor designs based on the investigated sensor technologies are going to be applied in future detectors to improve the tracking properties after several years of operation in a HEP detector as the ATLAS Experiment. The implementation of the planar and 3D sensors in the same layer as in the IBL might be a solution which could reappear in future detectors in order to profit from intrinsic sensor properties at a certain position in the experiment. Another option for future detectors could be the variation of sensor technologies between the individual layers or end caps. Overall it was shown that different sensor technologies are available for the implementation in the IBL and future pixel detectors. Depending on the position in the detector it needs to be demonstrated for the different sensor technologies that specific properties can be reached. Especially the combination of pixel sensor and read-out chip results shows that the current pixel detector modules already made a big step towards the application in the phase-2 upgrade of the ATLAS tracker.

A Additional Data and Measurement Results

Radioactive Sources

The radioactive sources available at CERN used to perform measurements with photons and electrons are summarized in Tab. A.1. In total there is one Cd-109, two Am-241 whereof one is equipped with different roentgen fluorescent targets and five Sr-90 sources available. While the Sr-90 source emits electrons are the remaining sources used for photon measurements. The corresponding spectra are shown in Fig. A.1.

Source ID	Isotope	Activity	Emission type
3735 RP	Sr-90	26.55 MBq	Beta
3746 RP	Sr-90	53.15 MBq	Beta
3875 RP	Cd-109	51.16 kBq	Gamma
4331 RP	Am-241	3.69 MBq	Gamma
4334 RP	Am-	369.64 MBq	Gamma
4428 RP	Sr-90	30 MBq	Beta
4429 RP	Sr-90	30 MBq	Beta
4430 RP	Sr-90	30 MBq	Beta

Table A.1: Radioactive sources available at CERN to perform measurements with photons and electrons. The source 4334 RP is the X-ray source using different roentgen fluorescent targets.

The gamma spectra of the photon sources shown in Fig. A.1 were measured by the CERN Radiation Protection (RP) Group in the gamma spectrometry laboratory in building 24/S-403 at CERN. The measurements were taken with two HPGe detectors which are normally used by the RP Group to perform gamma spectroscopies on different materials[1].

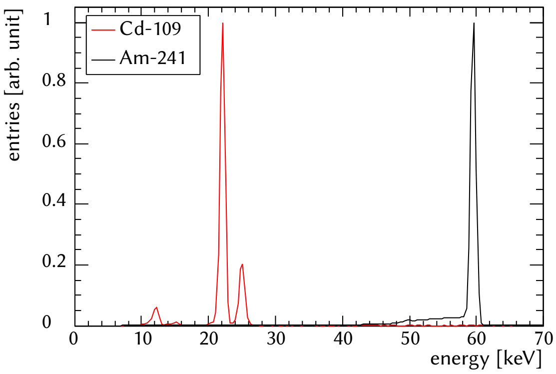

(a) spectrum of an Am-241 and a Cd-109

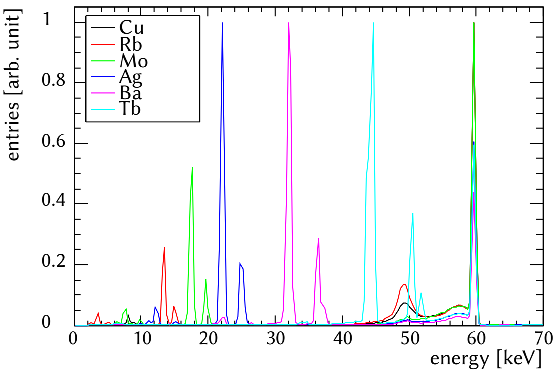

(b) spectrum of a X-ray source

Figure A.1: Spectra of the photon sources used in this work. The spectra of the Am-241 and the Cd-109 source are shown in Fig. A.1(a). The spectra of the different roentgen fluorescent targets in the X-ray source are shown in Fig. A.1(b).

[1] Uncertainty reported at 2 sigma (confidence interval 95.4 %)
Minimum Detectable Activity reported according to Currie method [130], confidence factor 5 %
Software: Genie-2000 V2.1 - Modelisation with G2K ISOCS/LabSOCS V4.1a
Detectors:
Ge1 HPGe coaxial (b01123) type P, Canberra
Relative efficiency at 1332 keV: 41.8 %
Resolution (FWHM) 1.81 keV at 1.33 MeV and 0.86 keV at 122 keV
Pic/Compton ratio 65:1
Ge5 HPGe coaxial (b01036) type P, Canberra
Relative efficiency at 1332 keV: 22.1 %
Resolution (FWHM) 1.79 keV at 1.33 MeV and 0.82 keV at 122 keV
Pic/Compton ratio 51:1

Leakage Current Measurements on FE-I3 modules

Leakage current measurements on FE-I3 modules focus on the analysis of the behavior before and after irradiation of 3D modules. This measurement was not possible for planar modules as the available climate chamber did not support enough cooling power to operate the modules at a temperature of −20 °C.
The two unirradiated modules FBK-I3-4E-#1 and FBK-I3-4E-#2 in Fig. 4.10 and Fig. 4.11 show the expected leakage current increase with increasing temperatures. Scaling the leakage current with Eq. 2.6 to a temperature of 20 °C shows for FBK-I3-4E-#1 in Fig. 4.10(b) a variation for the different temperatures. This is not the case for FBK-I3-4E-#2 in Fig. 4.11(b) which shows a high correlation over the temperature range. The obtained results indicate a surface current contribution to the leakage current of FBK-I3-4E-#1 as Eq. 2.6 is only scaling the bulk current. Module FBK-I3-4E-#2 on the other hand does not show a surface current contribution.

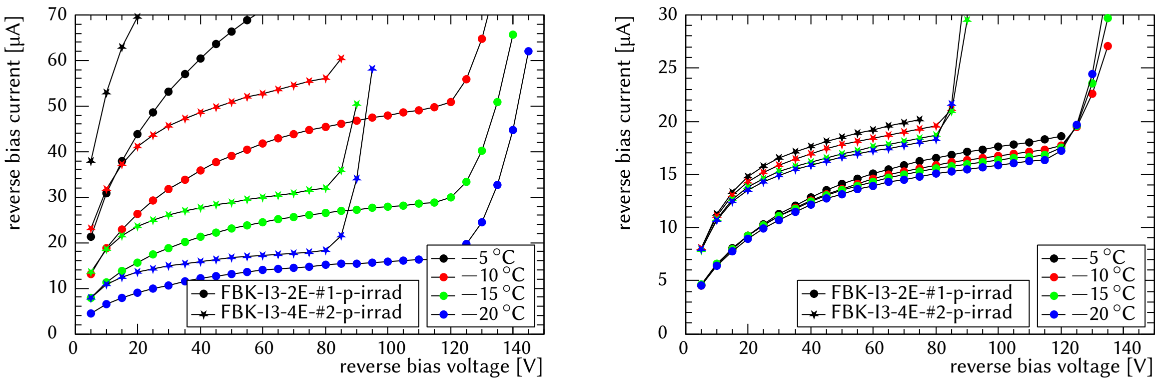

(a) measured leakage current (b) scaled leakage current

Figure A.2: Leakage current measurements of two $1.6 \cdot 10^{15}\ n_{eq}\ cm^{-2}$ proton irradiated (CERN PS) 3D-DDTC samples in the temperature range of −20 °C to −5 °C. The leakage current in function of the temperature is shown in Fig. A.2(a). A high correlation of the leakage current becomes visible in Fig. A.2(b) after scaling the measurements to −20 °C.

After irradiation of the two modules the leakage current increases due to the effect of the radiation damage on the bulk current. The temperature dependence after irradiation is still visible in Fig. A.2 while the offset due to the surface current in FBK-I3-4E-#1 is not visible after scaling anymore. This behavior is related to the shift of the surface/bulk current ratio after irradiation making it possible to neglect the surface current contribution.

Samples irradiated with protons (KIT) in Fig. A.3 show similar results as the two proton irradiated (CERN PS) samples in Fig. A.2. In case of the samples in Fig. A.3 the high correlation between the three modules is noticeable indicating a stable production process.

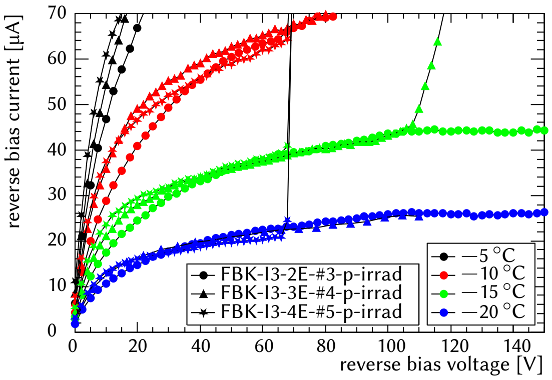

(a) measured leakage current

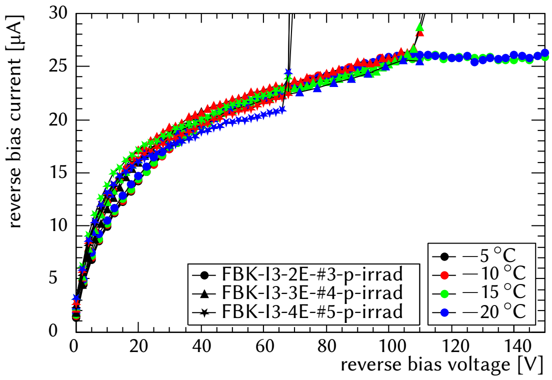

(b) scaled leakage current

Figure A.3: Leakage current measurements of three $1 \cdot 10^{15}\ n_{eq}\ cm^{-2}$ proton irradiated (KIT) 3D-DDTC samples in the temperature range of −20 °C to −5 °C. The leakage current in function of the temperature is shown in Fig. A.3(a). A high correlation of the leakage current becomes visible in Fig. A.3(b) after scaling the measurements to −20 °C.

Leakage Current Measurements on FE-I4 modules

Leakage current measurements focusing on the influence of the power dissipation of the FE-I4 chip on the sensor. For the analysis leakage current measurements with powered and un-powered front-end chip are compared to determine the temperature offset. The measurements with un-powered front-end chip is used as the reference for the analysis while the second leakage current is scaled to lower temperatures in order to compare the scaled result with the un-powered measurement. As a result it becomes possible to get a rough estimation of the power dissipation on the sensor temperature.

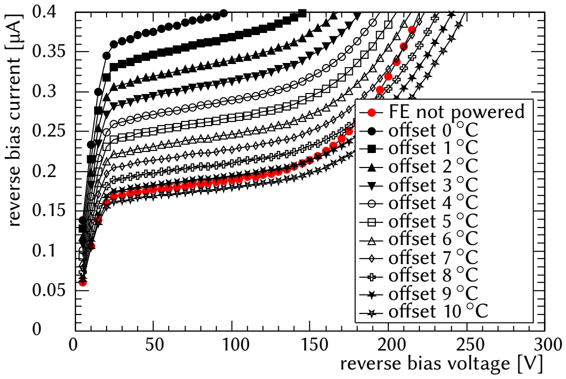

(a) CiS-I4-n-#03

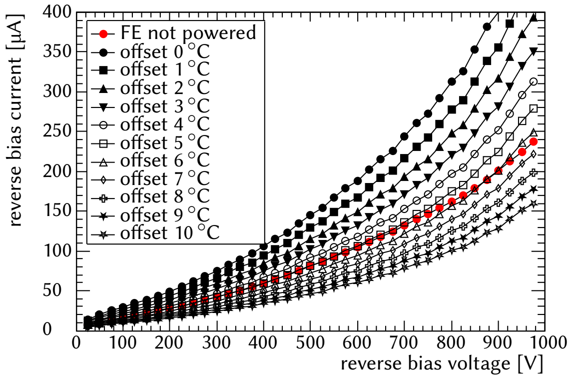

(b) CiS-I4-n-#11-p-irrad

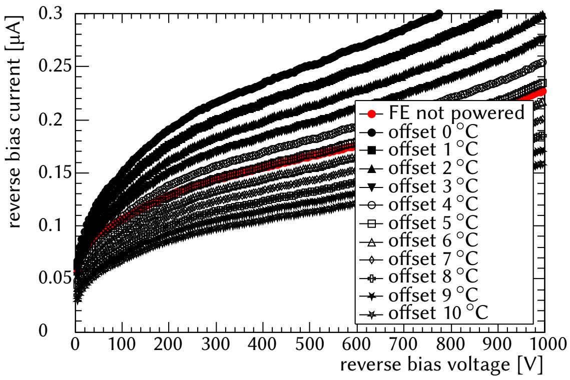

(c) HPK-I4-p-#1

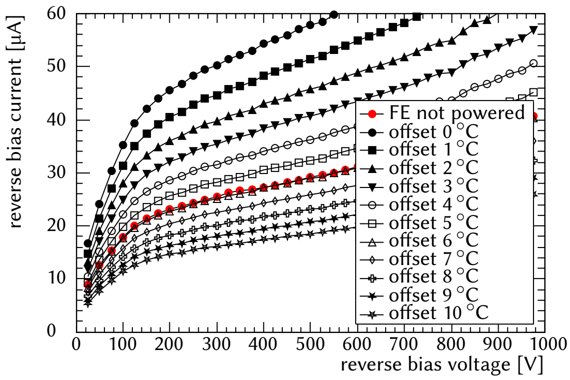

(d) HPK-I4-n-#2-p-irrad

Figure A.4: Leakage current measurements of planar FE-I4 modules build with n-in-n and n-in-p sensor before and after irradiation to determine the influence of the FE-I4 power dissipation on the sensor temperature.

As a result of the analysis a temperature offset between 5 °C and 9 °C at an air temperature of 20 °C has been determined for unirradiated planar modules. A reason for the wide temperature variation is the different module mounting procedure which effects the cooling properties of the Printed Circuit Board (PCB) used to mount the module. After irradiation the temperature offset shrinks to the range between 5 °C and 7 °C. This behavior is also explained by the mounting technique as the same technique is used for irradiated samples. In case of unirradiated 3D modules a temperature offset of about 4 °C was determined at an air temperature of 20 °C. This temperature offset also stayed stable between 4 °C and 5 °C after irradiation at an air temperature of −20 °C. Contrary to the planar modules the same mounting technique was used for all 3D modules which explains the reduced temperature variation.

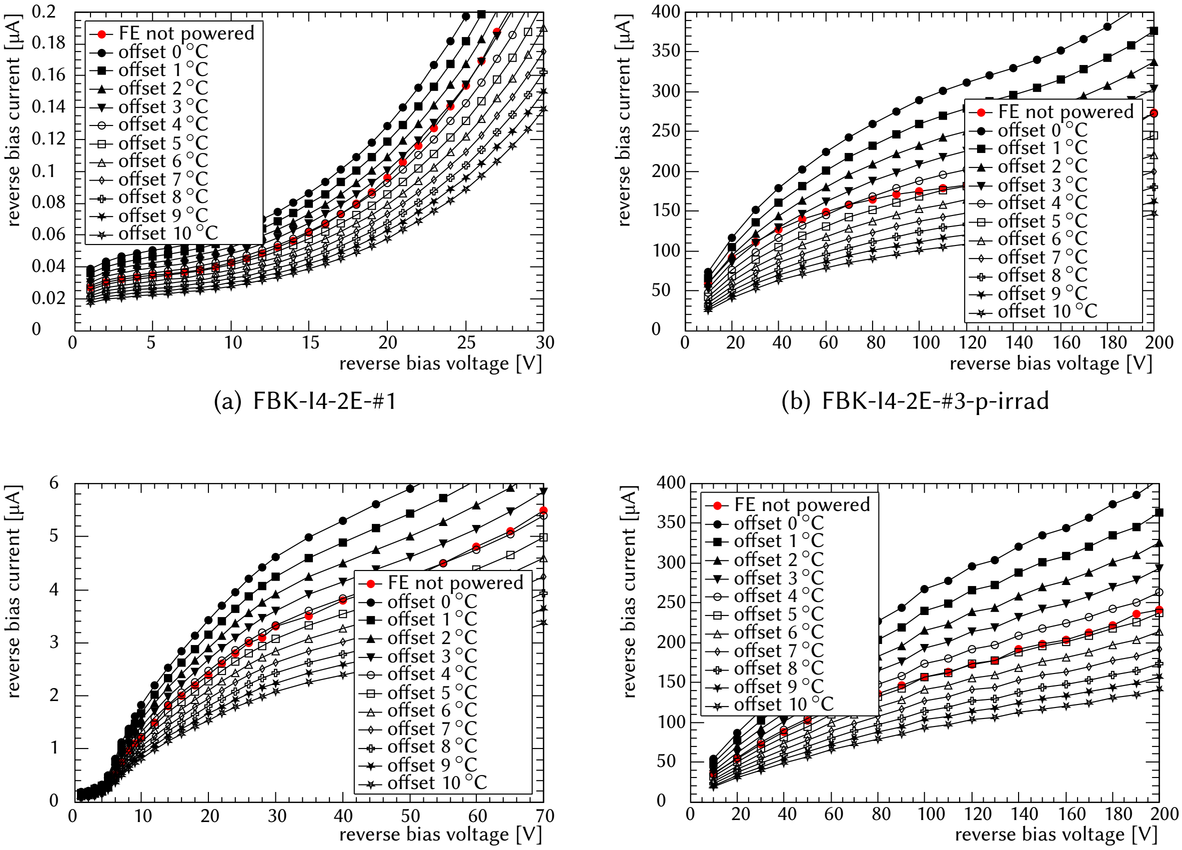

(a) FBK-I4-2E-#1

(b) FBK-I4-2E-#3-p-irrad

(c) CNM-I4-2E-#1

(d) CNM-I4-2E-#5-n-irrad

Figure A.5: Leakage current measurements of 3D FE-I4 modules fabricated at FBK and CNM before and after irradiation to determine the influence of the FE-I4 power dissipation on the sensor temperature.

Test-Beam Measurements on FE-I4 modules

The modules used for the TB analysis in Sec. 4.2.6 are summarized in Tab. A.2 showing the sensor name, the TB period and facility as well as the run number and the incident angle of the beam.

Sensor name	TB period	TB facility	run number range	Φ	used Figure
CiS-I4-n-#02	2011-06	CERN	50237-50253	0°	Fig. 4.34(a) (top)
	2011-09	CERN	61500-61511	0°	Fig. 4.35
	2011-06	CERN	50237-50253	0°	Fig. 4.38 (top)
CiS-I4-n-#08-n-irrad	2011-06	CERN	50468-50469	15°	Fig. 4.37(a) (top)
	2011-06	CERN	50471-50477	15°	Fig. 4.37(a) (center)
	2011-06	CERN	50482-50484	15°	Fig. 4.37(a) (bottom)
CiS-I4-n-#10-n-irrad	2011-09	CERN	61500-61511	0°	Fig. 4.34(a) (center)
	2011-09	CERN	61500-61511	0°	Fig. 4.35
	2011-09	CERN	61500-61511	0°	Fig. 4.38 (center)
CiS-I4-n-#12-p-irrad	2012-03	DESY	50914-50938	15°	Fig. 4.34(a) (bottom)
	2012-03	DESY	50914-50938	15°	Fig. 4.38 (bottom)
FBK-I4-2E-#1	2011-09	CERN	61500-61519	0°	Fig. 4.34(b) (top)
	2011-09	CERN	61500-61519	0°	Fig. 4.36
	2011-09	CERN	61500-61519	0°	Fig. 4.39(a) (top)
FBK-I4-2E-#2-p-irrad	2011-06	CERN	50482-50484	15°	Fig. 4.37(b) (center)
	2011-06	CERN	50482-50484	15°	Fig. 4.39(a) (center)
FBK-I4-2E-#3-p-irrad	2011-06	CERN	50459-50467	15°	Fig. 4.39(a) (bottom)
CNM-I4-2E-#3	2011-06	CERN	50237-50253	0°	Fig. 4.34(b) (center)
	2011-06	CERN	50237-50253	0°	Fig. 4.36
	2011-06	CERN	50237-50253	0°	Fig. 4.37(b) (top)
	2011-06	CERN	50237-50253	0°	Fig. 4.39(b) (top)
CNM-I4-2E-#4-p-irrad	2011-06	CERN	50237-50253	0°	Fig. 4.36
	2011-06	CERN	50237-50253	0°	Fig. 4.39(b) (center)
CNM-I4-2E-#5-n-irrad	2011-09	CERN	61500-61519	0°	Fig. 4.34(b) (bottom)
	2011-09	CERN	61500-61519	0°	Fig. 4.36
	2011-09	CERN	61500-61519	0°	Fig. 4.39(b) (bottom)
CNM-I4-2E-#6-n-irrad	2011-06	CERN	50470-50481	15°	Fig. 4.37(b) (bottom)

Table A.2: Table summarizing the sensor modules used for the TB analysis used in this work including the TB period and the run numbers used for the analysis.

Leakage Current Measurements on stave-0A modules

The leakage measurements of the individual modules which are connected to a common bias voltage supply on the stave-0A are summarized in Fig. A.6, Fig. A.7 and Fig. A.8 for planar modules and in Fig. A.9 for the 3D modules. Also the total leakage current of the combined module is given to evaluate the impact of the common measurement. Variations between the current on the modules and on the stave are expected as the measurements correspond to different temperatures.

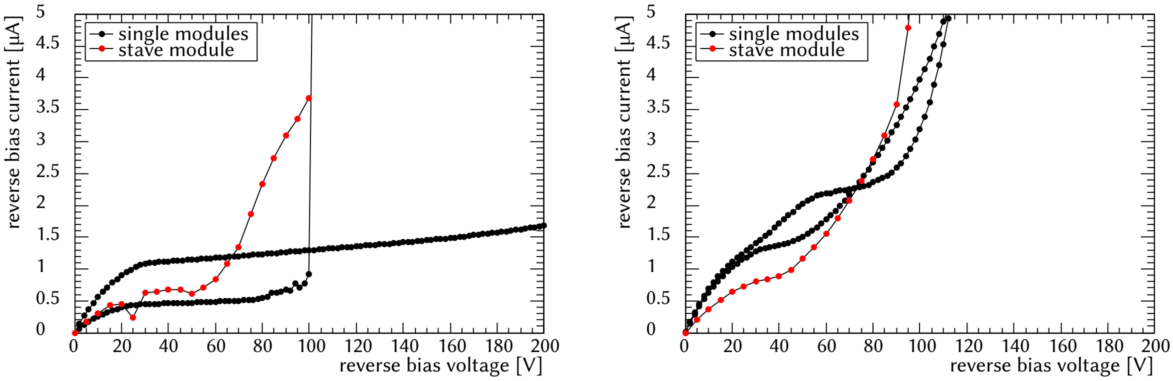

(a) M1A (b) M1C

Figure A.6: Leakage current measurements for the planar modules combined to M1

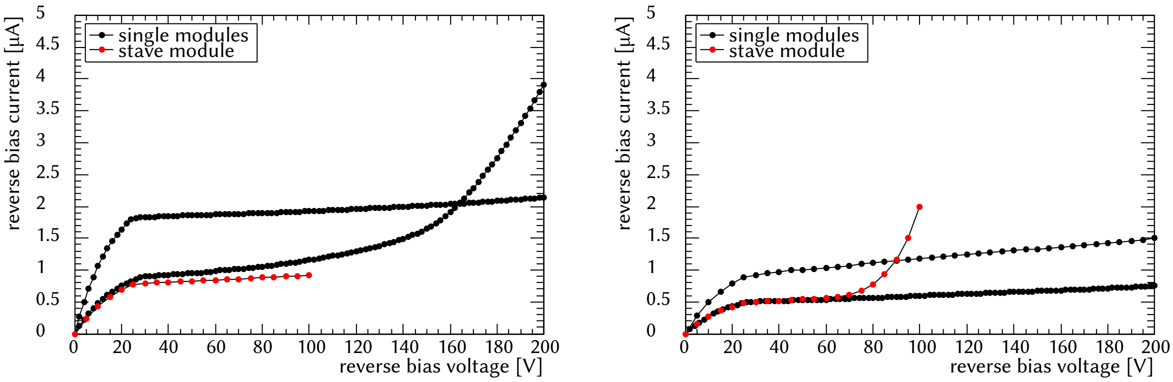

(a) M2A (b) M2C

Figure A.7: Leakage current measurements for the planar modules combined to M2

Comparing the results of the measurements shows a good correlation between the individual modules and the combined read-out on the stave. Noticeable is the breakdown shift to 80 V of M2C in Fig. A.7(b) which could indicate module damage which appeared during the mounting of the modules.

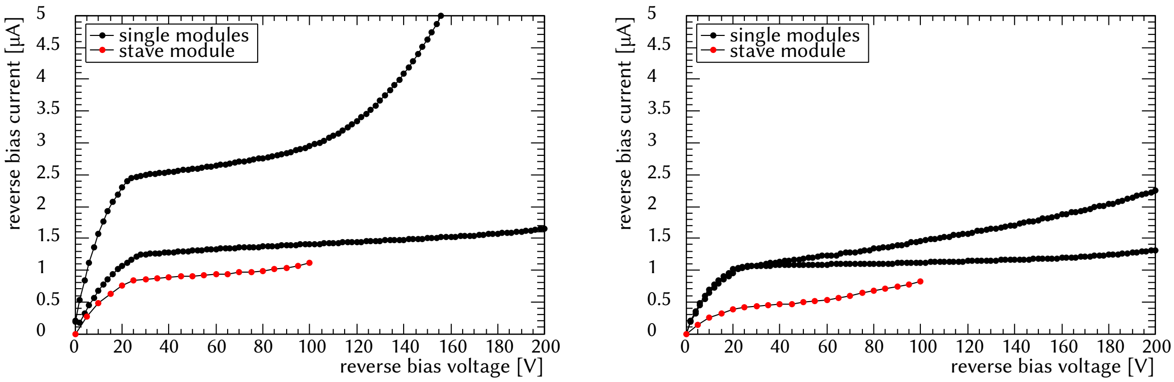

(a) M3A (b) M3C

Figure A.8: Leakage current measurements for the planar modules combined to M3

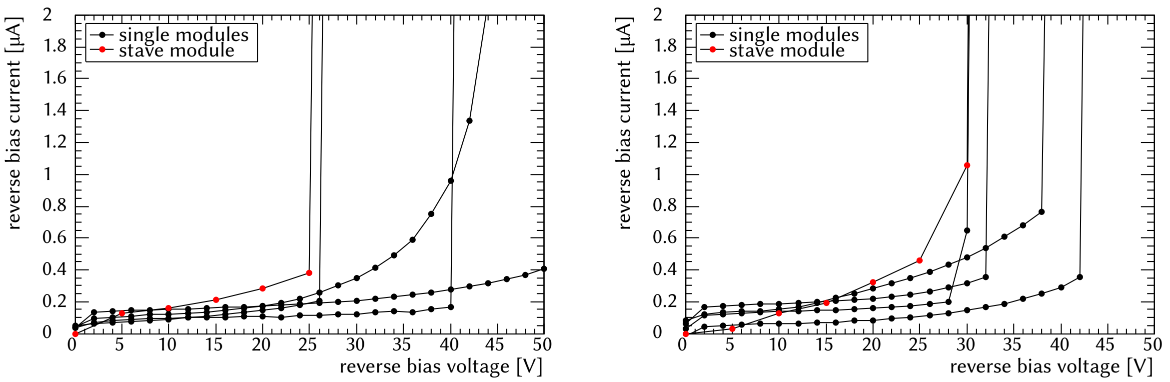

(a) M4A (b) M4C

Figure A.9: Leakage current measurements for the 3D modules combined to M4

Glossary

ALICE Experiment The ALICE Experiment is one of the particle detectors experiments connected to the LHC. http://aliceinfo.cern.ch/Public/Welcome.html

ATLAS Experiment The ATLAS Experiment is one of the particle detectors experiments connected to the LHC. http://atlas.ch/

ATLAS Pixel Detector front-end chip version I3 The ATLAS Pixel Detector front-end chip version I3 is the front-end chip used to build ATLAS Pixel Detector. A description of the chip is given in Sec. 3.2.1.

ATLAS Pixel Detector front-end chip version I4 The ATLAS Pixel Detector front-end chip version I4 is the pixel detector front-end chip to be used for the read-out of ATLAS IBL pixel detector modules. A prototype version FE-I4A was used during this work while an enhanced version FE-I4B is used for IBL modules. A description of the chip is given in Sec. 3.2.2.

bunch A bunch is collection of particles which are stored in a particle accelerator. The LHC was designed to hold in each proton beam up to 2808 bunches each containing about $1 \cdot 10^{11}$ protons.

bunch crossing frequency The bunch crossing frequency is the frequency bunches collide in an accelerator. In case of the LHC a maximum bunch crossing frequency of 40 MHz corresponding to 25 ns can be reached.

CMS Experiment The CMS Experiment is one of the particle detectors experiments connected to the LHC. http://cms.web.cern.ch/

Deutsches Elektronen-Synchrotron Deutsches Elektronen-Synchrotron is a research center in Germany with sites in Hamburg and Zeuthen. http://www.desy.de/

European Organization for Nuclear Research European Organization for Nuclear Research is an intergovernmental research center in Geneva, Switzerland. http://home.web.cern.ch/

fluence The fluence in particle physics represents the number of particles penetrating an area. It represents a unit of measure of the radiation damage a particle detector has sustained. Corresponding to the NIEL hypothesis in Sec. 2.2.3 a conversion is used to scale a given fluence to a neutron equivalent fluence ($n_{eq}\,cm^{-2}$).

integrated luminosity The integrated luminosity represents an amount of collisions in an particle accelerator. The recorded integrated luminosity of an experiment represents a fraction of the delivered integrated luminosity. The expected development of the integrated luminosity in the ATLAS Experiment in shown in Fig. 1.2.

LHCb Experiment The LHCb Experiment is one of the particle detector experiments connected to the LHC. http://lhcb-public.web.cern.ch/lhcb-public/

luminosity In accelerator physics the luminosity is one of the parameters used to describe the performance of an accelerator. For ring accelerators the luminosity is defined by the number of bunches stored in the accelerator, the number of particles stored in these bunches, the cross section of these bunches and the bunch crossing frequency. In order to reach a high statistical significance of the measurement it is desired to reach a high luminosity. By 2022 the LHC peak luminosity will be successively increased up to $5 \cdot 10^{34}\,\mathrm{cm}^{-2}\mathrm{s}^{-1}$. In total a integrated luminosity of $3000\,\mathrm{fb}^{-1}$ is expected during the operation time of the accelerator.

pseudorapidity In particle physics the pseudorapidity η describes the deflection of a particle relative to the beam axis. In case of the ATLAS Experiment which covers the pseudorapidity range $|\eta| < 2.5$ this corresponds to particles with an relative angle to the beam axis higher than about $9.39\,^{\circ}$.

stave A stave is a structural element of a detector which houses a certain number of detector modules. In order to avoid inactive regions in the detector several staves are mounted around the beam pipe overlapping each other. For the development of the IBL a prototype stave called stave-0A was build implementing FE-I4A modules. More details about the stave layout of the IBL can be found in Sec. 1.3.1

STControl STControl is a program to perform automated scans on pixel modules with the USBPix system.

TurboDAQ TurboDAQ is an analysis software dedicated to perform automated scans on ATLAS Pixel Detector modules and single chip modules. Further information about the software is given in Sec. 3.4.1. http://physik2.uni-goettingen.de/~jgrosse/TurboDAQ/

USBPix The USBPix system is a general purpose read-out system which is used for electrical testing of pixel detector modules. Further information about the system is given in Sec. 3.4.2. http://icwiki.physik.uni-bonn.de/twiki/bin/view/Systems/UsbPix

Acronyms

AC alternating current
ADC analog to digital converter
ALICE ALICE Experiment
ATLAS ATLAS Experiment

BCM Beam Conditions Monitor

CERN European Organization for Nuclear Research
CFRP carbon-fiber-reinforced polymer
CiS CiS Forschungsinstitut für Mikrosensorik und Photovoltaik GmbH
CMOS Complementary Metal-Oxide-Semiconductor
CMS CMS Experiment
CNM Centro Nacional de Microelectrónica - Instituto de Microelectrónica de Barcelona
CSA Charge-Sensitive Amplifier
CSC Cathode Strip Chambers
CTP Central Trigger Processor
CVD Chemical Vapor Deposition

DAC digital to analog converter
DAQ Data Acquisition
DBM Diamond Beam Monitor
DC direct current
DCM Double Chip Module
DCS Double Chip Sensor
DDL Diamond Detectors Ltd.
DDTC Double Side Double Type
DESY Deutsches Elektronen-Synchrotron
DICE Dual Interlocked storage Cell
DLL Dynamic Link Library
DRIE Deep Reactive Ion Etching
DUT Device Under Test

EEPROM Electrically Erasable Programmable Read-Only Memory
ENC equivalent noise charge
EOC end of column

FBK Fondazione Bruno Kessler
FDAC individual feedback current DAC
FE-I3 ATLAS Pixel Detector front-end chip version I3
FE-I4 ATLAS Pixel Detector front-end chip version I4
FPGA Field Programmable Gate Array
FTK Fast Tracker
FWHM full width half maximum

GDAC global threshold DAC

HEP High Energy Physics
HFCVD hot-filament CVD
HL-LHC High Luminosity LHC
HPK Hamamatsu Photonics K.K.

I^2C Inter-Integrated Circuit
IBL Insertable B-Layer
IEL Ionizing Energy Loss
ISS International Space Station
IST IBL Support Tube
ITK Inner Tracker
IZM Fraunhofer-Institut für Zuverlässigkeit und Mikrointegration

JSI Jožef Stefan Institute

KIT Karlsruher Institut für Technologie

LanGau Landau function convoluted with a Gaussian
LAr liquid argon
LHC Large Hadron Collider
LHCb LHCb Experiment
LUT look up table
LVDS Low Voltage Differential Signaling

MAC Module Adapter Card
MDT Monitored Drift Tubes

MIP Minimum Ionizing Particle
MOSFET metal oxide semiconductor field-effect transistor
Multi-IO multipurpose input-output
MWCVD microwave CVD

NIEL non Ionizing Energy Loss
nSQP new Service Quarter Panels

PCB Printed Circuit Board
pcCVD poly-crystalline CVD
PKA Primary Knock-on Atom
PMT photomultiplier tube
PPS Planar Pixel Sensor
PS Proton Synchrotron
PSI Paul Scherrer Institut

QA Quality Assurance
QC Quality Control

RP Radiation Protection
RPC Resistive Plate Chambers

SCM Single Chip Module
SCS Single Chip Sensor
SCT Semiconductor Tracker
sCVD single-crystalline CVD
SELEX SELEX Sistemi Integrati S.p.A.
SEU Single Event Upset
SNR Signal-to-Noise Ratio
SPI Serial Peripheral Interface
SPS Super Proton Synchrotron
SQP Service Quarter Panels
SRAM Static Random-Access Memory

TB Test-Beam
TDAC individual threshold DAC
TGC Thin Gap Chambers
TID total ionizing dose
ToT time-over-threshold

TPCC Turbo Pixel Control Card

TPLL Turbo Pixel Low Level

TRT Transition Radiation Tracker

UBM under bump metalization

USB Universal Serial Bus

VME Versa Module Eurocard

Acknowledgment

The realization of this thesis was only possible due to the help and support by many colleagues and friends. I want to use this opportunity to express my gratitude to all of you for your assistance, support and encouragement.

First I want to thank Prof. Dr. Christian Boit for the endorsement to take part in the PhD program and the opportunity to write my thesis with the department of Semiconductor Devices at the Technische Universität Berlin. Further many thanks go to Prof. Dr. Claus Gößling for becoming part of my examination board. Special thanks goes to my supervisor Dr. Heinz Pernegger for the possibility to spend time at CERN as well as your support and advice. Thanks for giving me the freedom to work independently which helped a lot to widen my knowledge and to gain experience to work as a scientist.

I also want to thank my colleagues and friends Alessandro La Rosa and Daniel Dobos who shared their knowledge with me and gave advice on so many things. Many thanks to the entire team of 301-1-007 who provided a place for me where I always felt home. It was great having experts on all kinds of fields around to talk to. Of course I did not forget the common time at the kebap place which was a fun way to relax after a long working day. Sadly missed are our fish "Sushi", "Paella" and "Staubsauger" who have left us before their time.

Taking test-beam data at CERN and DESY was an exciting yet sometimes exhausting work. Thanks to the test-beam crews and especially the test-beam coordinators from the 3D, PPS, RD42 and IBL collaboration some of the presented results would not have been possible without you. Many thanks to the students I was allowed to supervise, you were a great help and it was a pleasure having you around. Warm thanks to the bonding lab and especially to Ian McGill for the wire-bonding which was unfortunately to often required on short notice.

Herzlicher Dank geht natürlich an meine Eltern Judith und Günther sowie meine Schwester Cathrin, die es mir ermöglicht haben zu studieren und meinen Interessen zu folgen. Ohne Euch hätte ich es nicht soweit geschaft.
在此, 我要特别感谢我的岳父何磅养, 岳母陈丽萍, 小姨们何悦华和何悦婷以及舅子何伟洪对我的支持, 鼓励和帮助.
Besonderer Dank gebührt meiner Frau Shirley, die mich trotz räumlicher Trennung bei all meinen Vorhaben unterstützt hat. Danke, dass Du an mich glaubst und unsere gemeisame Zukunft mit mir verbringst. 520

Bibliography

[1] G. Aad et al., "ATLAS pixel detector electronics and sensors," *Journal of Instrumentation*, vol. 3, p. P07007, 2008.

[2] The ATLAS Collaboration, "ATLAS pixel detector: Technical Design Report." CERN-LHCC-98-013, 1998.

[3] I. Perić, L. Blanquart, G. Comes, P. Denes, K. Einsweiler, P. Fischer, E. Mandelli, and G. Meddeler, "The FEI3 readout chip for the ATLAS pixel detector," *Nuclear Instruments and Methods in Physics Research Section A*, vol. 565, p. 178, 2006.

[4] J. M. Klaiber-Lodewigs, *The ATLAS Pixel Sensor - properties, characterization and quality control.* PhD thesis, Technische Universität Dortmund, 2005.

[5] S. I. Parker, C. J. Kenney, and J. Segal, "3D - A proposed new architecture for solid-state radiation detectors," *Nuclear Instruments and Methods in Physics Research Section A*, vol. 395, p. 328, 1997.

[6] The RD42 Collaboration, "Development of diamond tracking detectors for high luminosity experiments at the LHC." CERN-LHCC-95-43, 1995.

[7] CERN, "Convention for the establishment of a european organization for nuclear research: Paris, 1st july, 1953 : as amended." CERN Document Server, 1971.

[8] Map data © OpenStreetMap contributors. http://www.openstreetmap.org/copyright, 2012. Please contact the author via e-mail to get access to the map material.

[9] The ATLAS Collaboration, "Observation of a new particle in the search for the Standard Model Higgs boson with the ATLAS detector at the LHC," *Physics Letters B*, vol. 716, p. 1, 2012.

[10] The CMS Collaboration, "Observation of a new boson at a mass of 125 GeV with the CMS experiment at the LHC," *Physics Letters B*, vol. 716, p. 30, 2012.

[11] L. Evans and P. Bryant, "LHC Machine," *Journal of Instrumentation*, vol. 3, p. S08001, 2008.

[12] R. Assmann, B. Dehning, M. Ferro-Luzzi, B. Goddard, M. Lamont, R. Schmidt, A. Siemko, J. Uythoven, J. Wenninger, and M. Zerlauth, "First operational experience with the LHC machine protection system when operating with beam energies beyond the 100 MJ range," in *Proceedings of IPAC2012*, p. THPPR040, 2012.

[13] L. Rossi and O. Brüning, "High Luminosity Large Hadron Collider: A description for the European Strategy Preparatory Group." CERN-ATS-2012-236, 2012.

[14] F. Gianotti et al., "Physics potential and experimental challenges of the LHC luminosity upgrade," *The European Physical Journal C*, vol. 39, p. 293, 2005.

[15] The ATLAS Collaboration, "AtlasPublic - LuminosityPublicResults." https://twiki.cern.ch/twiki/bin/view/AtlasPublic/LuminosityPublicResults, 2012.

[16] The ATLAS Collaboration, "The ATLAS Experiment at the CERN Large Hadron Collider," *Journal of Instrumentation*, vol. 3, p. S08003, 2008.

[17] The ATLAS Collaboration, "ATLAS Inner Detector: Technical Design Report, 1." CERN-LHCC-97-016, 1997.

[18] The ATLAS Collaboration, "The ATLAS Inner Detector commissioning and calibration," *The European Physical Journal C*, vol. 70, p. 787, 2010.

[19] The ATLAS Collaboration, "ATLAS Inner Detector: Technical Design Report, 2." CERN-LHCC-97-017, 1997.

[20] H. Pernegger, "The ATLAS Insertable B-Layer pixel detector," in *PoS(Vertex 2011)018*, 2011.

[21] Y. Unno, "ATLAS silicon microstrip detector system (SCT)," *Nuclear Instruments and Methods in Physics Research Section A*, vol. 511, p. 58, 2003.

[22] T. Kohriki et al., "Development of the hybrid structure for the barrel module of the ATLAS silicon-microstrip tracker," *IEEE Transactions on Nuclear Science*, vol. 49, p. 3278, 2002.

[23] The ATLAS TRT Collaboration, "The ATLAS Transition Radiation Tracker (TRT) proportional drift tube: design and performance," *Journal of Instrumentation*, vol. 3, p. P02013, 2008.

[24] J. D. Degenhardt, "ATLAS Transition Radiation Tracker (TRT) Electronics Operation Experience at High Rates." ATL-INDET-SLIDE-2012-515, 2012.

[25] C. Bini, "Study of the performance of the ATLAS muon spectrometer," in *Nuclear Science Symposium and Medical Imaging Conference (NSS/MIC), IEEE*, p. 1265, 2011.

[26] C. Gabaldon, "Performance of the ATLAS Trigger System," *Journal of Instrumentation*, vol. 7, p. C01092, 2012.

[27] The ATLAS Collaboration, "Letter of Intent for the Phase-I Upgrade of the ATLAS Experiment." CERN-LHCC-2011-012, 2011.

[28] The ATLAS Collaboration, "Letter of Intent for the Phase-II Upgrade of the ATLAS Experiment." CERN-LHCC-2012-022, 2012.

[29] The ATLAS Collaboration, "ATLAS Insertable B-Layer Technical Design Report." CERN-LHCC-2010-013, 2010.

[30] P. S. Miyagawa and I. Dawson, "Radiation background studies for the Phase II inner tracker upgrade." ATL-UPGRADE-PUB-2013-012, 2013.

[31] P. Vankov, "ATLAS Upgrade for the HL-LHC: meeting the challenges of a five-fold increase in collision rate," *EPJ Web of Conferences*, vol. 28, p. 12069, 2012.

[32] The ATLAS Collaboration, "IBL layout." CERN EDMS: 1141314, 2012.

[33] The ATLAS Collaboration, "ATLAS Insertable B-Layer Technical Design Report Addendum." CERN-LHCC-2012-009, 2012.

[34] S. Amerio et al., "ATLAS FTK: Fast Track Trigger," in *PoS(Vertex 2011)040*, 2011.

[35] D. Ferrere, "The upgrade of the ATLAS Inner Detector," *Nuclear Instruments and Methods in Physics Research Section A*, vol. 718, p. 30, 2012.

[36] The ATLAS Collaboration, "Final Report: ATLAS Phase-2 Tracker Upgrade Layout Task Force." ATL-UPGRADE-PUB-2012-004, 2012.

[37] S. M. Sze, *Physics of Semiconductor Devices.* Wiley, 1981.

[38] P. P. Altermatt, A. Schenk, F. Geelhaar, and G. Heiser, "Reassessment of the intrinsic carrier density in crystalline silicon in view of band-gap narrowing," *Journal of Applied Physics*, vol. 93, p. 1598, 2003.

[39] S. J. Rashid et al., "Numerical Parameterization of Chemical-Vapor-Deposited (CVD) Single-Crystal Diamond for Device Simulation and Analysis," *IEEE Transactions on Electron Devices*, vol. 55, p. 2744, 2008.

[40] L. Rossi, P. Fischer, T. Rohe, and N. Wermes, *Pixel Detectors: From Fundamentals to Applications.* Springer, 2006.

[41] M. Moll, *Radiation Damage in Silicon Particle Detectors.* PhD thesis, Universität Hamburg, 1999.

[42] H.-G. Wagemann and T. Schönauer, *Silizium-Planartechnologie: Grundprozesse, Physik und Bauelemente.* Teubner, 2003.

[43] M. S. Alam et al., "The ATLAS silicon pixel sensors," *Nuclear Instruments and Methods in Physics Research Section A*, vol. 456, p. 217, 2001.

[44] F. Hügging, *Der ATLAS-Pixelsensor.* PhD thesis, Technische Universität Dortmund, 2001.

[45] K. Misiakos and D. Tsamakis, "Accurate measurements of the silicon intrinsic carrier density from 78 to 340 K," *Journal of Applied Physics*, vol. 74, p. 3293, 1993.

[46] G. Kramberger, V. Cindro, I. Mandić, M. Mikuž, M. Milovanović, and M. Zavrtanik, ""Why p-type is Better than n-type" or Electric Field in Heavily Irradiated Silicon Detectors." presented at the 21th Anniversary International Workshop on Vertex Detectors (VERTEX 2012), 2012.

[47] G. Kramberger, V. Cindro, I. Mandić, M. Mikuž, M. Milovanović, and M. Zavrtanik, "Electric Field in Heavily Irradiated Silicon Detectors," in *PoS(Vertex 2012)022*, 2012.

[48] C. Piemonte, "Device simulations of isolation techniques for silicon microstrip detectors made on p-type substrates," *IEEE Transactions on Nuclear Science*, vol. 53, p. 1694, 2006.

[49] C. Goessling, R. Klingenberg, D. Muenstermann, and T. Wittig, "Evaluation of the breakdown behaviour of ATLAS silicon pixel sensors after partial guard-ring removal," *Nuclear Instruments and Methods in Physics Research Section A*, vol. 624, p. 410, 2010.

[50] M. Benoit, A. Lounis, and N. Dinu, "Simulation of guard ring influence on the performance of ATLAS pixel detectors for inner layer replacement," *Journal of Instrumentation*, vol. 4, p. P03025, 2009.

[51] M. Benoit, A. Lounis, and N. Dinu, "Simulation of Radiation Damage Effects on Planar Pixel Guard Ring Structure for ATLAS Inner Detector Upgrade," *IEEE Transactions on Nuclear Science*, vol. 56, p. 3236, 2009.

[52] C. Da Vià, E. Bolle, K. Einsweiler, M. Garcia-Sciveres, J. Hasi, C. Kenney, V. Linhart, S. Parker, S. Pospisil, O. Rohne, T. Slavicek, S. Watts, and N. Wermes, "3D active edge silicon sensors with different electrode configurations: Radiation hardness and noise performance," *Nuclear Instruments and Methods in Physics Research Section A*, vol. 56, p. 3236, 2009.

[53] M. Werner and R. Locher, "Growth and application of undoped and doped diamond films," *Reports on Progress in Physics*, vol. 61, p. 1665, 1999.

[54] F. Hörmann, H. Roll, M. Schreck, and B. Stritzker, "Epitaxial Ir layers on $SrTiO_3$ as substrates for diamond nucleation: deposition of the films and modification in the CVD environment," *Diamond and Related Materials*, vol. 9, p. 256, 2000.

[55] M. Mathes, *Development and Characterization of Diamond and 3D-Silicon Pixel Detectors with ATLAS-Pixel Readout Electronics.* PhD thesis, Universität Bonn, 2008.

[56] J.-W. Tsung, *Diamond and Silicon Pixel Detectors in High Radiation Environments.* PhD thesis, Universität Bonn, 2012.

[57] J.-W. Tsung, M. Havranek, F. Hügging, H. Kagan, H. Krüger, and N. Wermes, "Signal and noise of diamond pixel detectors at high radiation fluences," *Journal of Instrumentation*, vol. 7, p. P09009, 2012.

[58] The RD42 Collaboration, "Diamond pixel modules," *Nuclear Instruments and Methods in Physics Research Section A*, vol. 636, p. S125, 2011.

[59] R. C. Alig, S. Bloom, and C. W. Struck, "Scattering by ionization and phonon emission in semiconductors," *Physical Review B*, vol. 22, p. 5565, 1980.

[60] S. Zhao, *Characterization of the Electrical Properties of Polycrystalline Diamond Films.* PhD thesis, Ohio State University, 1994.

[61] H. Pernegger et al., "Charge-carrier properties in synthetic single-crystal diamond measured with the transient-current technique," *Journal of Applied Physics*, vol. 97, p. 073704, 2005.

[62] H. Jansen, D. Dobos, T. Eisel, H. Pernegger, V. Eremin, and N. Wermes, "Temperature dependence of charge carrier mobility in single-crystal chemical vapour deposition diamond," *Journal of Applied Physics*, vol. 113, p. 173706, 2013.

[63] M. J. Berger et al., "XCOM: Photon Cross Section Database (version 1.5)." http://physics.nist.gov/xcom, 2010. [Online] Available: [2012, November 14].

[64] J. Beringer et al. (Particle Data Group), "Review of Particle Physics," *Physical Review D*, vol. 86, p. 010001, 2012.

[65] M. J. Berger, J. S. Coursey, M. A. Zucker, and J. Chang, "ESTAR, PSTAR, and ASTAR: Computer Programs for Calculating Stopping-Power and Range Tables for Electrons, Protons, and Helium Ions (version 1.2.3).." http://physics.nist.gov/Star, 2005. [Online] Available: [2012, November 14].

[66] T. P. Ma and P. V. Dressendorfer, *Ionizing Radiation Effects in MOS Devices and Circuits*. Wiley, 1989.

[67] I. Pintilie, G. Lindstroem, A. Junkes, and E. Fretwurst, "Radiation-induced point- and cluster-related defects with strong impact on damage properties of silicon detectors," *Nuclear Instruments and Methods in Physics Research Section A*, vol. 611, p. 52, 2009.

[68] A. Vasilescu, "Fluence normalisation based on the NIEL scaling hypothesis." presented at the 3rd ROSE workshop on Radiation Hardening of Silicon Detectors, Hamburg University and DESY, in DESY-PROCEEDINGS-1998-02, 1998.

[69] R. Wunstorf, *Systematische Untersuchungen zur Strahlenresistenz von Silizium-Detektoren für die Verwendung in Hochenergiephysik-Experimenten*. PhD thesis, Universität Hamburg, 1992.

[70] R. Wunstorf, "Radiation hardness of silicon detectors: current status," *IEEE Transactions on Nuclear Science*, vol. 44, p. 806, 1997.

[71] S. Ramo, "Currents Induced by Electron Motion," *Proceedings of the IRE*, vol. 27, p. 584, 1939.

[72] H. Spieler, *Semiconductor Detector Systems (Semiconductor Science and Technology)*. Oxford University Press, USA, 2005.

[73] F. Krummenacher, "Pixel detectors with local intelligence: An IC designer point of view," *Nuclear Instruments and Methods in Physics Research Section A*, vol. 305, p. 527, 1991.

[74] A. Affolder, P. Allport, and G. Casse, "Charge Collection Efficiency Measurements of Heavily Irradiated Segmented n-in-p and p-in-n Silicon Detectors for Use at the Super-LHC," *IEEE Transactions on Nuclear Science*, vol. 56, p. 765, 2009.

[75] D. Dobos, *Commissioning Perspectives for the ATLAS Pixel Detector*. PhD thesis, Technische Universität Dortmund, 2008.

[76] T. Fritzsch, R. Jordan, O. Ehrmann, and H. Reichl, "ECD Wafer Bumping and Packaging for Pixel Detector Applications," in *Proceedings EMPC 2007 the 16th European Microelectronics and Packaging Conference & Exhibition*, p. 122, Curran Associates, Inc., 2007.

[77] The ATLAS IBL Collaboration, "Prototype ATLAS IBL modules using the FE-I4A front-end readout chip," *Journal of Instrumentation*, vol. 7, p. P11010, 2012.

[78] M. Backhaus, "Characterization of new hybrid pixel module concepts for the ATLAS Insertable B-Layer upgrade," *Journal of Instrumentation*, vol. 7, p. C01050, 2012.

[79] M. Backhaus, "Development of an USB-based test system for the FE-I3 readout chips of the ATLAS pixel detector and Noise Occupancy Studies," Master's thesis, Universität Bonn, 2009.

[80] J. Grosse-Knetter, "Vertex Measurement at a Hadron Collider - The ATLAS Pixel Detector," 2008. Habilitationsschrift: Universität Bonn.

[81] F. Hügging, "Front-End electronics and integration of ATLAS pixel modules," *Nuclear Instruments and Methods in Physics Research Section A*, vol. 549, p. 157, 2005.

[82] M. Barbero et al., "A new ATLAS pixel front-end IC for upgraded LHC luminosity," *Nuclear Instruments and Methods in Physics Research Section A*, vol. 604, p. 397, 2009.

[83] M. Garcia-Sciveres et al., "The FE-I4 pixel readout integrated circuit," *Nuclear Instruments and Methods in Physics Research Section A*, vol. 636, p. S155, 2011.

[84] M. Barbero et al., "FE-I4 pixel readout chip and IBL module," in *PoS(Vertex 2011)038*, 2011.

[85] T. Hemperek et al., "Digital architecture of the new ATLAS pixel chip FE-I4," in *Nuclear Science Symposium and Medical Imaging Conference (NSS/MIC), IEEE*, 2009.

[86] L. Caminada, J. Fleury, D. Gnani, M. Garcia-Sciveres, F. Jensen, Y. Lu, and ManYMore, "ATLAS FE-I4 ASIC," in *PoS(Vertex 2012)023*, 2012.

[87] V. Zivkovic et al., "The FE-I4 pixel readout system-on-chip resubmission for the insertable B-Layer project," *Journal of Instrumentation*, vol. 7, p. C02050, 2012.

[88] M. Karagounis, D. Arutinov, M. Barbero, R. Beccherle, D. Darbo, R. Ely, D. Fougeron, M. Garcia-Sciveres, D. Gnani, V. Gromov, T. Hemperek, H. Junker, M. Menouni, A. Mekkaoui, R. Kluit, and J. D. Schipper, "Development of the ATLAS FE-I4 pixel readout IC for b-layer Upgrade and Super-LHC," in *TWEPP-08 Topical Workshop on Electronics for Particle Physics*, 2008.

[89] C. Gallrapp, "Planar Pixel Sensors for the ATLAS tracker upgrade at HL-LHC," *Nuclear Instruments and Methods in Physics Research Section A*, vol. 718, p. 323, 2013.

[90] S. Altenheiner et al., "Planar slim-edge pixel sensors for the ATLAS upgrades," *Journal of Instrumentation*, vol. 7, pp. C02051–C02051, 2012.

[91] Y. Unno et al., "Development of novel n+-in-p Silicon Planar Pixel Sensors for HL-LHC," *Nuclear Instruments and Methods in Physics Research Section A*, vol. 699, p. 72, 2013.

[92] R. Nagai et al., "Evaluation of novel KEK/HPK n-in-p pixel sensors for ATLAS upgrade with testbeam," *Nuclear Instruments and Methods in Physics Research Section A*, vol. 699, p. 78, 2013.

[93] R. Klingenberg, "Quality control on planar n-in-n pixel sensors - Recent progress of ATLAS planar pixel sensors," *Nuclear Instruments and Methods in Physics Research Section A*, vol. 699, p. 56, 2013.

[94] P. Weigell et al., "Characterization and performance of silicon n-in-p pixel detectors for the ATLAS upgrades," *Nuclear Instruments and Methods in Physics Research Section A*, vol. 658, p. 36, 2011.

[95] C. Gallrapp et al., "Performance of novel silicon n-in-p planar pixel sensors," *Nuclear Instruments and Methods in Physics Research Section A*, vol. 679, p. 29, 2012.

[96] A. Macchiolo et al., "Performance of n-in-p pixel detectors irradiated at fluences up to $5x10^{15}$ n_{eq}/cm^2 for the future ATLAS upgrades," *Physics Procedia*, vol. 37, p. 1024, 2012.

[97] A. La Rosa et al., "Novel Silicon n-in-p Pixel Sensors for the future ATLAS Upgrades," *Nuclear Instruments and Methods in Physics Research Section A*, vol. 718, p. 329, 2013.

[98] P. Weigell, *Investigation of Properties of Novel Silicon Pixel Assemblies Employing Thin n-in-p Sensors and 3D-Integration.* PhD thesis, Technische Universität München, 2013.

[99] T.-E. Hansen et al., "First fabrication of full 3D-detectors at SINTEF," *Journal of Instrumentation*, vol. 4, p. P03010, 2009.

[100] G.-F. Dalla Betta et al., "Development of Modified 3D Detectors at FBK," in *Nuclear Science Symposium and Medical Imaging Conference (NSS/MIC), IEEE*, p. 382, 2010.

[101] C. J. Kenney, S. I. Parker, J. Segal, and C. Storment, "Silicon Detectors with 3-D Electrode Arrays: Fabrication and Initial Test Results," *IEEE Transactions on Nuclear Science*, vol. 46, p. 1224, 1999.

[102] C. J. Kenney, S. I. Parker, and E. Walckiers, "Results from 3-D silicon sensors with wall electrodes: near-cell-edge sensitivity measurements as a preview of active-edge sensors," *IEEE Transactions on Nuclear Science*, vol. 48, p. 2405, 2001.

[103] A. Zoboli et al., "Double-Sided, Double-Type-Column 3-D Detectors: Design, Fabrication, and Technology Evaluation," *IEEE Transactions on Nuclear Science*, vol. 55, p. 2775, 2008.

[104] G.-F. Dalla Betta et al., "Characterization of 3D-DDTC detectors on p-type substrates," in *Nuclear Science Symposium Conference Record (NSS/MIC), IEEE*, p. 29, 2009.

[105] A. La Rosa et al., "Preliminary results of 3D-DDTC pixel detectors for the ATLAS upgrade," in *PoS(RD09)032*, 2009.

[106] A. La Rosa et al., "Characterization of proton irradiated 3D-DDTC pixel sensor prototypes fabricated at FBK," *Nuclear Instruments and Methods in Physics Research Section A*, vol. 681, p. 25, 2012.

[107] C. Da Vià, M. Boscardin, G. Pellegrini, and G.-F. Dalla Betta, "Technical Specifications and Acceptance Criteria for the 3D Sensors of the ATLAS IBL." https://edms.cern.ch/document/1162203/1, 2011.

[108] C. Da Vià et al., "3D silicon sensors: Design, large area production and quality assurance for the ATLAS IBL pixel detector upgrade," *Nuclear Instruments and Methods in Physics Research Section A*, vol. 694, p. 321, 2012.

[109] I. Rubinskiy, "An EUDET/AIDA Pixel Beam Telescope for Detector Development," *Physics Procedia*, vol. 37, p. 923, 2012.

[110] C. Hu-Guo, J. Baudot, G. Bertolone, A. Besson, A. S. Brogna, C. Colledani, G. Claus, R. De Masi, Y. Degerli, A. Dorokhov, G. Doziere, W. Dulinski, X. Fang, M. Gelin, M. Goffea, F. Guillouxb, A. Himmi, K. Jaaskelainen, M. Koziel, F. Morel, F. Orsini, G. Santos, M. Specht, Q. Sun, O. Torheim, I. Valin, Y. Voutsinas, and M. Wintera, "A ten thou-

sand frames per second readout MAPS for the EUDET beam telescope," in *TWEPP-09 Topical Workshop on Electronics for Particle Physics*, 2009.

[111] EUDET JRA1 Group, "EUDET Pixel Telescope Data Taking Manual - Updated Version for M26." EUDET: Detector R&D towards the International Linear Collider, 2010.

[112] G. Troska, *Development and operation of a testbeam setup for qualification studies of ATLAS pixel sensors.* PhD thesis, Technische Universität Dortmund, 2013.

[113] L. Snoj, G. Žerovnik, and A. Trkov, "Computational analysis of irradiation facilities at the JSI TRIGA reactor.," *Applied Radiation and Isotopes*, vol. 70, p. 483, 2012.

[114] Karlsruhe Institute of Technology, "The Karlsruhe Irradiation Center." http://www.ekp.kit.edu/english/irradiation_center.php. [Online; accessed 01-May-2012].

[115] CERN radiation-test facility, "CERN irradiation facilities (East Hall)." https://irradiation.web.cern.ch/irradiation/. [Online; accessed 01-May-2012].

[116] R. Fruehwirt, H. Pernegger, and M. Friedl, "Convoluted landau and gaussian fitting function." http://root.cern.ch/root/html/tutorials/fit/langaus.C.html. as part of the ROOT - A Data Analysis Framework Tutorial.

[117] J. Weingarten, *System Test and Noise Performance Studies at The ATLAS Pixel Detector.* PhD thesis, Universität Bonn, 2007.

[118] G.-F. Dalla Betta et al., "Development of 3D-DDTC pixel detectors for the ATLAS upgrade," *Nuclear Instruments and Methods in Physics Research Section A*, vol. 636, p. S15, 2011.

[119] S. Altenheiner et al., "Radiation hardness studies of n^+-in-n planar pixel sensors for the ATLAS upgrades," *Nuclear Instruments and Methods in Physics Research Section A*, vol. 658, p. 25, 2011.

[120] C. Gallrapp, "Initial measurements on Pixel Detector modules for the ATLAS upgrades," in *12th European Conference on Radiation and Its Effects on Components and Systems (RADECS)*, p. 739, 2011.

[121] M. Mikuž et al., "Diamond pad detector telescope for beam conditions and luminosity monitoring in ATLAS," *Nuclear Instruments and Methods in Physics Research Section A*, vol. 579, p. 788, 2007.

[122] R. L. Bates et al., "Charge Collection Studies and Electrical Measurements of Heavily Irradiated 3D Double-Sided Sensors and Comparison to Planar Strip Detectors," *IEEE Transactions on Nuclear Science*, vol. 58, p. 3370, 2011.

[123] P. Grenier et al., "Test beam results of 3D silicon pixel sensors for the ATLAS upgrade," *Nuclear Instruments and Methods in Physics Research Section A*, vol. 638, p. 33, 2011.

[124] A. Micelli et al., "3D-FBK pixel sensors: Recent beam tests results with irradiated devices," *Nuclear Instruments and Methods in Physics Research Section A*, vol. 650, p. 150, 2011.

[125] H. Kagan, M. Mikuž, and W. Trischuk, "ATLAS Diamond Beam Monitor (DBM)." https://edms.cern.ch/document/1211792/1, 2012.

[126] R. Klingenberg, D. Muenstermann, and T. Wittig, "Sensor Specifications and Acceptance Criteria for Planar Pixel Sensors of the IBL at ATLAS." https://edms.cern.ch/document/1212891/1, 2011.

[127] J. Jentzsch, "Quality assurance and functionality tests on electrical components during the ATLAS IBL production," *Journal of Instrumentation*, vol. 8, p. C02048, 2013.

[128] B. Mandelli, "Final characterization of the atlas ibl detector modules with 241am during the construction phase." ATL-INDET-SLIDE-2012-586, 2012.

[129] T. Wittig, *Slim Edge Studies, Design and Quality Control of Planar ATLAS IBL Pixel Sensors*. PhD thesis, Technische Universität Dortmund, 2013.

[130] L. A. Currie, "Limits for qualitative detection and quantitative determination. Application to radiochemistry," *Analytical Chemistry*, 1968.